Thrust Network Analysis

Exploring Three-dimensional Equilibrium

by

Philippe Block

B.Sc., M.Sc. in Engineering Sciences – Architecture
Vrije Universiteit Brussel, 2003

S.M.Arch.S. in Design and Computation / Building Technology
Massachusetts Institute of Technology, 2005

Submitted to the Department of Architecture
in Partial Fulfillment of the Requirements for the Degree of

Doctor of Philosophy in Architecture : Building Technology

at the

Massachusetts Institute of Technology

June 2009

Signature of Author:

Department of Architecture
May 1, 2009

Certified by:

John A. Ochsendorf
Associate Professor of Building Technology
Thesis Supervisor

Accepted by:

Julian Beinart
Professor of Architecture
Chairman, Department Committee on Graduate Students

John A. Ochsendorf
Associate Professor of Building Technology
Massachusetts Institute of Technology
Thesis Supervisor

Jerome J. Connor, Jr.
Professor of Civil & Environmental Engineering
Massachusetts Institute of Technology
Thesis Reader

Chris J. K. Williams
Senior Lecturer of Architecture & Civil Engineering
University of Bath
Thesis Reader

Thrust Network Analysis

Exploring Three-dimensional Equilibrium

by

Philippe Block

Submitted to the Department of Architecture
on May 1, 2009 in Partial Fulfillment of the Requirements
for the Degree of Doctor of Philosophy in Architecture: Building Technology

Abstract

This dissertation presents Thrust Network Analysis, a new methodology for generating compression-only vaulted surfaces and networks. The method finds possible funicular solutions under gravitational loading within a defined envelope. Using projective geometry, duality theory and linear optimization, it provides a graphical and intuitive method, adopting the same advantages of techniques such as graphic statics, but offering a viable extension to fully three-dimensional problems. The proposed method is applicable for the analysis of vaulted historical structures, specifically in unreinforced masonry, as well as the design of new vaulted structures. This dissertation introduces the method and shows examples of applications in both fields.

Thrust Network Analysis, masonry, historic structures, compression-only structures, limit analysis, equilibrium analysis, funicular design, form-finding, structural optimization, Gothic vaults, reciprocal diagrams.

Thesis supervisor: John A. Ochsendorf
Title: Associate Professor of Building Technology

Acknowledgements

First of all, I would like to thank my advisor, Prof. John Ochsendorf, for guiding my research and for being an amazing mentor. I strongly value his endless assistance, input and support. I am particularly grateful to him for allowing me to explore and develop my own ideas, not only being supportive of them, but also having pushed them tremendously with his ever to-the-point feedback. I want to thank him for all the opportunities he has given me, and I am looking forward to many more collaborations in the future. John wants his students to excel, and even do better than him, but he is making that very hard to do. It is a privilege and a true honor to be one of his students.

I thank my readers, Profs. Jerry Connor and Chris Williams, for their constructive feedback and insightful comments, which have pushed this dissertation that one step further. I want to thank Chris especially for having sparked this entire research, for giving clues that caused exciting, new ideas and explorations, and for being such an inspiration.

I want to thank a few people in particular who have had an important part in making this dissertation possible. First of all, I am very grateful to have had the chance to work towards this degree together with Matt DeJong. Our many discussions have led to countless interesting questions, sparked many ideas, and resulted in several clarifications. I hope we can continue bouncing ideas off of each other in the future. Several crucial breakthroughs were possible thanks to Xuan Vinh Doan's invaluable help with setting up the optimization problems. I am extremely indebted to Tom Van Mele's help with converting this thesis into LaTeX, resulting in this neat document. Rory Clune's careful reading helped clarifying the most tedious parts of my thesis. Finally, I am thankful to have received a lot of feedback in the initial development stages from Prof. Axel Kilian.

I want to thank several people for their feedback, comments or help, including Prof. Christopher Calladine, Prof. Waclaw Zalewski, Prof. Ed Allen, Prof. Werner Sobek, the late Prof. Ture Wester, Prof. Frédo Durand, Neri Oxman, Kenny Verbeeck, Dr. Tom Van Mele, John Curry, David Escobedo, Jürgen Hennicke, Prof. Mark Goulthorpe, Patrick McCafferty, Prof. Laura De Lorenzis , Prof. Larry Sass, Prof. Barb Cutler, Prof. Pierre Smars, Laurent Ney, Prof. Sigrid Adriaenssens, Dr. Alessandra Romano, Prof. Les Norford, Prof. Leon Glicksman, Prof. Andrew Tallon, Wyly Brown, Stylianos Dritsas, Riccardo Merello, Duks Koschitz, Yaniv Junno Ophir, Paul Kassabian, and last, but certainly not least, my colleagues in the JAO-team, Jenn Furstenau and Emily Whiting.

I would like to thank the Department of Architecture, the Building Technology Group and Prof. Ochsendorf for their financial support. Some research experiences were possible thanks to the Harold Horowitz (1951) Student Research Fund, and the generous support of Escobedo Construction.

I thank Shun Kanda for nurturing my passion for architectural design e.g. by inviting me to co-teach an architectural design studio at MIT in the Spring of 2007, and Prof. Bill Porter for his continuing support behind the scenes.

I spent the Fall of 2007 at the School of Architecture of the Danish Royal Academy of Fine Arts in

Copenhagen, Denmark, working closely with the late Professor Ture Wester. I am very thankful for the many discussions we had and for being introduced into the magical world of structural (plate) systems in nature. I hope to continue the work we started on extending his Lattice-Plate Dualism [Wester, 1997]. R.I.P., Ture. This exchange was possible because of a Danish Government Scholarship, granted by the Danish Ministry of Science, Technology and Innovation (CIRIUS) and the School of Architecture, who provided an amazing – Arne Jacobsen and Poul Kjærholm furnished – apartment. In the Spring of 2008, I was fortunate to work at the Institute for Lightweight Structures and Conceptual Design in Stuttgart, Germany with Prof. Werner Sobek. It was incredibly inspiring to go to work every day in Frei Otto's historical equilibrium structure. This exchange was possible thanks to a DAAD Research Grant, granted by the German Academic Exchange Service.

I thank Michael Ramage for inviting me to contribute to the structural design of the vaults for a museum in Mapungubwe, South Africa, a project of which I am very proud of to have been a part.

I learned a lot about the stone masonry process working as an intern at Escobedo Construction in Buda, TX. I am looking forward to continue working with them to create exciting, new stone architecture. I am extremely thankful to David and Kathy Escobedo, their entire family, and my friend J.T. Van Zandt for showing me what this southern hospitality is all about. Thanks y'all!

I just cannot imagine how I would have survived these – often very challenging – six years at MIT, being so far from home, without the support of several very special people in my life: thanks for refusing to forget me, Tom en An, Kenny en Lisa, and Thomas en Uschi; for giving me an "American family", Matt and Cara; and for being so proud of me and for always being there for me in good, but certainly in the less good times, my loving family in Belgium. Dank u wel!

Table of Contents

List of Figures

Part I

Introduction

Chapter 1

Introduction

1.1 Introduction

This dissertation develops a new methodology for assessing historic masonry structures and for designing new compression structures.

1.1.1 Safety assessment of historic masonry structures

Much of the world's architectural heritage consists of buildings in unreinforced masonry which need to be preserved for future generations. Many of these structures have complex geometries and their static equilibrium is still poorly understood. Figure 1.1 shows some examples of intricate, three-dimensional vaults.

When looking at the vaults in Figure 1.1, questions immediately arise about how these vaults stand and how stable they are. They have complex three-dimensional geometry, unknowable material properties,

(a) (b) (c)

Figure 1.1 – Complex three-dimensional masonry vaults: (a) Hieronymites Monastery Church (Jerónimos), Lisbon, Portugal, 1499-1528; (b) King Henry VII's Lady Chapel, Westminster Abbey, London, England, 1503-1519; and (c) Pfarrkirche, Königswiesen, Austria, 1520.

and numerous cracks and voids due to support movements over the centuries. The safety of these historic structures is difficult to determine and current computational tools are unsatisfactory.

To emphasize the inappropriateness of linear finite element analysis (FEA) for understanding the structural behavior of masonry assemblies, the simple arch example from Block et al. [2006] is reproduced. Figure 1.2 shows a linear elastic finite element analysis showing internal stresses due to self-weight predicted in two semi-circular masonry arches with thickness to radius ratios of 0.08 (Figure 1.2a-c) and one of 0.16 (Figure 1.2b-d). The FEA outputs of the two arches are very similar and it is difficult for the analyst to note any significant difference between the two arches of Figure 1.2.

A simple equilibrium analysis, represented by a compressive thrust line, immediately reveals the major difference between the two arches: the first arch (Figure 1.2a-c) is too thin to contain a thrust line and therefore, would not stand under its own weight unless the arch material had some appreciable value of tensile capacity. The linear elastic finite element analysis gives an unsafe and deceptive result for the thinner arch by assuming that the material is capable of resisting tension. While the FEA shows one possible stress state in the material, a linear elastic analysis does not say anything about the stability or collapse of the arch. The analysis of masonry arches is a well known problem, and this example immediately shows how difficult it is to draw conclusions from stress analysis of unreinforced masonry, even for simple two-dimensional problems.

Assessing the structural safety of three-dimensional masonry vaults is a pressing and difficult problem.

1.1.2 Direction of design

Progressions in computer graphics, and in particular the rapidly expanding possibilities of computer aided design (CAD) software, allow the modeling of very complex three-dimensional shapes. These important technological and computational developments resulted in an explosion of formal explorations in architectural design, and made it possible to generate new, and complex shapes, regardless of their structural stability.

Unfortunately, the structural solutions necessary to make these new shapes possible typically use an awkward accumulation of material. Such an approach to building is intellectually, and often architecturally dissatisfactory. This situation occurs because of a lack of structural thinking during the design process. Figure 1.3 shows the Walt Disney Concert Hall in Los Angeles by Frank Gehry. This Pritzker prize-winning architect promotes an architectural process which is disconnected from structures, and purposefully ignores any structural input. The structural engineer comes in at the end of his process to make his creations (cf. his "sketch" in Figure 1.3a) stand. This unidirectional process results in heavy structures, waste of material and awkward details (Figure 1.3c).

The world today is faced with global warming and rapidly decreasing natural resources [Gore, 2008; Head, 2009]. The built environment is responsible for approximately half of the greenhouse gas emissions [Pew Center, 2008]. Architectural designers therefore have an important responsibility towards the preservation of the planet, since the built environment has a major impact on the natural environment.

Figure 1.4 shows a successful example of a more sustainable design approach in a recent project for a new museum at the World Heritage Site of Mapungubwe in South Africa designed by Peter Rich Architects, Michael Ramage (Cambridge University), Henry Fagan and John Ochsendorf (MIT) [Ramage et al., 2008]. By determining the shape of three-dimensional compression forms, the authors were able to design masonry vaults with no reinforcing steel. The low stresses further made it possible to use cement-stabilized tiles pressed on-site without any added energy and using local soil, hence reducing the shipping

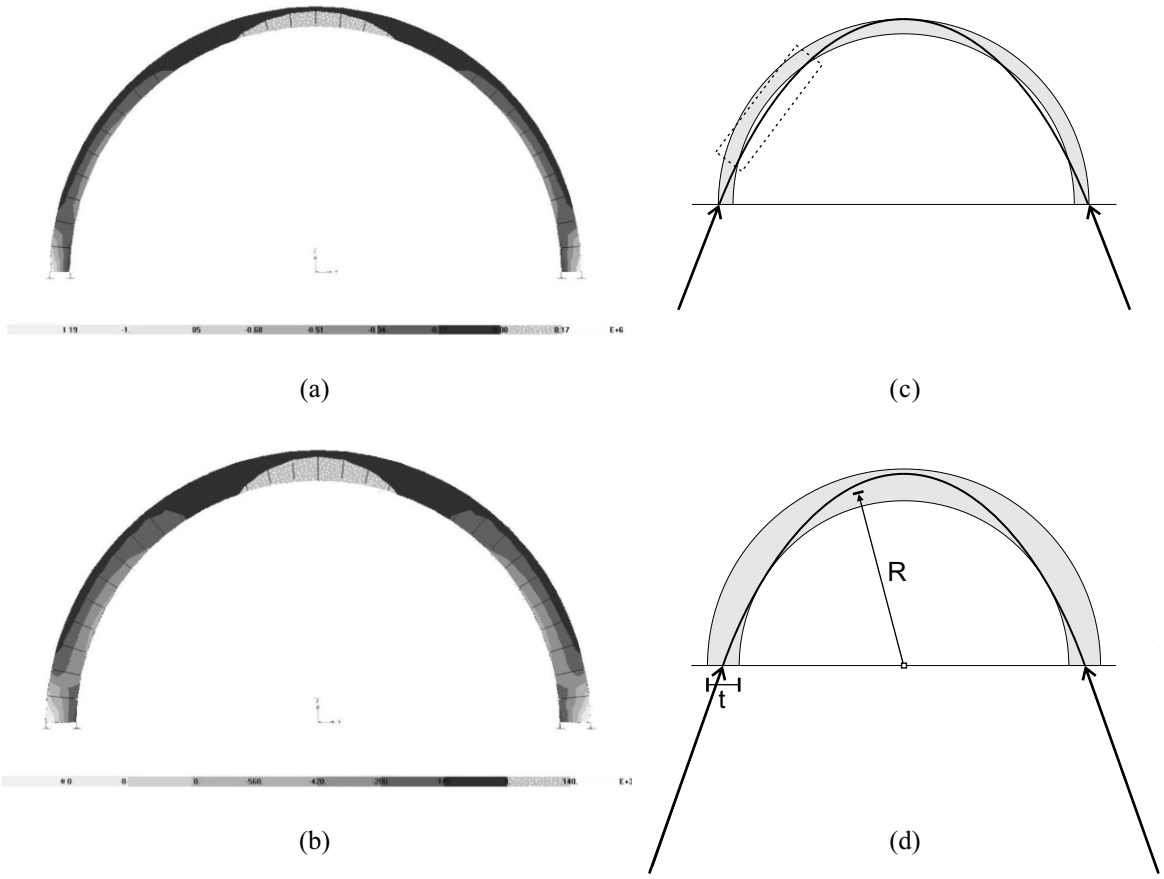

Figure 1.2 – Comparison between finite element analysis (a-b) and thrust line analysis (c-d) of two arches with t/R ratios of (a-c) 0.08 and (b-d) 0.16 [Block, 2005].

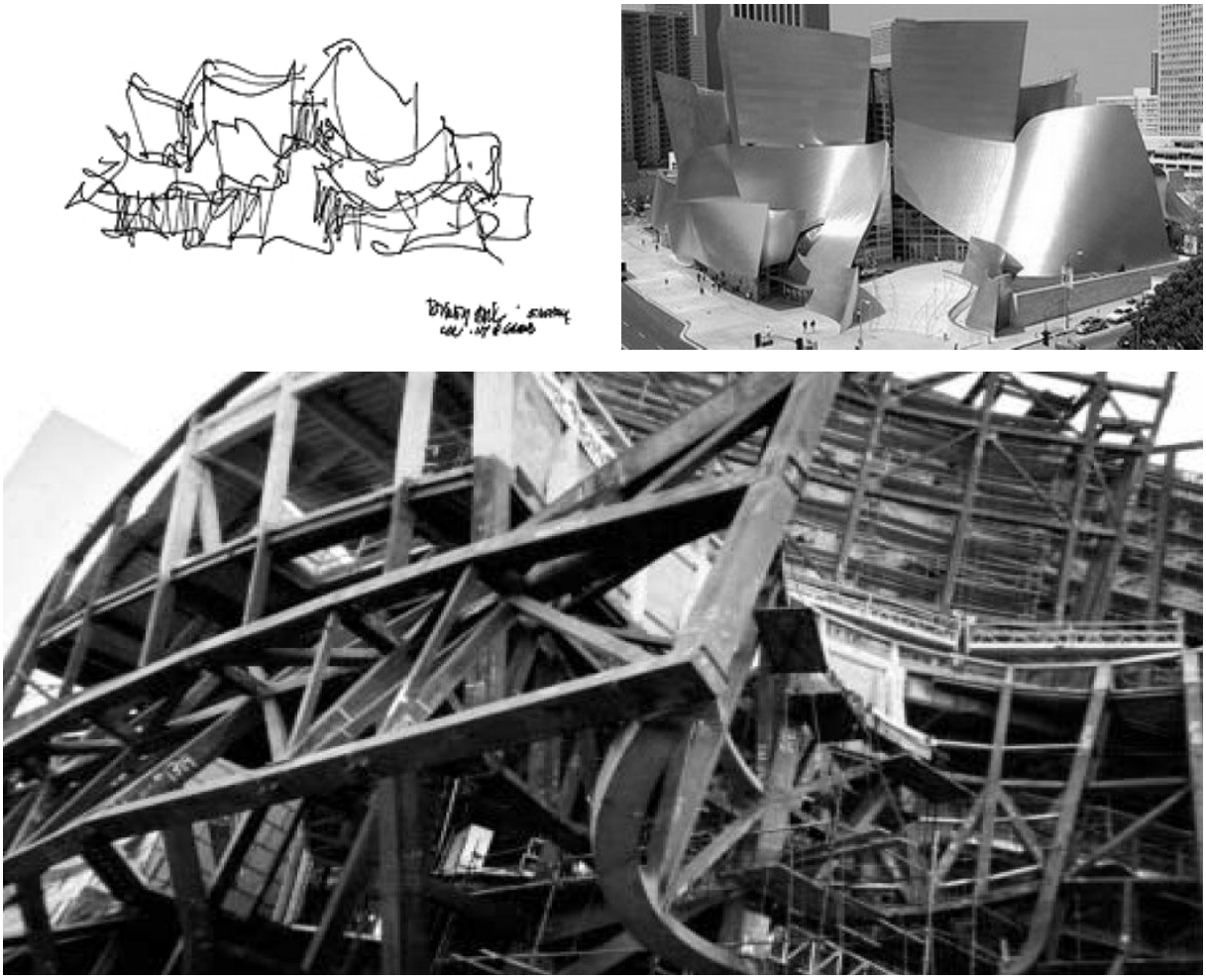

Figure 1.3 – (a) Conceptual sketch by Frank Gehry for the Walt Disney Concert Hall in Los Angeles, CA,1999-2003; (b) aerial view; and (c) the structure before receiving cladding [Tombesi, 2004].

(a)

(b)

(c)

Figure 1.4 – (a) New museum in Mapungubwe in South Africa, 2008-2009, using (b) cement-stabilized tiles made from local soil to build (c) structural compression vaults . Project credits: Peter Rich Architects, M. Ramage, J. Ochsendorf, M. Hodge, H. Fagan, A. Fitchett, P. Block and J. Bellamy. (Pictures by Peter Rich, Michael Ramage and James Bellamy).

of materials to the site. The Guastavino vaulting technique allowed the masons to build with minimal formwork resulting in very little waste. This project illustrates the potential for masonry compression forms in contemporary building design.

1.2 Statement of problem

From the previous discussion, two key problems can be distilled. There is an acute need for:

- better methods for assessing the safety of complex vaulted structures in unreinforced masonry; and
- new design tools which bring structural intuition into the design process, suggesting good form.

1.3 Equilibrium analysis of vaulted masonry structures

An equilibrium approach is necessary since not stresses, but stability is important for traditional masonry structures [Heyman, 1995; Huerta, 2001]. A better understanding of the mechanics of these discrete, compression-only structures is sorely needed to identify unsafe structures and to prevent unnecessary interventions.

The author's Masters thesis [Block, 2005; Block et al., 2006] developed tools for understanding and explaining the basic behavior of two-dimensional masonry structures. Such an intuitive approach is missing for three-dimensional structures. That thesis identified the potential of "thrust surfaces" for the analysis of 3-D systems and called for "the use of graphic statics for three-dimensional force network systems" [Block, 2005, p. 34].

1.4 Funicular design of vaulted structures

The most efficient way to transfer loads is through axial forces instead of by bending. Funicular systems act solely in compression or tension for a given loading. In a seminal paper, Heinz Isler [1959] suggested 39 shapes for funicular vaults, ending with "etc." to demonstrate the unlimited possibilities (Figure 1.5).

1.5 Outline of chapters

This dissertation presents a novel computational methodology for exploring three-dimensionalequilibrium shapes, Thrust Network Analysis (TNA). The approach allows the user to find possible funicular solutions under gravitational loading within a defined envelope. Through the use of intuitive graphical methods, the analyst gains control over the exploration of 3-D equilibrium solutions. The proposed method is applicable for the safety assessment of historic vaults with complex geometries in unreinforced masonry and for the design exploration of funicular shapes.

The dissertation is divided into four parts. In Part I, the motivation and goals of the research are defined and framed within the current state of the art.

Chapter 2 reviews the relevant literature and discusses the current state of equilibrium analysis of vaulted masonry structures, and the design of funicular structures. Previous methods for assessing the stability of three-dimensional vaulted masonry are reviewed and assessed, and a critical overview is given of the approaches used for designing three-dimensional funicular systems.

Part II presents Thrust Network Analysis (TNA), the new methodology developed in this dissertation.

Chapter 3 introduces the basic framework of the TNA method. It states the assumptions, fundamentals and key concepts; outlines the method in an overview of the main steps in the methodology; sets up the equilibrium constraints of the network model; formulates the problem as a linear optimization problem; and explains the solving procedure.

Chapter 4 elaborates on the implementation of TNA. It discusses how to discretize the structural action and loading conditions of three-dimensional vaults into discrete force network models, expanding on the geometric properties and constraints of allowed network topologies and the generation of their reciprocal

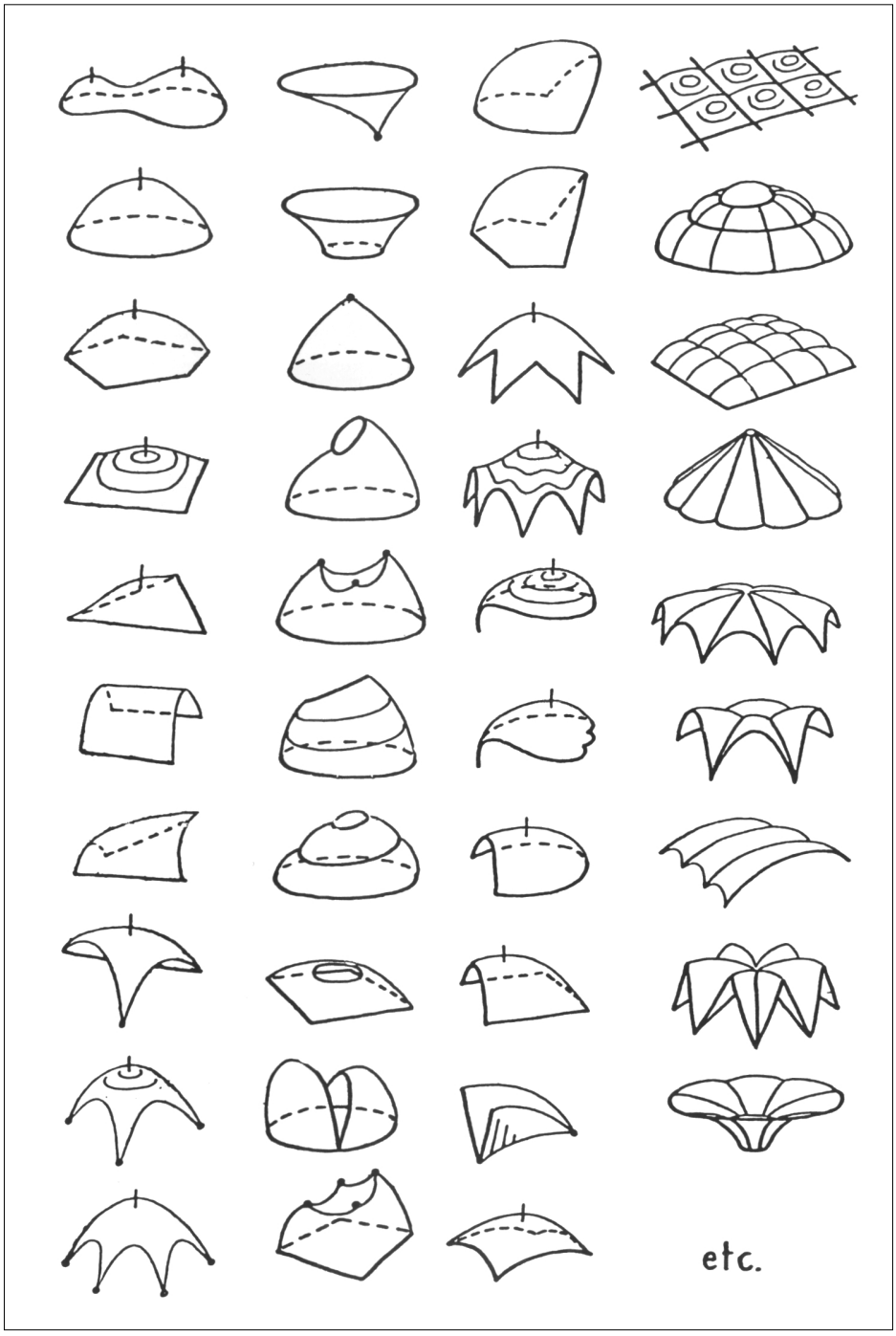

Figure 1.5 – Image from Heinz Isler's paper "New shapes for shells" at the First Congress of theInternational Association for Shell Structures(IASS) in 1959, featuring 39 shapes for funicular vaults [Isler, 1959].

force diagrams, which represent the forces in them. A new rule is introduced for deriving the degree of structural indeterminacy of three-dimensional network systems.

Chapter 5 discusses extensions to the basic TNA framework introduced in Chapter 3. Alternative objective functions are developed for the optimization problem; other loading cases and network configurations are discussed and the equivalence between reciprocal force diagrams and discrete Airy stress functions is explained. A non-linear extension to the basic framework is described, including the degrees of indeterminacy of complex three-dimensional networks.

Part III presents applications and results of TNA.

Chapter 6 shows the results of using TNA for the assessment of the stability of masonry vaults in order to validate the method. It discusses how to identify sensible force patterns to represent the structural action of different vault typologies and the requirements on the force networks for modeling pathologies. Several examples and case studies show the potential of this method to assess the stability of a wide range of complex vault types.

Chapter 7 demonstrates the power of the new method for the design exploration of compression-only structures.

In Part IV, Chapter 8 provides general conclusions and outlines future work in this field.

Chapter 2

Literature review

This chapter reviews the relevant literature. Previous equilibrium methods for assessing the stability of three-dimensional vaulted masonry are discussed, and a critical overview is given of the approaches used for designing three-dimensional funicular systems.

2.1 Equilibrium analysis of masonry vaults

Historic masonry constructions generally fail not due to lack of compressive strength, but due to instabilities caused by differential foundation settlements, earthquakes, or long-term deformations [Heyman, 1995; Ochsendorf, 2002]. Understanding the equilibrium of structures in unreinforced masonry is primarily a problem of stability. For structures to stand with negligible tensile capacity, they must have a good structural shape.

Boothby [2001] provides a critical overview of the different analysis methods for masonry arches and vaults, and calls for the development of an automated three-dimensional version of graphical equilibrium analysis. Huerta [2001; 2004] emphasizes the importance of an equilibrium approach for historic masonry structures and advocates the use of compressive thrust line analysis to explore the range of possible equilibrium states within the broader framework of limit analysis.

This section limits its scope to relevant precedents applying equilibrium analysis to masonry vaults. An extensive historical overview of equilibrium methods for the analysis of masonry structures was recently given by Huerta and Kurrer [2008] and Huerta [2008].

2.1.1 Ungewitter / Mohrmann's tables

In the third edition of Ungewitter's manual on Gothic construction [Ungewitter, 1890], Professor Mohrmann included a set of tables giving the horizontal thrusts for a set of vaults described by a series of parameters. Figure 2.1 shows one of these tables. They allow a rapid estimate of the thrust of masonry vaults, but are limited to common vault typologies.

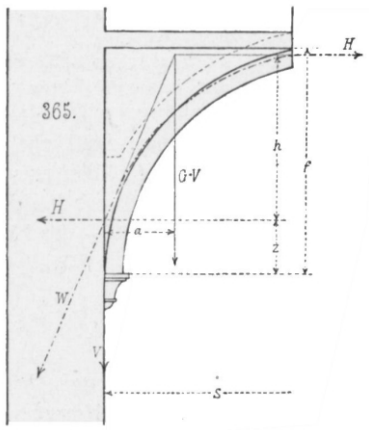

(a)

Tabelle 1.

Die Gewichte und Horizontalschübe der Gewölbe (s. Fig. 365).

Bezeichnung des Gewölbes	Gewicht von je 1 qm Grundriss-fläche V_0	Hebelarm des resultierenden Gewichtes a	Hebelarm der Horizontal-schübe h	Höhe des Widerlags-druckes über Gewölbebeginn Z	Horizontalschub für je 1 qm Grund-riss des lastenden Gewölbestückes H_0	Beispiel I. Gewölbe von 4.4 m Gewicht einer V	Schub Hälfte H	Beispiel II. Gewölbe von 8.8 m Gewicht einer V	Schub Hälfte H
I. Pfeilverhältnis 1 : 8.									
a. Kappen $^1/_2$ Stein aus porösen Ziegeln	200	0,22—0,23 s*	0,90 f**	$^1/_8$ bis $^1/_6$ f	360—400	1600	3200	6400	11500
b. $^1/_2$ Stein feste Ziegel oder $^3/_4$ Stein porös	270	rd $^2/_9$ s	oder		500—550	2160	4400	8600	16000
c. $^3/_4$ Stein feste Ziegel oder 1 Stein porös	370		$^1/_{10}$ s		700—750	2960	6000	11800	22400
d. 1 Stein feste Ziegel oder 20 cm dick Sandstein	500				950—1000	4000	8000	16000	30400
e. 30 cm dick Bruchstein	850				1600—1700	6800	13600	27200	51000
f. Überfülltes Ziegelgew., mit Fussb. 32 cm im Scheitel	—	0,20 s = $^1/_5$ s			—	5800	11000	26000	46000
II. Pfeilverhältnis 1 : 3.									
a. Kappen $^1/_2$ Stein aus porösen Ziegeln	230	0,19—0,21 s	0,85—0,75 f	$^1/_6$ bis $^1/_4$ f	160—180	1840	1440	7400	5100
b. $^1/_2$ Stein feste Ziegel oder $^3/_4$ Stein porös	310	rd $^1/_5$ s	oder		220—240	2480	1920	9900	7000
c. $^3/_4$ Stein feste Ziegel oder 1 Stein porös	420		$^3/_{10}$—$^1/_4$ s		300—330	3360	2640	13400	9600
d. 1 Stein feste Ziegel oder 20 cm dick Sandstein	570				420—450	4560	3600	18200	13400
e. 30 cm dick Bruchstein	1000				710—750	8000	6000	32000	22700
f. Überfülltes Ziegelgew., mit Fussb. 32 cm im Scheitel	—	0.17 s = $^1/_6$ s			—	7300	5200	37500	23000
III. Pfeilverhältnis 1 : 2.									
a. Kappen $^1/_2$ Stein aus porösen Ziegeln	260	0,17—0,20 s	0,80—0,70 f	$^1/_5$ bis $^1/_3$ f	110—120	2080	960	8300	3500
b. $^1/_2$ Stein feste Ziegel oder $^3/_4$ Stein porös	350	= $^1/_6$—$^1/_5$ s	oder		140—160	2800	1280	11200	4500
c. $^3/_4$ Stein feste Ziegel oder 1 Stein porös	480		$^2/_5$—$^1/_3$ s		190—220	3840	1760	15400	6100
d. 1 Stein feste Ziegel oder 20 cm dick Sandstein	700				280—320	5600	2560	22400	9000
e. 30 cm dick Bruchstein	1200				480—550	9600	4400	38500	15300
f. Überfülltes Ziegelgew., mit Fussb. 32 cm im Scheitel	—	0,16 s			—	8000	3800	41600	17600
IV. Pfeilverhältnis 2 : 3.									
a. Kappen $^1/_2$ Stein aus porösen Ziegeln	290	0,17—0,20 s	0,80—0,72	$^1/_5$ bis $^1/_4$ f	90—100	2320	800	9300	2900
b. $^1/_2$ Stein feste Ziegel oder $^3/_4$ Stein porös	380	= $^1/_6$—$^1/_5$ s	oder		110—130	3040	1040	12200	3500
c. $^3/_4$ Stein feste Ziegel oder 1 Stein porös	530		rd $^1/_2$ s		160—180	4240	1440	17000	5100
d. 1 Stein feste Ziegel oder 20 cm dick Sandstein	750				220—250	6000	2000	24000	7000
e. 30 cm dick Bruchstein	1300				400—430	10400	3440	41500	12800
f. Überfülltes Ziegelgew., mit Fussb. 32 cm im Scheitel	—	0,16 s			—	10500	3500	57900	17400
V. Pfeilverhältnis 5 : 6 bis 1.									
a. Kappen $^1/_2$ Stein aus porösen Ziegeln	340	0,16—0,19 s	0,80—0,75 f	$^1/_5$ bis $^1/_4$ f	80—90	2720	720	10900	2600
b. $^1/_2$ Stein feste Ziegel oder $^3/_4$ Stein porös	450		oder		100—110	3600	880	14400	3200
c. $^3/_4$ Stein feste Ziegel oder 1 Stein porös	650		rd $^2/_5$ s		150—160	5200	1280	20800	4800
d. 1 Stein feste Ziegel oder 20 cm dick Sandstein	900				210—230	7200	1840	28800	6700
e. 30 cm dick Bruchstein	1500				350—370	12000	2960	48000	11200
f. Überfülltes Ziegelgew., mit Fussb. 32 cm im Scheitel	—	0,15 s			—	13000	3000	77800	17500

* s = Spannweite, ** f = Pfeilhöhe.

(b)

Figure 2.1 – Mohrmann's tables in Ungewitter's "Lehrbuch der gotischen Konstruktionen" [1890] to rapidly calculate the thrust of masonry vaults.

2.1.2 Slicing technique

Thrust line analysis allows the understanding and exploration of the range of lower bound equilibrium solutions of masonry vaults, by showing the paths of the resultant compressive forces throughout the structure. For two-dimensional problems, it also suggests possible collapse mechanisms. Thrust line analysis is primarily a two-dimensional technique and is therefore most appropriate for the analysis of arches, flying buttresses or any structure which can be reduced to a sectional analysis [Nikolinakou et al., 2005]. Graphic statics can be used to compute thrust lines (see e.g. Wolfe [1921] or Swain [1927]). The main advantage of using graphic statics is the clear visual representation of the possible compressive forces in the system through the use of funicular polygons and thrust lines (Figure 2.2a).

Any three-dimensional vault can be analyzed using thrust line analysis when combined with the *slicing technique*, which was first discussed in Ungewitter [1890]. It slices the vault into two-dimensional imaginary strips, reducing the vault's structural behavior to a combination of two-dimensional problems which can be more easily analyzed (Figure 2.2b). Figure 2.2c shows one of Wittmann's applications of combining thrust line analysis with the slicing technique to analyze spatial vaults [Wittmann, 1879]. According to Huerta [2008], this is the first known application of this approach.

For most historic structures, such an analysis approach is appropriate and sufficient, although it obviously will not capture the full three-dimensional behavior of the structure and it relies heavily on the chosen slice geometry. The main drawback of such a methodology is that it is entirely manual and quickly becomes unwieldy and tedious [Boothby, 2001]. Barthel [1993] gives a thorough overview of the different levels of sophistication of the approximations necessary for thrust-line analysis of cross-vaults. Smars [2000] developed *Calipous*, software using an AutoCAD interface to perform pseudo-3D analysis in an automated fashion starting from the actual, measured geometry of the vaults (Figure 2.3a). Block [2005] and Block et al. [2006] proposed a method to produce models which contain the graphical construction

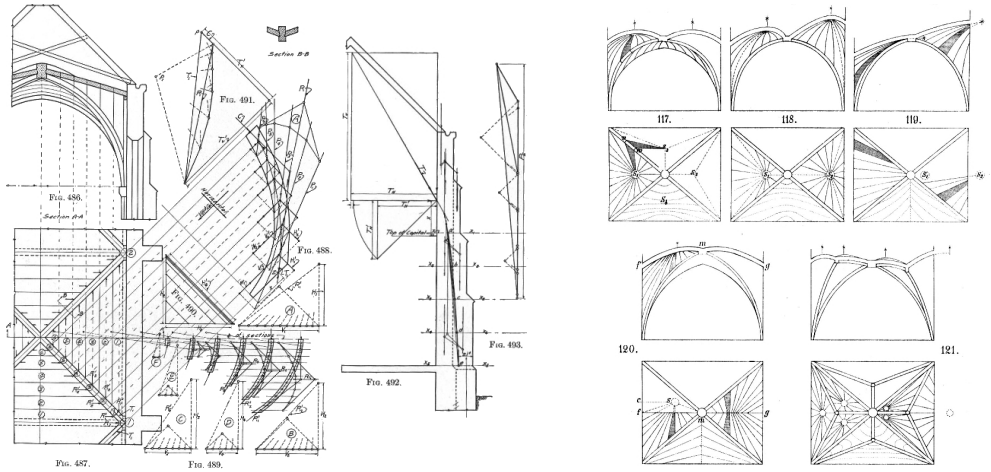

(a) (b)

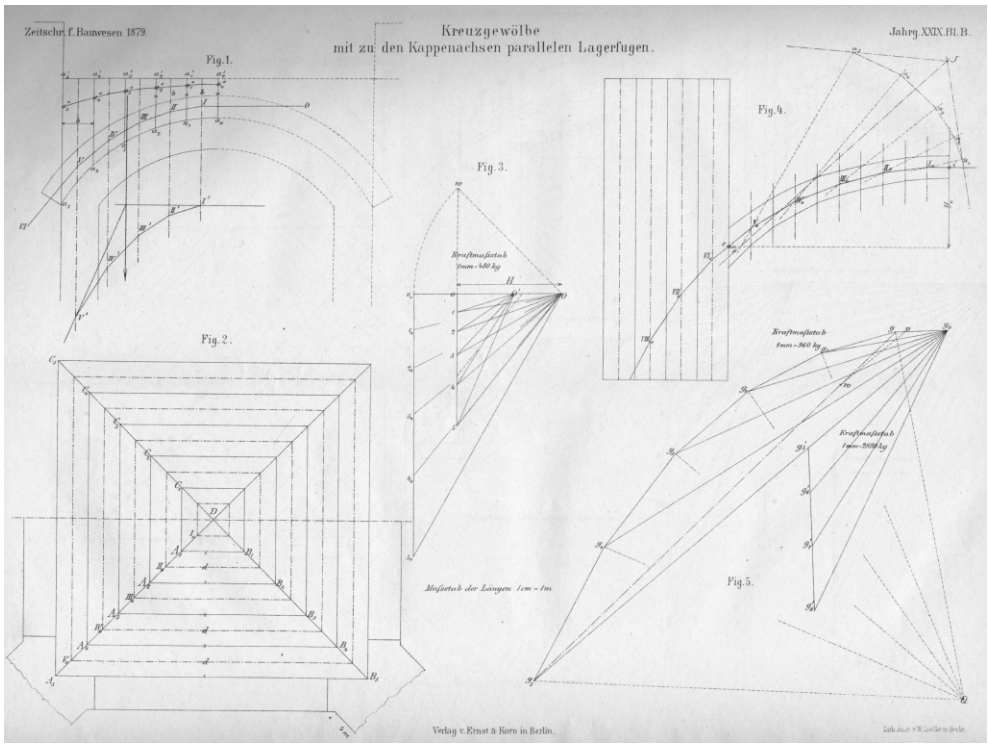

(c)

Figure 2.2 – (a) A pseudo-3D analysis of a gothic rib vault using the slicing technique and graphic statics by Wolfe [1921]. (b) Slicing technique applied to different web geometries introduced by Mohrmann [Ungewitter, 1890] and (c) the first known application of thrust-line analysis combined with the slicing technique by Wittmann [1879].

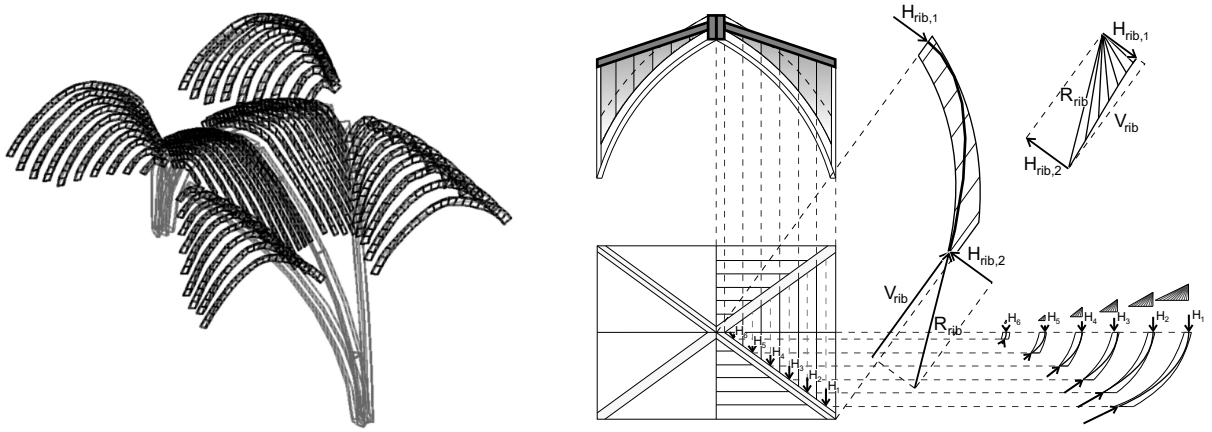

Figure 2.3 – (a) Thrust lines in slices taken through the vault's actual, deformed geometry [Smars, 2000]; and (b) interactive thrust line analysis allowing a parametric exploration of rib vault [Block, 2005].

but which are parametric and interactive, reducing the tedious iterative nature of traditional graphic methods (Figure 2.3b). However, the construction of these models is still quite complicated and time-consuming. Also, more complex vault geometries are hard to represent using only a combination of two-dimensional views. It is not surprising therefore that all of the above references deal mainly with cross vaults or groin vaults. For more complicated vault types, it becomes harder to assume appropriate cuts, and to understand how the different two-dimensional arches balance in three-dimensional space.

2.1.3 Equilibrium shell analysis

Heyman [1966] introduced a rigorous framework of limit analysis applied to masonry structures. For 3-D structures, instead of using graphical methods, he used membrane solutions [Green and Zerna, 1968; Calladine, 1983] for specific vault typologies, such as domes, groin and rib vaults or fan vaults (Figure 2.4), to use them in an equilibrium analysis by checking if these membrane solutions fit within the vault section. He often used the slicing technique to inform the derivation of these formulations, resulting in equilibrium shell equations usable for a wide range of related structures [Heyman, 1977].

This approach gives the thrust values for vaults based on the membrane solution, but it is not clear how changes in the level of fill for example are taken into consideration in these general formulations. While membrane solutions find an equilibrium state that lies near the centerline of the vault, the result is a safe lower bound approach and does not take full advantage of the actual thickness of the vault to carry the loads.

2.1.4 Rigid block limit analysis

The structural behavior of historical masonry is a problem of stability and not of stresses, since these are typically very low in these structures. As a result, scaled block models with sufficient friction can be used to model the stability of actual vaults. Figure 2.5a shows explorations by Danyzy [1732] to test the

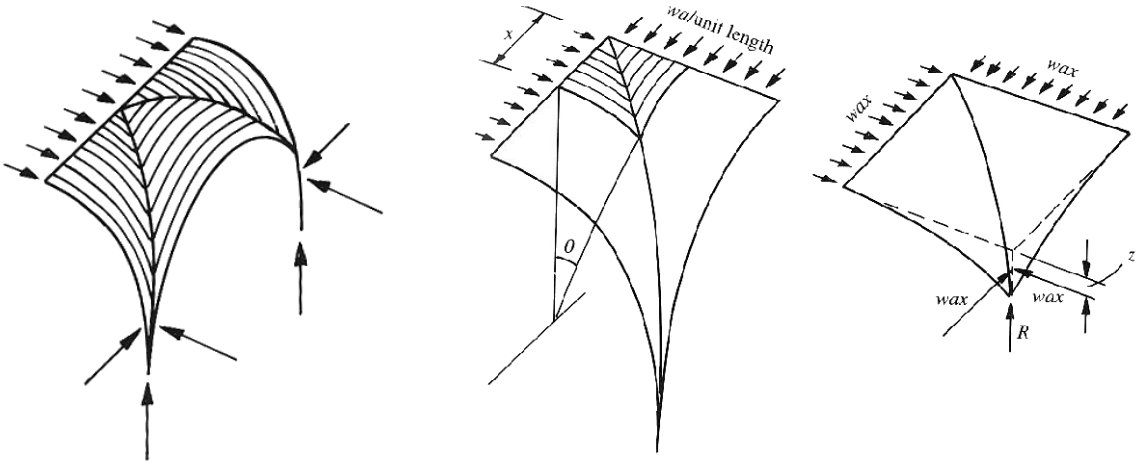

(a) (b) (c)

Figure 2.4 – (a) Groin vault sliced into parallel arches and (b-c) parameter definition, taken from a detail of (a), to set up the equilibrium shell equations [Heyman, 1977].

collapse modes of arches on buttresses.

Livesley applied limit analysis to three-dimensional rigid block assemblies by modeling the interaction forces at the interface between all stones [Livesley, 1978, 1992]. All the interaction forces between voussoirs are computed in an overall optimization scheme. His approach is perhaps the most rigorous way of describing the stability of a rigid block assembly. Whiting et al. [2009] use Livesley's framework in combination with procedural modeling to explore the limits of stability by exploration. The contact points of the resultants at each interface can be seen as the three-dimensional *locus of pressure points* of the vault [Moseley, 1833; Ochsendorf, 2002]. The surface going through these points is related to a surface of thrust.

2.1.5 Force network method

The main challenge of analyzing three-dimensional masonry vaults is that they are highly indeterminate structures. For a typical vault, there are infinite compressive solutions which could explain its safety: different assumptions can be made about the flow of forces, the force distributions, and the support conditions.

O'Dwyer [1991; 1999] proposed a promising three-dimensional equilibrium approach based on force networks, which goes beyond two-dimensional thrust lines. He implemented optimization methods to investigate masonry vaults by finding possible compression-only force networks which are entirely contained within the boundaries of the vault. His work set up a powerful framework allowing different choices of force patterns to represent the infinite internal force equilibrium of the highly indeterminate masonry structures (i.e. not limited to a singular structural action as in the slicing technique). He also incorporated loading and structural discontinuities, and vault pathologies such as cracks.

The main drawback of O'Dwyer's approach is the inability to deal with the high degree of indeterminacy of three-dimensional force networks which represent possible internal force paths in the vaults, limiting

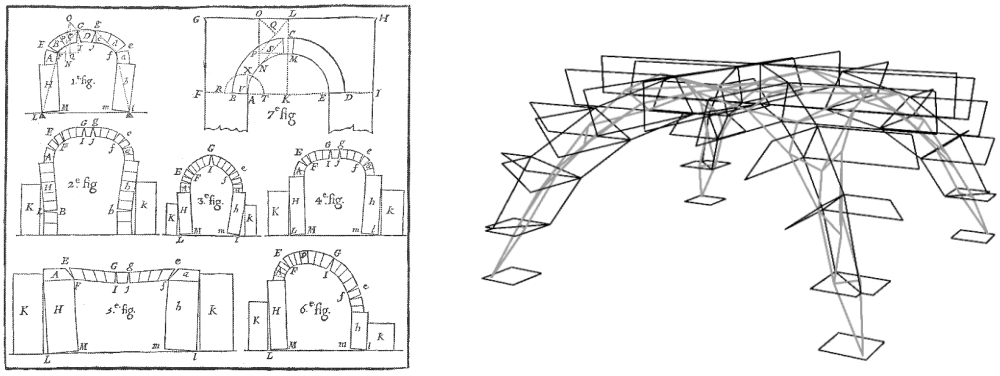

(a) (b)

Figure 2.5 – (a) Drawings of plaster model experiments of arch collapse [Danyzy, 1732]; and (b) limit analysis applied to a groin vault, the intersection points of the resultants at each face can be connected to form a thrust surface, or more accurately a 3-D locus of pressure points [Whiting et al., 2009].

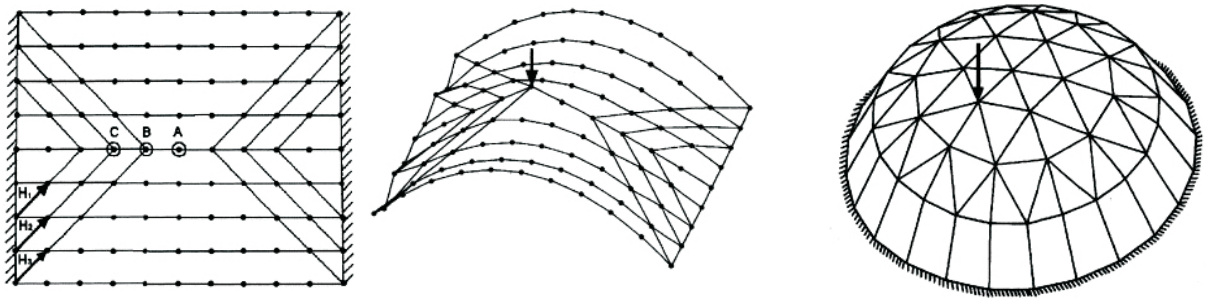

(a) (b)

Figure 2.6 – (a) The chosen force network topology and equilibrium solution for a barrel vault with point load, and (b) the compression-only solution of a dome with a point load [O'Dwyer, 1999].

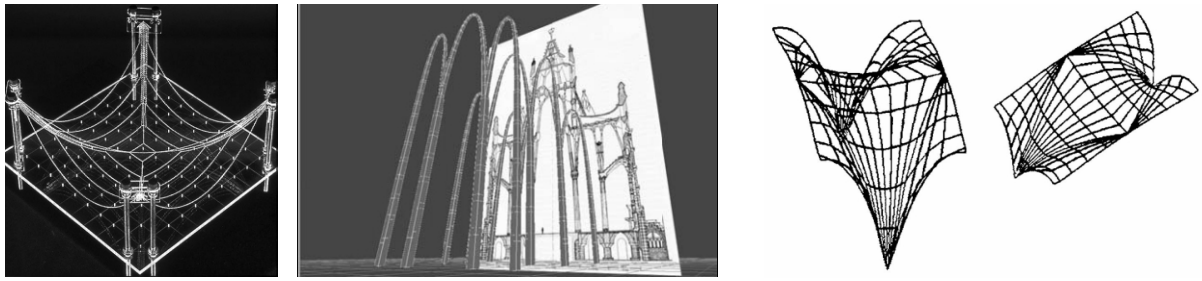

(a) (b) (c)

Figure 2.7 – (a) Hanging model of groin vault (Institut für Leichtbau Entwerfen und Konstruieren, ILEK); (b) fitting catenary solution in section using visual clues [Kilian, 2007]; and (c) 3-D solution using a funicular network model and optimization [Andreu et al., 2007].

the applications to problems where assumptions could be made on the force distribution, such as simple network topologies or networks with a high level of symmetry. Although different force path assumptions can be included in the force network, the solutions are still dependent on the mesh choice. The analyst needs to make an informed guess for the geometry of the force network based on experience or intuition. It is nonetheless surprising that this promising approach has not been explored further.

2.1.6 Funicular model

Poleni [1748] used Robert Hooke's [1675] hanging chain idea – *As hangs the flexible line, so but inverted will stand the rigid arch* – for the analysis of the cracked dome of St. Peter's in Rome. He assessed the stability of the dome by hanging a string loaded with weights proportional to segments of a radial slice of the dome in front of a scaled drawing of a section through the dome. This becomes very challenging and time-consuming for a three-dimensional network. Furthermore, it becomes quite difficult to relate the hanging shape to the geometry of the vault. Also, not every network topology works and tweaking the hanging model to fit within the section is hard to achieve for more involved networks than a simple groin vault (Figure 2.7a).

Physical models are too cumbersome for the analysis of complex 3-D vaulted masonry. Virtual hanging models overcome some of the issues of the physical models. Kilian [Kilian, 2007] develops a virtual hanging model and shows how to steer the funicular network using visual or geometric clues to constrain the models (Figure 2.7b). Recently, the problem of finding a virtual hanging-string (i.e. funicular) network constrained within the limits of a vault has been implemented within an optimization framework by Andreu et al. [Andreu et al., 2007], as shown in Figure 2.7c. This approach is promising and complete as an approach for the assessment of vaulted masonry. It is not clear how the edges of the network, which is free to find its equilibrium within the vault's section, can be controlled in the case of discrete or partially supported vaults. Also, the optimization problem may want to be reformulated to produce the range of possible thrust values instead of the one solution closest to the center line of the vault.

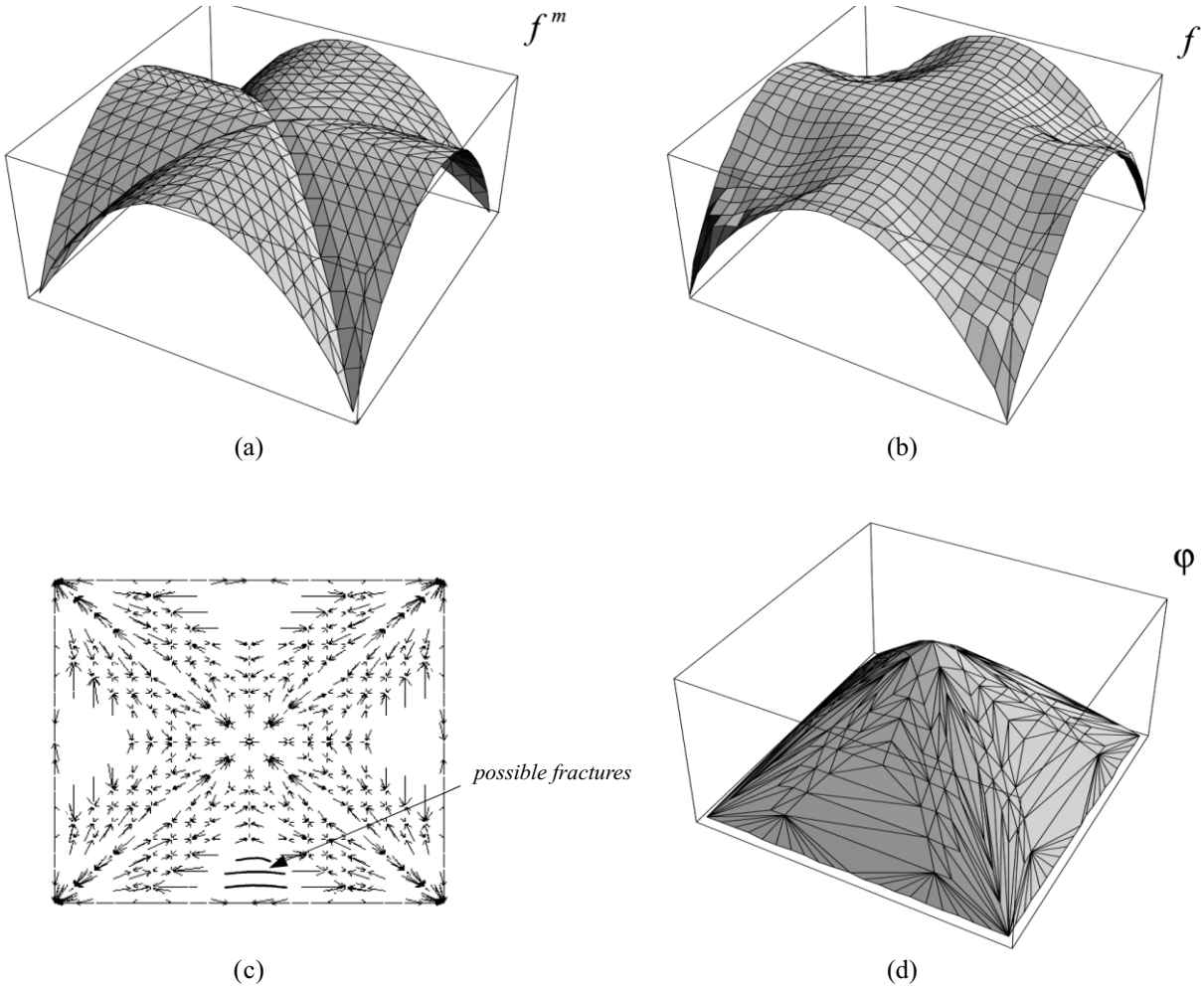

Figure 2.8 – (a) The starting mesh, before the optimization, (b) visualization of the optimal thrust surface, (c) visualization of the flow of forces in the obtained form (d) the optimized discrete Airy stress function [Fraternali and Rocchetta, 2002].

2.1.7 Stress functions

Fraternali and Rocchetta [2002] and Fraternali [2003] proposed a new approach for masonry vaults using piecewise-linearly approximated thrust surfaces. Their force equilibrium is related to discrete Airy stress functions, and this approach is a 3-D application of the *lumped stress method* [Fraternali et al., 2002].

The method finds the optimal shape of the discretized thrust surface to fit within the section of the vault using a geometrical algorithm on the polyhedral stress function. This approach optimizes the thrust surface by manipulating the discrete stress function iteratively. Because the stress function and topology of the discretized thrust surface are a direct mapping of each other, this results in a progressive combined topological and geometrical optimization, so it is not dependent on the initial topology.

Although it could be achieved using the combination of discrete thrust surfaces and Airy stress functions, the employed solving algorithm does not allow the incorporation of structural discontinuities. But if

started from the initial, perfect geometry, the authors claim that this approach suggests where cracking might occur for the specific vault geometry being analyzed. The generality and validity of their approach to identify possible areas of cracking needs to be further investigated. As an assessment tool for masonry, it will only provide a yes/no answer on the stability of the vault. The solving procedure also does not address situations with non-properly supported vaults, e.g. only reactions at the corners.

Although several promising approaches have been identified, a versatile equilibrium approach to assess the safety of three-dimensional masonry structures is still needed.

2.2 Design of funicular vaults

This section will give an overview of three-dimensional approaches for the design of funicular vaults. There are not many precedents for this, since funicularity is not often used as a starting point in design. Instead, the design often develops without any structural considerations and is then optimized for stresses or deflections [Ramm et al., 1993, 1997]. There are some promising trends in this area, such as *morphogenesis* [Pugnale and Sassone, 2007], but in essence, the start of the design process is often an un-informed, structurally poor shape. The form-finding processes discussed in this section all inherently have a structural rationale, seeking axial-force-only solutions.

2.2.1 Graphic statics

Graphic statics is a powerful and intuitive methodology for exploring funicular form in 2-D [Culmann, 1866, 1875; Cremona, 1879, 1890; Zalewski and Allen, 1998]. The force polygon and force diagram are linked through geometric constraints and changes can occur in both the form polygon and force polygon [Kilian, 2006a]. This allows exploration of either form or forces while each change in one representation affects the results in the other through the geometric constraints. *Active Statics* implements these graphical methods into an interactive, real-time tool, which allows for an interactive design exploration [Greenwold and Allen, 2001]. However, the method is limited to two-dimensional systems. Figure 2.9 shows a three-dimensional extension of graphic statics by Föppl [1892]. The process becomes very complicated, requiring the knowledge of the many rules and specific constructions of graphic statics and descriptive geometry. This process is challenging because three-dimensional structures are analyzed on flat sheets of paper. Furthermore, the approach only deals with statically determinate, rigid, 3-D bar-node systems.

2.2.2 Physical hanging models

Heinrich Hübsch (1795–1863) used simple hanging string models for building designs in the 19th century [Tomlow et al., 1989; Gerhardt, 2002a]. Most famously, Antoni Gaudí (1852-1926) used three-dimensional hanging models (Figure 2.10a) for the crypt of the Colònia Güell. The hanging model of the crypt was realized by a highly skilled team from 1898 to 1908 [Tomlow et al., 1989]. Making the physical model was tedious and time-consuming. An initial topology for the network of connected strings had to be chosen for the network which was adapted and regularly updated to move towards design ideas. For hanging models, the effect of removing, adding or adjusting the lengths of strings is not straightforward at all, since any local changes to the network influenced the global equilibrium solution. It was hard to control or achieve the desired shape. Furthermore, the weights had to be updated constantly as the nodes move

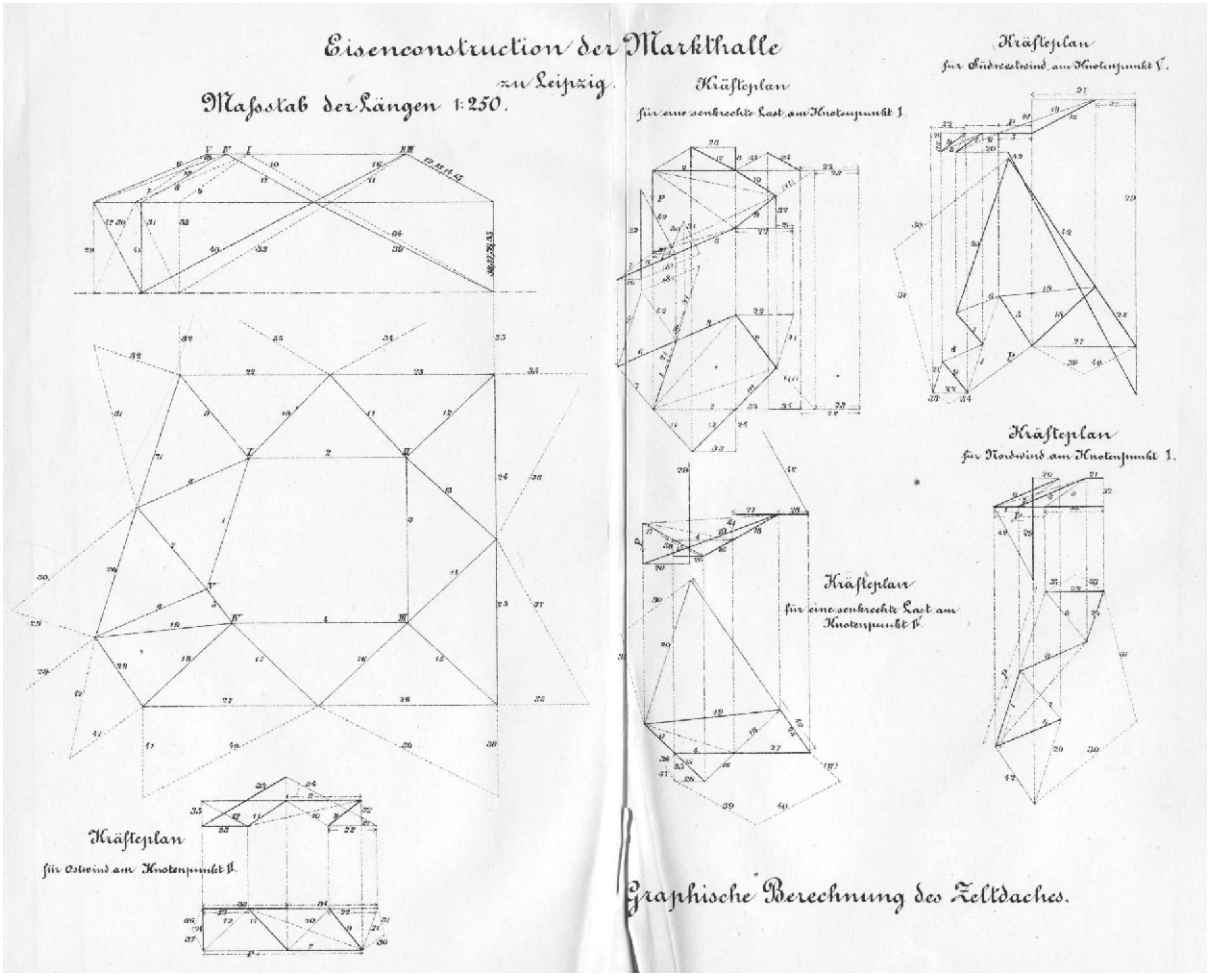

Figure 2.9 – Three-dimensional graphic statics using projective geometry for a determinate frame [Föppl, 1892].

around in space, which then again influenced the equilibrium causing the nodes to shift again to find a new equilibrium. The entire process demands a careful, iterative approach.

Physical hanging models are excellent design explorers since they address both structural and formal considerations and present the designer at all times with a status of the design that reflects the cumulative changes applied to the model [Kilian, 2006a]. Large models can facilitate and encourage creative team work and hanging models are still relevant today [Addis, 2007].

Heinz Isler (1926–) perfected a technique of hanging cloth models, dipped in plaster or self-setting polyester. After hardening, these perfect tension models were inverted to become a compression-only shell. The measured shape is then scaled up to the actual size of the vault [Chilton, 2000]. Although Isler explored different form-finding techniques, the obtainable shapes depend heavily on the materials and techniques used. A real issue in using this technique is that it requires the experience, structural intuition, and skills that Isler acquired over decades of working. Furthermore, the process demands meticulous detail and a lot of patience.

Frei Otto (1925-) and his team at the Institut für Leichte Flächentragwerke (IL) at the University of Stuttgart explored a variety of physical form-finding techniques, from hanging models to soap models. The shape of the lattice grid shell of the Multihalle in Mannheim, for example, was found using a very accurate hanging model (Figure 2.10e). These models gave the designers flexibility over the shape of the vaults, but again, it was a tedious and iterative process. An important disadvantage of using these physical hanging models is that the forces in the members are only found at the end. This means that the designer receives feedback about the overall geometry of the vault but not about the forces necessary to achieve a certain equilibrium shape. The first digital model at the IL was created in 1966 by Klaus Linkwitz [Serebryakova, 2006], announcing a new era of computational form-finding.

2.2.3 Computational Form-finding

For the form-finding of tension structures today, one of the main approaches is the force density method introduced by Linkwitz and Schek [1971] for finding the equilibrium shape of tension networks (Figure 2.11). By introducing force densities, which are defined as the ratio of the axial force of a branch to its length, the equations expressing the equilibrium of the networks could be linearized. Due to the development of sparse matrix techniques, these linear equations could be solved efficiently [Gründig et al., 2000]. Although developed and used mainly for finding the equilibrium shape of pre-tensioned membranes or cable nets and inflated structures, the force density method can also be used to model hanging networks.

Initial values for these force densities need to be chosen for the first-order form-finding. Note that if constant force densities are used throughout the network except at the corners and edges where stress concentrations can occur its shape forms a minimal surface between the given boundaries. The equilibrium values of the force densities are found in an iterative optimization process. So, the relations between the choice of force densities and the three-dimensional equilibrium solution are not straightforward. There is nothing that informs the user on how to distribute the forces to obtain a desired three-dimensional shape. There is also no option to constrain a solution to a predefined solution space.

The other main category of methods is based on dynamic relaxation (DR) [Barnes, 1999]. DR is mostly used to improve given input shapes, but does not allow the designer to easily interact with the optimization process. New, interactive evolutions of DR systems, which will be discussed in the next section, are important improvement relating designer input, reducing most of the shortcomings of DR.

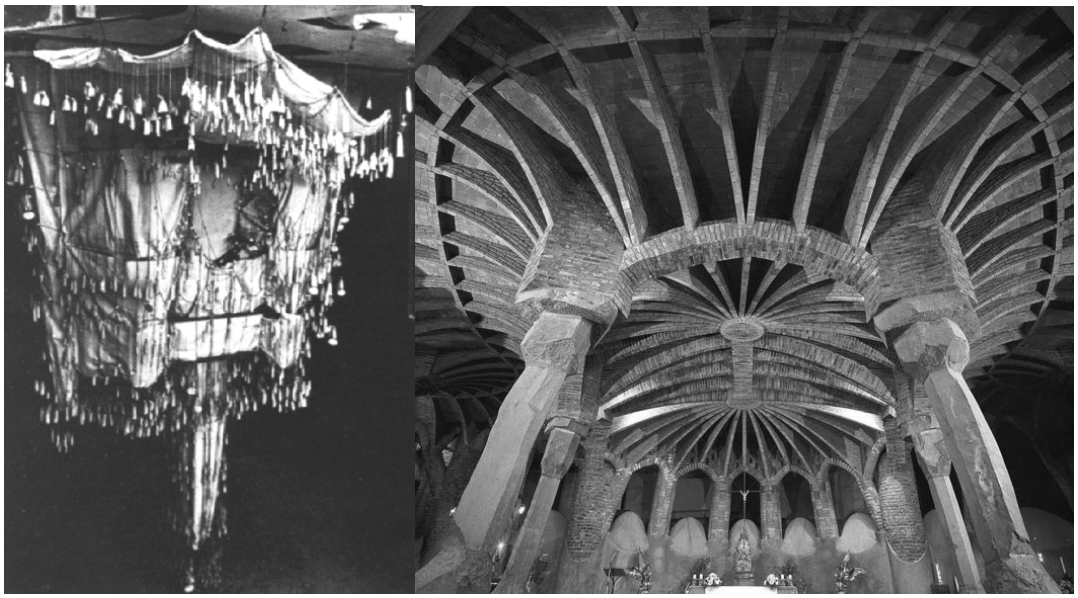

(a)

(b)

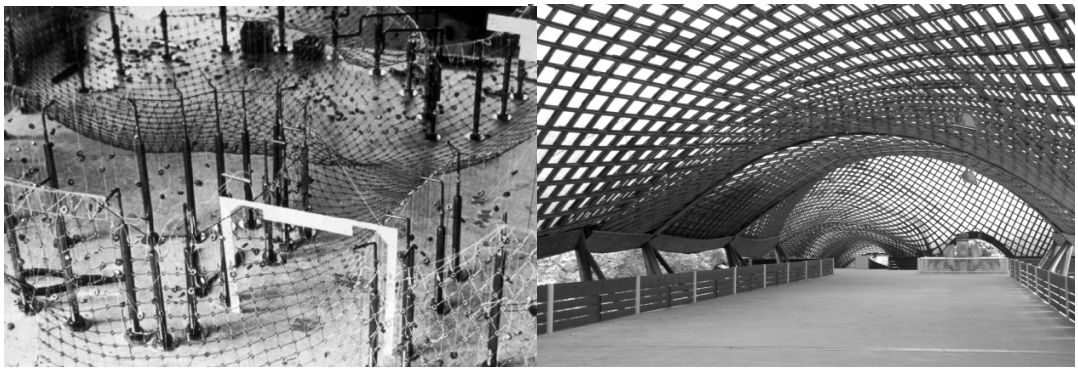

(c)

Figure 2.10 – (a) Antoni Gaudí's hanging model [Tomlow et al., 1989] for the crypt of the chapel of the Colònia Güell, 1898-1916 (Picture by Pedro Uhart); (b) Heinz Isler's hanging model and Isler's tennis hall shells, Heimberg, 1978 [Chilton, 2000]; (c) hanging model by Frei Otto's team at the Institut für Leichte Flächentragwerke (IL) in Stuttgart [Addis, 2005] for the Multihalle in Mannheim, Germany, 1975.

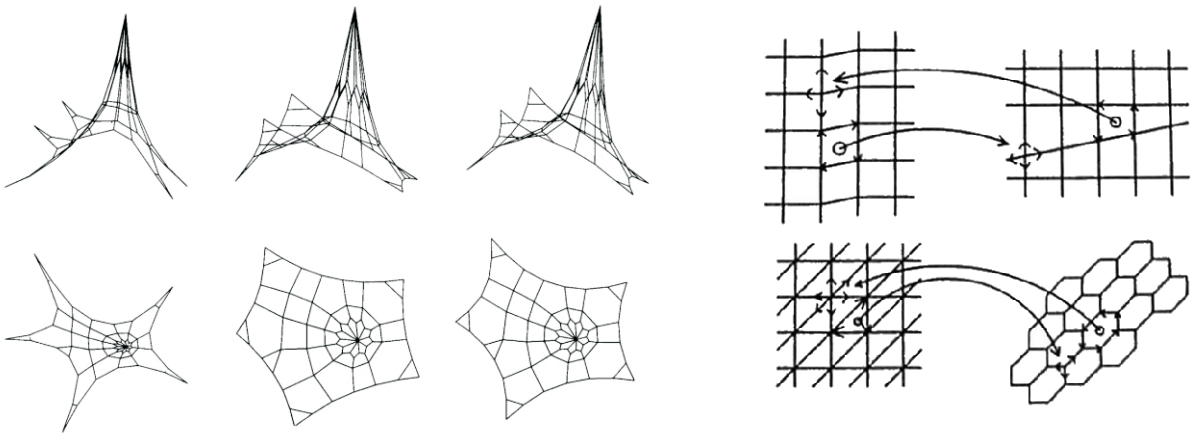

(a) (b)

Figure 2.11 – (a) Series of tensioned equilibrium networks found between five low points and one high point with different proportions of force densities for the inside of the network compared to the edges [Schek, 1974]; (b) reciprocal surfaces from Williams [1986].

An important reference for this disseration, which will be expanded on later, is Williams' [1986] use of reciprocal figures which describe the in-plane equilibrium of unloaded tensile membranes, represented by a discretized network (Figure 2.11b). This mapping of reciprocal figures onto two reciprocal surfaces to solve for its 3-D equilibrium is very powerful, but possible because the surfaces are only loaded by in-plane pre-stress without external, out-of-plane loading.

2.2.4 Interactive form-finding

Inspired by cloth simulation in the computer graphics community, Simon Greenwold wrote a Particle Spring (PS) library for Processing [Reas and Fry, 2007] which is basically an application of dynamic relaxation [Barnes, 1999]. Since 2002, Axel Kilian has been developing the CADenary for virtual explorations of hanging strings and meshes [Kilian, 2004a, 2006b] (Figure 2.12). The novelty of his implementation is to combine the dynamic simulation and interactive environment to find equilibrium and to allow the user to playfully explore these constantly evolving structures [Kilian, 2004b; Kilian and Ochsendorf, 2005]. He argues that discovery of form can occur in transitional, pre-optimized states.

This design tool allows the user to explore hanging models in the virtual world [Kilian and Ochsendorf, 2005], but as with physical models, it is hard to control and predict how the final shape of the compression network will look if local changes are being made or a string model is being assembled and hung under gravity. Kilian [2004b] tried to address the issue of translating this wire frame representation into an actual structure by creating connection rules for extruding sections to the form-finder. That aspect can be considered more as a way of giving feedback about the relative sizes of the forces in the system.

Interactive design tools are very powerful, but their manipulation and control has to be improved for satisfactory and flexible design exploration.

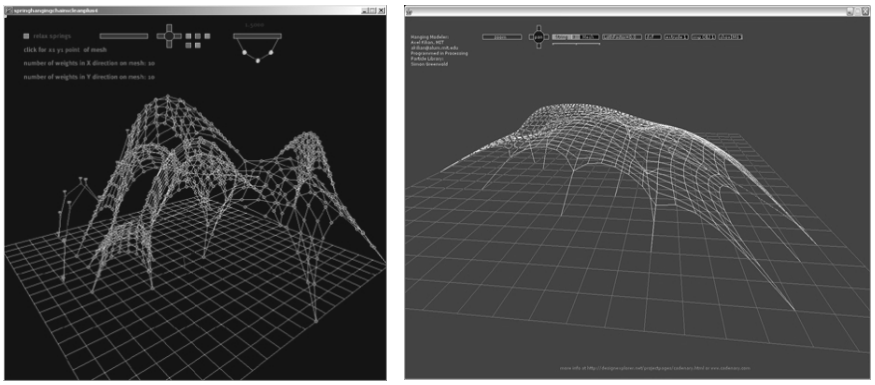

(a) (b)

Figure 2.12 – Real-time virtual catenary exploration tool by Kilian: CADenary v.1 [Kilian, 2004a], and v.2 [Kilian, 2006b].

2.3 Summary

This chapter provided a critical overview of the key references and precedents relevant to equilibrium analysis of vaulted masonry structures and the design of funicular structures.

With contributions by O'Dwyer [1999], Fraternali and Rocchetta [2002], Andreu et al. [2007] and Whiting et al. [2009], in recent years there have been significant developments and evolutions in computational equilibrium analysis methods for masonry vaults. From this review, we conclude that modeling three-dimensional historical masonry is very challenging, particularly since the approaches need to deal with significant structural, material, loading, and support discontinuities. Other crucial issues are how to deal with the high level of indeterminacy of three-dimensional vaults, how to put boundaries on the stability of a vault and how to develop an assessment procedure which is independent of the user input. The slicing technique strongly influences the results. The initial mesh topology or chosen force pattern limit the possible equilibrium shapes in a funicular analysis or for the force network approach. An important aspect also is how the results are being communicated, particularly the relation between geometry and relative stability or the flow of forces.

There are many precedents for funicular design. The main aspect which is missing in all the discussed approaches is the balance between control and freedom. The interactivity and speed of the new computational exploration tools opens up promising directions, but still deal with the same issues of control as the physical approaches.

There is a need for interactive three-dimensional equilibrium methods which offer control and flexibility to the designer, and which allow the user to understand the interdependencies of the hard constraints enforced by gravity.

Part II

Thrust Network Analysis

Chapter 3

Methodology: Thrust network analysis

3.1 Introduction

Graphic statics is a powerful method for exploring the infinite possible equilibrium solutions, both for the analysis of historic structures in unreinforced masonry and for the design of new funicular structures. The main drawback is the limitation to two-dimensional problems. This thesis develops a three-dimensional version of thrust-line analysis which uses reciprocal diagrams so that the approach maintains the strengths of the two-dimensional applications using graphic statics.

To be effective, the following features of graphical statics should be preserved:

- a graphical and intuitive representation of the forces in the system; and
- an interactive exploration of the range of equilibrium solutions bounded by a minimum and maximum thrust.

To cope with the challenges of the high degree of indeterminacy of three-dimensional problems, the user should be able to

- identify and control the many unknowns (degrees of freedom) of the equilibrium system; and
- negotiate between the unknowns by formulating an optimization problem with different objective functions.

The new methodology developed in this thesis, *Thrust Network Analysis* (TNA), extends O'Dwyer's Force Network Method for funicular analysis of vaulted masonry structures [O'Dwyer, 1999]. Inspired by Williams [1986], reciprocal figures are introduced to relate the geometry of the three-dimensional equilibrium networks to their internal forces. This linearizes the constraints and deals with the high level of indeterminacy of fully three-dimensional funicular networks. A similar framework as for the Force Density Method is used to describe the problem elegantly [Schek, 1974].

3.2 Fundamentals

3.2.1 Assumptions

To develop Thrust Network Analysis for the assessment of unreinforced masonry structures, four key assumptions must be made. Assumptions b) and c) are specific for masonry.

a) *The structural action of the vault is represented by a discrete network of forces with discrete loads applied at the vertices.*

It is common practice for structural engineers to use truss analogies for modeling reinforced concrete and unreinforced masonry structures (see e.g. [Schlaich and Schäfer, 1991; O'Dwyer, 1999]). A system of discrete forces facilitates the modeling of applied loads, cracks and other structural discontinuities [O'Dwyer, 1999]. This is discussed further in Chapters 4 and 6.

Discrete force networks allow the user to clearly visualize the possible force paths in the vault, and by using reciprocal diagrams, to determine a satisfactory distribution of internal forces. Discrete reciprocal force diagrams are graphical and intuitive, and their visual nature allows a graphical verification of the process [Maxwell, 1869]. The solutions can be checked more easily than numerical or arithmetic methods, and the method is very transparent. The denser the network mesh, the closer it will approximate a continuous thrust surface, i.e. a continuous bending-free surface in equilibrium with the applied loads.

b) *A compression-only solution in equilibrium with the applied loads and contained within the vault's geometry represents a valid, i.e. stable, equilibrium state of the vault.*

The safe theorem, also called the *lower-bound theorem*, has been developed within the framework of limit analysis for masonry structures by Heyman [1966]. To use this framework, Heyman introduced the three assumptions stated in (c). To prove that an unreinforced masonry vault will stand, the analyst must find a network of compressive forces in equilibrium with the applied loads that fits everywhere within the volume of the vault. If one such network is found and the assumptions in (c) are not being violated, then the *safe theorem* guarantees that the vault will be safe even though it might not be the "true" state of internal forces in the real vault.

c) *Masonry has no tensile capacity; sliding does not occur; and the stresses are low enough so that crushing does not occur (infinite compression strength is assumed).*

The first assumption of no tensile strength is a conservative assumption. Even though stone, brick and mortar have some tensile capacity, because of the material's brittle behavior and the heterogeneity observed in all historic structures, it is best to neglect those contributions. The latter two assumptions are unconservative, but not unreasonable. They need to be checked locally.

From the above, the network must have the following properties:

- branches have axial compression forces only;
- branches meet at nodes, which are in equilibrium with external forces applied to the nodes; and
- all nodes are contained within the masonry envelope.

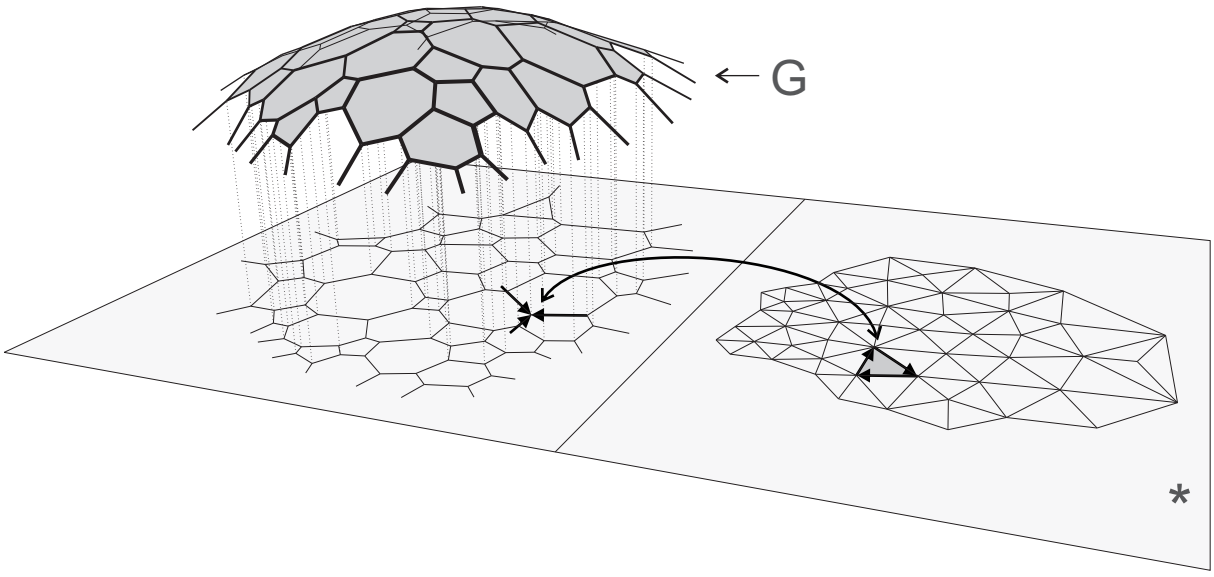

Figure 3.1 – Relationship between the compression equilibrium shape, the thrust network (G), its planar projection (primal grid Γ) and the reciprocal diagram (dual grid Γ^*).

Since the solutions are funicular, which in our case means compression-only, this also means that they can never fold back onto themselves, which would demand that some elements act in tension. Note that there are no constraints on the length of the branches or the planarity of the facets of the solution.

d) *All loads need to be vertical.*

This is a strong and very constraining assumption. The reason for this assumption will be discussed in §3.2.4. It is appropriate for vaults with a dominant, and parallel, loading case such as heavy masonry structures. Possibilities of this framework and extension to other loading cases will be discussed in Chapters 4 and 5.

3.2.2 Nomenclature

Figure 3.1 shows the relationship between the primal grid Γ, which is the horizontal projection of the funicular equilibrium solution, the thrust network G, and the planar dual grid Γ^*, which is the reciprocal force diagram of the primal grid Γ. When referring to elements or properties of the dual grid Γ^*, an asterix symbol (*) will be used.

In this dissertation, equilibrium structures (or solutions) refer to compression funicular structures, i.e. a structure in equilibrium with the applied loads using only compressive, axial forces, without any internal bending.

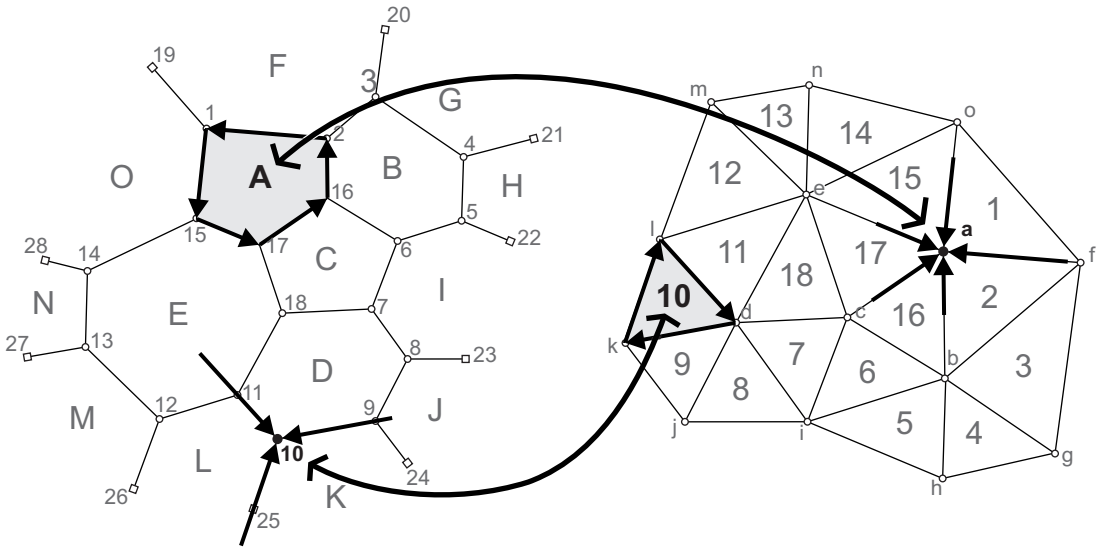

Figure 3.2 – The primal grid Γ and dual grid Γ* are related by a reciprocal relationship. The equilibrium of a node in one of them is guaranteed by a closed polygon in the other and vice versa. The labeling uses Bow's notation [Zalewski and Allen, 1998; Bow, 1873].

3.2.3 Reciprocal Figures

Reciprocal figures are geometrically related such that corresponding branches are parallel and branches which come together in a node in one of the networks form a closed polygon in the other and vice versa [Maxwell, 1864]. If applied to structural mechanics, the closed polygons on the reciprocal figure represent the static equilibrium of the nodes in the original figure and the lengths of the branches in it are proportional to the axial forces along the corresponding branches in the original figure (Figure 3.2). For a clear overview of the history, development and applications of reciprocal figures, see the 1911 edition of the British Encyclopedia [LoveToKnow, 2006]. Graphical methods, such as graphic statics, are applications in structural analysis and design of reciprocal figures [Cremona, 1879, 1890]. Micheletti [2008] gives a clear and rigorous description of the mathematical relationship of reciprocal diagrams for self-stressed frameworks based on graph theory.

The solution G should be compression-only. As will be shown in the next section, this is true when its horizontal projection Γ is entirely in compression in its plane. The static force equilibrium of Γ is represented by its closed reciprocal figure Γ*. Γ and Γ* satisfy Maxwell's geometrical definition of reciprocal figures. His definition is true in general, but does not guarantee that the force diagram is in compression-only as the nertworks considered here demand. To guarantee that the primal grid is in compression-only, Williams [1986] added the following constraint to the dual grid Γ* (Figure 3.3a): the closed polygons representing the equilibrium of the (compression) nodes in the primal grid are formed clock-wise in the dual grid (Figure 3.3b).

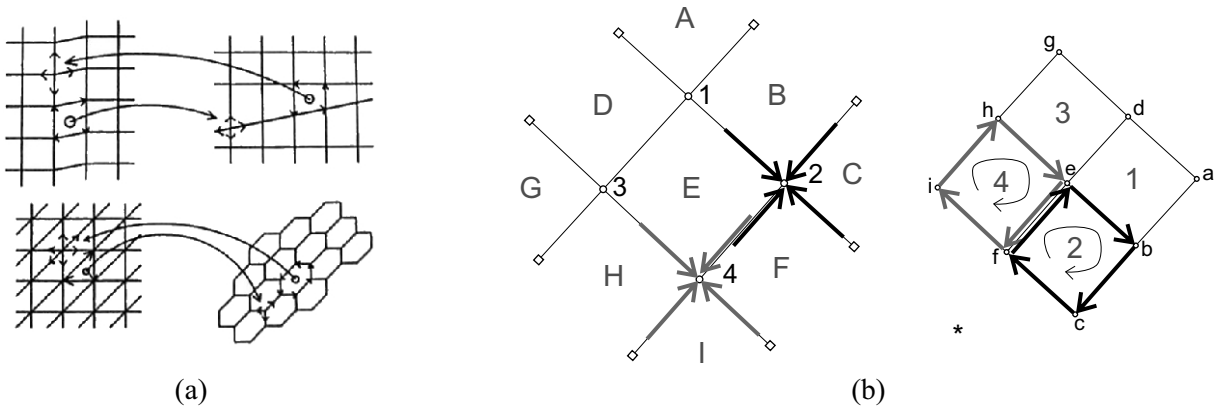

Figure 3.3 – (a) Reciprocal surfaces from Williams [1986], and (b) closed polygons representing the equilibrium of compressive nodes in the primal grid are formed clock-wise in the dual grid.

3.2.4 Key concept I: Parallel Loads

From descriptive geometry, we know that if a set of vectors is in equilibrium in space then their projection along any direction onto a plane will also be in equilibrium [Henrici and Turner, 1903] (Figure 3.4a).

Consider first the case in which the geometry of the 3-D network G is known and in equilibrium, i.e. with all bars in compression, with a set of vertical loads. This equilibrium could for example have been found by inverting the resulting shape of a hanging string model with the same set of loads hung from each node. The network G shown in Figure 3.1 is funicular for equal loads applied at each node.

Because the 3-D network of forces in G is in equilibrium, we know that the 2D graph Γ, which is the horizontal projection of G, will also be in equilibrium. The in-plane equilibrium of Γ can be found and visualized using the planar reciprocal force diagram Γ^* and this equilibrium represents the horizontal, i.e. the xy-, equilibrium of network G.

By projecting this system of forces on a horizontal plane, which is perpendicular to the externally applied vertical loads (Assumption 3.2.1), the applied loads reduce to a point in the planar projection Γ (Figure 3.4b). In constructing the reciprocal diagram Γ^*, because there are no external loads to give scale to the reciprocal diagram, the geometric reciprocal relationships between Γ and Γ^*, as defined in in §3.2.3, are true regardless of the size of Γ^*. In this case, since the geometry of G is assumed known and in 3-D equilibrium with the applied loads, the size, represented by the scale factor ζ, of Γ^* is uniquely defined and is related to the geometry (depth) of that specific solution. The forces in the system can then easily be found by measuring the lengths of the corresponding branches in the dual grid multiplied by the scale ζ and using trigonometry.

Rather than seeking the internal forces in a known 3-D equilibrium system, the presented methodology can be used to find the geometry of G in equilibrium with a given set of vertical loads. Starting from the grid Γ in Figure 3.1, which is the horizontal projection of the as-yet unknown 3D network G, it has a corresponding Γ^* whose triangulated geometry is uniquely defined, but not its scale ζ. It is said that Γ has only one *self stress* [Ash et al., 1988]. This scale is the only parameter in this system.

Choosing a scale ζ gives a unique solution G. Increasing ζ corresponds with increasing the size of Γ^* or, equivalently, scaling up the magnitude of all horizontal forces in the system which results in a decrease of

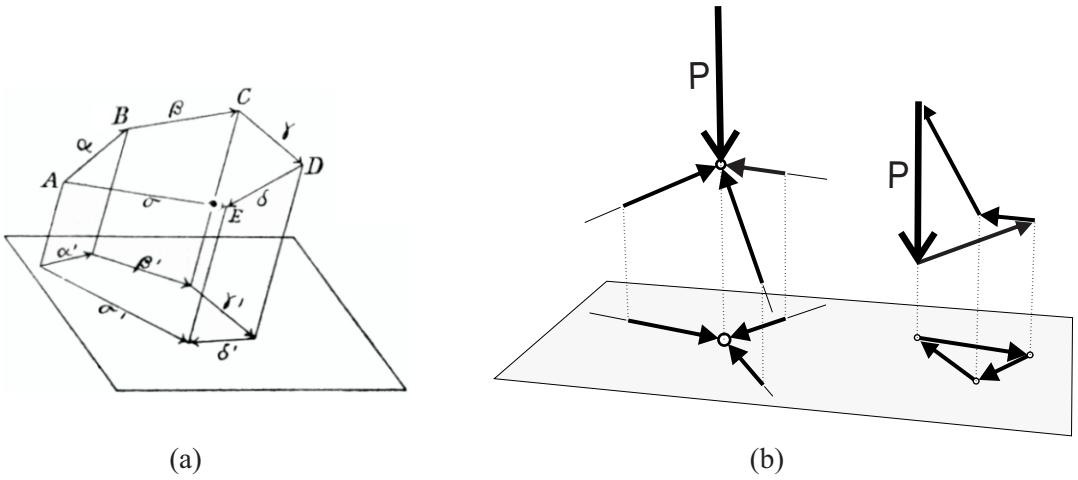

Figure 3.4 – (a) Henrici and Turner [1903] show that the projection of a combination of force vecotrs in equilibrium in space is also in equilibrium when projected along any direction onto a plane. (b) Projecting the bar forces on the horizontal plane, i.e. perpendicular to the vertical load P reduces it to a point in the planar projection. The external load P therefore also does not appear in the closed polygon representing the horizontal equilibrium of the node.

the depth of the solution (Figure 3.5a). The height of each node of two solutions with different ζ's with respect to a planar *closing surface* is inverse proportional to the thrust in each system, represented by the scale of their respective dual grids, ζ. If an equilibrium solution $G^{(0)}$, with nodal heights $z^{(0)}$ and dual scale $\zeta^{(0)}$, is found, an entire family of solutions can immediately be obtained which are all proportionally related to $G^{(0)}$. A possible equilibrium for the same set of loads, $G^{(j)}$, is related to $G^{(0)}$ as follows

$$\frac{\zeta^{(j)}}{\zeta^{(0)}} = \frac{\Delta z_i^{(j)}}{\Delta z_i^{(0)}} \qquad \forall i \tag{3.1}$$

So, from (3.1) we see that with one parameter, the scale ζ, the procedure can generate an infinite number of three-dimensional solutions. The height differences, measured from the closing surface to the nodes, of these solutions with the same force pattern and internal force distribution are inversely proportional to the scale of their dual grids. This relationship of course holds since all externally applied loads are vertical. This is equivalent in graphic statics to moving the pole of the funicular diagram on a line parallel to the closing string (Figure 3.5b).

3.2.5 Key concept II: Indeterminate networks

The network G, or its planar projection Γ, in Figure 3.1 is peculiar: all nodes in the network are three-valent, i.e. three branches come together at each node. In three dimensions, the forces in a three-valent network are uniquely defined. This is clearly represented in the reciprocal diagram Γ^*: because it is triangulated, it is locked and uniquely defined, except for the scale factor ζ (Figure 3.2). A 3-D three-valent network is *statically determinate* with respect to its specific funicular loading.

A *statically indeterminate* primal grid Γ, with nodes with a higher valency than three, has several possible

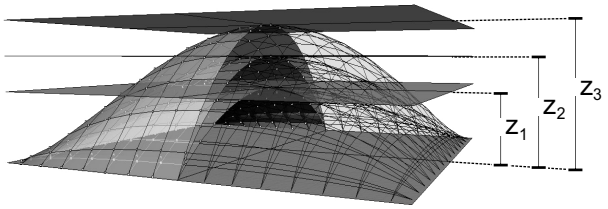

z_{max}	5	7.5	10
	16	12	8

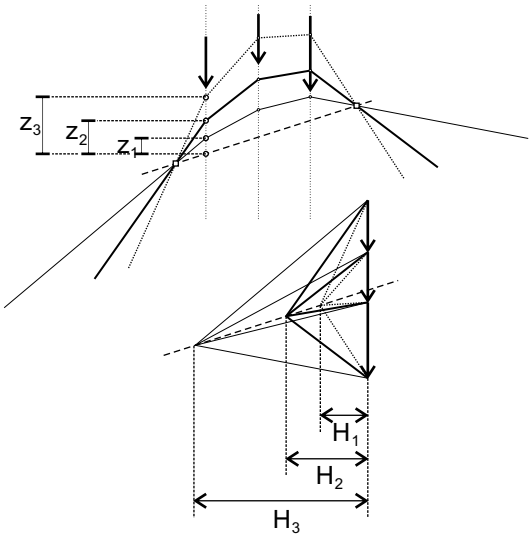

(a) (b)

Figure 3.5 – (a) Decreasing the scale factor of the dual grid means overall lower horizontal forces in the system and hence a deeper solution for the same set of applied loads. (b) This is equivalent to moving the pole in the funicular polygon of a graphic statics construction along the closing string.

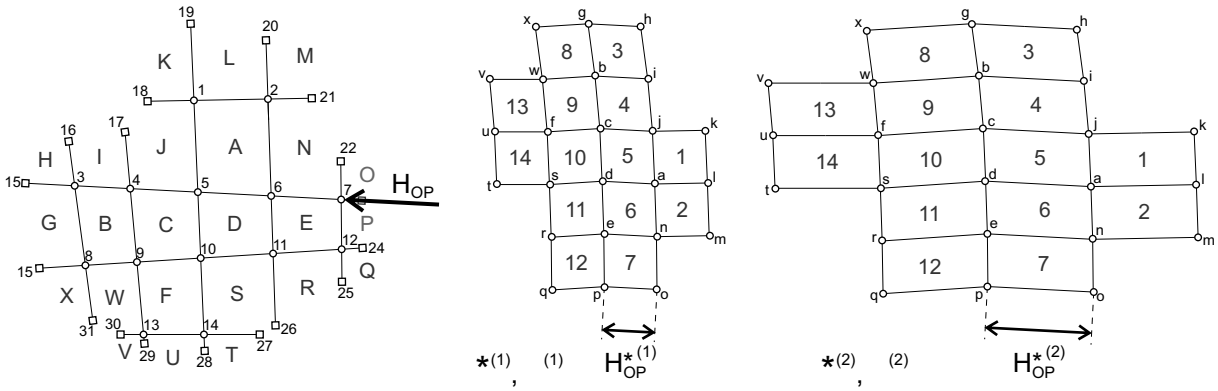

(a) (b) (c)

Figure 3.6 – (a) For an indeterminate primal grid, (b-c) multiple dual grids corresponding to different internal distribution of the (horizontal) forces are possible.

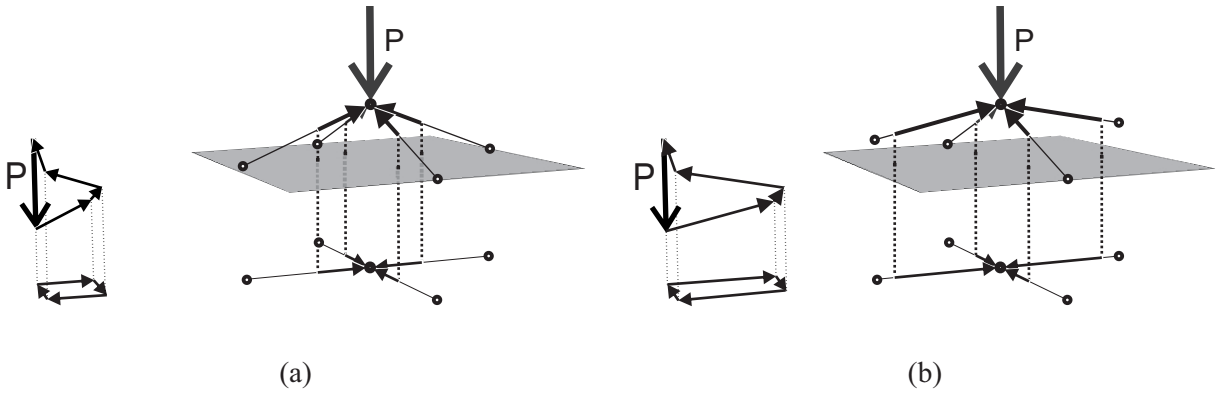

Figure 3.7 – Two indeterminate four-bar structures with the same load P, force pattern Γ, and depth of the structure, but changes in the force diagram Γ^*, i.e. changing the internal distributions of the forces. The diagram Γ^* of (b) is stretched to double the size in one direction compared to (a), resulting in the doubling of the horizontal forces in that direction and therefore also in a structure half as deep in that direction.

reciprocal diagrams Γ^*. This means that different states of self stress exist, i.e. different distributions of the internal forces are possible. Maxwell [1864] stated that the forces are indeterminate, so that more than one force needs to be known in order to determine all forces in the system, or else that certain relations among them had to be given, for example based on the elasticity of different parts of the frame. The elastic solution represents one of an infinite number of possible equilibrium solutions for a statically indeterminate grid.

In Figure 3.6b, two possible dual grids are shown for the chosen two-way primal grid. In $\Gamma^{*(1)}$, the dual branch lengths are approximately equal, meaning that the structure will have approximately constant horizontal thrust in both directions. In $\Gamma^{*(2)}$, the dual branch lengths in one direction are on average three times larger than the branches in the other direction, meaning that a preferred thrusting direction is given to the vault. The solution resulting from the second dual grid will attract more force in the direction the dual is "stretched." More force being attracted along certain force lines also means that the structure will become shallower along those lines. This is clearly shown for the simple four-branch network in Figure 3.7.

The notion that the infinite stress states of an indeterminate planar truss can be explored graphically was shown by Kilian and Ochsendorf [2005] (Figure 3.8).

3.3 Overview of the main steps

The following section will provide an overview of the main steps of the method.

a) *Constructing the primal grid* Γ

The structural action of the vault is represented by a discrete network of forces. The branches represent possible load paths throughout the structure. In plan, a possible force pattern topology is constructed. This is the primal grid Γ in Figure 3.9a which is the horizontal projection of the final solution G.

b) *Formulating nodal height constraints* z^{LB} *and* z^{UB}

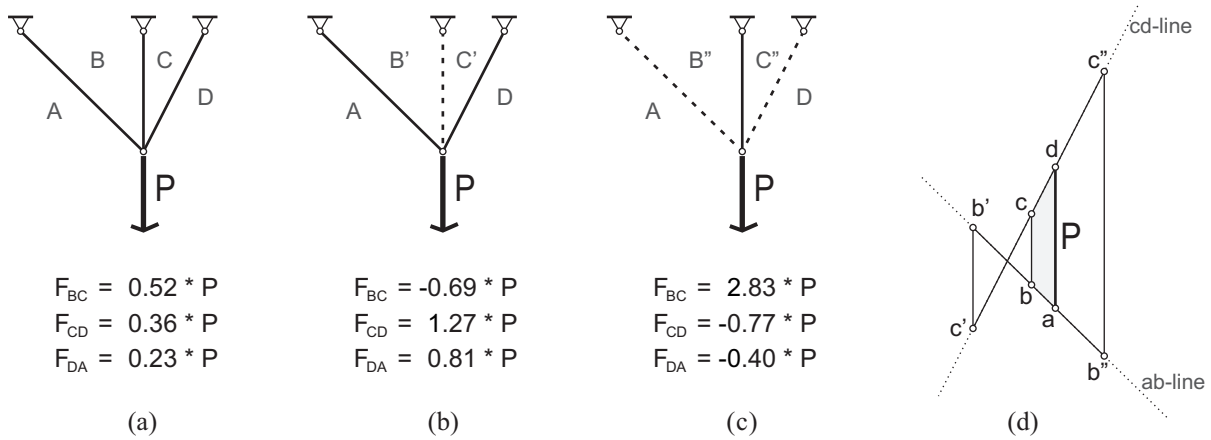

Figure 3.8 – For the well-known indeterminate problem of a weight on three bars, (a), (b) and (c) show different, possible states of self-stress of this system. Case (a) corresponds with the linear elastic solution. (d) shows the indeterminate force polygon for this problem (after Block and Ochsendorf [2005]).

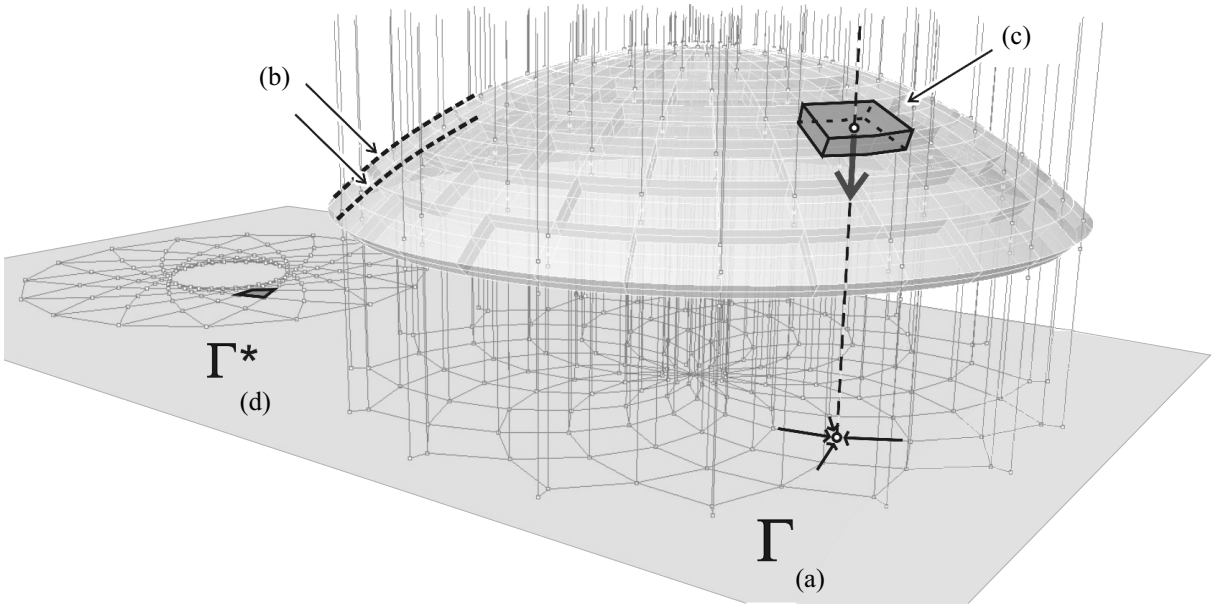

Figure 3.9 – Input for Thrust Network Analysis: (a) a possible force pattern Γ, defined on the horizontal plane; and (b) the boundaries, the intrados and extrados of a masonry vault. (c) The weight associated per node comes from the vault's self-weight and other imposed loads. (d) A possible reciprocal force diagram Γ^* is produced from Γ.

Possible solutions must lie within a solution space. This envelope can be related to a masonry vault's section, defined by an intrados and an extrados (Figure 3.9b) and obtained from the actual vault's geometry. These put lower- and upper-bounds, z^{LB} and z^{UB} respectively, on the nodal heights of the equilibrium solution G.

c) *Attributing nodal loads p*

Because of the discrete character of the force network, the loads need to be discretized as well. The load p applied per node can be divided into a dead load and a live load component. The dead load component comes from the self-weight of the vault. The self-weight is distributed and lumped to the nodes of Γ, and hence G, using 3-D tributary areas with respect to the nodes (Figure 3.9c). In addition to the loads due to the lumped self-weight, loads such as asymmetric live loads can be applied, as long as they are vertical.

d) *Formulating nodal vertical equilibrium constraints*

All branches coming together per node need to be in equilibrium with the applied nodal loads. The vertical equilibrium is written as a function of the branch lengths of the primal grid Γ, and the unknown horizontal components of the axial branch forces of G and nodal heights z.

e) *Generating dual grid* Γ^*

A dual grid Γ^* is produced from the primal grid Γ following to extended reciprocal rules as defined in §3.2.3 (Figure 3.9d). This dual grid, multiplied by a scale ζ (still unknown at this point), represents the horizontal equilibrium of a possible final thrust network G.

f) *Linearizing the constraints*

By using the dual grid, the non-linear vertical constraints can be linearized as a function of the unknown nodal heights z and the scale of the dual grid, ζ. The dual branch lengths are proportional to the branch forces in the primal grid Γ, and hence the horizontal components of the axial branch forces of G.

g) *Solving for the result G using linear optimization*

Using the geometry of both primal (Γ) and dual (Γ^*) grid, the weights applied at the nodes and the boundary conditions, this problem can be solved using a one-step linear optimization. We solve simultaneously for the nodal heights of G and the scale ζ of the dual grid Γ^*. The horizontal components of the forces in the solution G can be found by measuring the lengths of the branches in the dual grid and multiplying them by the scale ζ.

h) *Updating the dual grid*

Using the automatically generated dual grid in (e) does not always render a feasible or satisfactory equilibrium solution G. In the case of an indeterminate primal grid, i.e. a grid with nodes with a higher valency than three, the force distribution can be altered by manipulating the dual grid. This will be explained in detail in §4.2. The constraints are then updated with the new dual branch lengths and a new solution G is found. Steps (h) and (g) are repeated until a satisfactory result is obtained. An automated solving procedure will be presented in §5.2.

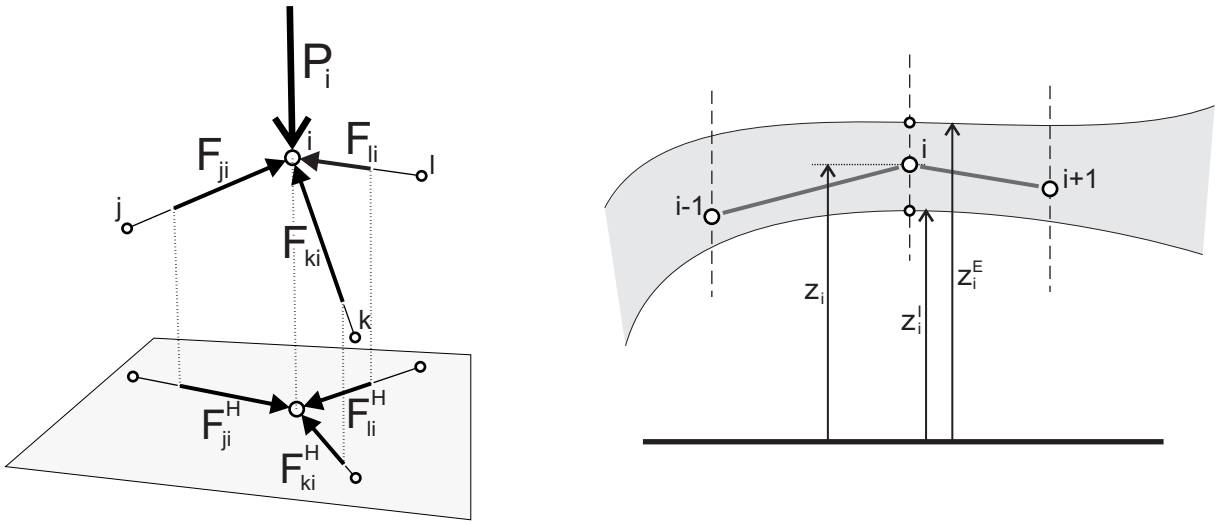

(a) (b)

Figure 3.10 – The constraints come from (a) static equilibrium in every node under the applied loading, rendering the equilibrium constraints, and (b) the boundaries, resulting in nodal height constraints.

3.4 Thrust network model

3.4.1 Formulation of the constraints

The first set of constraints comes from enforcing static equilibrium at all nodes. The vertical equilibrium of a typical internal node i shown in Figure 3.10a gives

$$F_{ji}^{\mathrm{V}} + F_{ki}^{\mathrm{V}} + F_{li}^{\mathrm{V}} = P_i \tag{3.2}$$

where F_{ji}^{V} are the vertical components of the branches forces coming together in node i, and P_i are the vertical loads applied at node i.

There are n_i equilibrium equations (3.2), one for each internal node of the primal grid Γ. The number of internal nodes n_i is the difference between the total number of nodes n and the number of boundary nodes n_b ($n_i = n - n_b$).

It is sufficient to describe only the vertical equilibrium of the nodes of G since their x- and y-coordinates are defined by the choice of a primal grid Γ. Section 4.1 will discuss the requirements for feasible primal grids. The horizontal equilibrium of the network is then guaranteed when a compression reciprocal diagram, i.e. a dual grid Γ^*, exists for the horizontal projection of G, i.e. the primal grid Γ.

We can describe (3.2) as a function of F_{ji}^{H}, the horizontal components of the forces, and the geometry of

the network G (Figure 3.9a).

$$F_{ji}^{\mathrm{H}} \cdot \frac{(z_i - z_j)}{\sqrt{(x_i - x_j)^2 + (y_i - y_j)^2}} + F_{ki}^{\mathrm{H}} \cdot \frac{(z_i - z_k)}{\sqrt{(x_i - x_k)^2 + (y_i - y_k)^2}} + F_{li}^{\mathrm{H}} \cdot \frac{(z_i - z_l)}{\sqrt{(x_i - x_l)^2 + (y_i - y_l)^2}} = P_i \tag{3.3}$$

The lengths of branches ji in the primal grid are defined as L_{ji}^{H}.

$$L_{ji}^{\mathrm{H}} = \sqrt{(x_i - x_j)^2 + (y_i - y_j)^2} \tag{3.4}$$

Equation (3.3) becomes

$$F_{ji}^{\mathrm{H}} \cdot \frac{(z_i - z_j)}{L_{ji}^{\mathrm{H}}} + F_{ki}^{\mathrm{H}} \cdot \frac{(z_i - z_k)}{L_{ki}^{\mathrm{H}}} + F_{li}^{\mathrm{H}} \cdot \frac{(z_i - z_l)}{L_{li}^{\mathrm{H}}} = P_i \tag{3.5}$$

To find an equilibrium network G, i.e. a network with all branches acting under compression under the set of loads P_i, all nodes i must satisfy 3.5. These equations are nonlinear since both the nodal heights z_i and the horizontal components of the axial branch forces of G are unknown.

A second set of constraints comes from the limits put on the nodal heights. We want the solutions to lie within the given boundaries, z_i^{LB} and z_i^{UB}, defined by an intrados and an extrados.

$$z_i^{\mathrm{LB}} \leq z_i \leq z_i^{\mathrm{UB}} \tag{3.6}$$

The intersections of the verticals through the nodes of the primal grid and the intrados and extrados give z_i^{I} and z_i^{E} respectively (Figure 3.10b). For masonry structures, we seek solutions within the section of the vault. In that case, z_i^{LB} and z_i^{UB} become

$$z_i^{\mathrm{LB}} = z_i^{\mathrm{I}} \tag{3.7a}$$
$$z_i^{\mathrm{UB}} = z_i^{\mathrm{E}} \tag{3.7b}$$

To guarantee that the entire section stays in compression without any hinging, the solution may be further contained within the middle-third, or *kern*, of the vault. Then, z_i^{LB} and z_i^{UB} become

$$z_i^{\mathrm{LB}} = z_i^{\mathrm{I}} + \frac{1}{3}(z_i^{\mathrm{E}} - z_i^{\mathrm{I}}) \tag{3.8a}$$
$$z_i^{\mathrm{UB}} = z_i^{\mathrm{E}} - \frac{1}{3}(z_i^{\mathrm{E}} - z_i^{\mathrm{I}}) \tag{3.8b}$$

The inequalities (3.8) give $2n$ additional constraints, so, in total, there are $n_i + 2n$ constraints on the equilibrium of the network G.

3.4.2 Linearization of the constraints

Because the primal grid Γ and the dual grid Γ^* are reciprocal, the branch forces F_{ji}^{H} of the primal, hence the horizontal components of the axial forces in the solution G, are equal to the corresponding branch lengths $L_{ji}^{\mathrm{H}*}$ in the dual grid, multiplied with the as-yet unknown scale factor ζ.

$$F_{ji}^{\mathrm{H}} = \zeta \cdot L_{ji}^{\mathrm{H}*} \tag{3.9}$$

where the dual branch lengths L_{ji}^{H*} are also defined as a function of the dual nodes

$$L_{ji}^{\mathrm{H}*} = \sqrt{(x_i^* - x_j^*)^2 + (y_i^* - y_j^*)^2} \tag{3.10}$$

Using (3.9), and plugging it into the nodal equilibrium equations (3.5), after dividing both sides by ζ, gives

$$L_{ji}^{\mathrm{H}*} \cdot \frac{z_i - z_j}{L_{ji}^{\mathrm{H}}} + L_{ki}^{\mathrm{H}*} \cdot \frac{z_i - z_k}{L_{ki}^{\mathrm{H}}} + L_{li}^{\mathrm{H}*} \cdot \frac{z_i - z_l}{L_{li}^{\mathrm{H}}} = \frac{1}{\zeta} \cdot P_i \tag{3.11}$$

Rearranging gives

$$\left(\frac{L_{ji}^{\mathrm{H}\,*}}{L_{ji}^{\mathrm{H}}} + \frac{L_{ki}^{\mathrm{H}\,*}}{L_{ki}^{\mathrm{H}}} + \frac{L_{li}^{\mathrm{H}\,*}}{L_{li}^{\mathrm{H}}} \right) \cdot z_i - \frac{L_{ji}^{\mathrm{H}\,*}}{L_{ji}^{\mathrm{H}}} \cdot z_j - \frac{L_{ki}^{\mathrm{H}\,*}}{L_{ki}^{\mathrm{H}}} \cdot z_k - \frac{L_{li}^{\mathrm{H}\,*}}{L_{li}^{\mathrm{H}}} \cdot z_l - P_i \cdot r = 0 \tag{3.12}$$

where r is the inverse of the unknown scale of the dual grid, ζ. We can re-write equation (3.12) as

$$d_{ii} \cdot z_i + d_{ji} \cdot z_j + d_{ki} \cdot z_k + d_{li} \cdot z_l - P_i \cdot r = 0 \tag{3.13}$$

where the constants d_{ni} are a function of the known primal and dual branch lengths.

The equilibrium constraints of the nodes (3.13) are written as a linear combination of z_i, the unknown nodal heights, and r, the inverse of the unknown scale ζ of the dual grid Γ^*. With the information provided by the dual grid (3.9) and by treating r as a variable, the nonlinear constraints (3.5) are made linear. Because lengths (absolute values) are used, this formulation guarantees that all solutions G will be compression-only.

3.4.3 Computational set-up

The notation used throughout this dissertation follows the conventions by Schek [1974]. They are repeated here for clarity. A vector is defined as a one-column-matrix and written in lower-case and bold, and a matrix in upper-case and bold. The same symbols are used for the components but not in bold and

with indices i and j. The m-dimensional vector $\boldsymbol{a}$ – called the m-vector $\boldsymbol{a}$ – has therefore a_j as the j^{th} component. Often the diagonal matrix $\boldsymbol{A}$ to any vector $\boldsymbol{a}$ is used. $\boldsymbol{A}$ then has $\boldsymbol{a}$ as its diagonal, e.g.

$$\boldsymbol{a} = \begin{bmatrix} 1 \\ 2 \\ 3 \end{bmatrix} \quad , \quad \boldsymbol{A} = \begin{bmatrix} 1 & 0 & 0 \\ 0 & 2 & 0 \\ 0 & 0 & 3 \end{bmatrix} \tag{3.14}$$

Using a *branch-node matrix*, it is possible to write the nodal equilibrium constraints elegantly in matrix form. The branch-node matrix $\boldsymbol{C}$ captures the topology and connectivity of a bar-node network [Fenves and Branin, 1963; Argyris, 1964]. Note that the transpose of $\boldsymbol{C}$ is defined as the *incidence matrix* in graph theory [Bondy and Murty, 1976; Biggs, 1993]. To construct the primal branch-node matrix $\boldsymbol{C}$ of a network, it can be treated as a directed graph. In a directed graph, all edges of the network are directional. As a convention, the internal nodes are numbered first and then the boundary nodes. So, the $(n \times 1)$ coordinate vectors $\boldsymbol{x}$, $\boldsymbol{y}$ and $\boldsymbol{z}$ have the following form

$$\boldsymbol{x} = \begin{bmatrix} \boldsymbol{x_i} \\ \boldsymbol{x_b} \end{bmatrix} \quad , \quad \boldsymbol{y} = \begin{bmatrix} \boldsymbol{y_i} \\ \boldsymbol{y_b} \end{bmatrix} \quad , \quad \boldsymbol{z} = \begin{bmatrix} \boldsymbol{z_i} \\ \boldsymbol{z_b} \end{bmatrix} \tag{3.15}$$

with the $(n_i \times 1)$ vectors $\boldsymbol{x_i}$, $\boldsymbol{y_i}$ and $\boldsymbol{z_i}$ listing the x-, y- and z-coordinates of the internal nodes and the $(n_b \times 1)$ vectors $\boldsymbol{x_i}$, $\boldsymbol{y_i}$ and $\boldsymbol{z_i}$ of the boundary nodes.

Equivalently, the internal bracnhes are numbered before the boundary branches. The branches in the primal directed graph are oriented from the node with the higher index to the node with the lower index. So, the tail of the directed branch is always the higher index node and the head is the lower index node. For a primal grid with m branches and n nodes, the $(m \times n)$ matrix $\boldsymbol{C}$ is constructed as follows: each row represents a branch and the column value of the tail- and head-node receive a –1 or 1 respectively.

$$\boldsymbol{C}(i,j) = \begin{cases} 1 & \text{if node } j \text{ is the head-node of branch } i \\ -1 & \text{if node } j \text{ is the tail-node of branch } i \\ 0 & \text{otherwise} \end{cases} \tag{3.16}$$

Because of , the $(m \times n)$ branch-node matrix $\boldsymbol{C}$ can be separated into the $(m \times n_i)$ matrix $\boldsymbol{C_i}$ and the $(m \times n_b)$ matrix $\boldsymbol{C_b}$ corresponding with the internal nodes and boundary nodes.

$$\boldsymbol{C} = \left[\begin{array}{c|c} \boldsymbol{C_i} & \boldsymbol{C_b} \end{array}\right] \tag{3.17}$$

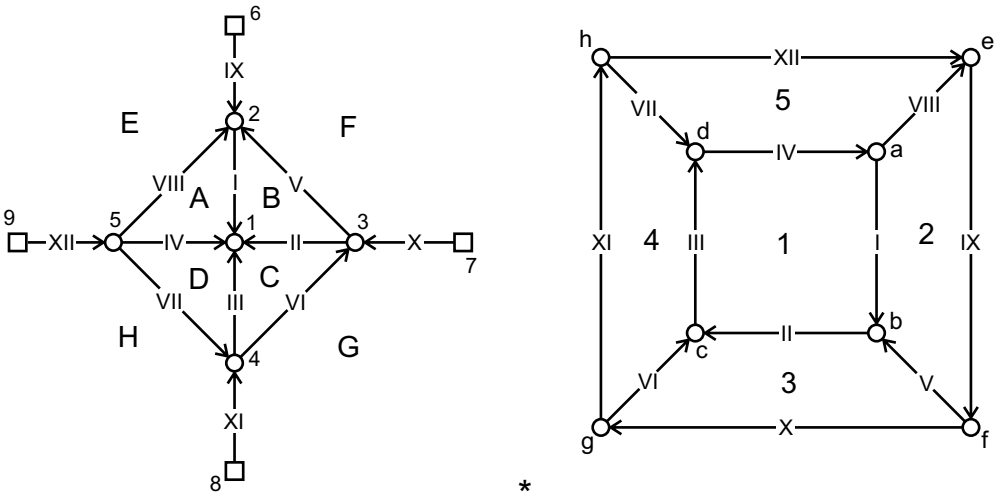

Figure 3.11 – Directed primal (a) and dual (b) graphs. Primal nodes and corresponding dual spaces are labeled using numbers, primal faces and dual nodes using letters, and primal and dual branches using roman numbers.

For the network of Figure 3.11 the $\boldsymbol{C}$-matrix becomes

$$\boldsymbol{C} = \begin{array}{c} \begin{array}{cccccc|ccc} 1 & 2 & 3 & 4 & 5 & 6 & 7 & 8 & 9 \end{array} \\ \left[\begin{array}{cccccc|ccc} 1 & -1 & \cdot & \cdot & \cdot & \cdot & \cdot & \cdot & \cdot \\ 1 & \cdot & -1 & \cdot & \cdot & \cdot & \cdot & \cdot & \cdot \\ 1 & \cdot & \cdot & -1 & \cdot & \cdot & \cdot & \cdot & \cdot \\ 1 & \cdot & \cdot & \cdot & -1 & \cdot & \cdot & \cdot & \cdot \\ \cdot & 1 & -1 & \cdot & \cdot & \cdot & \cdot & \cdot & \cdot \\ \cdot & \cdot & 1 & -1 & \cdot & \cdot & \cdot & \cdot & \cdot \\ \cdot & \cdot & \cdot & 1 & -1 & \cdot & \cdot & \cdot & \cdot \\ \cdot & 1 & \cdot & \cdot & -1 & \cdot & \cdot & \cdot & \cdot \\ \cdot & 1 & \cdot & \cdot & \cdot & -1 & \cdot & \cdot & \cdot \\ \cdot & \cdot & 1 & \cdot & \cdot & \cdot & -1 & \cdot & \cdot \\ \cdot & \cdot & \cdot & 1 & \cdot & \cdot & \cdot & -1 & \cdot \\ \cdot & \cdot & \cdot & \cdot & 1 & \cdot & \cdot & \cdot & -1 \end{array}\right] \end{array} \begin{array}{c} \\ \text{I} \\ \text{II} \\ \text{III} \\ \text{IV} \\ \text{V} \\ \text{VI} \\ \text{VII} \\ \text{VIII} \\ \text{IX} \\ \text{X} \\ \text{XI} \\ \text{XII} \end{array} \tag{3.18}$$

The dual branch-node matrix $\boldsymbol{C}^*$ $(m \times n^*)$ represents the topology and connectivity of the dual grid. The dual grid has n^* nodes, equal to the number of faces in the primal grid, f. The $(m \times 1)$ column vectors of $\boldsymbol{C}^*$ can easily be constructed from the primal grid by cycling its spaces counter-clockwise. If the space cycle traverses an edge in the same or opposite direction than its orientation then that entry gets a 1 or –1 respectively. Notice that this results in corresponding branches in primal and dual graph being oriented in the same direction. The relation between $\boldsymbol{C}$ and $\boldsymbol{C}^*$ is further discussed in §4.2.

For the network of Figure 3.11 the $\boldsymbol{C}^*$-matrix thus becomes

$$\boldsymbol{C}^* = \begin{array}{c} \begin{array}{cccccccc} \text{a} & \text{b} & \text{c} & \text{d} & \text{e} & \text{f} & \text{g} & \text{h} \end{array} \\ \left[\begin{array}{cccccccc} \text{i} & & & & & & & \\ -1 & 1 & \cdot & \cdot & \cdot & \cdot & \cdot & \cdot \\ \cdot & -1 & 1 & \cdot & \cdot & \cdot & \cdot & \cdot \\ \cdot & \cdot & -1 & 1 & \cdot & \cdot & \cdot & \cdot \\ 1 & \cdot & \cdot & -1 & \cdot & \cdot & \cdot & \cdot \\ \cdot & 1 & \cdot & \cdot & \cdot & -1 & \cdot & \cdot \\ \cdot & \cdot & 1 & \cdot & \cdot & \cdot & -1 & \cdot \\ \cdot & \cdot & \cdot & 1 & \cdot & \cdot & \cdot & -1 \\ -1 & \cdot & \cdot & \cdot & 1 & \cdot & \cdot & \cdot \\ \cdot & \cdot & \cdot & \cdot & -1 & 1 & \cdot & \cdot \\ \cdot & \cdot & \cdot & \cdot & \cdot & -1 & 1 & \cdot \\ \cdot & \cdot & \cdot & \cdot & \cdot & \cdot & -1 & 1 \\ \cdot & \cdot & \cdot & \cdot & 1 & \cdot & \cdot & -1 \end{array}\right] \begin{array}{l} \text{I} \\ \text{II} \\ \text{III} \\ \text{IV} \\ \text{V} \\ \text{VI} \\ \text{VII} \\ \text{VIII} \\ \text{IX} \\ \text{X} \\ \text{XI} \\ \text{XII} \end{array} \end{array} \tag{3.19}$$

Using the coordinate vectors (3.15) of the final solution G, and the branch-node matrix $\boldsymbol{C}$, the $(m \times 1)$ branch coordinate difference vectors $\boldsymbol{u}$, $\boldsymbol{v}$, $\boldsymbol{w}$ are

$$\boldsymbol{u} = \boldsymbol{C}\boldsymbol{x} = \boldsymbol{C}_i\boldsymbol{x}_i + \boldsymbol{C}_b\boldsymbol{x}_b \tag{3.20a}$$
$$\boldsymbol{v} = \boldsymbol{C}\boldsymbol{y} = \boldsymbol{C}_i\boldsymbol{y}_i + \boldsymbol{C}_b\boldsymbol{y}_b \tag{3.20b}$$
$$\boldsymbol{w} = \boldsymbol{C}\boldsymbol{z} = \boldsymbol{C}_i\boldsymbol{z}_i + \boldsymbol{C}_b\boldsymbol{z}_b \tag{3.20c}$$

The vectors $\boldsymbol{u}$ and $\boldsymbol{v}$ are of course also the branch coordinate vectors of the primal grid Γ. Similarly, the dual branch difference vectors can be set up using the dual nodes $\boldsymbol{x}^*$, $\boldsymbol{y}^*$ and the dual branch-node matrix $\boldsymbol{C}^*$. The dual grid Γ^* is planar and therefore $\boldsymbol{z}^* = \boldsymbol{0}$.

$$\boldsymbol{u}^* = \boldsymbol{C}^*\boldsymbol{x}^* \tag{3.21a}$$
$$\boldsymbol{v}^* = \boldsymbol{C}^*\boldsymbol{y}^* \tag{3.21b}$$

$\boldsymbol{U}$, $\boldsymbol{V}$, $\boldsymbol{W}$, $\boldsymbol{U}^*$ and $\boldsymbol{V}^*$ are the diagonalized square matrices of $\boldsymbol{u}$, $\boldsymbol{v}$, $\boldsymbol{w}$, $\boldsymbol{u}^*$ and $\boldsymbol{v}^*$ respectively. The diagonalized primal and dual branch length matrices $\boldsymbol{L}_\mathbf{H}$ and $\boldsymbol{L}^*_\mathbf{H}$ are then found as

$$\boldsymbol{L}_\mathbf{H} = \sqrt{\boldsymbol{U}^\mathbf{t}\,\boldsymbol{U} + \boldsymbol{V}^\mathbf{t}\,\boldsymbol{V}} \tag{3.22a}$$
$$\boldsymbol{L}^*_\mathbf{H} = \sqrt{\boldsymbol{U}^{*\mathbf{t}}\,\boldsymbol{U}^* + \boldsymbol{V}^{*\mathbf{t}}\,\boldsymbol{V}^*} \tag{3.22b}$$

From Schek [1974], the $3n_i$ equilibrium equations for the internal nodes in a loaded equilibrium network are

$$\boldsymbol{C_i^t\, U L^{-1} s = p_x} \tag{3.23a}$$
$$\boldsymbol{C_i^t\, V L^{-1} s = p_y} \tag{3.23b}$$
$$\boldsymbol{C_i^t\, W L^{-1} s = p_z} \tag{3.23c}$$

where $\boldsymbol{p_x}$, $\boldsymbol{p_y}$, $\boldsymbol{p_z}$ are the component vectors of the forces applied at the nodes, the vector $\boldsymbol{s}$ contains the axial branch forces of the equilibrium solution and $\boldsymbol{L}$ is the diagonalized matrix of $\boldsymbol{l}$, the vector listing the branch lengths of G, with

$$\boldsymbol{L} = \sqrt{\boldsymbol{U^t\, U} + \boldsymbol{V^t\, V} + \boldsymbol{W^t\, W}} = \sqrt{\boldsymbol{L_H^t L_H} + \boldsymbol{W^t\, W}} \tag{3.24}$$

Equations (3.23a) and (3.23b) are trivial since $\boldsymbol{p_x}$ and $\boldsymbol{p_y}$ are zero, and since the horizontal equilibrium of the solution is guaranteed by the existence of a feasible dual grid. It is therefore sufficient to only consider (3.23c).

Linkwitz and Schek [1971] introduced *force densities* $\boldsymbol{q}$, defined as the ratio of the branch forces $\boldsymbol{s}$ over the branch lengths $\boldsymbol{L}$ to linearize (3.23c). These are also sometimes referred to as *tension coefficients*. As in equation (3.5), the vertical equilibrium equations are written as a function of the horizontal components of the forces, because they are known from the dual grid. The force densities $\boldsymbol{q}$ can be expressed as a function of $\boldsymbol{s_H}$ and $\boldsymbol{l_H}$, the horizontal components of branch forces and lengths respectively.

$$\boldsymbol{q = L^{-1} s = L_H^{-1} s_H} \tag{3.25}$$

The force densities (3.25) were introduced to linearize (3.23). So, (3.23c) becomes

$$\boldsymbol{C_i^t\, W q = p_z} \tag{3.26}$$

and using that $\boldsymbol{Wq = Qw}$, since $\boldsymbol{W}$ and $\boldsymbol{Q}$ are diagonal matrices, gives

$$\boldsymbol{C_i^t\, Q C z = p_z} \tag{3.27}$$

Equivalent to equation (3.9), the horizontal components $\boldsymbol{s_H}$ of the branch forces $\boldsymbol{s}$ are obtained by measuring the corresponding branch lengths in the dual grid Γ^* and multiplying them by the scale of Γ^*, ζ:

$$\boldsymbol{s_H = L_H^* \zeta} \tag{3.28}$$

with $\boldsymbol{\zeta}$ the $(m \times 1)$ branch scale vector with in this case all entries equal to the overall scale factor ζ. Combining (3.25) and (3.28), the force densities $\boldsymbol{q}$ can be written in function of the branch lengths of both primal and dual grid and the scale:

$$\boldsymbol{q = L_H^{-1} L_H^* \zeta} \tag{3.29}$$

Using (3.25) in (3.27) and dividing with the scalar ζ gives

$$\boldsymbol{C_i^t}(\boldsymbol{L_H^{-1}}\boldsymbol{L_H^*})\boldsymbol{Cz} - \boldsymbol{p_z}r = \boldsymbol{0} \tag{3.30}$$

3.5 Solving procedure

Equation (3.30) can be written as a function of $\boldsymbol{z_i}$ and $\boldsymbol{z_b}$

$$\boldsymbol{C_i^t}(\boldsymbol{L_H^{-1}}\boldsymbol{L_H^*})\boldsymbol{C_i z_i} + \boldsymbol{C_i^t}(\boldsymbol{L_H^{-1}}\boldsymbol{L_H^*})\boldsymbol{C_b z_b} - \boldsymbol{p_z} = \boldsymbol{0} \tag{3.31}$$

To simplify (3.31), the $(n_i \times n_i)$ constraint matrix $\boldsymbol{D}$ is introduced:

$$\boldsymbol{D} = \left[\begin{array}{c|c} & \\ \boldsymbol{D_i} & \boldsymbol{D_b} \\ & \end{array}\right] \tag{3.32}$$

with the $(n_i \times n_i)$ matrix $\boldsymbol{D_i}$ and $(n_i \times n_b)$ matrix $\boldsymbol{D_b}$ defined as

$$\boldsymbol{D_i} = \boldsymbol{C_i^t}(\boldsymbol{L_H^{-1}}\boldsymbol{L_H^*})\boldsymbol{C_i} \tag{3.33a}$$
$$\boldsymbol{D_b} = \boldsymbol{C_i^t}(\boldsymbol{L_H^{-1}}\boldsymbol{L_H^*})\boldsymbol{C_b} \tag{3.33b}$$

Note that the matrix $\boldsymbol{D_i}$ is positive definite since $(\boldsymbol{L_H^{-1}}\boldsymbol{L_H^*})$, the ratios of dual and primal branch lengths, are all positive. Therefore, $\boldsymbol{D_i}$ will always be invertible.

Using (3.32) and (3.33), equation (3.31) simplifies to

$$\boldsymbol{D_i z_i} - \boldsymbol{D_b z_b} - \boldsymbol{p_z}r = \boldsymbol{Dz} - \boldsymbol{p_z}r = \boldsymbol{0} \tag{3.34}$$

First, consider the situation where the scale ζ and the boundary heights z_b are known. The inside geometry of the equilibrium network G is then immediately found:

$$\boldsymbol{z_i} = \boldsymbol{D_i^{-1}}\left(\boldsymbol{p_z}r - \boldsymbol{D_b z_b}\right) \tag{3.35}$$

This solution does not consider the bounds on the nodal heights. To find a solution which fits within the given boundaries, we must include the nodal height constraints (3.6). This can be formulated as

an optimization problem. The most general form of an optimization problem with k variables and r constraints is [Bertsimas and Tsitsiklis, 1997]

$$\begin{aligned} &\text{minimize} && \mathrm{f}\left(x_1, \ldots, x_k\right) \\ &\text{subject to} && \mathrm{g}_1\left(x_1, \ldots, x_k\right) \leq 0 \\ & && \vdots \\ & && \mathrm{g}_\mathrm{r}\left(x_1, \ldots, x_k\right) \leq 0 \end{aligned} \tag{3.36}$$

In the case that both the objective function f and all the constraints $g_1, \ldots, g_r$ are linear combinations of the variables $x_1, \ldots, x_n$, it is a linear optimization (LO) problem. The following non-standard form, used by *linprog*, the LO solver in the *Optimization Toolbox* in MATLAB [The Mathworks, 2009c], can be used to describe the linear optimization problem

$$\min_{\boldsymbol{x}} \boldsymbol{c}^{\mathbf{t}}\boldsymbol{x} \quad \text{such that} \quad \begin{cases} \boldsymbol{A}\boldsymbol{x} \leq \boldsymbol{b} \\ \boldsymbol{A}_{\boldsymbol{eq}}\boldsymbol{x} = \boldsymbol{b}_{\boldsymbol{eq}} \\ \boldsymbol{lb} \leq \boldsymbol{x} \leq \boldsymbol{ub} \end{cases} \tag{3.37}$$

where $\boldsymbol{c}$ is the objective (or cost) function vector, $\boldsymbol{x}$ are the variables, $\boldsymbol{A}$ and $\boldsymbol{A}_{\boldsymbol{eq}}$ are the inequalities and equalities constraint matrices with $\boldsymbol{b}$ and $\boldsymbol{beq}$ the corresponding right hand sides, and $\boldsymbol{lb}$ and $\boldsymbol{ub}$ the lower and upper bounds on the value of the variables.

The $(n+1 \times 1)$ variables vector $\boldsymbol{x}$ is

$$\boldsymbol{x} = \left[\begin{array}{c} \boldsymbol{z} \\ \hline r \end{array}\right] \tag{3.38}$$

The objective function $(n+1 \times 1)$ vector $\boldsymbol{c}$ has all zero entries except for the $n+1^{\text{th}}$ entry, and therefore the objective (or cost) of the minimization becomes

$$\boldsymbol{c}^{\mathbf{t}}\boldsymbol{x} = \left[\begin{array}{c|c} \mathbf{0} & \pm 1 \end{array}\right] \cdot \left[\begin{array}{c} \boldsymbol{z} \\ \hline r \end{array}\right] = \pm r \tag{3.39}$$

If $\boldsymbol{c}^{\mathbf{t}}\boldsymbol{x}$ is positive, r is being minimized which means that ζ is being maximized, resulting in the shallowest solution contained within the boundaries. This corresponds to the maximum horizontal force possible for the grid being considered. Alternatively, if $\boldsymbol{c}^{\mathbf{t}}\boldsymbol{x}$ is negative, r is being maximized which means that ζ is being minimized, resulting in the deepest solution contained within the boundaries. This corresponds to the minimum horizontal force possible for the grid being considered. Other possible objective functions will be discussed in §5.1.

Since there are no inequality constraints, the matrix $\boldsymbol{A}$ and vector $\boldsymbol{b}$ are empty.

$$\boldsymbol{A} = \begin{bmatrix} \ \end{bmatrix} \quad , \quad \boldsymbol{b} = \begin{bmatrix} \ \end{bmatrix} \tag{3.40}$$

From the second equality of (3.34) and (3.38), the $(n_i \times n + 1)$ equality constraints matrix $\boldsymbol{A_{eq}}$ and its corresponding $(n + 1 \times 1)$ right-hand-side vector $\boldsymbol{b_{eq}}$ are

$$\boldsymbol{A_{eq}} = \left[\begin{array}{c|c} \boldsymbol{D} & \boldsymbol{p_z} \end{array}\right] \quad , \quad \boldsymbol{b_{eq}} = \begin{bmatrix} \boldsymbol{0} \end{bmatrix} \tag{3.41}$$

Finally, from (3.6) and using that ζ needs to be positive for the solution to be a compression solution, the $(n + 1 \times 1)$ lower and upper bound vectors $\boldsymbol{lb}$ and $\boldsymbol{ub}$ are

$$\boldsymbol{lb} = \begin{bmatrix} \boldsymbol{z^{LB}} \\ \hline 0 \end{bmatrix} \quad , \quad \boldsymbol{ub} = \begin{bmatrix} \boldsymbol{z^{UB}} \\ \hline +\infty \end{bmatrix} \tag{3.42}$$

The LO problem, written in the form of (3.37), becomes

$$\min_{z,r} \pm r \quad \text{such that} \quad \begin{cases} \boldsymbol{Dz} - \boldsymbol{p_z} r = \boldsymbol{0} \\ \boldsymbol{z^{LB}} \leq \boldsymbol{z} \leq \boldsymbol{z^{UB}} \\ 0 \leq r \leq +\infty \end{cases} \tag{3.43}$$

The nodal heights $\boldsymbol{z}$ and scale factor r are solved for simultaneously. The actual scale factor of the dual grid is then found by taking the inverse of r. From (3.28), the horizontal components $\boldsymbol{s_H}$ of the branch forces $\boldsymbol{s}$ of the final compression-only solution G can easily be found by multiplying the dual branch lengths $\boldsymbol{l^*_H}$ by the actual scale ζ, and the axial branch forces $\boldsymbol{s}$ of the thrust network G are then found by combining (3.25) and (3.29):

$$\boldsymbol{s} = \boldsymbol{Lq} = \boldsymbol{L}\boldsymbol{L_H^{-1}}\boldsymbol{L_H^*}\boldsymbol{\zeta} \tag{3.44}$$

3.6 TNA framework

Figure 3.12 summarizes the TNA framework. Steps 2, 3 and 6 are the steps where user input is required. In §5.2, an extended framework will be presented for which step 6 is no longer a user input, but incorporated in an overall optimization set-up. Step 4 translates the user input, primal grid Γ (step 2) and the vault's geometry (step 6), into height limits, $\boldsymbol{z^I}$ and $\boldsymbol{z^E}$, nodal weights $\boldsymbol{p_z}$ and primal branch-node matrix $\boldsymbol{C}$. Step 5 generates the dual branch-node matrix $\boldsymbol{C^*}$ and a possible dual grid Γ^* using linear optimization. This step and step 6 will be developed and expanded on in §4.2. Step 7 sets up the main LO problem solving for the geometry and internal forces of the equilibrium solution G. Step 8 visualizes the results, allowing the user to update some parameters (step 9) and re-run the optimization.

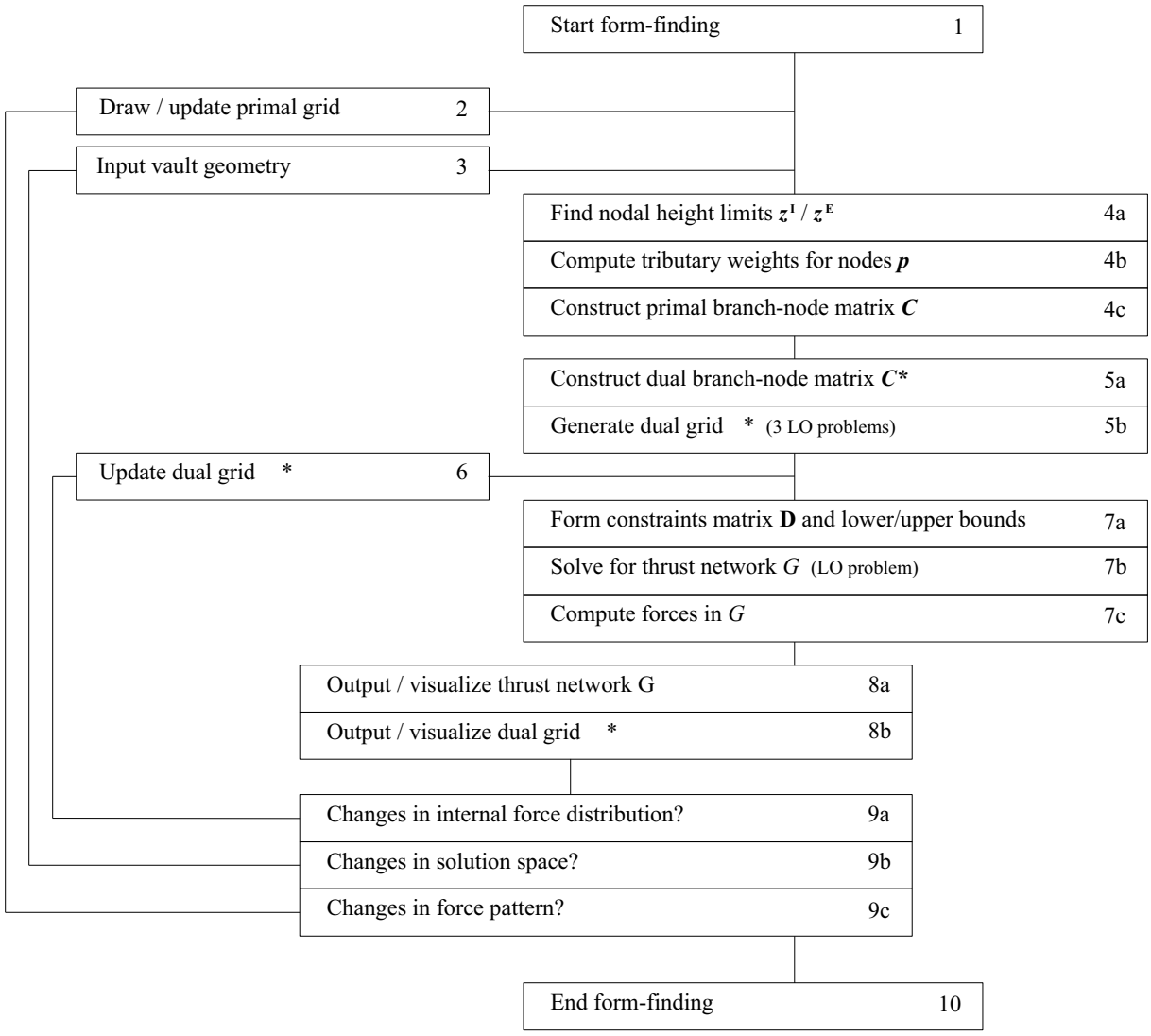

Figure 3.12 – Overview of the TNA framework.

A working prototype has been developed using the Optimization Toolbox [The Mathworks, 2009c] in MATLAB [The Mathworks, 2009b] and RhinoScripting [Rutten, 2007] for Rhinoceros [McNeel, 2007], and will be discussed in §4.5.

3.7 Summary

This chapter has introduced the Thrust Network Analysis (TNA) method. It provides a viable three-dimensional extension for thrust-line analysis. Key features are

- clear graphical representation of forces in the system (through the use of reciprocal force diagrams, i.e. the dual grids);
- a high level of control, allowing the exploration of different possible equilibrium solutions; and
- fast solving times because of the formulation as a simple linear optimization problem.

Chapters 4 and 5 will discuss the details of the implementation of TNA and how the basic framework presented in this chapter can be extended.

Chapter 6 will show that TNA offers an improved lower-bound method for the assessment of the stability of masonry vaults with complex geometries, and Chapter 7 will demonstrate that TNA can also be used as a flexible, intuitive and interactive design tool for finding three-dimensional equilibrium of compression-only surfaces and systems.

Chapter 4

Implementation

This chapter elaborates on the implementation of Thrust Network Analysis (TNA). It discusses how to represent the structural action and loading conditions of three-dimensional vaults into discrete force network models, and expands on the geometric properties and constraints of allowed network topologies and their reciprocal force diagrams. A new rule is introduced for deriving the degree of structural indeterminacy of three-dimensional network systems. Finally, it shows how TNA can be used to automate thrust line analysis.

4.1 Force patterns

4.1.1 Force paths and network topologies

The principal structural action of the vault should be represented in the chosen primal grid. The equilibrium solution and its force distribution are highly dependent on the choice of primal grid Γ. Using an appropriate network is very important. Kilian [2004b; 2006a] argues that a change in network topology can have much greater effect on the forces in a vault than the geometric optimization of a sub-optimal network. The choice of network topology also influences the obtainable geometries of the equilibrium shapes, as will be discussed in Chapter 7. Although the primal grid can be chosen freely, based on the experience and intuition of the analyst, simple methods can be used to help identify the principal structural actions of a vault. For example, it is often suggested that the forces "flow" to the supports as water would flow over its surface (e.g by Abraham [1934]), so the force lines follow the paths of steepest descent (Figure 4.1a). Alternatively, the forces could be attracted to the supports by forming the shortest paths over the surface (Figure 4.1b). Ideally, the chosen network topology would reflect all imaginable structural logics (Figure 4.1c). This represents better the indeterminate character of three-dimensional masonry vaults [O'Dwyer, 1999].

The appropriateness of force patterns is furthermore highly dependent on the specific loading conditions. O'Dwyer's barrel vault is a clear example (Figure 4.2). For a barrel vault, a set of parallel arches is a realistic assumption for its load-bearing action under self weight. For a point load at mid span, this set of force lines, which was most appropriate for the dead loading case, will not represent the three-dimensional capacity of the vault well. If the imposed load has to be carried by a single arch, the load capacity of

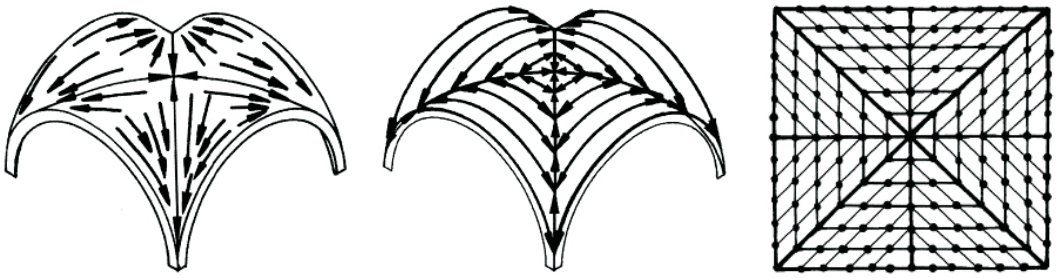

(a) (b) (c)

Figure 4.1 – Different structural actions can be assumed for a groin vault [O'Dwyer, 1999]: (a) parallel arches spanning between ribs, and (b) forces directly flowing towards the corners. The network topology in (c) represents both structural actions.

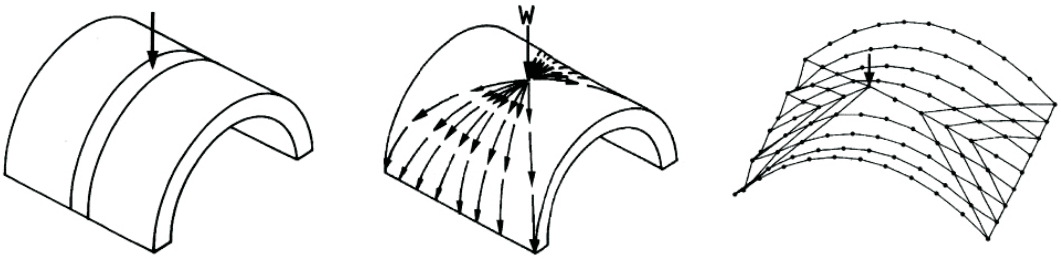

(a) (b) (c)

Figure 4.2 – (a) A point load is acted to a barrel vault, which acts as a very two-dimensional structure under self-weight only. (b) shows an appropriate force pattern to carry a point load applied at mid span down to line supports, and (c) is an equilibrium solution for the overlaid dead-load and live-load pattern (from O'Dwyer [1999]).

the vault will be limited by the capacity of that one arch (Figure 4.2a). For a point load at midspan, a fanning pattern would bring down the forces to the line supports (Figure 4.2b). So, a superposition of these two networks represents better the combined loading. O'Dwyer quantifies the difference between both assumptions using a collapse load factor. By increasing the point load λP until a funicular solution can no longer be found in the vault's section, the collapse load factor λ_c is found. The collapse load factor increases for the combined network with 325% compared to the parallel arches network. This shows clearly that a poor choice of force network can lead to an overly conservative and unrealistical assessment.

The resulting equilibrium network G is a discrete representation of a continuous *thrust surface*, a continuous surface representing the compression resultants throughout the structure. Although the choice of primal grid heavily dictates the equilibrium, the resulting discretized thrust surface is still a possible lower-bound solution. This approach is also used by Fraternali and Rocchetta [2002] using discrete Airy stress function instead of reciprocal diagrams, which will be discussed in §5.5.

Constraining the solutions to connected networks, which represent a possible discretization of a thrust surface, is in some cases very conservative. It is possible to find "better" solutions, e.g. with less horizontal thrust, if force lines can cross each other in space without intersecting (Figure 4.3). The equilibrium of a masonry unit, or *voussoir*, in the vault does not require all forces to meet at one point in 3-D space.

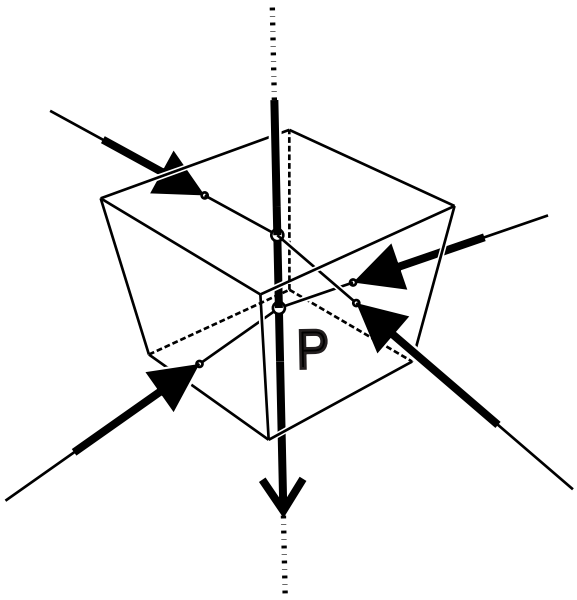

Figure 4.3 – Equilibrium of a stone voussoir with disconnected thrust lines.

The choice of force patterns can also define the boundary conditions which will be discussed in §4.1.3.

4.1.2 Properties and requirements

Valid primal grids need to be in equilibrium in the plane with all branches in compression. The inverse of these are defined as *spider webs* by Ash et al. [1988]. Spider webs refer to equilibrated tension-only solutions, but their properties can be used to look at the requirements for compression-only frameworks since this only requires the reaction forces at the boundaries to be inverted.

Based on the properties of a spider web as defined by Ash et al. [1988], a primal grid will be compression-only if it is a *proper cell decomposition of the plane* and has a *convex reciprocal* (Figure 4.4a). A proper cell decomposition divides the plane into convex and unbounded convex polygons such that (i) every point in the plane belongs to at least one cell (or space); (ii) the cells have disjoint, i.e. non-overlapping, interiors; and (iii) any two cells are separated by exactly one edge. A convex reciprocal is made out of *disjoint* convex polygons. In §4.5, the special case of a primal grid with two-valent nodes, which clearly violates condition (iii), will be discussed.

The following three statements for defining a valid primal grid Γ are equivalent [Ash et al., 1988]: (i) Γ is a *proper cell decomposition of the plane* and has a *convex polygon*; (ii) Γ has only branches in compression; and (iii) Γ is the projection of a *concave polyhedral bowl*. This concave polyhedral bowl is actually the discrete *Airy stress function* representing the compression-only equilibrium of the primal grid Γ as will be shown in §5.5.

If the primal grid has a higher valency than three, i.e. all nodes have at least four branches coming together per node, and it is a proper cell decomposition of the plane, then at least one spider web stress (represented by a convex reciprocal diagram) can be found for it by choosing appropriate reaction forces at the boundaries. This is not always true if the grid has at least one three-valent node (Figure 4.4b).

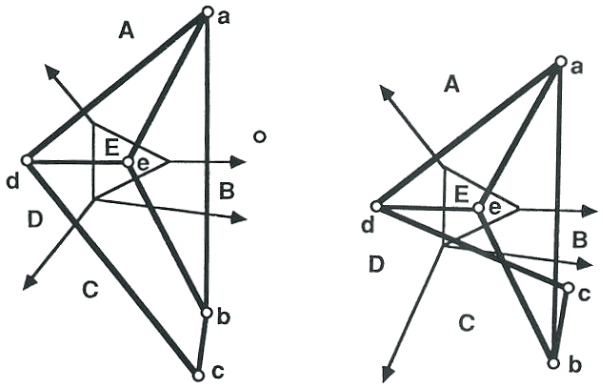

Figure 4.4 – Two proper cell decompositions of the plane with a (a) convex and (b) non-convex reciprocal [Ash et al., 1988]

A statically determinate, three-valent primal grid has one state of self-stress, dependent on a scaling factor. Because their in-plane equilibrium is unique, as represented by a triangulated, and thus "locked", dual grid, all allowable three-valent primal grids are spider webs. If not, the chosen three-valent network cannot serve as primal grid. This is shown in Figure 4.5: the arbitrarily chosen three-valent geometry is not in equilibrium within its plane since no reciprocal force diagram can be constructed from it. The dotted lines in Figure 4.5 show a possible correction of the pattern to make it compression-only, by closing its dual grid.

A theoretical spider web can intuitively be understood as follows: its geometry is stable in its plane and in equilibrium when "all the branches are replaced by rubber bands" and the boundary branches are pinned down at the boundary nodes [Ash et al., 1988]. It could be checked if a three-valent primal grid is a spider web using a computational equivalent to the rubber band analogy, i.e. by looking at it as a planar particle spring system where all branches are replaced by springs. The closest spider web to the non-equilibrated primal grid could then be found after applying a dynamic mesh relaxation in which the nodes are allowed to move slightly in the xy–plane.

The necessity of the primal grid to be a spider web is perhaps the most important difference between the thrust network method and the force density method (FDM). The *horizontal force densities* in TNA cannot be chosen randomly like the force densities in FDM. This is because the x– and y–coordinates of the nodes are defined by the choice of primal grid which imposes a number of constraints on the ratios of the force densities associated to each branch due to the requirements of valid (i.e. representing compression-only) dual grids (see §3.2.3).

The late Professor Ture Wester pointed out the analogy between TNA and spider webs in nature (Personal communication 2007). A spider makes its web, stable and in equilibrium within its plane (this is the primal grid Γ). For the web to be in equilibrium, it is naturally being pre-stressed (this corresponds to the proportions of a certain dual grid Γ^*, scaled by ζ). Under out-of-plane parallel loading, due to wind or an insect flying into it, the web becomes a perfect funicular, i.e. tension-only, 3-D net in equilibrium with the applied loading (this is the thrust network G). The depth of the web is then proportional to the fixed pre-stress (equivalent to the relationship between the scale ζ and the depth of G).

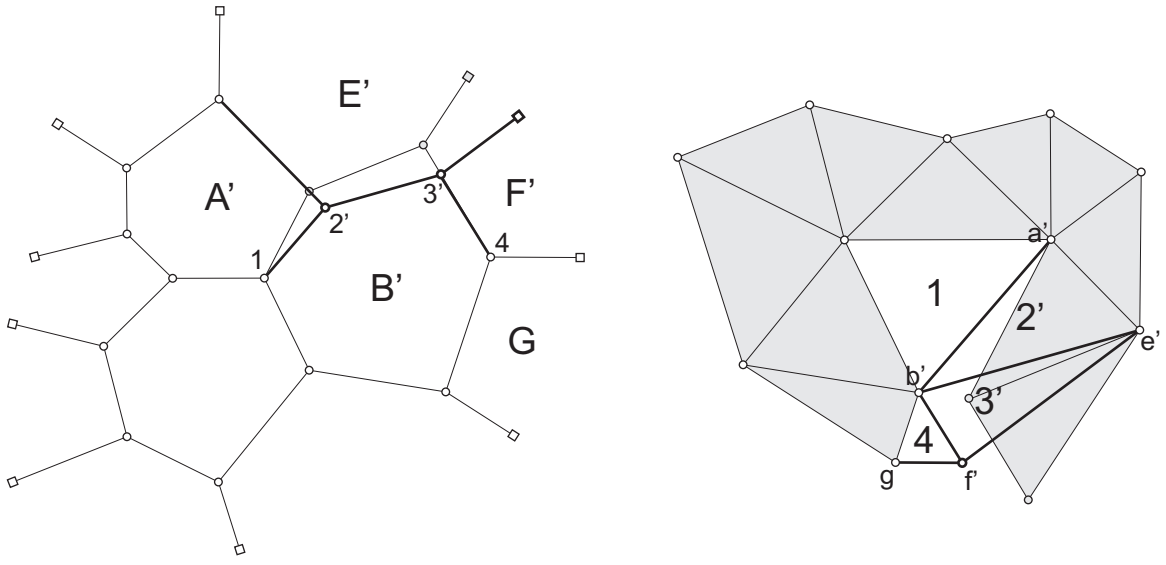

(a) (b)

Figure 4.5 – (a) A three-valent grid not in equilibrium: (b) its reciprocal does not close, and a possible "correction" (in bold).

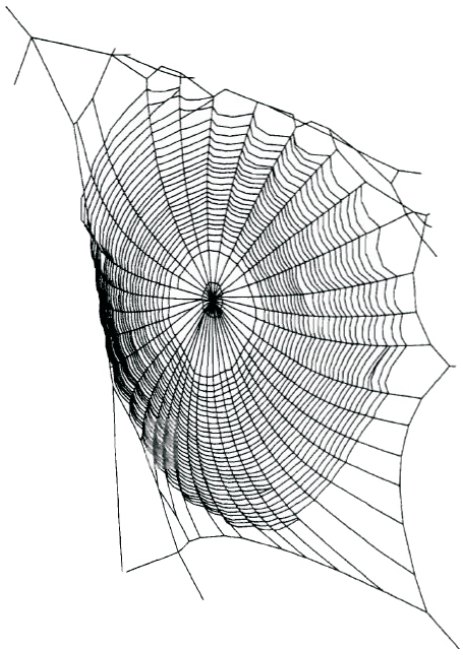

Figure 4.6 – A deformed spider web in nature, loaded out-of plane by the wind [Lin and Sobek, 1998].

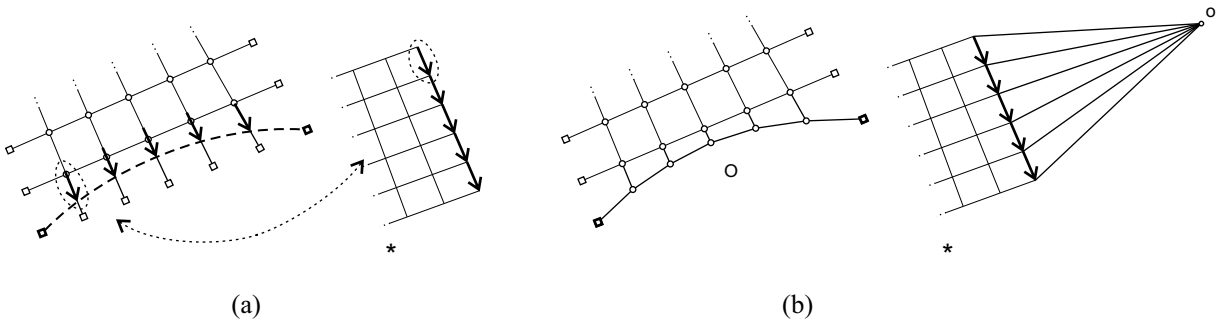

Figure 4.7 – (a) Primal grid without edge arch, and its corresponding reciprocal diagram. (b) The equilibrium of the funicular edge arch is represented by attaching a funicular polygon to the side of the reciprocal diagram.

4.1.3 Edge conditions and openings

Rather than having a continuous line support at the boundaries of a vault, the forces may go to a number of discrete supports, such as columns or buttresses. In the case of a simple 3-D force network made of a combination of arches, this is often obvious and inherent to the chosen network, but for fully three-dimensional meshes, the equilibria of the freed-up edges need to be considered.

There are two options to find the equilibrium of funicular edge arches: (i) the internal force distribution of the mesh is chosen first and the edge arch's shape then follows from that or (ii) the geometry of the edge arch is defined first in the horizontal plan, which then dictates the internal force distribution. For case (i), the shape of the edge arch in the primal grid Γ is funicular for the loading resulting from the forces in the branches connecting to it (Figure 4.7a). The values of these branch forces are found from the corresponding branch lengths in the dual grid Γ^* of the interior grid, without an edge arch (Figure 4.7).

In case (ii), the horizontal projection of the edge arch is chosen first and because this edge needs to be funicular in plan to be in global equilibrium, it thus dictates the forces in the branches ending in it, hence fixing the lengths of the corresponding dual branches. For the example in Figure 4.8, the freed-up inner edge of that vault is circular in plan. The circle is a funicular shape for radially applied uniform loading. In Figure 4.8c, it can be seen that as a result all the dual branches of the branches ending in it have equal lengths.

Another example is the circular compression ring of an oculus in a dome which demands that all horizontal thrusts from the radial arches ending into it have the same value. This idea will be expanded on in §6.5.

In both cases, once the geometry of the edge arch and a corresponding internal force distribution of the mesh are defined, then these primal and dual grids can be used in the one-step linear optimization as set up in Chapter 3 to find the equilibrium shape G.

Understanding the equilibrium of the free edge arch is not obvious. Since the branches from the interior of the vault end up on a single arch, it consists of only three-valent nodes. Although the edge arch seems to have an infinite number of possible equilibrium states (Figure 4.9a), the single edge arch will be uniquely defined by one parameter, e.g. the sag of the arch d in plan (Figure 4.9b-c).

In Figure 4.9), the most simple edge arch condition is considered, a triangular support bringing down the end reactions of a single parabolic arch, to show that the equilibrium of the edge arch is unique. From rotational equilibrium around the axis aa' (Figure 4.9c)or just from geometry (the triangular edge needs

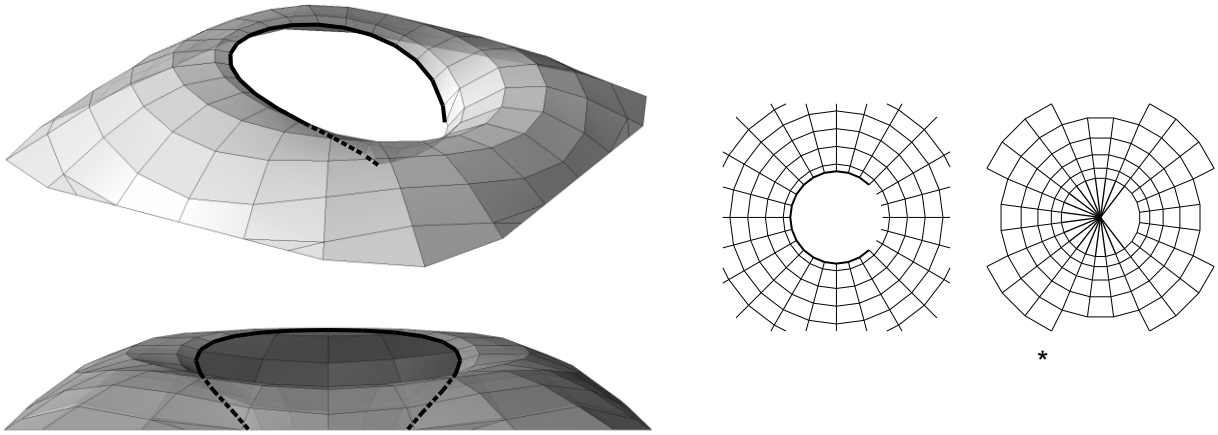

Figure 4.8 – (a) Equilibrium shape with a pre-defined geometry of the edge arch. (b) The circular edge arch requires (c) equal horizontal thrusts ending in it.

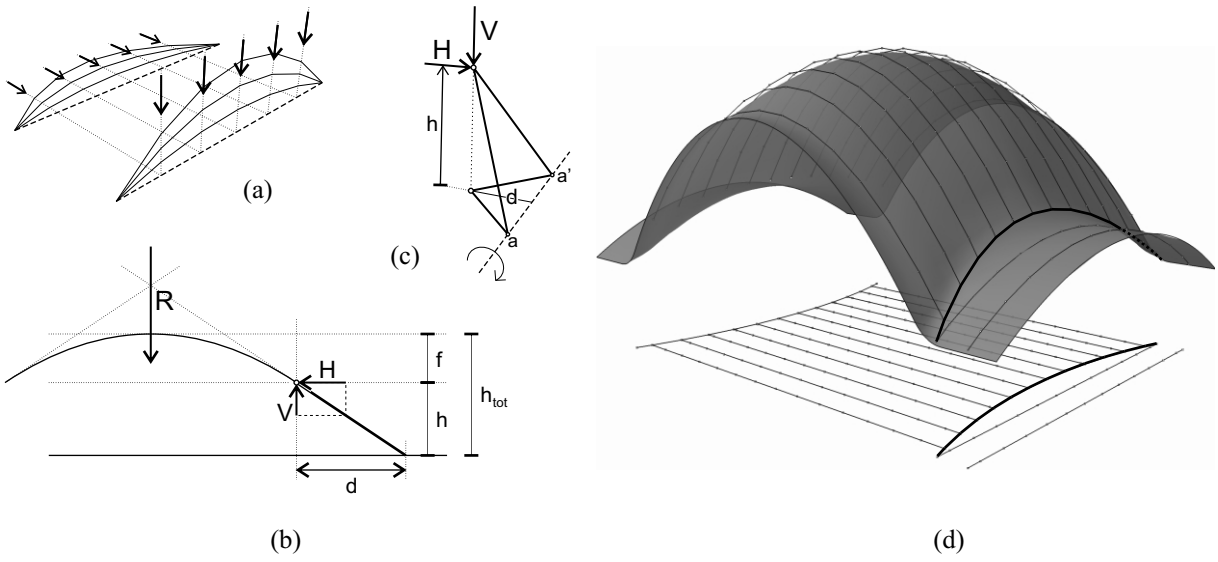

Figure 4.9 – (a) An edge arch - incorrectly - seems to have an infinite number of equilibrium solutions. A simple edge arch condition is considered: (b) profile of a parabola ending into a triangular edge "arch" and (c) the equilibrium of the triangular edge condition. (d) is a part of the pseudo 3-D analysis of a vault for Mapungubwe in South Africa (see §1.1).

to lie in the direction of the resultant of the parabola to be in equilibrium), the following has to be true

$$\frac{V}{H} = \frac{h}{d} \tag{4.1}$$

where V and H are the vertical and horizontal end reactions of the parabola, and h and d are the vertical and horizontal sag of the edge arch. A parabola is the funicular shape to bring down a uniformly distributed load w applied over its span L. Its horizontal and vertical end reaction forces, H and V, can be related to its geometry:

$$H = \frac{wL^2}{8f} = \frac{1}{C_1 f} \tag{4.2a}$$

$$V = \frac{wL}{2} = \frac{1}{C_2} \tag{4.2b}$$

with f the sag of the parabola. Since both w and L are known and constant, the terms $wL^2/8$ and $wL/2$ are replaced by $1/C_1$ and $1/C_2$ for simplicity. Using (4.1), (4.2) and that $h_{tot} = f + h$, the equilibrium of the edge arch can be written as

$$h = \frac{C_1 h_{tot}}{\left(C_1 + \frac{C_2}{d}\right)} \tag{4.3}$$

Since h_{tot} is a given, the equilibrium of the arch is therefore indeed only dependent on one parameter, either h or d in (4.3). This consideration was important in assessing the safety of the vaults of Mapungubwe in South Africa (Figure 4.9d) for which a two-dimensional approach was chosen initially, but the edge arch required a fully three-dimensional approach.

4.2 Reciprocal diagrams

4.2.1 Degrees of freedom of reciprocal diagrams

The dual branch-node matrix $\boldsymbol{C}^*$ gives the connectivity of the dual grid, i.e. the reciprocal force diagram. In the statically determinate case, i.e. a three-valent primal grid and corresponding triangulated dual grid, $\boldsymbol{C}^*$ is enough to construct the dual grid. After choosing one branch of the dual, the entire grid can be constructed incrementally from that first space. In the indeterminate case, because of the degrees of freedom of the dual grid, such a straightforward, procedural approach cannot be used. Section 4.2.3 will discuss how this problem can be solved using linear optimization.

Maxwell's [1864] rule for the construction of stiff frames said that in a two-dimensional framework every point in that framework can be determined if

$$m = 2n - 3 \tag{4.4}$$

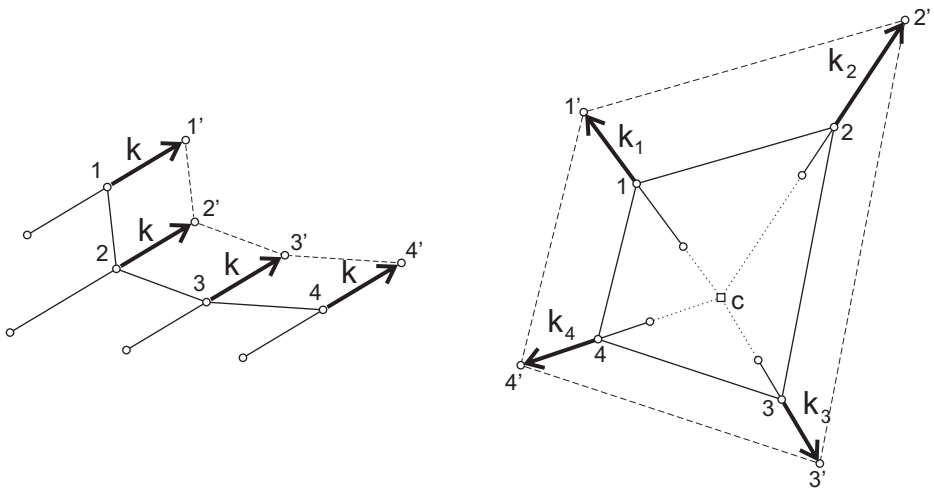

(a) (b)

Figure 4.10 – Types of dual grid adjustments: (a) stretch parallel edges by the same value k and (b) stretch incident branches proportional to their intersection point c.

To understand the behavior of frameworks which have too few bars to satisfy (4.4), Calladine [1978] introduced the *Extended Maxwell rule*

$$m - 2n + 3 = s - q \tag{4.5}$$

where s is the number of independent states of self-stress and q is the number of mechanisms of the frameworks.

Equation (4.5) can be used to define the indeterminacy, or different states of self-stress, of the primal grid, which is represented by the degrees of freedom of the dual grid. Since the dual grid is convex, i.e. each cell is a convex polyhedron, it does not have any state of self-stress, so $s^* = 0$. Therefore, the dual grid has q^* mechanisms

$$\begin{aligned} q^* &= 2n^* - m^* - 3 \\ &= 2f - m - 3 \end{aligned} \tag{4.6}$$

with $m^* = m$ and $n^* = f$, where m and m^* are the number of primal and dual branches, n^* the number of dual nodes and f the number of primal faces. The allowable adjustments of the dual grid are shown in Figure 4.10. The parallel relationship between the two reciprocal figures is preserved if (i) parallel edges are being stretched by the same amount; (ii) edges which if extended all meet in one point are stretched proportionally with respect to that intersection point; or (iii) in a combination of (i) and (ii).

For type (i) (Figure 4.10a), the new dual branch lengths are related to the original branch lengths as

$$l'_i = l_i + \xi_j^{(\mathrm{i})} \tag{4.7}$$

and for (ii) (Figure 4.10b),

$$\vec{ci'} = \xi_j^{(\mathrm{ii})} \cdot \vec{ci} \tag{4.8}$$

In both cases, ξ_j is the same constant for all branches related to and controlled by the $j^{\,\mathrm{th}}$ degree of freedom of the dual grid Γ^*. For type (i) variations, all edges are stretched by the same amount, while for (ii) variations this is not the case.

The independent mechanisms q^* of the dual grid are degrees of freedom (DOF) of type (i). The examples (a) to (c) of Figure 4.11 are dual grids with only type (i) DOFs. The overall scale can be considered as an additional degree of freedom of the dual grid, it is a DOF of type (i). Degrees of freedom of the grid of type (ii) occur when in the primal grid closed loops can be recognized (Figure 4.11d). These closed polygonal loops in the primal grid are in equilibrium which means that their force vectors intersect in the dual grid, hence satisfying that their branches will intersect when extended. So, by inspection of the primal grid only, the total number of DOFs k of the dual grid can be found:

$$\begin{aligned} k &= q^* + c + 1 \\ &= 2f - m + c - 2 \end{aligned} \tag{4.9}$$

where c is the number of closed loops in the primal grid. Relation (4.9) is a new rule introduced by the author to determine the DOFs of indeterminate reciprocal diagrams.

4.2.2 Allowed variations of the dual grid

For each of the k degrees of freedom, there is an (independent) parameter which controls a set of branches in the dual grid. In order to manage these variables in an optimization process, the branches in the dual grid, dependent of each parameter, need to be identified. Pellegrino and Calladine [1986] developed an algorithm to detect and identify the mechanisms of kinematically indeterminate frameworks, which give the DOFs of type (i).

Figure 4.12 shows for the example network used in Figure 3.11 which set of branches are linked and controlled by each parameter. Figure 4.11d shows that the dual grid has three DOFs ($k = 3$), giving three parameters ξ_j.

Figure 4.12 demonstrates that the set of branches $\{I, III, IX, XI\}$ and $\{II, IV, X, XII\}$ are controlled by $\xi_1^{(\mathrm{i})}$ and $\xi_2^{(\mathrm{i})}$, parameters of type (i), and the set of branches $\{V, VI, VII, XI\}$ by $\xi_3^{(\mathrm{ii})}$, a parameter of type (ii). These k parameters ξ_j will be used in §5.2 to incorporate the degrees of freedom of the dual grid in an overall optimization process.

Each of the m dual branches has a local scale factor ζ_i associated with it and these are not independent, but controlled by the k parameters ξ_j ($k < m$). The parameters of type (i) are listed first and the $(m \times k)$ matrix $\boldsymbol{F}$ relates the ξ_j to the ζ_i as follows:

$$\boldsymbol{\zeta} = \boldsymbol{F}\boldsymbol{\xi} = \left[\begin{array}{c|c} \boldsymbol{F}^{(\mathbf{i})} & \boldsymbol{F}^{(\mathbf{ii})} \end{array}\right] \left[\begin{array}{c} \boldsymbol{\xi}^{(\mathbf{i})} \\ \hline \boldsymbol{\xi}^{(\mathbf{ii})} \end{array}\right] = \boldsymbol{F}^{(\mathbf{i})}\boldsymbol{\xi}^{(\mathbf{i})} + \boldsymbol{F}^{(\mathbf{ii})}\boldsymbol{\xi}^{(\mathbf{ii})} \tag{4.10}$$

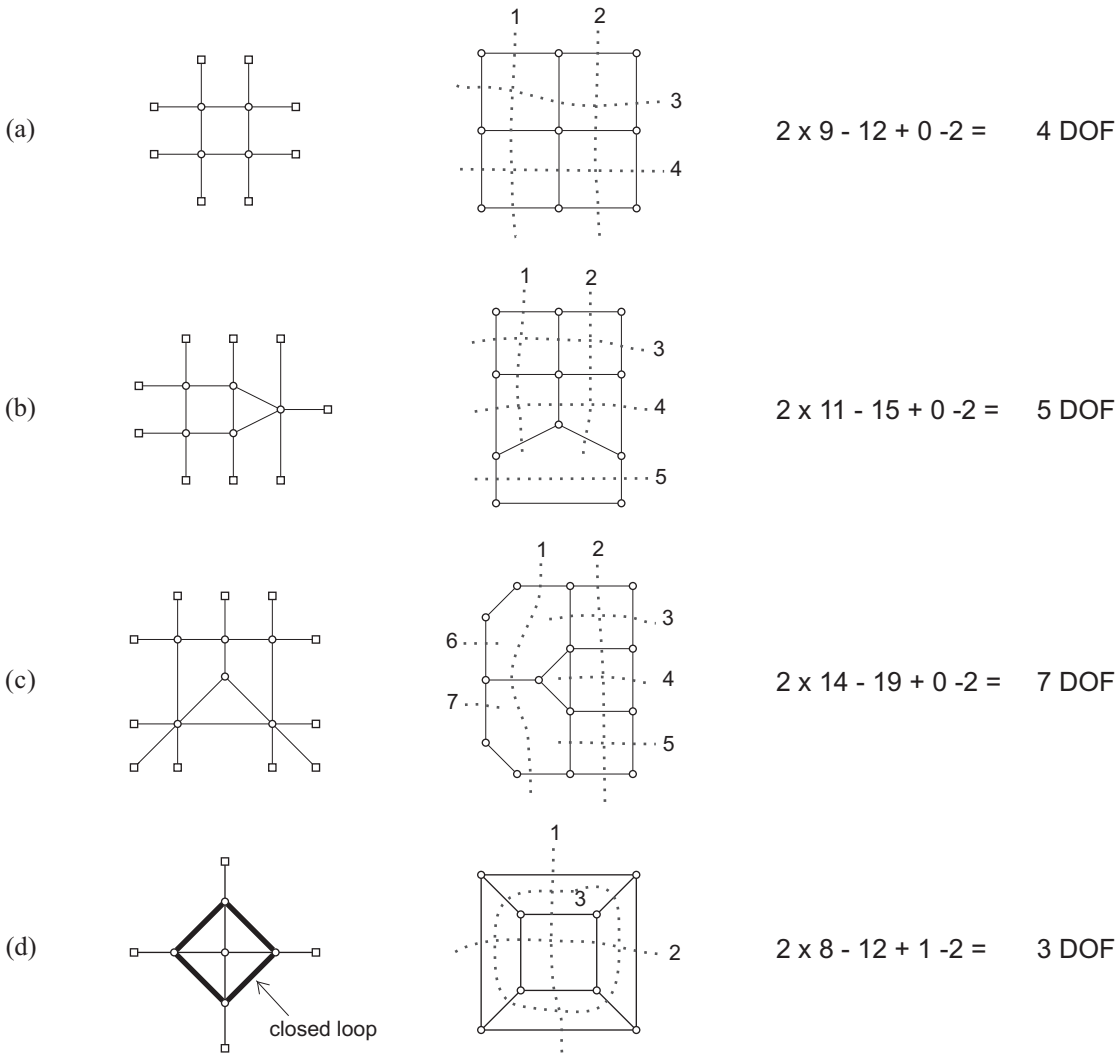

Figure 4.11 – Examples of application of the DOF rule (4.9). Example (d) has one closed loop in the primal grid. The dottes lines label the DOFs, crossing the branches controlled by the same, independent parameter.

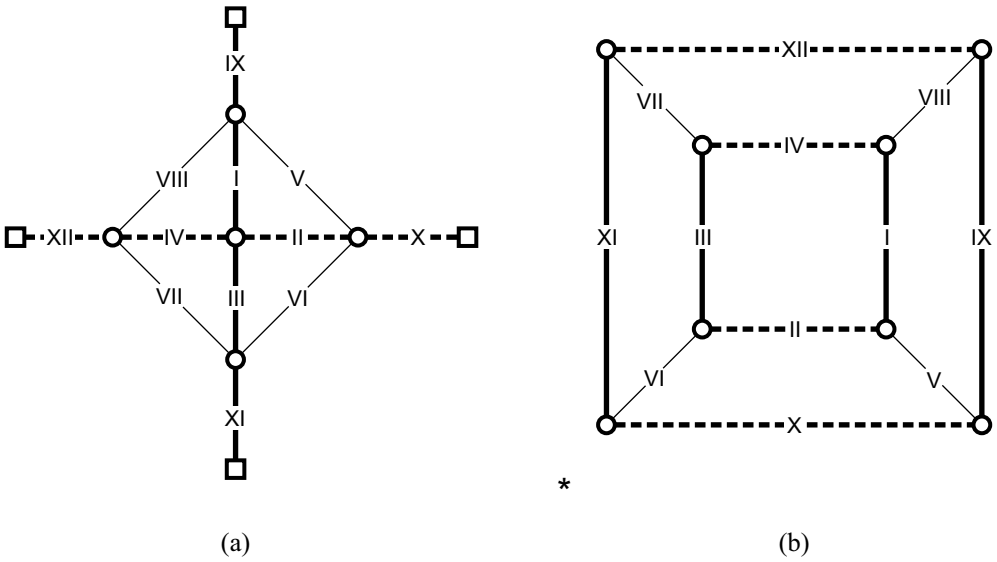

Figure 4.12 – The set of branches marked with thick, solid lines and with thick, dotted lines are controlled by parameters of type (i), and the set of branches with thin, solid lines by a parameter of type (ii).

For the example in Figure 4.12, the $\boldsymbol{F}$ matrix becomes

$$\boldsymbol{F} = \left[\begin{array}{cccccccccccc} 1 & \cdot & 1 & \cdot & \cdot & \cdot & \cdot & \cdot & 1 & \cdot & 1 & \cdot \\ \cdot & 1 & \cdot & 1 & \cdot & \cdot & \cdot & \cdot & \cdot & 1 & \cdot & 1 \\ \hline \cdot & \cdot & \cdot & \cdot & 1 & 1 & 1 & 1 & \cdot & \cdot & \cdot & \cdot \end{array}\right]^{\mathrm{t}} \tag{4.11}$$

The scale vector $\boldsymbol{\zeta}$ relates the new dual branch lengths to the branch lengths in the original dual grid.

$$(\boldsymbol{l}^*_{\mathbf{H}})_{\mathrm{new}} = (\boldsymbol{L}^*_{\mathbf{H}})_{\mathrm{old}}\, \boldsymbol{\zeta} \tag{4.12}$$

Using (4.7) and (4.10), the relation between ζ and ξ for branches of type (i) is

$$\boldsymbol{\zeta}^{(\mathbf{i})} = {\boldsymbol{L}^*_{\mathbf{H}}}^{-\mathbf{1}} \left(\boldsymbol{l}^*_{\mathbf{H}} + \boldsymbol{F}^{(\mathbf{i})}\boldsymbol{\xi}^{(\mathbf{i})}\right) = \mathbf{1}_m + {\boldsymbol{L}^*_{\mathbf{H}}}^{-\mathbf{1}} \boldsymbol{F}^{(\mathbf{i})}\boldsymbol{\xi}^{(\mathbf{i})} \tag{4.13}$$

where $\mathbf{1}_m$ is the $(m \times 1)$ ones vector; and using (4.9) and (4.10) for type (ii) branches

$$\boldsymbol{\zeta}^{(\mathbf{ii})} = {\boldsymbol{L}^*_{\mathbf{H}}}^{-\mathbf{1}} \left(\boldsymbol{L}^*_c + \boldsymbol{L}^*_{\mathbf{H}}\right) \boldsymbol{F}^{(\mathbf{ii})}\boldsymbol{\xi}^{(\mathbf{ii})} \tag{4.14}$$

in which $\boldsymbol{L}_c$ is the diagonal matrix with the lengths between the intersection point c of the incident vectors and their starting nodes (as shown in Figure 4.10b).

$$\boldsymbol{\zeta}^{(\mathbf{ii})} = {\boldsymbol{L}^*_{\mathbf{H}}}^{-\mathbf{1}} \left(\boldsymbol{L}^*_c + \boldsymbol{L}^*_{\mathbf{H}}\right) \boldsymbol{F}^{(\mathbf{ii})}\boldsymbol{\xi}^{(\mathbf{ii})} \tag{4.15}$$

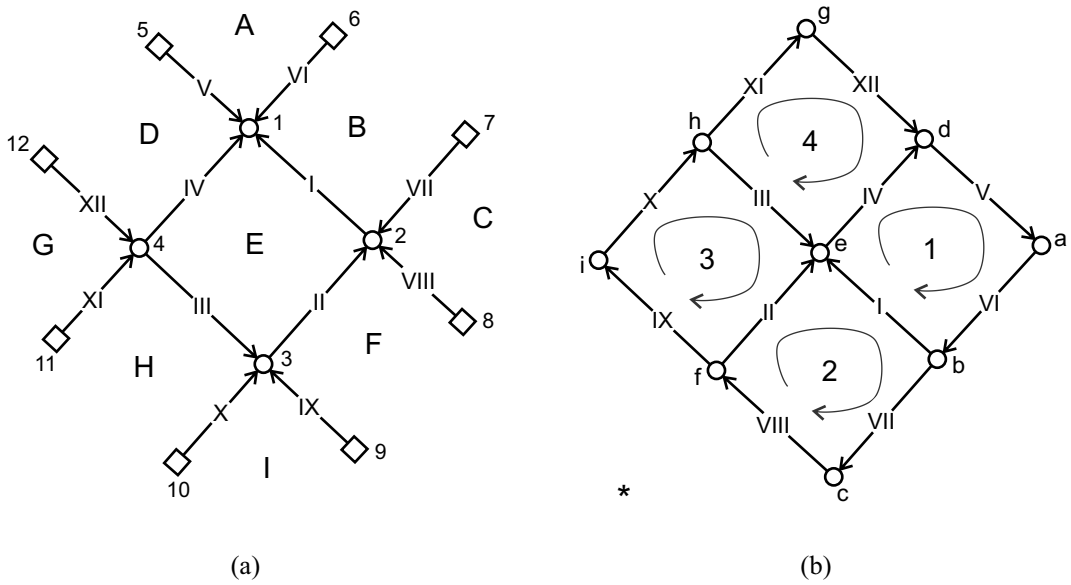

Figure 4.13 – Oriented graphs of (a) primal and (b) dual grids. Note that corresponding branch vectors are parallel and have the same direction.

4.2.3 Automatic production of reciprocals

A procedural approach to construct the dual grid from a given primal grid is no longer possible for an indeterminate primal grid because of the many DOFs of the dual. To manage all these DOFs and find a compatible distribution, i.e. resulting in a possible dual grid satisfying the requirements in §3.2.3, this translation is formulated as an optimization problem. A possible dual grid Γ^* from a given primal grid Γ can be produced with a sequence of three linear optimization problems.

Following the conventions introduced in §3.4.3, the internal nodes are labeled first, and the primal branch vectors always go from a node with higher index to one with a lower index. The numbering of the branches is arbitrary. Both primal and dual grids are defined as oriented graphs (Figure 4.13), so each branch can be written as a vector. The corresponding primal and dual branch vectors are $\underline{\boldsymbol{l}}_{\boldsymbol{i}}$ and $\underline{\boldsymbol{l}}^*_{\boldsymbol{i}}$ respectively which have the x– and y–coordinate difference vectors u and v as horizontal and vertical components.

$$\underline{\boldsymbol{l}}_{\boldsymbol{i}} = \begin{bmatrix} \underline{l}_{i,x} \\ \underline{l}_{i,y} \end{bmatrix}^{\mathrm{t}} = \begin{bmatrix} u_i \\ v_i \end{bmatrix}^{\mathrm{t}} = \begin{bmatrix} C_{ij}x_j \\ C_{ij}y_j \end{bmatrix}^{\mathrm{t}} \quad , \quad \underline{\boldsymbol{l}}^*_{\boldsymbol{i}} = \begin{bmatrix} \underline{l}^*_{i,x} \\ \underline{l}^*_{i,y} \end{bmatrix}^{\mathrm{t}} = \begin{bmatrix} u^*_i \\ v^*_i \end{bmatrix}^{\mathrm{t}} = \begin{bmatrix} C^*_{ij}x^*_k \\ C^*_{ij}y^*_k \end{bmatrix}^{\mathrm{t}} \tag{4.16}$$

For the first LO problem, the reciprocal rules for compression-only networks are converted into constraints for the optimization problem.

The branch vectors in the primal and dual grid are parallel and need to have the same direction. Corresponding primal and dual branch vectors placed in the origin are coincident, meaning that each dual branch vector $\underline{\boldsymbol{l}}^*_{\boldsymbol{i}}$ can be written as a function of its corresponding primal branch $\underline{\boldsymbol{l}}_{\boldsymbol{i}}$ multiplied by a positive scalar t_i (Figure 4.14).

$$\underline{\boldsymbol{l}}^*_{\boldsymbol{i}} = t_i \cdot \underline{\boldsymbol{l}}_{\boldsymbol{i}} \tag{4.17}$$

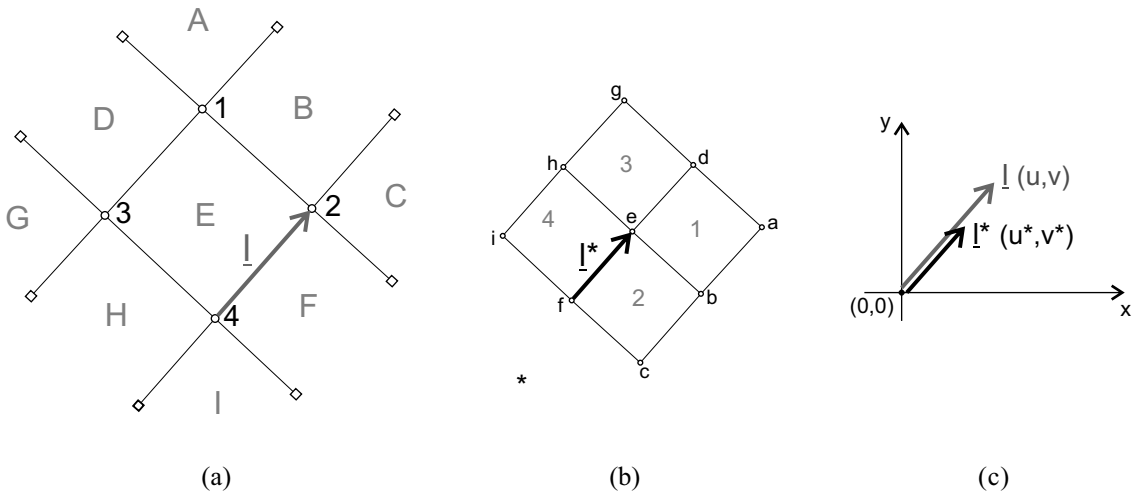

Figure 4.14 – (a) The primal branch vector $\underline{l}$ is scaled compared to (b) the dual branch vector $\underline{l}^*$, (c) which is clear if placed in the origin.

Using (4.16) in (4.17) and after rearranging gives the following linear constraints:

$$\begin{cases} u_i^* - u_i \cdot t_i = 0 \\ v_i^* - v_i \cdot t_i = 0 \quad \text{for} \quad i = 1 \dots m \\ t_i \geq 0 \end{cases} \tag{4.18}$$

where u_i and v_i are known since the geometry of the primal grid Γ is given. The unknowns in (4.18) are u_i^*, v_i^* and t_i. In matrix form (4.18) becomes

$$\begin{cases} \boldsymbol{U}^* - \boldsymbol{U}\boldsymbol{t} = \boldsymbol{I_m}\boldsymbol{u}^* - \boldsymbol{U}\boldsymbol{t} = \boldsymbol{0} \\ \boldsymbol{V}^* - \boldsymbol{V}\boldsymbol{t} = \boldsymbol{I_m}\boldsymbol{v}^* - \boldsymbol{V}\boldsymbol{t} = \boldsymbol{0} \\ \boldsymbol{t} \geq \boldsymbol{0} \end{cases} \tag{4.19}$$

where $\boldsymbol{I_m}$ is the identity matrix of size m.

The set of constraints (4.19) guarantee that corresponding branches in primal and dual are parallel and oriented in the same direction. It still needs to be enforced that branches coming together in a node in the primal grid form a closed polygon in the dual grid and that these polygonal cells are formed clockwise to guarantee a compression node, as discussed in §3.2.3.

Shown in Figure 4.15, the equilibrium of the compressive branch forces coming together in a node of the primal is represented by a closed force polygon, formed clockwise with respect to that node (Figure 4.15b). By combining all these polygons together, the dual grid is formed (Figure 4.15c). When comparing Figure 4.13b and Figure 4.15c, it is clear that only half of the interior branches of the dual oriented graph are oriented correctly with respect to the clock-wise cycling rule. Equivalently, when going around a node in the primal grid, only half of the directed branches of Figure 4.13a are pointing towards that node. For

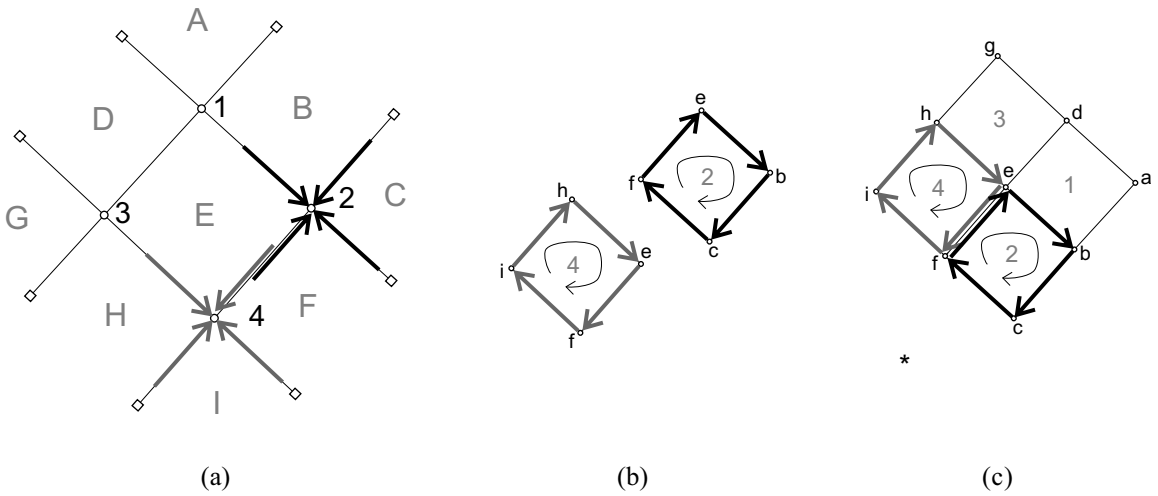

(a) (b) (c)

Figure 4.15 – (a) Compressive branches "push" the nodes. Their nodal equilibrium is represented by (b) closed polygons formed clockwise and (c) assembled to form the dual grid .

compatibility, this information needs to be added to (4.19). For node 2 in Figure 4.15 e.g.:

$$-\underline{l}^*_{be} + \underline{l}^*_{bc} + \underline{l}^*_{cf} + \underline{l}^*_{fe} = 0 \tag{4.20}$$

or

$$\begin{cases} -u^*_{be} + u^*_{bc} + u^*_{cf} + u^*_{fe} = 0 \\ -v^*_{be} + v^*_{bc} + v^*_{cf} + v^*_{fe} = 0 \end{cases} \tag{4.21}$$

Using the branch numbering in Figure 4.13, (4.22) is

$$-\underline{l}^*_{\mathrm{I}} + \underline{l}^*_{\mathrm{VII}} + \underline{l}^*_{\mathrm{VIII}} + \underline{l}^*_{\mathrm{II}} = 0 \tag{4.22}$$

Doing this for all n_i primal nodes, or dual spaces, gives the following $(n_i \times m)$ matrix $\boldsymbol{A}_{\boldsymbol{eq},+}$ for the grid in Figure 4.13.

$$\boldsymbol{A}_{\boldsymbol{eq},+} = \begin{bmatrix} 1 & \cdot & \cdot & 1 & 1 & 1 & \cdot & \cdot & \cdot & \cdot & \cdot & \cdot \\ -1 & 1 & \cdot & \cdot & \cdot & \cdot & 1 & 1 & \cdot & \cdot & \cdot & \cdot \\ \cdot & -1 & 1 & \cdot & \cdot & \cdot & \cdot & \cdot & 1 & 1 & \cdot & \cdot \\ \cdot & \cdot & -1 & -1 & \cdot & \cdot & \cdot & \cdot & \cdot & \cdot & 1 & 1 \end{bmatrix} \tag{4.23}$$

The matrix $\boldsymbol{A}_{\boldsymbol{eq},+}$ is described by the *row space*, or *cutset space*, of the incidence matrix of the primal oriented graph, which is the transpose of the primal branch-node matrix, $\boldsymbol{C}^{\mathbf{t}}$ (§3.4.3).

$$\boldsymbol{A}_{\boldsymbol{eq},+} = \mathrm{Im}\left(\boldsymbol{C}^{\mathbf{t}}\right) = \boldsymbol{C}^{\mathbf{t}}_{\boldsymbol{i}} \tag{4.24}$$

where $\mathrm{Im}\left(\boldsymbol{C}^{\mathbf{t}}\right)$ means the row space, or cutset space, of $\boldsymbol{C}^{\mathbf{t}}$.

The equations of the form of (4.21) become in matrix notation

$$\begin{cases} \boldsymbol{C}_i^{\mathbf{t}} \boldsymbol{u}^* = \mathbf{0} \\ \boldsymbol{C}_i^{\mathbf{t}} \boldsymbol{v}^* = \mathbf{0} \end{cases} \tag{4.25}$$

The automatic generation of the dual grid can be described as a linear optimization problem in the form of (3.28). The variables vector $\boldsymbol{x}$ becomes a $(3m \times 1)$ vector, listing the unknowns $\boldsymbol{u}^*$, $\boldsymbol{v}^*$ and $\boldsymbol{t}$

$$\boldsymbol{x} = \left[\begin{array}{c} \boldsymbol{u}^* \\ \hline \boldsymbol{v}^* \\ \hline \boldsymbol{t} \end{array}\right] \tag{4.26}$$

Since there are no inequality constraints, the matrix $\boldsymbol{A}$ and vector $\boldsymbol{b}$ are empty.

$$\boldsymbol{A} = [\ \ ] \quad , \quad \boldsymbol{b} = [\ \ ] \tag{4.27}$$

Combining the constraints (4.19) and (4.25), the $(2m + 2n_i \times 3m)$ equality constraints matrix $\boldsymbol{A_{eq}}$ and $(2m + 2n_i \times 1)$ vector $\boldsymbol{b_{eq}}$ become

$$\boldsymbol{A_{eq}} = \left[\begin{array}{c|c} \boldsymbol{I_{2m}} & \begin{array}{c} \boldsymbol{-U} \\ \boldsymbol{-V} \end{array} \\ \hline \begin{array}{c|c} \boldsymbol{C_i^t} & \boldsymbol{0} \\ \hline \boldsymbol{0} & \boldsymbol{C_i^t} \end{array} & \boldsymbol{0} \end{array}\right] \tag{4.28}$$

To solve the problem using optimization, a cost vector $\boldsymbol{c}$ still needs to be defined. The goal is to find one possible starting dual grid. If the objective (4.29) is used, the cells will have approximately equal sizes or equivalently the dual branches lengths will be equalized. This solution corresponds to an approximately equalized or distributed thrust network. The objective function becomes then

$$\min_{t_i} \quad \sum_i t_i \quad \text{with} \quad t_i \geq \frac{d}{l_i} \tag{4.29}$$

where d is a positive scalar.

So, the cost $\boldsymbol{c}^{\mathbf{t}}\boldsymbol{x}$ of the optimization becomes

$$c^t x = \left[\begin{array}{c|c|c} \mathbf{0} & \mathbf{0} & \mathbf{1}^{\mathbf{t}}\boldsymbol{m} \end{array}\right] \cdot \left[\begin{array}{c} \boldsymbol{u}^* \\ \hline \boldsymbol{v}^* \\ \hline \boldsymbol{t} \end{array}\right] = \sum \boldsymbol{t} \tag{4.30}$$

The bounds on the variables are

$$\boldsymbol{lb} = \begin{bmatrix} -\infty \\ \hline -\infty \\ \hline \boldsymbol{d/l} \end{bmatrix} \quad , \quad \boldsymbol{ub} = [\quad] \tag{4.31}$$

The first LO problem then becomes

$$\min_{\boldsymbol{u}^*, \boldsymbol{v}^*, \boldsymbol{t}} \quad \sum t \quad \text{such that} \quad \begin{cases} \boldsymbol{I_m u^*} - \boldsymbol{Ut} = \boldsymbol{0} \\ \boldsymbol{I_m v^*} - \boldsymbol{Vt} = \boldsymbol{0} \\ \boldsymbol{C_i^t u^*} = \boldsymbol{0} \\ \boldsymbol{C_i^t v^*} = \boldsymbol{0} \\ \boldsymbol{L^{-1} d} \leq \boldsymbol{t} \leq +\boldsymbol{\infty} \end{cases} \tag{4.32}$$

Solving this first optimization problem does not yet give the dual grid; it gives the dual coordinate difference vectors, $\boldsymbol{u}^*$ and $\boldsymbol{v}^*$. The actual dual coordinates $\boldsymbol{x}^*$ and $\boldsymbol{y}^*$ now can be found from the relationship between $\boldsymbol{u}^*$, $\boldsymbol{v}^*$ and $\boldsymbol{x}^*$, $\boldsymbol{y}^*$ from (3.19)

$$\boldsymbol{u}^* = \boldsymbol{C}^* \boldsymbol{x}^* \quad , \quad \boldsymbol{v}^* = \boldsymbol{C}^* \boldsymbol{y}^* \tag{4.33}$$

where $\boldsymbol{u}^*$ and $\boldsymbol{v}^*$ have just been found in the first LO optimization.

The dual branch-node matrix $\boldsymbol{C}^*$ has dimensions $(m \times n^*)$ and can therefore not be inverted to directly find the unknown dual coordinates $\boldsymbol{x}^*$ and $\boldsymbol{y}^*$. Equation (4.33) is solvable using linear optimization. Two separate LO problems are solved, one to find x_1^* and one to find y_1^*. The two LO problems then simply become

$$\min_{\boldsymbol{x}^*} \quad x_1^* \quad \text{such that} \quad \begin{cases} \boldsymbol{C}^* \boldsymbol{x}^* = \boldsymbol{u}^* \\ x_1^* = x^0 \end{cases} \tag{4.34}$$

and

$$\min_{\boldsymbol{y}^*} \quad y_1^* \quad \text{such that} \quad \begin{cases} \boldsymbol{C}^* \boldsymbol{y}^* = \boldsymbol{u}^* \\ y_1^* = y^0 \end{cases} \tag{4.35}$$

to find $\boldsymbol{x}^*$ and $\boldsymbol{y}^*$ respectively. One coordinate (x^0, y^0) of the dual grid needs to be chosen, and that node gives a unique solution for the dual grid on the plane. Linear optimization in and is only used to solve the equation $\boldsymbol{C}^* \boldsymbol{x}^* = \boldsymbol{u}^*$ with a wide matrix $\boldsymbol{C}^*$. Furthermore, the objective function and if it is a maximization or minimization does not matter.

The first LO problem of the automatic dual generation, formulation (4.32), is computationally the bottleneck of the entire TNA set-up. Particularly the $(2m + 2n_i \times 3m)$ equality constraints matrix $\boldsymbol{Aeq}$ given in (4.28) increases the computation time drastically and the *linprog* solver in MATLAB seems to have problems finding the solution for networks with more than ca. 700 branches. The heavier, and sometimes

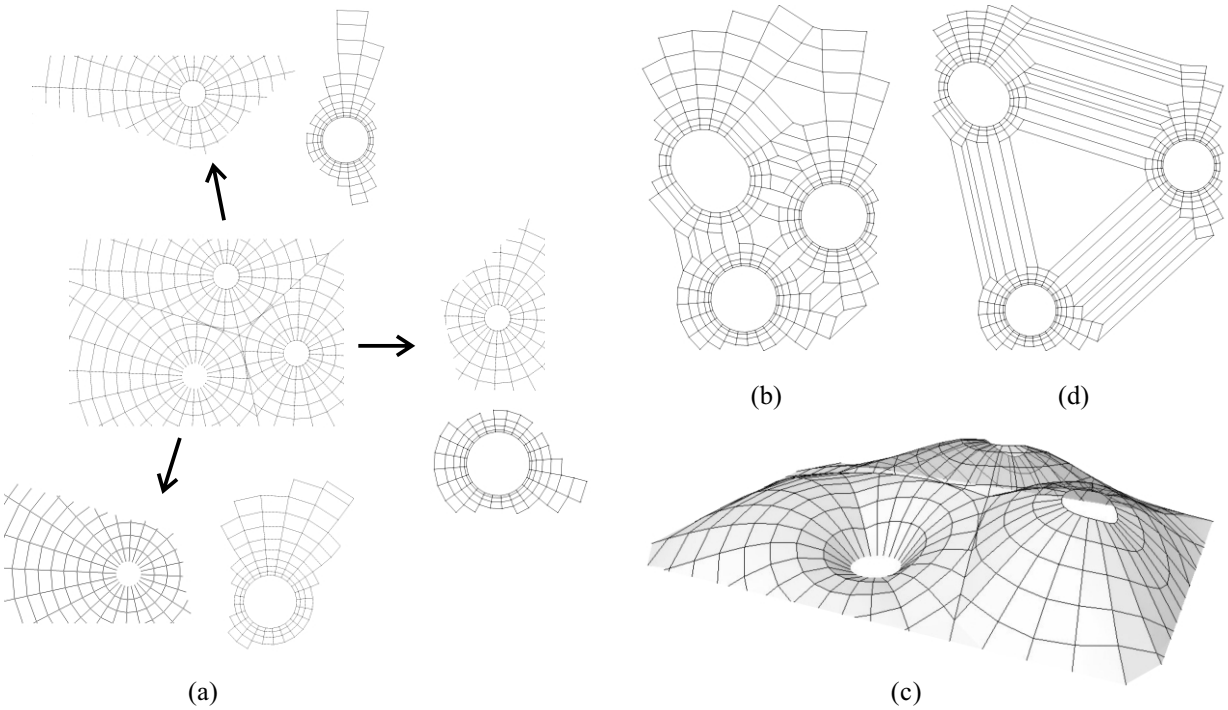

Figure 4.16 – (a) A large network is divided into sub-networks, whose dual grids can be found fast. (b) These dual grids are linked to form the dual grid of the original network. (c) The overall equilibrium network is found, with (d) as its adjusted dual grid.

problematic, computation of (4.32) can be reduced by considering sub-networks, i.e. by cutting up the primal grid into more manageable parts, as illustrated in Figure 4.16a. In a second optimization, the separate dual sub-grids are connected, using an intermediate optimization step, to form the dual grid of the entire network (Figure 4.16b). This approach is used for more complex networks as e.g. the one shown in Figure 4.16c. Figure 4.16d shows the final, adjusted dual grid which results in that equilibrium shape.

4.3 Loading

Because of the discrete character of the networks, the loads on the structure need to be discretized and lumped into the nodes. For the self weight of the vault, tributary volumes for each node should be defined and then the live loads can be superposed.

4.3.1 Tributary volumes

Several strategies have been implemented for distributing the weight of the vault to the different nodes:

(i) The volume of the vault is first cut up into pieces (these can be related to the *voussoirs* if it is a stone vault) and their *centroids* are then projected onto the horizontal plane defining the nodes of the primal

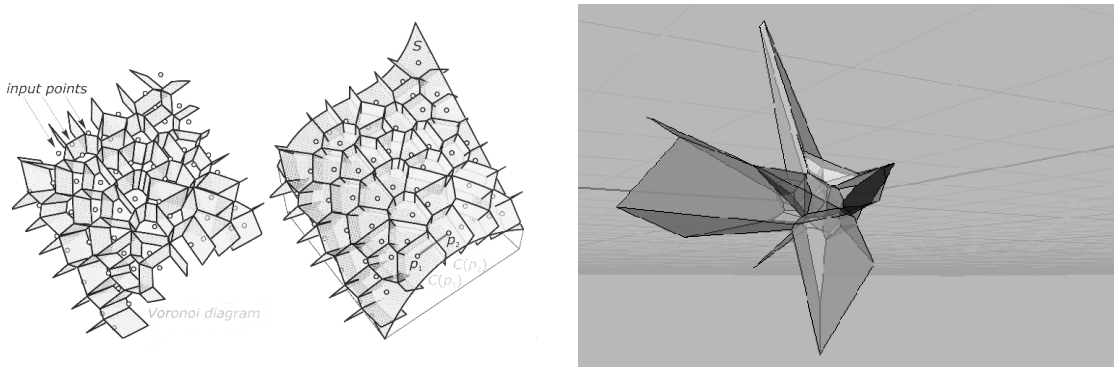

Figure 4.17 – (a) Spatial Voronoi cells generated from seeds on an input surface [Pottmann et al., 2007], and (b) a RhinoScript implementation of Qhull [Dritsas, 2006].

grid as was shown in Figure 3.9. This approach constrains the possible topologies of the primal grid since the main nodes are defined. Using secondary, unloaded nodes, topologies which are not constrained only to the projected centroids can be formed (see also option (iii)), but adding these nodes increases the computation times.

(ii) Identifying the principal structural actions and choosing a primal grid accordingly, as described in §4.1.1, does not guarantee that its nodes are the vertical projections of centroids of the vault above, so now the appropriate weights need to be attributed to each loaded node. This can be done using three-dimensional tributary volumes computed using spatial *Voronoi diagrams* [Voronoi, 1907; Preparata and Shamos, 1985]. The nodes of the primal grid are projected onto the middle surface of the vault. These projection nodes are then the seeds for the spatial Voronoi tessellation (Figure 4.17a). For this, the open source software *Qhull* can be used [Barber et al., 1996], for which a RhinoScripting implementation has been written by Dritsas [2006] (Figure 4.17b).

(iii) The vault is cut up into small volumes and the centroids are connected with a continuous mesh, the main force lines are super-imposed to this mesh (Figure 4.18a). The nodes formed at the intersections of the self-weight mesh and the forces lines patterns are unloaded nodes. This avoids making a decision on the discretization; instead, the forces are attracted along primary force lines, loaded by three-dimensional meshes in between them (Figure 4.18c). A major drawback of this approach is that it drastically increases the number of branches and nodes.

4.3.2 Live loading

Live loading can be added, but also needs to be discretized and lumped to the nodes, and applied parallel to the gravity loads. The load P_i applied at each node i can therefore be divided into a dead load $D_{z,i}$ and live load $L_{z,i}$ component:

$$P_i = D_{z,i} + L_{z,i} \tag{4.36}$$

To guarantee the stability of a masonry vault under the expected live loads, the equilibrium solutions

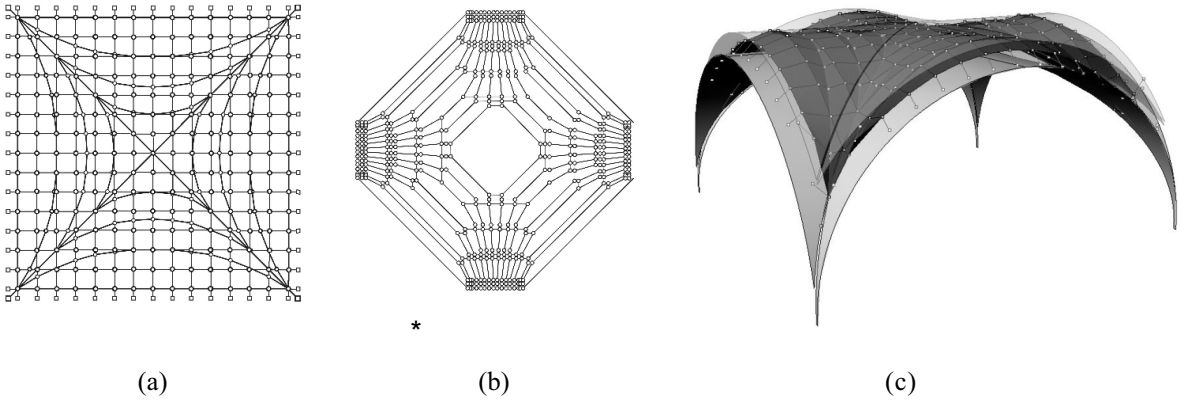

(a) (b) (c)

Figure 4.18 – The (a) primal and (b) dual grids of (c) a fully three-dimensional solution with primary force lines (thicker lines) and a continuous mesh in between which distributes the forces in a 3-D manner to those force lines.

found for the new set of loads, including live loading, also needs to fit within the section of vault. As discussed in §4.1.1 the results of this assessment can be overly conservative. In some cases, no equilibrium could be found if a poor choice of network topology is used: the dead load force pattern is not necessarily a feasible path for the combined dead and live loading. In the case of historical masonry vaults, live loads can typically be neglected since the self-weight of these structures is dominant.

4.4 Half-Edge data structure

To manage the networks, a *data structure* had to be implemented. A data structure is a method of organizing and connecting objects so that they can be identified, referenced and manipulated [Eastman, 1982]. This is done by creating a dynamic collection of mesh components, e.g. faces, edges and vertices. In a data structure, objects can identify themselves and the objects with which they are associated.

For TNA, the *Half-Edge* data structure is implemented [Eastman, 1982; Legakis, 1998]. Since all primal grids have to be disjointed (see §4.1.2), the resulting networks will always be *orientable surfaces*, which is a necessary requirement for the networks to apply this data structure. As seen in Figure 4.19, every edge is represented by two *directed* Half-Edge structures with opposite directions, each associated with exactly one vertex, one edge and one face: the Vertex at the end of the directed half-edge, the original *Edge* and the *Face* "to the right" of the directed half-edge. The last relationship is defined oppositely rather than conventionally, but this is equivalent if done consistently.

The topology and geometry of the network is entirely described in the list of half-edges and vertices respectively. The $\boldsymbol{C}$ and $\boldsymbol{C}^*$ branch-node matrices in TNA can be generated from the data structure. Attribution information can be added to the vertices, half-edges and faces. Because of the unique associations between elements, information is never stored twice and the time complexity is therefore linear in the amount of information gathered, independent of the global complexity of the system [Legakis, 1998]. The implementation uses three pointers: *Vertex*, *Sym*, and *Next*. *Vertex* points to the vertex at the end of the half-edge (Figure 4.19a); *Sym* points to the symmetric half-edge, which contains the same edge, the opposite vertex and the opposite face (Figure 4.19b); and *Next* points to the half-edge to the right if going clock-wise around a face, which contains the same face, the vertex to the right and the edge to the right (Figure 4.19c).

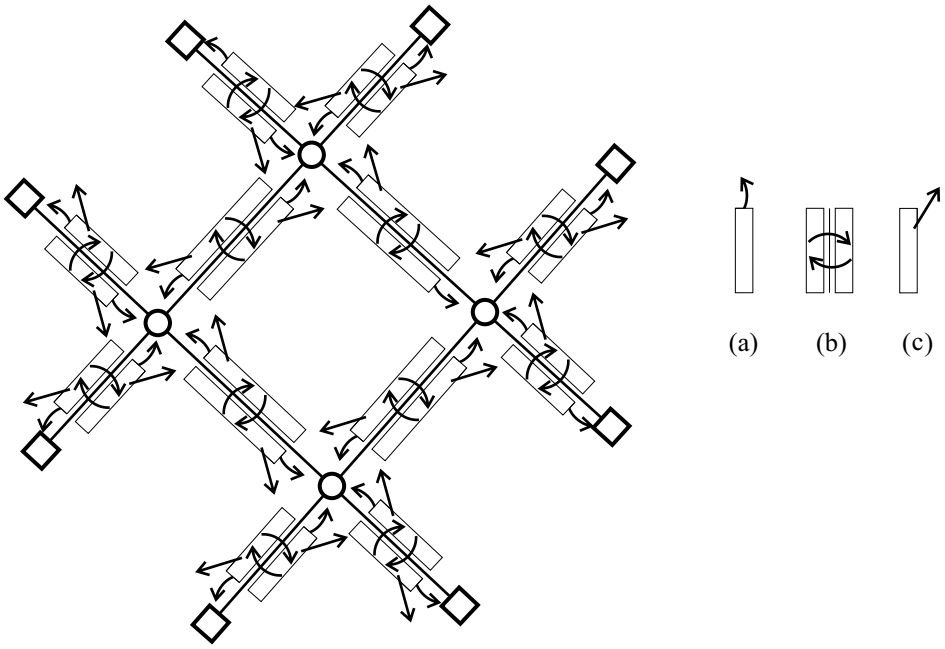

Figure 4.19 – Half-Edge data structure, showing the conventions for the three pointers: (a) *Vertex*, (b) *Sym* and (c) *Next* (after Legakis [1998]).

The Half-Edge data structure keeps track of the geometry in an organized and efficient manner. With some careful bookkeeping, it allows flexible changes in topology, such as dividing a space with a new edge, deleting edges, or adding vertices and edges. This would not be obvious using just the branch-node matrices. The importance of this property of the Half-Edge data structure is crucial for extending the TNA framework with topological optimization algorithms and for developing a fully interactive and flexible design and analysis environment. This will be further discussed in §8.2.

Notice also that because the half-edges around a face are defined to be oriented and connected clock-wise, for the dual grid this means that the set of directed half-edges around that dual face represents the closed force polygon of the branch forces coming together in the corresponding primal node (see Figure 4.15).

4.5 Automated thrust line analysis

4.5.1 Two-dimensional analysis

The TNA framework can also be used for two-dimensional arch analysis. Using TNA for thrustline analysis has several advantages over using graphic statics, even in its interactive version as proposed by Block [2005] and Block et al. [2006].

An important advantage over using graphic statics is that no tedious graphical constructions are needed. With this framework, it is straightforward to consider deformed geometries and model hinges and cracks (Figure 4.20a). The geometry of the actual vault is obtained from CAD models or other input data.

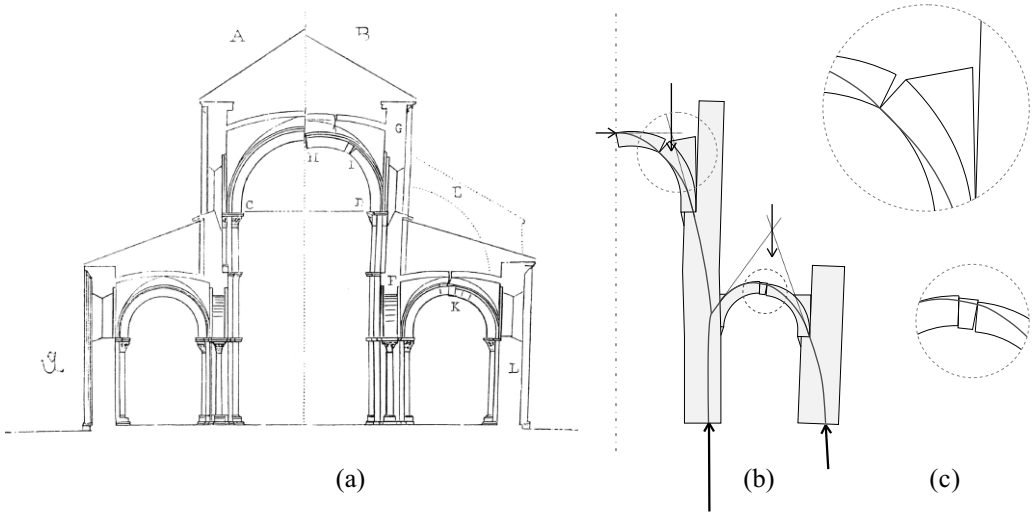

Figure 4.20 – (a) Section of the abbey church at Vézelay, France, drawn in the 19th-century by Viollet-le-Duc [1868], showing its ideal undeformed (left) and deformed state at the time it was drawn (right); and (b-c) a possible thrust line through the deformed section.

Instant computation of minimum and maximum thrust states allows the iteration of the geometry, e.g. to simulate support settlements or other displacements, and graphic feedback is visualized over the CAD geometry of the vault (Figure 4.20b).

For an arch in the xz-plane, (3.12) becomes

$$-\frac{1}{u_{i-1,j}} \cdot z_{i-1} + \left(\frac{1}{u_{i-1,j}} + \frac{1}{u_{i,j+1}}\right) \cdot z_i - \frac{1}{u_{i,j+1}} \cdot z_{i+1} - P_i \cdot \left(\frac{1}{H}\right) = 0 \tag{4.37}$$

where H is the constant horizontal thrust of the arch. The horizontal coordinate difference vector u is

$$\boldsymbol{u} = \boldsymbol{C}\boldsymbol{x} = \begin{bmatrix} -1 & 1 & & & \\ & -1 & 1 & & \\ & & \ddots & & \\ & & & -1 & 1 \end{bmatrix} \begin{bmatrix} \boldsymbol{x_1} \\ \vdots \\ \boldsymbol{x_n} \end{bmatrix} \tag{4.38}$$

With $\boldsymbol{U} = \mathrm{diag}(\boldsymbol{u})$, (3.26) simplifies for a two-dimensional problem to

$$\boldsymbol{C_i^t}\,\boldsymbol{U^{-1}}\,\boldsymbol{C}\boldsymbol{z} - \boldsymbol{p_z} \cdot \left(\frac{1}{H}\right) = 0 \tag{4.39}$$

So, the problem reduces to minimizing or maximizing $1/H$ to find the shallowest or deepest solution within the arch's geometry, which corresponds to the minimum and maximum thrust state of the arched structure. From the solution, the corresponding *funicular polygons* can be constructed geometrically.

4.5.2 Pseudo three-dimensional analysis

Even without using the entire TNA framework, reciprocal diagrams for planar projections are a valuable addition to the tools and techniques provided by graphical statics. For a three-dimensional system, such as the vault shown in Figure 4.21, these can be used to understand the equilibrium of all thrust values of the combination of two-dimensional arches in space. This section introduces the *horizontal thrust diagram* (Figure 4.21d) which supplements the familiar funicular polygons for three-dimensional problems.

It can be seen in Figure 4.22a that the primal grid now has two-valent nodes. Two spaces are therefore sometimes separated by more than one edge, violating part (iii) of the definition of a proper cell decomposition (see §4.1.2) which is necessary to have a spider web, i.e. a compression-only solution. There are m_h collinear branches separating the same two spaces in the primal grid (e.g. spaces C and D in Figure 4.22a), which all connect the same two dual nodes corresponding to these spaces in the dual grid (Figure 4.22b). Their dual branches therefore all coincide resulting in equal lengths which means that the corresponding branches in the primal have the same horizontal force component. This makes sense since these independent inverted "hanging string" pieces have a constant horizontal thrust in them (Figure 4.22e). This is why in the case of pseudo-3-D networks the dual grid can be understood as a *horizontal thrust diagram*.

In Figure 4.22c, the spaces around a node connecting different arches are labeled and its closed force polygon is identified in the dual grid. The resultant thrust value at the corners of the vault can be found by measuring the outside segments of the thrust diagram.

Two-valent nodes give problems for the automatic generation of the dual grid. This is solved by introducing the reduced branch-node matrix $\boldsymbol{C}^-$ which replaces each string of collinear branches in the primal corresponding to one arch with a single branch. The reduced network with the corresponding $\boldsymbol{C}^-$ is a proper cell decomposition of the plane and has therefore a convex reciprocal(see §4.1.2). Using $\boldsymbol{C}^-$ results in the reduced dual branch-node matrix $\boldsymbol{C}^{*-}$. The actual dual branch-node matrix of the system $\boldsymbol{C}^*$ is then constructed by using the row of $\boldsymbol{C}^{*-}$ corresponding to the substituted branch as row for each sub-branch of that hanging string piece.

4.6 Implementation of prototype

A computational prototype for TNA has been implemented using Rhinoceros [McNeel, 2007], RhinoScripting [Rutten, 2007] and MATLAB [The Mathworks, 2009b].

The geometry of the primal grid, drawn in Rhinoceros, is exported using the OBJ file format. The OBJ file format is a dataformat that represents 3-D geometry as a text file, listing all the vertices of the lines and faces of the object. A custom parser was written to translate the OBJ files and import the geometrical data into MATLAB. The topological information of the primal grid is translated into the Half-Edge data structure, which allows the generation of the primal and dual branch-node matrices. A rhinoscript has been written to obtain the nodal height limits and compute the nodal weights for the system directly from a three-dimensional model of the vault, without the need for abstraction or simplification.

The implementation of the data structure and the solving is done in MATLAB. For the linear optimization problems MATLAB's *linprog* LO solver is used [The Mathworks, 2009c]. Rhinoscripts are produced in MATLAB to generate and visualize the results, i.e. the dual grid Γ^* and the thrust network G, in Rhinoceros.

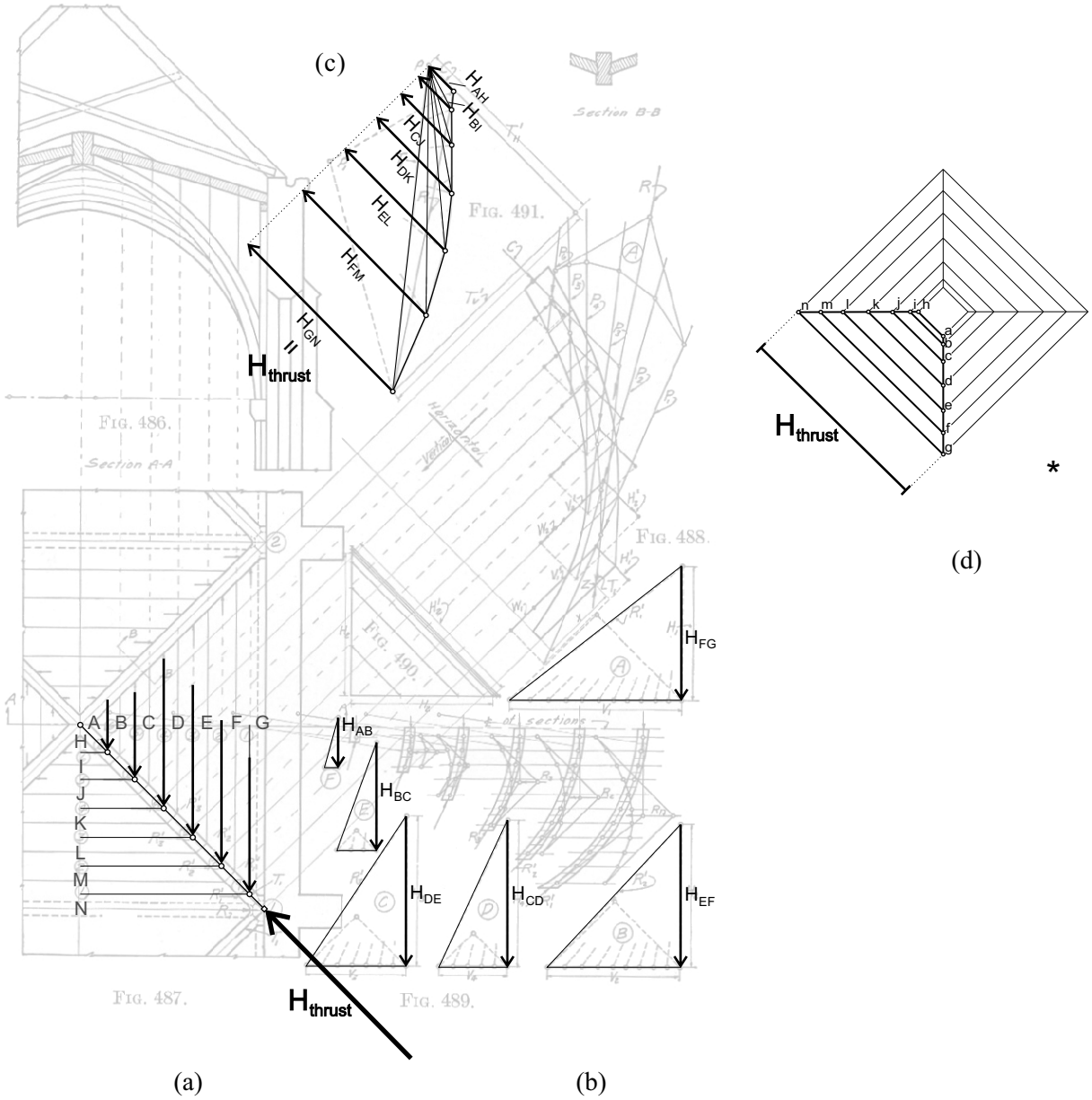

Figure 4.21 – Graphic analysis of quadripartite vault [Wolfe, 1921]: (a) the interacting arches in plan, with (b) their respective forces polygons; (c) overlaid over the funicular polygon of the rib, the horizontal force components in the branches of the rib are shown; and (d) the overall equilibrium of the system is clarified by the *horizontal thrust diagram* using the thrust components from (b) and (c).

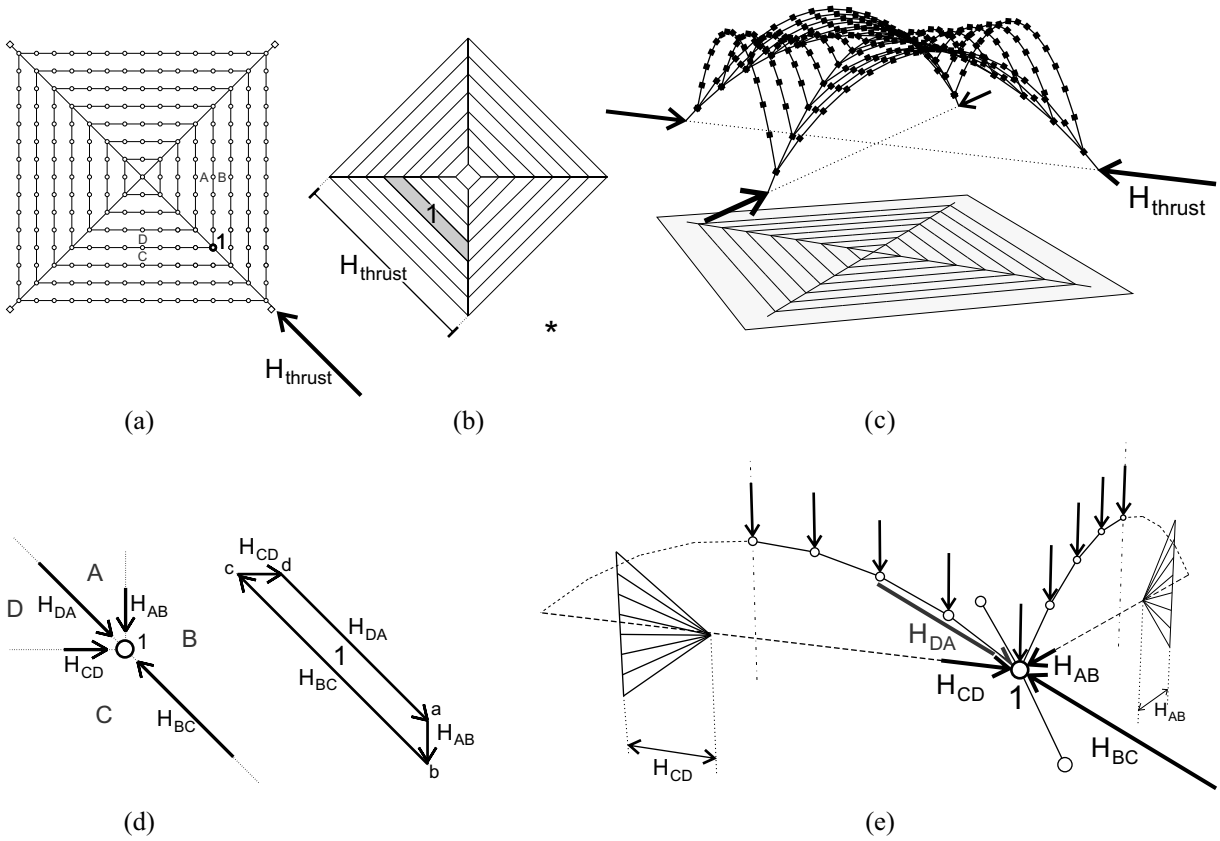

Figure 4.22 – (a) Primal and (b) dual grids of a network of connected two-dimensional arches, and (c) the resulting equilibrium network for a groin vault.(d) shows the equilibrium of the node highlighted in (a). (e) The dual branches of the collinear branches separating e.g. spaces C and D connect the same dual nodes c and d, resulting in equal horizontal force in each of these branches, the constant horizontal thrust H_{CD} in that arch.

In Rhinoceros, the dual grid can be updated by actual dragging of the nodes of the grid, respecting the parallel constraints. A rhinoscript exports the geometry of the updated Γ^*, and in MATLAB the new equilibrium shape is found which can again be visualized in Rhinoceros. For each iteration, the updated geometry of the dual grid is used directly, removing the time-consuming step of generating the dual grid.

Because of the large number of variables, the LO problem (3.39) is a large-scale problem and more efficient solving methods than those based on the Simplex algorithm should be used [Bertsimas and Tsitsiklis, 1997]. MATLAB's *linprog* solver for large-scale LO problems is used, which is based on LIPSOL [Zhang, 1995], a variant of the predictor-corrector algorithm by Mehrotra [1992], which is a primal-dual interior-point method.

4.7 Summary

This chapter discussed the properties and requirements for allowable primal grids, their meaning, generation and geometrical constraints.

A linear optimization approach is presented to generate possible dual grids for indeterminate networks, guaranteeing no-tension equilibrium solutions. A new rule is introduced to reduce the high level of indeterminacy of the dual grid to a specific number of allowable variations which maintain equilibrium. This provides understanding of how to control the equilibrium and identifies the degrees of freedom of the system, by inspection of the topology of the primal grid.

Several strategies to compute the nodal weights have been developed and discussed. The details of the Half-Edge data structure as implemented in TNA, allowing for flexible topology management, has been explained.

Finally, the implementation of a computational prototype for TNA using Rhinoceros, RhinoScripting and MATLAB's Optimization Toolbox has been described.

Using the TNA framework, automated two-dimensional and three-dimensional thrust line analysis implementations are shown. The concept of a thrust diagram is introduced to visualize how a series of thrust lines equilibrate in space.

Chapter 5 will discuss and suggest extensions of TNA beyond the basic framework considered until now.

Chapter 5

Extensions

This chapter discusses extensions to the basic thrust network method described in Chapter 3. Alternative objective functions for the optimization problem are introduced. In addition, nonlinear extensions to the basic framework are developed, which include the degrees of indeterminacy of the three-dimensional network in an overall optimization set-up. Other loading cases and overlapping network configurations are discussed. Finally, the relation between of reciprocal force diagrams and discrete Airy stress functions is described.

5.1 Alternative objectives

Until now the objective function has been to minimize or maximize the scale factor ζ, finding the minimum and maximum thrust states which fit within the solution space (Figure 5.1a). This section will identify two alternative objective functions, each using a linear optimization set-up. The first one (Figure 5.1b) defines the *geometric safety factor* of an arched structure indicating its sensitivity to asymmetric loading. The next objective function results in an upper-bound analysis which quantifies the limit of stability of the structure under a point load by increasing it until the structure becomes unstable (Figure 5.1c). Finally, the problem is inversed: instead of finding the equilibrium geometry under certain set of loads, the loading is found which would cause a pre-determined network geometry to be funicular for a chosen network topology.

5.1.1 Geometric safety factor

The *geometric safety factor* (GSF) is defined as the proportion of the total depth of the cross section D to the minimum depth d required to contain the thrust line [Heyman, 1982].

To find the geometric safety factor D/d, a new variable β is introduced in the upper- and lower-bounds on the nodal heights z_i [O'Dwyer, 1999]. It relates the width of the strip containing the entire equilibrium solution to the full section of the vault.

$$z_i^{\mathrm{I}} + \left(z_i^{\mathrm{E}} - z_i^{\mathrm{I}}\right)\beta \leq z_i \leq z_i^{\mathrm{E}} - \left(z_i^{\mathrm{E}} - z_i^{\mathrm{I}}\right)\beta \tag{5.1}$$

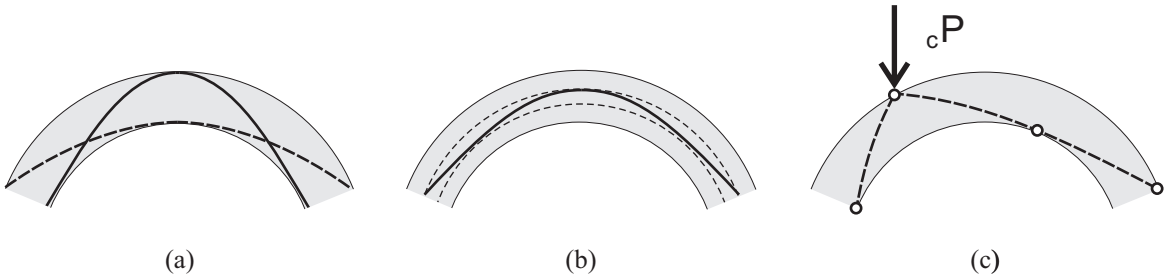

Figure 5.1 – Some possible objective functions: (a) min/max thrust, (b) geometric safety factor, and (c) collapse load factor.

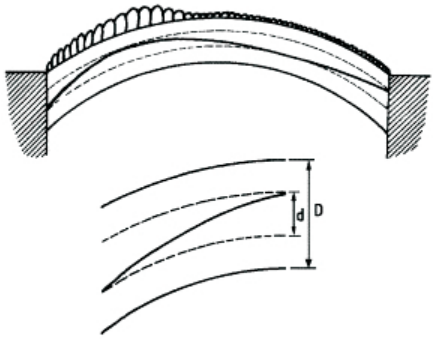

Figure 5.2 – Definition of the geometric safety factor [O'Dwyer, 1999].

From (5.1), the GSF can thus be found by maximizing β:

$$\text{GSF} = \frac{D}{d} = \max_{\beta} \frac{1}{1-2\beta} \tag{5.2}$$

The bounds (5.1) translate to the following $2n_i$ inequality constraints:

$$\begin{cases} -z_i + \left(z_i^{\text{E}} - z_i^{\text{I}}\right)\beta \leq z_i^{\text{I}} \\ z_i + \left(z_i^{\text{E}} - z_i^{\text{I}}\right)\beta \leq z_i^{\text{E}} \end{cases} \tag{5.3}$$

The parameter β can be related to the proportion D/d and this puts a value on the geometrical safety of the structure.

$$\begin{cases} \beta < 0 & d > D & \text{GSF} \leq 1 \\ 0 \leq \beta \leq \frac{1}{2} & d \leq D & \text{GSF} \geq 1 \\ \frac{1}{3} \leq \beta \leq \frac{1}{2} & d \leq \frac{1}{3} \cdot D & \text{GSF} \geq 3 \end{cases} \tag{5.4}$$

Feasible solutions from a stability standpoint, i.e. solutions within the vault's section, are solutions with a GSF ≥ 1, i.e. $d \leq D$ or $0 \leq \beta \leq \frac{1}{2}$. We can identify different limit states from equation (5.4). If $\beta = 0$, or GSF $= 1$, the vault is on the verge of collapse. If $\beta \geq \frac{1}{3}$, the solution lies inside the middle third ensuring no tensile forces on the section, hence no cracks or hinging in the vault. If $\beta = \frac{1}{2}$, the solution is a membrane solution for that vault, meaning that this shape could theoretically support the applied loads with zero thickness.

In matrix form, the linear optimization problem (3.40) changes to

$$\min_{\boldsymbol{z},r,\beta} \; -\beta \quad \text{such that} \quad \begin{cases} \boldsymbol{D}\boldsymbol{z} - \boldsymbol{p}_{\boldsymbol{z}}\boldsymbol{r} = 0 \\ -\boldsymbol{z} + \left(\boldsymbol{z}^{\mathbf{E}} - \boldsymbol{z}^{\mathbf{I}}\right)\beta \leq \boldsymbol{z}^{\mathbf{I}} \\ \boldsymbol{z} + \left(\boldsymbol{z}^{\mathbf{E}} - \boldsymbol{z}^{\mathbf{I}}\right)\beta \leq \boldsymbol{z}^{\mathbf{E}} \\ 0 \leq r \leq +\infty \\ -\infty \leq \beta < \frac{1}{2} \end{cases} \tag{5.5}$$

This objective function (and added constraints) guarantees that the optimization problem always has a solution, even if this solution does not lie within the section ($d > D$). In that case, the cost becomes negative (GSF < 0) and this value is indicative of how far the solution is from being a possible lower-bound solution of the vault. This optimization set-up is therefore better than the original formulation in (3.40) which would not find a feasible solution and would return an error for a solution with d larger than D.

The GSFs found using this set-up will be the actual geometric safety factor of the structure only in the case of a two-dimensional analysis, since the thrust line has only one parameter, the horizontal thrust H. For a three-dimensional system, the solution is highly dependent on the choice of primal grid and, more importantly, on the geometry of its dual grid. The main benefit of using this objective function over (3.40) is that it guarantees a solution at each step allowing the user to manually and iteratively move towards a better solution. Section 5.2 will introduce a nonlinear extension to the basic TNA framework

which includes the parameters of the dual grid (see §4.2), to obtain a realistic GSF for a certain network geometry in the case of three-dimensional structures.

5.1.2 Collapse load factor

A *load factor* λ is added to equation (4.36) which divides P_i into the fractions due to the constant dead load, $D_{z,i}$ and live load, $L_{z,i}$:

$$P_i = D_{\mathrm{z},i} + \lambda L_{\mathrm{z},i} \tag{5.6}$$

The sensitivity of the structure under live loading can be explored by using a *collapse load factor* λ_c. By increasing λ, which multiplies the live load component $L_{z,i}$, until a funicular solution can no longer be found within the vault's cross-section, the collapse load factor λ_c is found. This factor defines the maximum point load that the structure can safely carry at that specific location for a chosen force pattern.

Using (5.6), the linear nodal equilibrium constraints (3.12) of the LO become

$$d_{ii} \cdot z_i + d_{ji} \cdot z_j + d_{ki} \cdot z_k + d_{li} \cdot z_l - D_{\mathrm{z},i} \cdot r - L_{\mathrm{z},i} \cdot \lambda' = 0 \tag{5.7}$$

with $\lambda' = \lambda r = \frac{\lambda}{\zeta}$.

To find the collapse load factor λ_c, the following LO problem needs to be solved:

$$\min_{\mathbf{z},r,\lambda'} \; -\lambda' \quad \text{such that} \quad \begin{cases} \boldsymbol{D}\boldsymbol{z} - \boldsymbol{d}_{\boldsymbol{z}}\boldsymbol{r} - \boldsymbol{l}_{\boldsymbol{z}}\lambda' = \mathbf{0} \\ \boldsymbol{z}^{\mathbf{LB}} \leq \boldsymbol{z} \leq \boldsymbol{z}^{\mathbf{UB}} \\ 0 \leq r, \lambda' \leq +\infty \end{cases} \tag{5.8}$$

and the collapse load factor λ_c is then found by dividing λ' by r. Maximizing λ' maximizes both λ and r, but at collapse, the equilibrium state is unique because it is an upper-bound solution; minimizing or maximizing r gives the same solution. Note that, as clearly shown in the barrel vault example in §4.1.1, this approach is irrelevant if no appropriate force pattern has been overlaid on the dead load force pattern to bring down the point load.

5.1.3 Funicular loading

It may be desirable to find the loading which causes the middle surface to be a membrane solution under those loads [Williams, 1990]. This set of loads is called the *funicular loading* of that vault. For this objective, the nodal heights $\boldsymbol{z}$ are given and, for a chosen force logic, the only unknowns are then the funicular loading $\boldsymbol{p_f}$ and the overall scale of the dual grid ζ. Rearranging equation (3.30), and after dividing by r and using (3.20c), gives

$$\boldsymbol{C}_{\boldsymbol{i}}^{\mathbf{t}} \left(\boldsymbol{L}_{\mathbf{H}}^{-\mathbf{1}} \boldsymbol{L}_{\mathbf{H}}^{*} \right) \boldsymbol{w}\zeta - \boldsymbol{p}_{\mathbf{f}} = \mathbf{0} \tag{5.9}$$

This is again a linear problem, but the optimization process now defines the loading $\boldsymbol{p_f}$ and the overall scale of the dual grid ζ causing a pre-defined shape to be funicular under prescribed assumptions of how forces are distributed. The solution obtained using equation (5.9) is of course dependent on a choice of the dual grid.

Section 4.2 showed how to identify the k DOFs and corresponding control parameters ξ_j of the dual grid and relate them to the local dual branch scalars, ζ_i. So, equation (5.9) can be generalized to

$$\boldsymbol{C_i^t} \left(\boldsymbol{L_H^{-1}} \boldsymbol{L_H^*}\right) \boldsymbol{W\zeta(\xi)} - \boldsymbol{p_f} = \boldsymbol{0} \tag{5.10}$$

Using equations (4.14) and (4.15), (5.10) can be written as a function of the ξ_j of both type.

$$\boldsymbol{C_i^t} \left(\boldsymbol{L_H^{-1}} \boldsymbol{L_H^*}\right) \boldsymbol{W}\left(\boldsymbol{1}_m + \boldsymbol{L_H^{*\,-1}} \boldsymbol{F^{(i)}\xi^{(i)}} + \boldsymbol{L_H^{*\,-1}} \left(\boldsymbol{L_c^*} + \boldsymbol{L_H^*}\right) \boldsymbol{F^{(ii)}\xi^{(ii)}}\right) - \boldsymbol{p_f} = 0 \tag{5.11}$$

Rearranging (5.11) gives the following linear constraints in $\boldsymbol{\xi^{(i)}}$, $\boldsymbol{\xi^{(ii)}}$ and $\boldsymbol{p_f}$:

$$\boldsymbol{C_i^t L_H^{-1} W}\left(\boldsymbol{F^{(i)}\xi^{(i)}} + \left(\boldsymbol{L_c^*} + \boldsymbol{L_H^*}\right) \boldsymbol{F^{(ii)}\xi^{(ii)}}\right) - \boldsymbol{p_f} = -\boldsymbol{C_i^t} \left(\boldsymbol{L_H^{-1}} \boldsymbol{L_H^*}\right) \boldsymbol{w} \tag{5.12}$$

The funicular loading for a given input network is then found with the LO problem

$$\min_{\boldsymbol{\xi}, p_f} \boldsymbol{1_k^t \xi} \quad \text{such that} \quad \begin{cases} \boldsymbol{C_i^t L_H^{-1} W}\left(\boldsymbol{F^{(i)}\xi^{(i)}} + \left(\boldsymbol{L_c^*} + \boldsymbol{L_H^*}\right) \boldsymbol{F^{(ii)}\xi^{(ii)}}\right) - \boldsymbol{p_f} \\ \qquad\qquad = -\boldsymbol{C_i^t} \left(\boldsymbol{L_H^{-1}} \boldsymbol{L_H^*}\right) \boldsymbol{w} \\ \boldsymbol{\xi^{LB}} \leq \boldsymbol{\xi} \leq \boldsymbol{\xi^{UB}} \end{cases} \tag{5.13}$$

This approach can be used to define the optimal level of fill for a masonry vault with a given intrados such that the thrust network follows the central surface of the vault or, in other words, to find the best extrados for a chosen intrados geometry. If no feasible solution exists for (5.12), then the input shape can never be funicular using the chosen network topology, represented by the primal grid.

5.2 Force distribution optimization

5.2.1 Problem statement

In the main set-up described in Chapter 3, the geometry of the dual grid Γ^* is considered fixed, i.e. the internal distribution of the forces in the primal grid Γ were decided in advance and kept unaltered. This reduces the optimization problems to linear problems, resulting in fast computation of the results. As will be illustrated in Chapter 7, such a set-up, particularly when extended with the GSF objective introduced in §5.1.1, is entirely appropriate for designing new structures. An initial solution is found within given boundaries and the user can interactively explore three-dimensional equilibrium by tweaking the dual grid and exploring different network topologies. With fast solving times, quasi-real-time feedback is achieved which makes the interactive set-up possible.

For the safety assessment of masonry structures on the other hand, this iterative approach becomes very tedious and unwieldy. First of all, the linear optimization problem as described in (3.40) does not guarantee that a feasible solution can be found, i.e. that a compression-only funicular solution exists within the vault's section for the starting point provided by the automatically generated dual grid. This was resolved using the LO variant introduced in §5.1.1. This approach guarantees a solution for the optimization problem and furthermore gives a measure of how far the solution is from fitting inside the vault. It does not suggest though which adjustments of the dual grid will move the result in the direction of a feasible or better solution.

For simple choices of force patterns, this process can be done by hand, based on intuition, experience or perseverance, but for more sophisticated and interconnected primal grids the process quickly becomes too challenging. It is furthermore impossible to get to the lowest geometric safety factor or the absolute minimal horizontal thrust state manually, due to the infinite possibilities of the complex three-dimensional system of forces. It therefore becomes important to control the degrees of freedom of the dual grid in an overall optimization process.

Such a set-up also opens possibilities for making structurally informed design decisions by finding the closest funicular network to an arbitrary input surface. This is a difficult problem which has not been solved satisfactorily [Sobek, 1987].

5.2.2 Problem description

Starting again from the vertical equilibrium equations (3.4) of a typical node i, the horizontal branch forces F_{ji}^{H} are now no longer all directly proportional to the geometry of the dual grid, represented by the one scalar ζ as in (3.8). Instead, there are now m scalars ζ_{ji} associated with each dual branch.

$$F_{ji}^{\mathrm{H}} = \zeta_{ji} \cdot L_{ji}^{\mathrm{H}^*} \tag{5.14}$$

and plugged into (3.4),

$$\zeta_{ji}\,(z_i - z_j)\,\frac{L_{ji}^{\mathrm{H}^*}}{L_{ji}^{\mathrm{H}}} + \zeta_{ki}\,(z_i - z_k)\,\frac{L_{ki}^{\mathrm{H}^*}}{L_{ki}^{\mathrm{H}}} + \zeta_{li}\,(z_i - z_l)\,\frac{L_{li}^{\mathrm{H}^*}}{L_{li}^{\mathrm{H}}} = P_i \tag{5.15}$$

The unknowns in (5.15) are the dual branch scalars ζ_{ji} and the nodal heights z_i. These ζ_{ji} cannot be chosen arbitrarily because the dual grid is constrained geometrically to maintain compression-only solutions (§3.2.3). The dual grid has a particular number of degrees of freedom, k, controlled by the parameters ξ_k. Section 4.2 introduced rule (4.9) to obtain the number of DOFs of a dual grid by inspection of the primal grid, their corresponding parameters ξ_k and relation to the dual branch scaling factors ζ_{ji}. So, (5.14) becomes

$$F_{ji}^{\mathrm{H}} = \zeta_{ji}\,(\xi_k) \cdot L_{ji}^{\mathrm{H}^*} \tag{5.16}$$

The inital goal is to set up an optimization problem to find a set $\boldsymbol{\xi} = \{\xi_1 \dots \xi_k\}$ such that the funicular solution G is contained within the section of the vault, i.e.

$$\boldsymbol{z}^{\mathbf{LB}} \leq \boldsymbol{z} \leq \boldsymbol{z}^{\mathbf{UB}} \tag{5.17}$$

As discussed above, the height constraints (5.17) can be too strong to find an initial feasible solution. The hard constraints on $\boldsymbol{z}$ in (5.17) can be relaxed by replacing them with penalty terms $f_i(z_i)$ related to the middle surface of the vault, and minimizing these penalty terms, summed over all the nodes, in the objective function $f(\boldsymbol{z})$:

$$f(\boldsymbol{z}) = \sum_i f_i(z_i) = \sum_i \left(z_i - z_i^{\mathrm{M}}\right)^2 = \left\|\boldsymbol{z} - \boldsymbol{z}^{\mathbf{M}}\right\|_2^2 \tag{5.18}$$

where $\boldsymbol{z}^{\mathbf{M}} = \frac{\boldsymbol{z}^{\mathbf{LB}} + \boldsymbol{z}^{\mathbf{UB}}}{2}$.

The sum of all penalty terms $f_i(z_i)$ needs to be minimized, resulting in the optimization problem

$$\min_{\boldsymbol{z},\boldsymbol{\xi}} \quad f(\boldsymbol{z}) \quad \text{such that} \quad \begin{cases} \boldsymbol{D}(\boldsymbol{\xi})\boldsymbol{z} = \boldsymbol{p}_{\mathbf{z}} \\ \boldsymbol{\xi} \geq \boldsymbol{\xi}^{\mathbf{LB}} \end{cases} \tag{5.19}$$

Minimizing $f(\boldsymbol{z})$ in (5.19) would render the $\boldsymbol{z}$ and $\boldsymbol{\xi}$, representing the equilibrium solution which maximizes the GSF of the vault for that choice of primal grid. Minimizing $f(\boldsymbol{z})$ is a least squares problem, but by adding the equilibrium constraints of the form (5.15), which are bilinear in $\boldsymbol{\xi}$ and $\boldsymbol{z}$, the problem (5.19) becomes a complex nonlinear, constrained optimization problem for which there exists no direct solving algorithm.

The nonlinear optimization problem (5.19) can be solved using an iterative gradient approach. Because the height constraints have been brought into the objective function, a similar strategy can be used as for the nonlinear extensions to the Force Density Method [Schek, 1974]. If at each iteration an improved set of parameters $\boldsymbol{\xi}$ is obtained and is considered as known, the problem (5.19) reduces to a linearly constrained least-squares optimization problem which can readily be solved using the *lsqlin* solver of MATLAB's Optimization Toolbox [The Mathworks, 2009c]. The *lsqlin* solver is a sequential quadratic programming method described by Gill et al. [1981].

5.2.3 Outline solving procedure

The starting set of parameters $\boldsymbol{\xi}^{(\mathbf{0})}$ is obtained from the automatically generated dual (see §4.2) which guarantees that they represent a possible stress state of the primal grid, but resulting in a solution which is not necessarily contained within the boundaries. The constraints in (5.19) become linear in $\boldsymbol{z}$ because the parameters $\boldsymbol{\xi}$ are now known from $\boldsymbol{\xi}^{(\mathbf{0})}$. The geometry of the equilibrium solution $\boldsymbol{z}^{(\mathbf{0})}$ corresponding to the inital set of parameters $\boldsymbol{\xi}^{(\mathbf{0})}$ is found by solving the optimization problem

$$\min_{\boldsymbol{z}} \quad f(\boldsymbol{z}) \quad \text{such that} \quad \boldsymbol{D}(\boldsymbol{\xi}^{(\mathbf{0})})\boldsymbol{z} = \boldsymbol{p}_{\mathbf{z}} \tag{5.20}$$

which is a linearly constrained least squares problem. This renders the cost $f(\boldsymbol{z}^{(\mathbf{0})})$ which will be used to steer the overall optimization problem:

$$\boldsymbol{\xi}^{(\mathbf{0})} \rightarrow \boldsymbol{\zeta}^{(\mathbf{0})} \overset{lsqlin}{\rightarrow} \boldsymbol{z}^{(\mathbf{0})} \rightarrow f(\boldsymbol{z}^{(\mathbf{0})}) \tag{5.21}$$

For the next iterations, the optimization wants to move in a direction which reduces the cost f, i.e. reducing the sum of the penalties which means approaching the middle surface of the boundaries. The set of the parameters $\boldsymbol{\xi}$ at the next iteration is defined as

$$\boldsymbol{\xi}^{(\mathbf{0})} := \boldsymbol{\xi}^{(\mathbf{0})} + \boldsymbol{\Delta\xi} \tag{5.22}$$

with $\boldsymbol{\Delta\xi}$, the change of the parameters $\boldsymbol{\xi}$, which is generated such that

$$f(\boldsymbol{\xi}^{(\mathbf{0})} + \boldsymbol{\Delta\xi}) < f(\boldsymbol{\xi}^{(\mathbf{0})}) \tag{5.23}$$

At each iteration, the linearly constrained least squares problem (5.20) needs to be solved. The stopping criteria for this iterative procedure is

$$f(\boldsymbol{\xi}^{(\mathbf{0})}) - f(\boldsymbol{\xi}^{(\mathbf{0})} + \boldsymbol{\Delta\xi}) < \varepsilon \tag{5.24}$$

with ε a given tolerance. The resulting $\boldsymbol{z}^{(\mathbf{GSF})}$ and $\boldsymbol{\xi}^{(\mathbf{GSF})}$ are the values defining the equilibrium network $G^{(\mathrm{GSF})}$ which maximizes the geometric safety factor.

The difficulty is to find appropriate variations $\boldsymbol{\Delta\xi}$ in (5.22). The *Levenberg – Marquardt Algorithm* (LMA) is used to find the search direction from the following set of linear equations, evaluated at $\boldsymbol{\xi}^{(\mathbf{0})}$, the parameter set at the current iteration [Levenberg, 1944; Marquardt, 1963; Gill and Murray, 1978]:

$$\boldsymbol{\Delta\xi} = \left(\boldsymbol{J}^{\mathbf{t}}\boldsymbol{J} + \boldsymbol{\lambda I}\right)^{-\mathbf{1}} \boldsymbol{J}^{\mathbf{t}} f(\boldsymbol{\xi}^{(\mathbf{0})}) \tag{5.25}$$

where $\boldsymbol{J}$ is the sensitivity, or Jacobian, matrix of f with respect to $\boldsymbol{\xi}$, $\boldsymbol{\lambda}$ is the damping coefficients vector, $\boldsymbol{I}$ the identity matrix and f the objective function. The damping coefficients vector $\boldsymbol{\lambda}$ is introduced to help with the computation of the inverse of $\boldsymbol{J}^{\mathbf{t}}\boldsymbol{J}$, the Gaussian transformation of $\boldsymbol{J}$. Section 5.2.5 will derive the Jacobian matrix $\boldsymbol{J}$.

Instead of finding the geometric safety factor of a vaulted structure, it is often more valuable to find the range of horizontal thrust, defined by a minimum and maximum state, it exerts or can exert onto its neighboring elements. If an equilibrium solution exists for the vault and a sensible network topology is chosen, then the $G^{(\mathrm{GSF})}$ obtained with the procedure described above will be a possible lower-bound solution for the vault, i.e. a compression-only equilibrium solution which is entirely contained within the vault. The corresponding set $\boldsymbol{\xi}^{(\mathbf{GSF})}$ and $\boldsymbol{z}^{(\mathbf{GSF})}$ are therefore feasible starting values for a new optimization which reintroduces the hard nodal height constraints from (5.17). The new optimization problem, minimizing the horizontal thrusts at the boundaries, thus becomes

$$\min_{z} \quad -f(\boldsymbol{z}) \quad \text{such that} \quad \begin{cases} \boldsymbol{D}(\boldsymbol{\xi}^{(\mathbf{GSF})})\boldsymbol{z} = \boldsymbol{p_z} \\ \boldsymbol{z}^{\mathbf{LB}} \leq \boldsymbol{z} \leq \boldsymbol{z}^{\mathbf{UB}} \end{cases} \tag{5.26}$$

The objective is now to maximize the GSF while keeping the solution within the boundaries (GSF $\rightarrow 1$). this will render the overall minimimum horizontal thrust state for the chosen network topology. The problem (5.26) can be solved using the same iterative procedure described above, but now starting from $G^{(\mathrm{GSF})}$ and driving the optimization in the opposite direction.

5.2.4 Implementation

An iterative gradient search method is used to solve the difficult nonlinear optimization problem (5.19), implementing the Levenberg – Marquardt algorithm to find appropriate search directions and step lengths. At each iteration, the linearly constrained least squares problem (5.20) needs to be solved. The *lsqlin* solver in MATLAB's Optimization Toolbox uses the following form for least squares optimization problems with linear constraints:

$$\min_{x} \quad \|\boldsymbol{C}\boldsymbol{x}-\boldsymbol{d}\|_2^2 \quad \text{such that} \quad \begin{cases} \boldsymbol{A}\boldsymbol{x} \leq \boldsymbol{b} \\ \boldsymbol{A}_{\boldsymbol{eq}}\boldsymbol{x} = \boldsymbol{b}_{\boldsymbol{eq}} \\ \boldsymbol{lb} \leq \boldsymbol{x} \leq \boldsymbol{ub} \end{cases} \tag{5.27}$$

where $\boldsymbol{x}$ are the variables, $\boldsymbol{C}$ and $\boldsymbol{d}$ the cost matrix and vector, $\boldsymbol{A}$ and $\boldsymbol{A}_{\boldsymbol{eq}}$ the inequalities and equalities constraint matrices with $\boldsymbol{b}$ and $\boldsymbol{b}_{\boldsymbol{eq}}$ their corresponding right hand sides, and $\boldsymbol{lb}$ and $\boldsymbol{ub}$ the lower and upper bounds on the value of the variables. This problem converges to a global minimum, if $\boldsymbol{C}$ in (5.27) is positive definite. From (5.18) and (5.21), the linearly constrained least squares problem becomes

$$\min_{\boldsymbol{z}} \quad \left\|\boldsymbol{I}_n\boldsymbol{z}-\boldsymbol{z}^{\mathbf{M}}\right\|_2^2 \quad \text{such that} \quad \begin{cases} \boldsymbol{D}(\boldsymbol{\xi})\boldsymbol{z} = \boldsymbol{p}_{\mathbf{z}} \\ \left(\boldsymbol{z}^{\mathbf{LB}} \leq \boldsymbol{z} \leq \boldsymbol{z}^{\mathbf{UB}}\right) \end{cases} \tag{5.28}$$

where the height constraints $\boldsymbol{z}^{\mathbf{LB}} \leq \boldsymbol{z} \leq \boldsymbol{z}^{\mathbf{UB}}$ are only included for the minimum thrust optimization. The problem (5.28) converges to a global minimum, since $\boldsymbol{C} = \boldsymbol{I}_n$, the identity matrix of size n.

For the overall search procedure, since the damping coefficients vector $\boldsymbol{\lambda}$ is being dynamically updated in the Levenberg – Marquardt algorithm to optimize the convergence, the search algorithm tends to converge to a solution even for starting values which are far from the optimal solution, i.e. the solution that minimizes the objective [Gill and Murray, 1978]. The resulting solution is not necessarily the global optimum though. In the case that the penalties $f_i(z_i^{(0)})$ vary too much, the optimization search may terminate at a local minimum. In this case, the problematic $f_i(z_i)$'s need to be identified and multiplied by weighting coefficients α_i. This helps the solution to be "pushed" out of a local minimum. So, adding weighting coefficients α_i to (5.18), the objective for the constrained least-squares problem becomes

$$f(\boldsymbol{z}) = \sum_i \alpha_i \cdot f_i(z_i) = \sum_i \alpha_i \left(z_i - z_i^{\mathrm{M}}\right)^2 = A\left\|\boldsymbol{z}-\boldsymbol{z}^{\mathbf{M}}\right\|_2^2 \tag{5.29}$$

5.2.5 Representation of the Jacobian matrix J

For the first optimization problem , finding the derivatives with respect to $\boldsymbol{\xi}$ of the objective function f is not obvious since f is not explicitly given as a function of $\boldsymbol{\xi}$. Using the *chain rule*, the Jacobian matrix of the multi-convoluted function f can be obtained as

$$\boldsymbol{J} = \frac{\partial f\left(\boldsymbol{z}\left(\boldsymbol{\zeta}\left(\boldsymbol{\xi}\right)\right)\right)}{\partial \boldsymbol{\xi}} = \frac{\partial f}{\partial \boldsymbol{z}}\frac{\partial \boldsymbol{z}}{\partial \boldsymbol{\zeta}}\frac{\partial \boldsymbol{\zeta}}{\partial \boldsymbol{\xi}} \tag{5.30}$$

The $\frac{\partial f}{\partial z}$ matrix is found by deriving with respect to $\boldsymbol{z}$:

$$\frac{\partial f}{\partial \boldsymbol{z}} = \left(\boldsymbol{Z} - \boldsymbol{Z}^{\mathbf{M}}\right) \tag{5.31}$$

Schek shows how to derive the matrix $\frac{\partial z}{\partial \zeta}$ by starting from the nodal equilibrium equations [Schek, 1974]:

$$\boldsymbol{C}_i^{\mathbf{t}}\, \boldsymbol{W}(z)\, \boldsymbol{q}(\boldsymbol{\zeta}) = \boldsymbol{p}_{\mathbf{z}} \tag{5.32}$$

Each change in $\mathbf{d}\boldsymbol{\xi}$ or $\mathbf{dz}$ needs to keep the equilibrium untouched, so

$$\mathrm{d}\left(\boldsymbol{C}_i^{\mathbf{t}}\, \boldsymbol{W}\boldsymbol{q}\right) = \frac{\partial\left(\boldsymbol{C}_i^{\mathbf{t}}\, \boldsymbol{W}\boldsymbol{q}\right)}{\partial \boldsymbol{\zeta}}\mathrm{d}\boldsymbol{\zeta} + \frac{\partial\left(\boldsymbol{C}_i^{\mathbf{t}}\, \boldsymbol{W}\boldsymbol{q}\right)}{\partial \boldsymbol{z}}\mathrm{d}\boldsymbol{z} = 0 \tag{5.33}$$

As in equation (3.29), the force densities $\boldsymbol{q}$ can be written as a function of the $(m \times 1)$ vector $\boldsymbol{\zeta}$, listing all the dual branch scale factors ξ_{ji}, which are no longer assumed to be equal as in the basic TNA framework. Using (3.29) in (5.33) gives

$$\frac{\partial\left(\boldsymbol{C}_i^{\mathbf{t}}\, \boldsymbol{W}\boldsymbol{q}\right)}{\partial \boldsymbol{\zeta}} = \frac{\partial\left(\boldsymbol{C}_i^{\mathbf{t}}\, \boldsymbol{W}\boldsymbol{L}_{\mathbf{H}}^{-\mathbf{1}}\boldsymbol{L}_{\mathbf{H}}^{*}\boldsymbol{\zeta}\right)}{\partial \boldsymbol{\zeta}} = \boldsymbol{C}_i^{\mathbf{t}}\, \boldsymbol{W}\boldsymbol{L}_{\mathbf{H}}^{-\mathbf{1}}\boldsymbol{L}_{\mathbf{H}}^{*} \tag{5.34}$$

and

$$\frac{\partial\left(\boldsymbol{C}_i^{\mathbf{t}}\, \boldsymbol{W}\boldsymbol{q}\right)}{\partial \boldsymbol{z}} = \frac{\partial\left(\boldsymbol{C}_i^{\mathbf{t}}\, \boldsymbol{Q}\boldsymbol{w}\right)}{\partial \boldsymbol{z}} = \frac{\partial\left(\boldsymbol{C}_i^{\mathbf{t}}\, \boldsymbol{Q}\boldsymbol{C}\boldsymbol{z}\right)}{\partial \boldsymbol{z}} = \boldsymbol{C}_i^{\mathbf{t}}\boldsymbol{L}_{\mathbf{H}}^{-\mathbf{1}}\boldsymbol{L}_{\mathbf{H}}^{*}\mathbf{Z}\boldsymbol{C} \tag{5.35}$$

so that the desired matrix $\frac{\partial z}{\partial \zeta}$ becomes

$$\frac{\partial \boldsymbol{z}}{\partial \boldsymbol{\zeta}} = -\left(\boldsymbol{C}_i^{\mathbf{t}}\boldsymbol{L}_{\mathbf{H}}^{-\mathbf{1}}\mathbf{Z}\boldsymbol{L}_{\mathbf{H}}^{*}\boldsymbol{C}\right)^{-1}\boldsymbol{C}_i^{\mathbf{t}}\, \boldsymbol{W}\boldsymbol{L}_{\mathbf{H}}^{-\mathbf{1}}\boldsymbol{L}_{\mathbf{H}}^{*} = -\boldsymbol{D}^{-\mathbf{1}}\boldsymbol{C}_i^{\mathbf{t}}\, \boldsymbol{W}\boldsymbol{L}_{\mathbf{H}}^{-\mathbf{1}}\boldsymbol{L}_{\mathbf{H}}^{*} \tag{5.36}$$

To find the matrix $\frac{\partial \zeta}{\partial \xi}$, the relation between the dual branch scales $\boldsymbol{\zeta}$ and parameters $\boldsymbol{\xi}$ of both types has to be derived. Using the chain rule, this gives

$$\frac{\partial \boldsymbol{\zeta}}{\partial \boldsymbol{\xi}} = \frac{\partial \boldsymbol{\zeta}}{\partial \boldsymbol{\xi}^{(\mathbf{i})}}\frac{\partial \boldsymbol{\xi}^{(\mathbf{i})}}{\partial \boldsymbol{\xi}} + \frac{\partial \boldsymbol{\zeta}}{\partial \boldsymbol{\xi}^{(\mathbf{ii})}}\frac{\partial \boldsymbol{\xi}^{(\mathbf{ii})}}{\partial \boldsymbol{\xi}} \tag{5.37}$$

From (4.14), $\frac{\partial \zeta}{\partial \boldsymbol{\xi}^{(\mathbf{i})}}$ is found as

$$\frac{\partial \boldsymbol{\zeta}}{\partial \boldsymbol{\xi}^{(\mathbf{i})}} = \frac{\partial}{\partial \boldsymbol{\xi}^{(\mathbf{i})}}\left(\mathbf{1}_{k^{(\mathrm{i})}} + \boldsymbol{L}_{\mathbf{H}}^{*\,-\mathbf{1}}\boldsymbol{F}^{(\mathbf{i})}\boldsymbol{\xi}^{(\mathbf{i})}\right) = \boldsymbol{L}_{\mathbf{H}}^{*\,-\mathbf{1}}\boldsymbol{F}^{(\mathbf{i})} \tag{5.38}$$

and from (4.12), $\frac{\partial \boldsymbol{\zeta}}{\partial \boldsymbol{\xi}^{(\mathbf{ii})}}$ becomes

$$\frac{\partial \boldsymbol{\zeta}}{\partial \boldsymbol{\xi}^{(\mathbf{ii})}} = \frac{\partial}{\partial \boldsymbol{\xi}^{(\mathbf{ii})}} \left(\boldsymbol{L}_{\mathbf{H}}^{*\,-\mathbf{1}} \left(\boldsymbol{L}_{c}^{*} + \boldsymbol{L}_{\mathbf{H}}^{*} \right) \boldsymbol{F}^{(\mathbf{ii})} \boldsymbol{\xi}^{(\mathbf{ii})} \right) = \boldsymbol{L}\mathbf{H}^{*\,-\mathbf{1}} \left(\boldsymbol{L}_{\mathbf{c}}^{*} + \boldsymbol{L}_{\mathbf{H}}^{*} \right) \boldsymbol{F}^{(\mathbf{ii})} \tag{5.39}$$

The relation between $\boldsymbol{\xi}^{(\mathbf{i})}$, $\boldsymbol{\xi}^{(\mathbf{ii})}$ and $\boldsymbol{\xi}$ is

$$\begin{bmatrix} \boldsymbol{\xi}^{(\mathbf{i})} \\ \hline \boldsymbol{\xi}^{(\mathbf{ii})} \end{bmatrix} = \left[\begin{array}{c|c} \boldsymbol{I}_{k^{(\mathrm{i})}} & \mathbf{0} \\ \hline \mathbf{0} & \boldsymbol{I}_{k^{(\mathrm{ii})}} \end{array}\right] \boldsymbol{\xi} = \begin{bmatrix} \boldsymbol{\Xi}^{(\mathbf{i})} \\ \hline \boldsymbol{\Xi}^{(\mathbf{ii})} \end{bmatrix} \boldsymbol{\xi} \tag{5.40}$$

with $k^{(i)}$ and $k^{(ii)}$ the number of DOFs of type (i) and (ii) respectively, and $k^{(i)} + k^{(ii)} = k$. Thus the $(k^{(i)} \times k)$ matrix $\frac{\partial \boldsymbol{\xi}^{(\mathbf{i})}}{\partial \boldsymbol{\xi}}$ and $(k^{(ii)} \times k)$ matrix $\frac{\partial \boldsymbol{\xi}^{(\mathbf{ii})}}{\partial \boldsymbol{\xi}}$ become

$$\frac{\partial \boldsymbol{\xi}^{(\mathbf{i})}}{\partial \boldsymbol{\xi}} = \boldsymbol{\Xi}^{(\mathbf{i})} \tag{5.41a}$$

$$\frac{\partial \boldsymbol{\xi}^{(\mathbf{ii})}}{\partial \boldsymbol{\xi}} = \boldsymbol{\Xi}^{(\mathbf{ii})} \tag{5.41b}$$

Plugging (5.38), (5.39) and (5.41) into (5.37), the desired matrix $\frac{\partial \boldsymbol{\zeta}}{\partial \boldsymbol{\xi}}$ becomes

$$\frac{\partial \boldsymbol{\zeta}}{\partial \boldsymbol{\xi}} = \boldsymbol{L}_{\mathbf{H}}^{*\,-\mathbf{1}} \left(\boldsymbol{F}^{(\mathbf{i})} \boldsymbol{\Xi}^{(\mathbf{i})} + \left(\boldsymbol{L}_{c}^{*} + \boldsymbol{L}_{\mathbf{H}}^{*} \right) \boldsymbol{F}^{(\mathbf{ii})} \boldsymbol{\Xi}^{(\mathbf{ii})} \right) \tag{5.42}$$

Combining (5.31), (5.36) and (5.42), the Jacobian matrix $\boldsymbol{J}$ becomes

$$\boldsymbol{J} = \frac{\partial f}{\partial \boldsymbol{z}} \frac{\partial \boldsymbol{z}}{\partial \boldsymbol{\zeta}} \frac{\partial \boldsymbol{\zeta}}{\partial \boldsymbol{\xi}} = -\left(\boldsymbol{Z} - \boldsymbol{Z}^{\mathbf{M}} \right) \boldsymbol{D}^{-\mathbf{1}} \boldsymbol{C}^{\mathbf{t}} \boldsymbol{W} \boldsymbol{L}_{\mathbf{H}}^{-\mathbf{1}} \left(\boldsymbol{F}^{(\mathbf{i})} \boldsymbol{\Xi}^{(\mathbf{i})} + \left(\boldsymbol{L}_{c}^{*} + \boldsymbol{L}_{\mathbf{H}}^{*} \right) \boldsymbol{F}^{(\mathbf{ii})} \boldsymbol{\Xi}^{(\mathbf{ii})} \right) \tag{5.43}$$

5.3 Non-vertical loads

For both design and analysis, the case of non-parallel loads should also be considered. As can be seen in Figure 5.3, the horizontal components of the non-parallel loads will appear in the dual diagram.

It can be seen that the number of DOFs k of the dual grid is the same as in the case without non-vertical loads. The primal branch-node matrix $\boldsymbol{C}$ and dual branch-node matrix $\boldsymbol{C}^*$ stay unchanged with the occurrence of the non-vertical loads; their topology and connectivity stay indeed unaltered. The external horizontal force components, as shown in Figure 5.3c, do influence the altered dual branch lengths $\boldsymbol{L}_{\mathbf{H}}^{*}$. It is clear from Figure 5.3 that the dual grid becomes much less legible and intuitive.

The same optimization set-up as for the parallel loading case can be used if the dual branch lengths $\boldsymbol{L}_{\mathbf{H}}^{*}$ are updated to accommodate the non-parallel loads, i.e. to guarantee equilibrium in the horizontal plane. After using (3.40) the funicular solution for this set of random loads will be found, with the nodes still constrained to only move up and down.

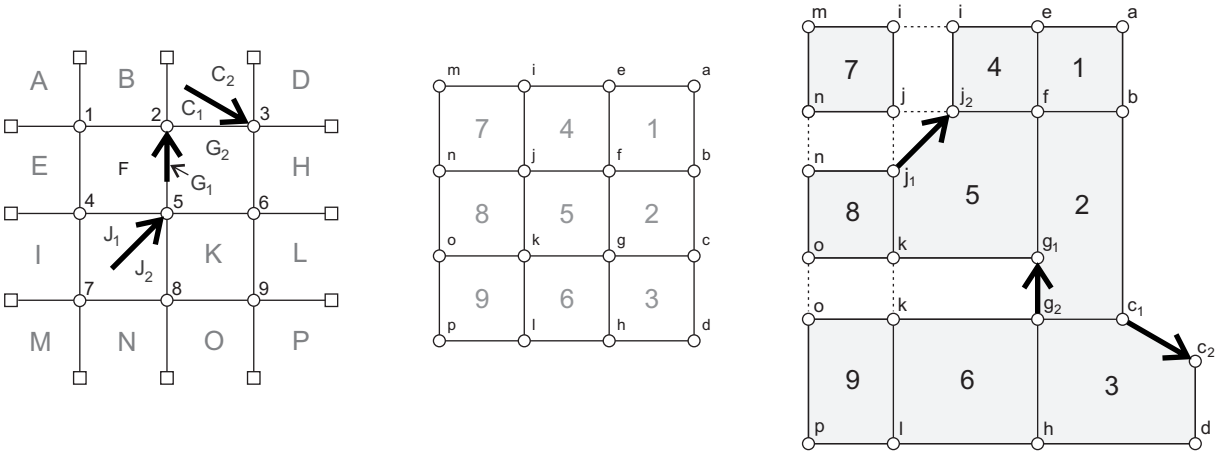

(a) (b) (c)

Figure 5.3 – Projections of non-parallel loads: (a) primal grid with horizontal components of these forces; (b) dual grid ignoring the horizontal components from the non-parallel loads; (c) the closed polygons representing the horizontal equilibrium of the nodes 2, 3 and 5 must include the externally applied loads and the dual grid adapts to the horizontal components.

For a given primal grid, but not for every set of non-vertical loads, a solution can be found.

5.4 Overlapping networks

In some cases it may be useful to consider the equilibrium of multiple overlapping networks, such as the mesh supported at discrete points by the polygonal arch shown in Figure 5.4a.

The interaction of the continuous mesh and the supporting arch can be modeled as shown in Figure 5.4. Their interaction is quite complex, but can be modeled using linear programming by adding interaction forces V_i. If described properly, the unknown interaction forces can be found in the same optimization that simultaneously finds $G^{(\text{mesh})}$ and $G^{(\text{arch})}$, the equilibrium shapes of the mesh and arch.

The interaction can be split into two connected actions: the supporting action on the mesh by the arch (Figure 5.4b) and the loading action of the mesh on the arch (Figure 5.4c). For the equilibrium equations of the mesh, the forces on the nodes from the arch are incorporated as shown in Figure 5.5.

V_i^* are defined as function of the V_i and the scale of the dual grid of the mesh, $\zeta^{(\text{mesh})}$,

$$V_i = \zeta^{(\text{mesh})} \cdot V_i^* = \frac{1}{r^{(\text{mesh})}} \cdot V_i^* \tag{5.44}$$

This allows the V_i^* to be introduced in the linear equilibrium constraints (3.13) as "negative" weights:

$$d_{ii} \cdot z_i^{(\text{mesh})} + d_{ji} \cdot z_j^{(\text{mesh})} + d_{ki} \cdot z_k^{(\text{mesh})} + d_{li} \cdot z_l^{(\text{mesh})} + V_i^* - P_i \cdot r^{(\text{mesh})} = 0 \tag{5.45}$$

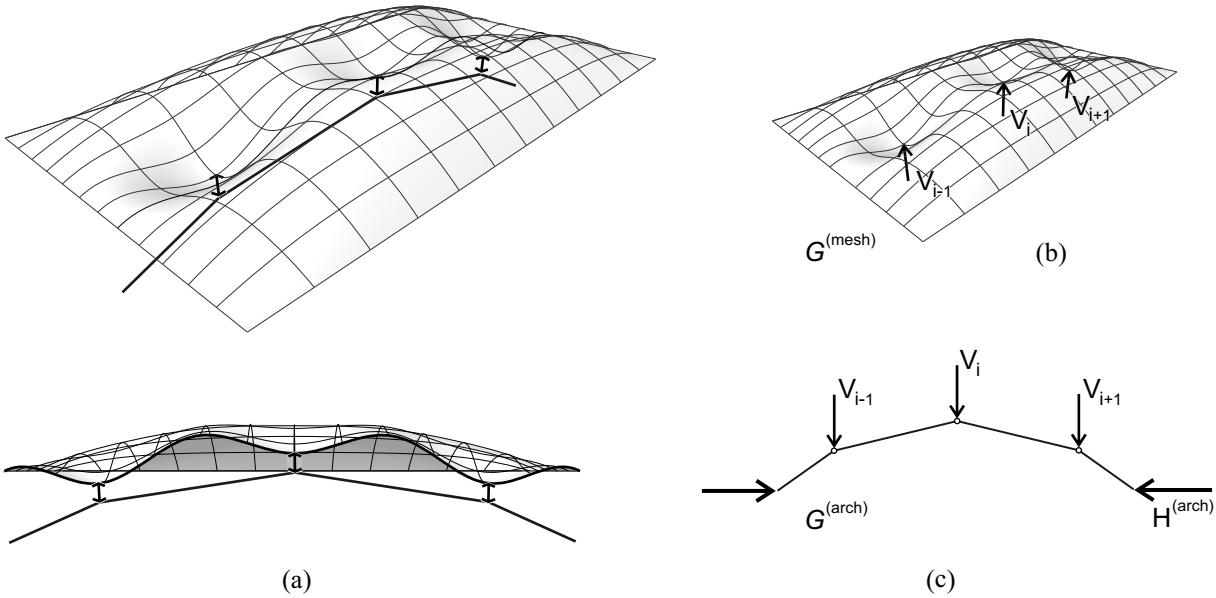

Figure 5.4 – Modeling of overlapping networks: (a) compressive arch supports a compressive mesh in a discrete set of contact points; (b) the mesh is supported in points by the polygonal arch; and (c) the arch is loaded by these inverted vertical reactions forces from the mesh.

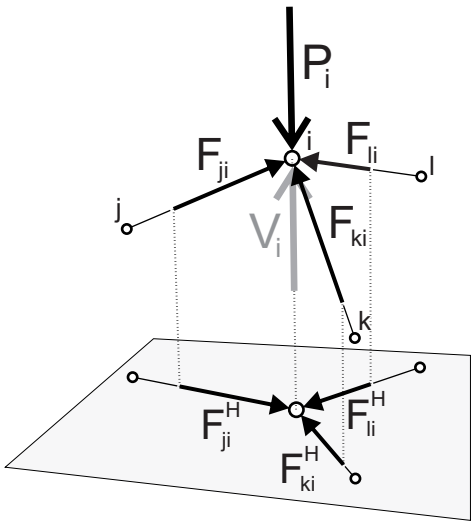

Figure 5.5 – The equilibrium of a typical node i of the mesh which interacts with the arch. V_i is the interaction force at that node between the mesh and its supporting arch, modeled as a "negative" load.

with the unknowns $z_i^{(\text{mesh})}$, V_i^* and $r^{(\text{mesh})}$.

The nodal heights of the mesh nodes which are connected to the supporting arch are not free but are constrained by the equilibrium of the arch, which will be funicular for the contact forces V_i^*. To describe the action of the mesh on the arch, equation (4.37) can be rewritten using (5.44) as

$$-\frac{1}{l_{i-1,i}} \cdot z_{i-1}^{(\text{arch})} + \left(\frac{1}{l_{i-1,i}} + \frac{1}{l_{i,i+1}}\right) \cdot z_i^{(\text{arch})} - \frac{1}{l_{i,i+1}} \cdot z_{i+1}^{(\text{arch})} - V_i^* \cdot R = 0 \tag{5.46}$$

with $R = \frac{r^{(\text{arch})}}{r^{(\text{mesh})}}$, in which $r^{(\text{arch})} = \frac{1}{H^{(\text{arch})}}$ and $r^{(\text{mesh})} = \frac{1}{\zeta^{(\text{mesh})}}$.

If R is chosen, the constraint equations of the supporting arch (5.46) also become linear, in the unknowns $z_i^{(\text{arch})}$ and the same interaction forces V_i^*.

The overall equilibrium of the interacting $G^{(\text{mesh})}$ and $G^{(\text{arch})}$ is guaranteed because the equilibrium constraints (5.45) and (5.46) are coupled by the interaction forces V_i^*, but also by introducing an additional set of constraints demanding that the mesh and the arch touch in the discrete contact points connected by the interaction forces V_i^*. The linear optimization problem to obtain global equilibrium has the following form:

$$\min_{\boldsymbol{z}^{(\text{mesh})}, r^{(\text{mesh})}, \boldsymbol{z}^{(\text{arch})}, \boldsymbol{v}^*} \pm r^{(\text{mesh})} \quad \text{such that} \quad \begin{cases} \boldsymbol{D}^{(\text{mesh})} \boldsymbol{z}^{(\text{mesh})} + \boldsymbol{v}^* - \boldsymbol{p}_z r^{(\text{mesh})} = \boldsymbol{0} \\ \left[\boldsymbol{C}_i^{\mathbf{t}} \boldsymbol{L}_{\mathbf{H}}^{-\mathbf{1}} \boldsymbol{C}\right]^{(\text{arch})} \boldsymbol{z}^{(\text{arch})} - \boldsymbol{v}^* \cdot R = \boldsymbol{0} \\ \boldsymbol{z}^{(\text{arch})} - \boldsymbol{N} \boldsymbol{z}^{(\text{mesh})} = \boldsymbol{0} \\ \boldsymbol{z}^{\mathbf{LB}} \leq \boldsymbol{z}^{(\text{mesh})}, \boldsymbol{z}^{(\text{arch})} \leq \boldsymbol{z}^{\mathbf{UB}} \\ 0 \leq r^{(\text{mesh})} \leq +\infty \end{cases} \tag{5.47}$$

where $\boldsymbol{N}$ is an $(n_i^{(\text{arch})} \times n_i^{(\text{mesh})})$ matrix describing which points of the mesh are supported by the arch. The entry $N\,(i,j)$ receives a "1" if the i^{th} node of the supporting arch is connected to the j^{th} node of the supported equilibrium mesh, and a "0" otherwise.

This implementation of overlapping networks has been illustrated using the interaction between an arch and a mesh. It can also connect several in plan overlapping meshes, which opens exciting possibilities for design.

5.5 Links with Airy stress functions

This section will discuss the relation between reciprocal figures and discrete, i.e. polyhedral, *Airy stress functions* [Airy, 1863]. Their correlation was first pointed out and proven analytically by Maxwell [1869].

Section 4.1.2 demonstrated the equivalence between a primal grid which has a convex dual, and the projection on the horizontal plane of a convex (or equivalently concave) polyhedral bowl. Ash et al. [1988] discussed the geometrical construction to go from the reciprocal dual grid to the polyhedral bowl which has the primal as horizontal projection (Figure 5.6a). This polyhedral bowl is actually a discrete

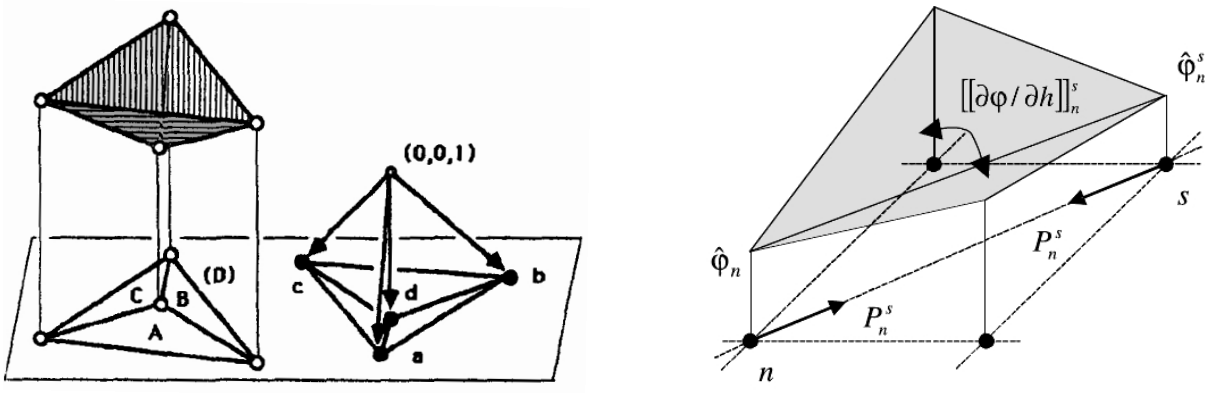

(a) (b)

Figure 5.6 – (a) The geometrical relationship between discrete Airy stress functions and reciprocal figures as first described by Maxwell [1869], clarified and illustrated by Whiteley [1986]. (b) The change in angle of the discrete stress function along an edge of the primal grid [Fraternali et al., 2002].

stress function representing one of the possible horizontal equilibrium states of the thrust network G. This will be proven by the following discussion.

Equation (3.5) can be generalized for j branches coming together in node i as

$$\sum_j F^{\mathrm{H}}_{ji} \cdot \frac{(z_i - z_j)}{L^{\mathrm{H}}_{ji}} - P_i = 0 \tag{5.48}$$

From Fraternali and Rocchetta [2002], but with the notation used this dissertation, the equilibrium constraint equation of a typical node i with j branches ending in it can be written as

$$\sum_j \hat{F}_{ji} \cdot \frac{(z_i - z_j)}{L^{\mathrm{H}}_{ji}} - P_i = 0 \tag{5.49}$$

in which $\hat{F}_{ji} = \left[\left[\partial\hat{\varphi}/\partial l^h\right]\right]^j_i$ denotes the jump in the directional derivative $\partial\hat{\varphi}/\partial l^h$ across the edge ij of the polygonal stress function $\hat{\varphi}$, which is considered to be a piece-wise linear approximation of a continuous thrust surface. As shown in Figure 5.6b, this jump $\left[\left[\partial\hat{\varphi}/\partial l^h\right]\right]^j_i$ can also be understood as the change in angle going clock-wise along the edge ij of the discrete stress function $\hat{\varphi}$.

Comparing (5.48) and (5.49) then renders the relationship between the horizontal component F^{H}_{ji} of the axial force in the branch ij and the change in angle across that edge of the Airy stress function $\hat{\varphi}$ describing its equilibrium:

$$F^{\mathrm{H}}_{ji} = \left[\left[\partial\hat{\varphi}/\partial l^h\right]\right]^j_i \tag{5.50}$$

and using (3.9),

$$\zeta \cdot L_{ji}^{\mathrm{H}^*} = \left[\left[\partial\hat{\varphi}/\partial l^h\right]\right]_i^j \tag{5.51}$$

Equation (5.51) relates the two representations of the horizontal equilibrium of the thrust network G: its dual grid Γ^* and its discrete Airy stress function $\hat{\varphi}$. The dual branch lengths $L_{ji}^{\mathrm{H}^*}$, multiplied by the overall scale of the dual grid ζ, give the value of the change in angle over that edge of the discrete stress function $\left[\left[\partial\hat{\varphi}/\partial l^h\right]\right]_i^j$.

Fraternali and Rocchetta [2002] point out that a compression-only network corresponds to a concave stress function, and equivalently a tension-only network to a convex stress function. A concave, polyhedral stress function indeed has consistently the same sign for the angles between its planar facets, corresponding to the positive force densities in a compression-only network. This ties up the argument since we know from Ash et al. [1988] that tension-only grids are the horizontal projections of convex polyhedral bowls.

Although the Thrust Network Analysis approach in this dissertation was developed independently from Fraternali and Rocchetta [2002], both approaches use a nearly identical framework but TNA uses reciprocal force diagrams instead of discrete Airy stress for the *lumped stress method* [Fraternali and Rocchetta, 2002]). The advantages and disadvantages of their approach over TNA were discussed in the literature review (§2.2.7). The correlation between discrete Airy stress functions and reciprocal diagrams discussed in this section needs to be further explored so that the strengths of both approaches can be complemented and extended. Particularly the predictor-corrector strategy by Fraternali and Rocchetta [2002], a geometric technique based on the convex hull [Avis and Fukuda, 1992] to optimize the shape of the thrust surface within the boundaries of a vault, could be valuable in the TNA framework.

5.6 Summary

This chapter discussed several alternative objective functions for the basic Thrust Network Analysis framework. The idea of the funicular loading of a given vaulted shape has been translated into a linear optimization problem.

An important nonlinear extension to the basic TNA framework allows the incorporation of the degrees of freedom of the dual grid, i.e. the infinite variations of internal forces in a statically indeterminate network. It optimizes the internal force distribution in order to obtain the absolute minimum thrust or geometric safety factor using complex networks. This nonlinear extension of the TNA framework is an important step towards making Thrust Network Analysis a viable and versatile assessment method for complex vaulted masonry structures. It also opens up new possibilities for approximating free-form designs using funicular structures.

Procedures have been presented to extend the TNA framework beyond parallel-only loading cases and non-overlapping surfaces. The equivalence between the reciprocal diagrams used in TNA and discrete Airy stress functions has been shown. This relation opens up the possibility to utilize solving procedures and algorithms from computational geometry.

Part III

Applications and Results

Chapter 6

Analysis of masonry vaults

6.1 Introduction

This chapter shows results of using Thrust Network Analysis for the equilibrium assessment of masonry vaults in order to validate the method. The method is particularly appropriate for historic masonry vaults because their self-weight is the dominant load. It discusses how to identify sensible force patterns for representing the structural action of different vault typologies and the requirements on the force networks for modeling pathologies. Several examples and case studies show the potential of this method to assess the stability for a wide range of complex vault types.

6.1.1 Force patterns

The principal challenge for the analysis of masonry structures is to define an appropriate network of forces to model a plausible flow of forces in a three-dimensional structure. There has been extensive debate on the structural behavior of masonry vaults, with a particular emphasis on the perceived role of the rib in Gothic vaults [Viollet-le Duc, 1868; Sabouret, 1928; Abraham, 1934; Heyman, 1968; Mark, 1982]. Many assumed that the vault forces "flow" to the supports in the same manner as water would drain off the vault's upper surface or as a cannonball would roll off the surface of a vault, as Abraham [1934] shows in Figure 6.1a. In Figure 6.1b, Abraham compares Viollet-le-Duc's "wrong" assumption (A) and his "correct" assumption (B) on how the forces travel to the supports. Mark [1982] uses photo-elastic analysis on carefully machined, perfectly homogeneous and smooth, plastic models to show the elastic path of forces in a groin vault (Figure 6.1c).

Regardless of the above discussion, the safe theorem shows that it is not important or even possible to know the exact internal state of the vault. However, as discussed in §4.1.1, it is useful to seek help in choosing a sensible logic for the force patterns. Ungewitter [1890] and Rave [1939] for example apply the same idea as Abraham to assume force paths for a wide range of cross vaults with different cap geometries. They cut the vault into imaginary tributary strips which are informed by the curvature of the vaults (Figure 6.2). The main force lines follow the principal directions of curvature. These lines of steepest descent run perpendicular to the height isolines. This strategy for slicing up a vault seems to be generally considered as the most sensible, and would therefore be the best choice when a combination of

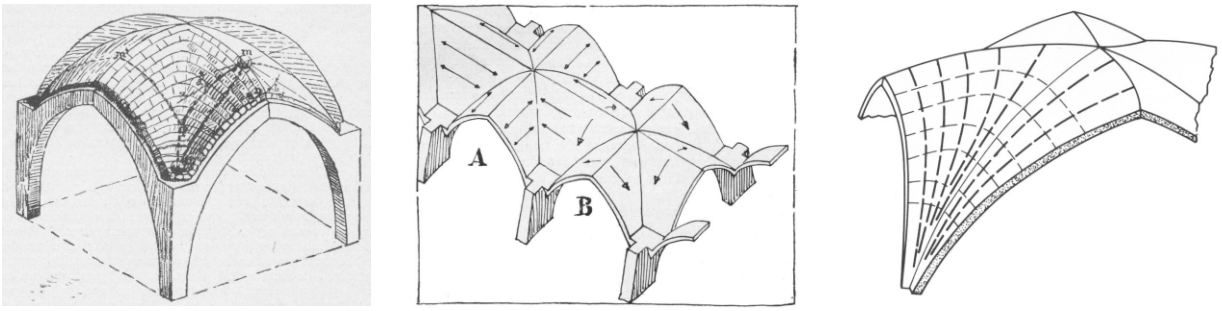

(a) (b) (c)

Figure 6.1 – Different assumptions on how the forces flow to the supports in a quadripartite vault, according to (a) Abraham [1934], (b) Viollet-le-Duc in part A [Abraham, 1934], and (c) Mark [1982].

two-dimensional analyses is used.

By using Thrust Network Analysis the different force pattern assumptions can be compared, though the real power of the approach lies in the ability to superpose multiple assumptions on the structural behavior of the vault (Figure 4.1). As pointed out by O'Dwyer [1999], the resulting combined patterns represent better the highly indeterminate character of three-dimensional vaults. Alternatively, the example in Figure 4.18 showed a fully three-dimensional network distinguishing primary and secondary force lines. The location of these main force lines can for example be inspired by the location of ribs in the actual vault, since such elements could attract more force, but also because often the ribs were laid out along the lines of principal curvature [Pottmann et al., 2007].

6.1.2 Modeling pathologies

For historic masonry vaults, it is important to observe cracks and deformations to make informed assumptions on how the structure might act. The chosen primal grid should then reflect these structural discontinuities. Due to support displacements, Sabouret cracks [Sabouret, 1928] often occur parallel to the walls in cross vaults (Figure 6.4a) and radial cracks often occur in domes [Heyman, 1995]. Pieper [1983] and Barthel [1993] give an overview of common cracking patterns for different vault typologies (Figure 6.4b).

A system of discrete forces allows cracks and other structural discontinuities to be modeled easily. These defects put geometric constraints on the thrust network G, and hence the allowed primal grid. Branches of the force network which would cross holes or open cracks need to be removed, since no compressive forces can be transmitted over them. For more intricate force patterns, the equilibrium of the opening edge needs to be checked (see §4.1.3). Hinging cracks force branches crossing them to go through them, either on the intrados or extrados (see Figure 4.20). Forcing the thrust network to go through the hinge lines is achieved by introducing weightless nodes at the intersection of the traversing force lines and the hinge line and constraining their z-coordinates on the hinge line, which is either at the intrados or extrados opposite to the opening crack. This is done by making the lower and upper bounds on their z-coordinate equal to that value.

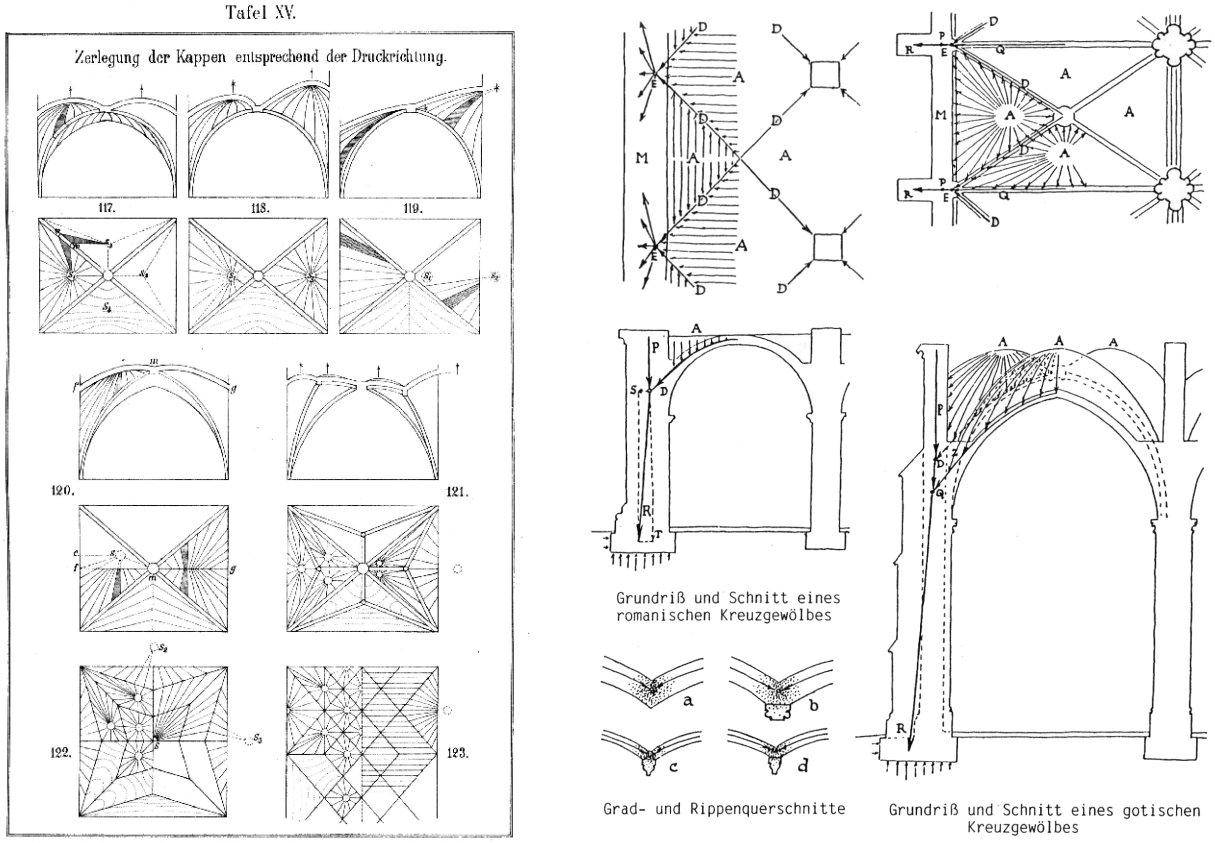

(a) (b)

Figure 6.2 – Historical examples for proposals to cut up a three-dimensional structure using the slicing technique by following the curvatures of the vaults by (a) Ungewitter [1890] and (b) Rave [1939].

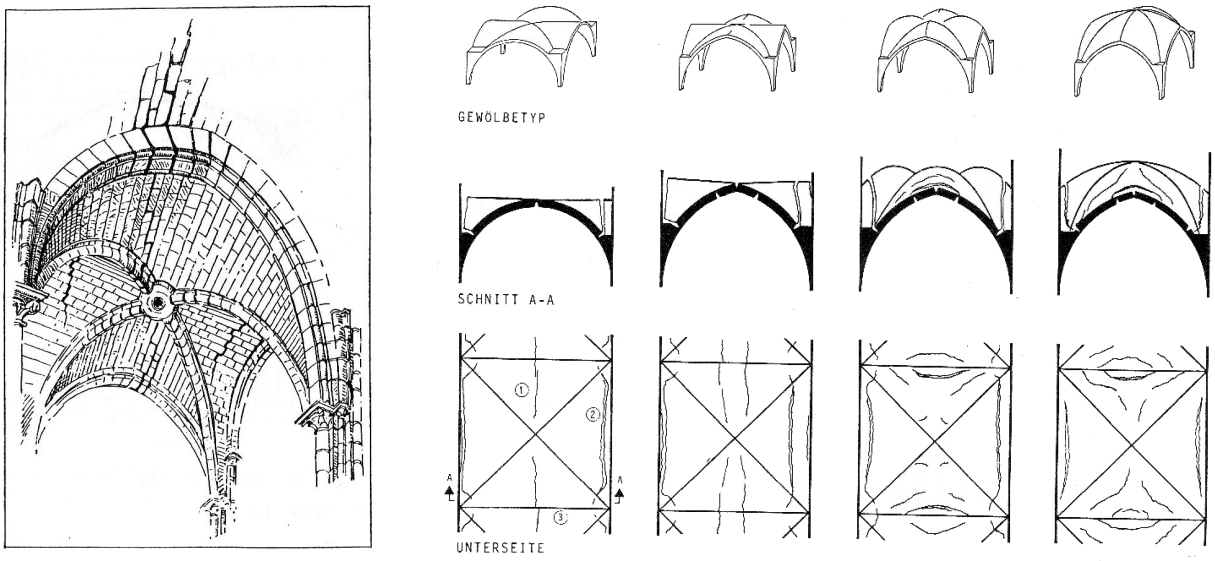

(a) (b)

Figure 6.3 – Typical crack patterns for masonry vaults: (a) The cracks running parallel with the side walls are called Sabouret cracks [Abraham, 1934]. (b) For some common vaults, Barthel [1993] shows their typical pathologies.

6.2 Groin and rib vaults

The range of possible equilibrium states, bounded by a minimum and maximum thrust, can be produced easily and quickly using TNA (Figure 6.4). The range of thrust values provides the most useful characterization of the structural behavior of a masonry vault. The minimum (or passive) thrust state represents the least amount this vault will push sideways onto its neighboring elements, as a function of its self-weight and shape. The maximum (or active) state of thrust on the other hand represents the largest horizontal force this vault can provide. So, this value demonstrates how much horizontal force this vault can exert on its neighboring elements.

Figure 6.5 shows different force patterns responding to the geometry of three generic types of cross vaults: (a) a groin vault; (b) a pointed quadripartite vault; and (c) a vault with domical caps. Their respective topographical map, resulting force pattern and force diagram are shown. These vault typologies are a selection from Barthel's classification [Barthel, 1993]. The first force pattern (Figure 6.5a) has main rib arches going from corner to corner and web arches spanning in between them, as used for the groin vault example in Figure 6.4. The second pattern (Figure 6.5b) shows a different assumption on how the forces could travel through the structure: all force lines go directly to the corner supports. The force diagrams represent in a clear fashion the equilibrium of the corner nodes and center node. A similar pattern will be used to analyze the fan vaults in §6.3. Both patterns only have thrusting reactions at the corners, but the first one relies heavily on forces in the ribs, while the latter has the web spanning independently of the ribs, which would be a more sensible choice of force pattern in the common case where the web is separated from the ribs in the actual structure.

As pointed out in §4.5.2, although the force patterns in Figure 6.5 are merely a combination of two-dimensional force lines, the use of reciprocal force diagrams is valuable for understanding how the different

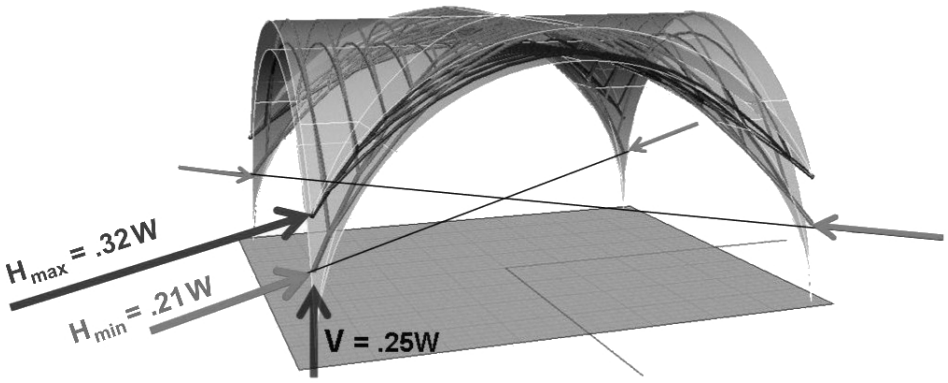

Figure 6.4 – Possible thrust values for this groin vault range from a minimum thrust of 0.21W to a maximum thrust of 0.32W, with W the total weight of the vault.

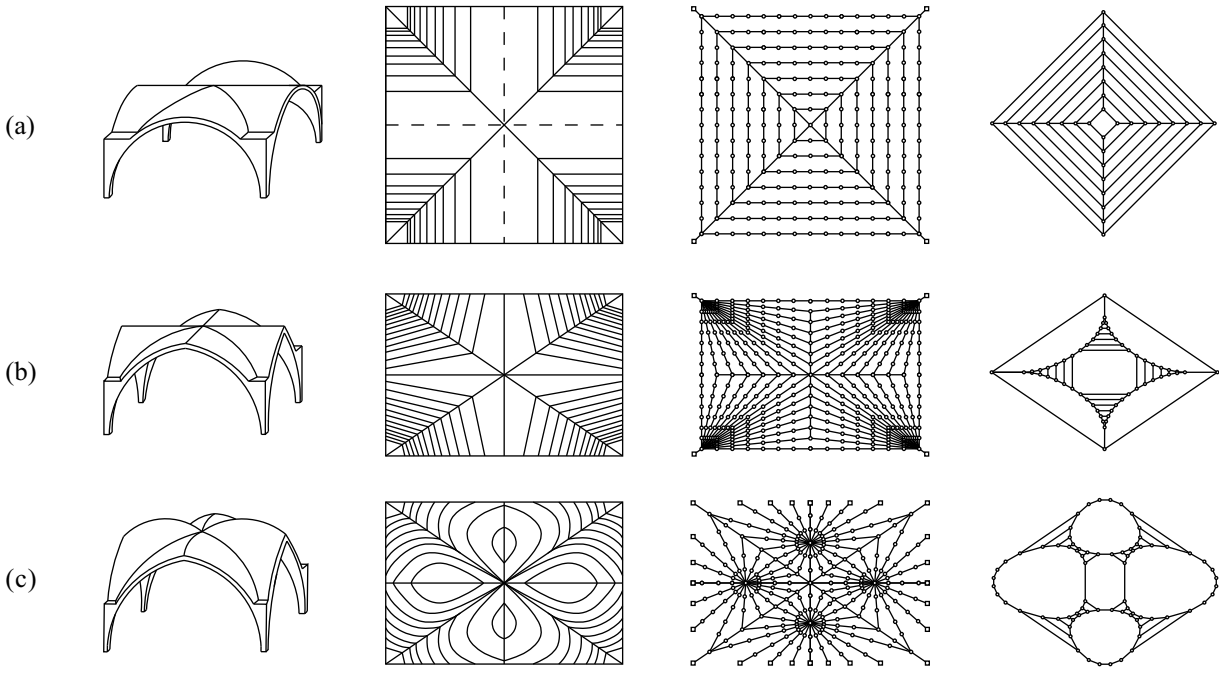

Figure 6.5 – Three generic types of cross vaults: (a) a groin vault from two intersecting barrel vaults, (b) a pointed quadripartite vault, and (c) a vault with domical caps. Their respective topographical map, sensible force pattern reflecting the geometry of the vault, and reciprocal force diagram are shown.

thrust lines combine to create a three-dimensional network. The reciprocal force diagrams clearly show how the forces interact, what thrust values are interdependent and how many degrees of freedom (to redistribute the forces internally) are in the chosen system. A radial force pattern would be appropriate for cross-vaults with domed caps (Figure 6.5c). An important difference with the previous two assumptions is that for the network in Figure 6.5c the forces no longer only go to the corner supports, but a part of the vault is carried along the edges. If Sabouret cracks are present in the vault, separating the web from the supporting walls, this pattern would not be appropriate for the assumed path of the forces.

6.3 Fan vaults

The fan vaults of King's College Chapel in Cambridge, England were constructed between 1512 and 1515 by master mason John Wastell (Figure 6.6a) [Leedy, 1980]. These doubly-curved vaults were first analyzed by Heyman [1967; 1977; 1995] using membrane theory. The static equilibrium of these vaults and an estimation of the horizontal thrust acting on each buttress can be obtained using a simple slicing approach and TNA. The difference between the results of both approaches will be discussed and compared to Heyman's results.

From available documentation (Figure 6.6b) [Mackenzie, 1840; Leedy, 1980], a detailed three-dimensional CAD model is constructed (Figure 6.6c-d). This model is used to obtain the nodal height constraints and to approximate the weights applied at each node of the assumed force networks. The vault has cracks between the conoid fan vaults and the transverse arches and also along the side walls [Leedy, 1980]. The transverse arches and the fan vaults are therefore assumed to work independently of each other. The chosen cuts in the slicing technique or the chosen force pattern in TNA reflect this, i.e. no branches cross the interfaces between the fan vault and the transverse arch. With more information about where exactly cracks and openings have developed, some interaction between the transverse arches and the conoid vaults could occur but it is conservative to assume that there is no interaction.

The resulting two-dimensional minimum thrust lines obtained using the slicing technique are visualized in Figure 6.7a. The thrust line solutions barely fit within the fan vault's geometry. This would suggest that the vault is close to a unique upper bound solution, which means close to instability. Using the crude, two-dimensional approach the vault is found to be barely stable. In reality though, there are many three-dimensional force paths which are neglected by this simplified "arch" approach. However, the arch action demonstrates one possible lower bound solution and the vault is significantly more stable than this solution suggests.

The thrust lines traveling through the part of the vault labeled "B" in Figure 6.7a-b are very shallow and travel through the high level of fill at the haunches. These result in large thrust values, which moreover enter the buttresses at a higher point. On the other hand, in part "A", the added height and weight over the transverse ridges between two adjacent fan vaults (Figure 6.6c) causes a kink in the thrust lines in the short direction of the vaults such that they fit in the very steep section. Without this added surcharge no thrust lines could be found which stay inside the vault's section in region A when using the slicing technique. The thrust lines were obtained using the two-dimensional automated thrust-line analysis version of TNA, as described in §4.5.1. The resulting thrust values of the fan vaults transferred onto the buttresses is about four times higher than the resulting thrust from Heyman [1995].

This huge discrepancy can be explained by the inability of the two-dimensional arches to redistribute forces. This becomes most critical in the arches along the diagonal of the bay (highlighted in Figure 6.7b). Figure 6.7c shows a half section of the vault taken along the diagonal. It can be seen that the arched profile becomes very flat towards the middle of the span. On top of that this, this singular arch carries

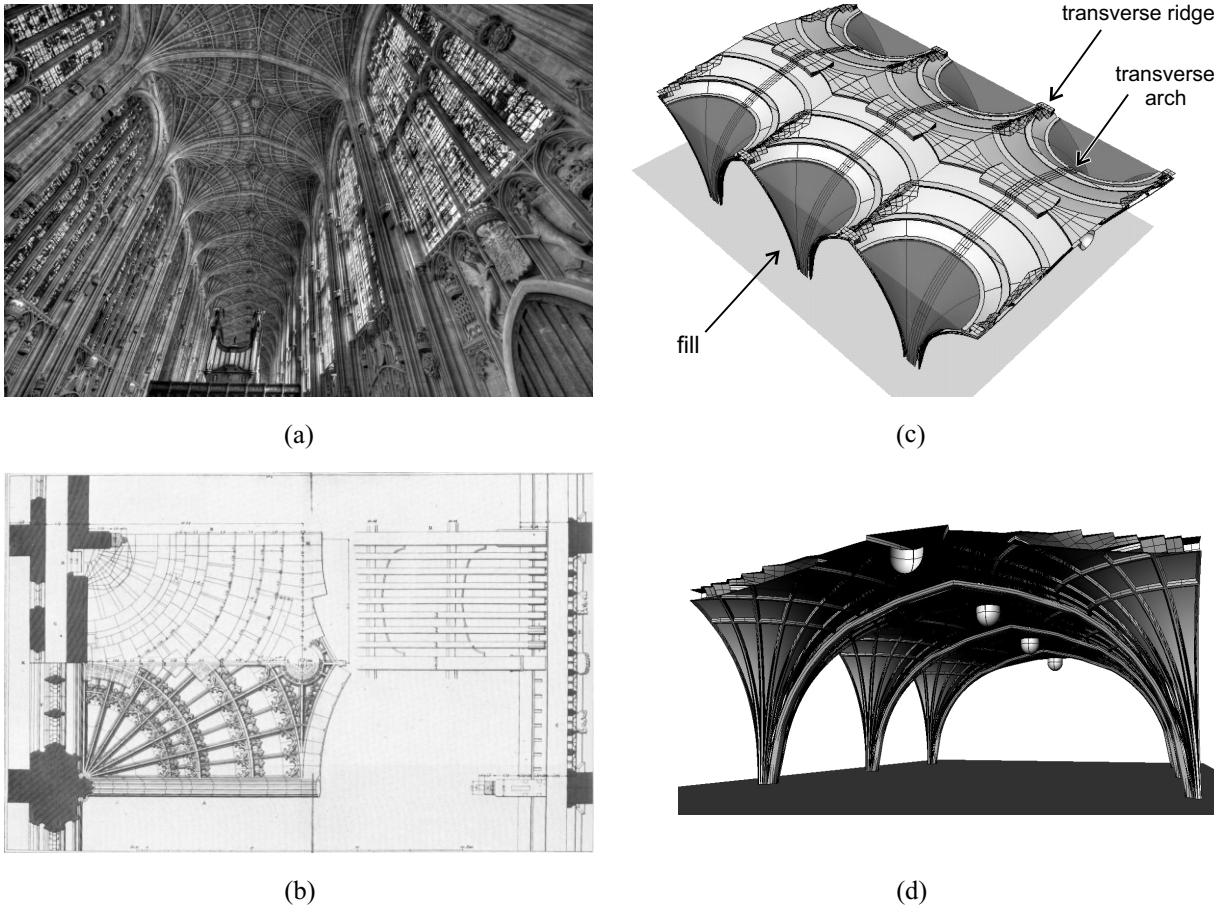

Figure 6.6 – King's College Chapel in Cambridge, England: (a) interior view of the fan vaults, and (b) one of the detailed drawings of the geometry by Mackenzie [1840], used to produce (c-d) the detailed CAD model of the vault geometry to obtain accurate boundaries and weights.

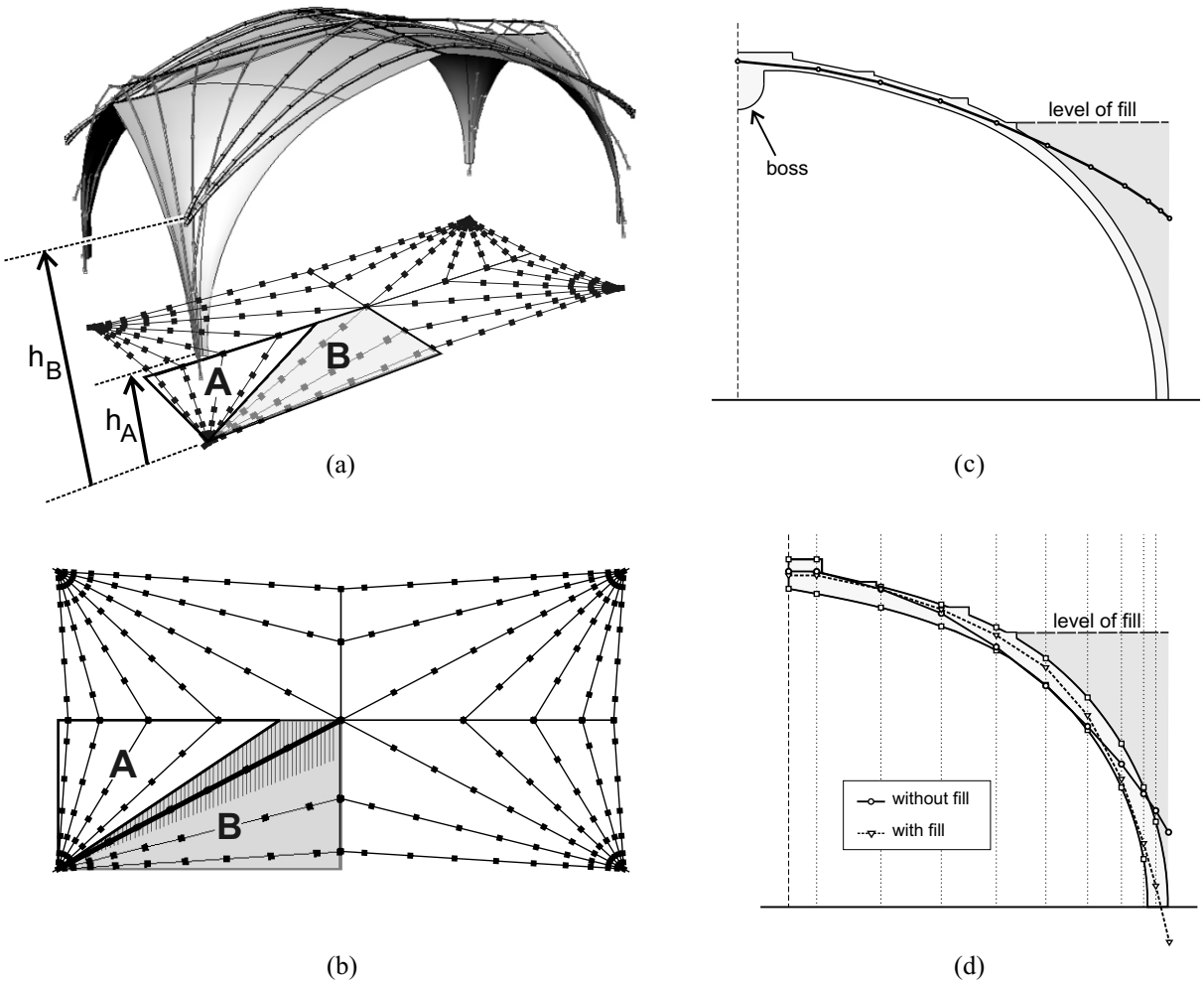

Figure 6.7 – For a typical bay of the King's College Chapel vaulted ceiling, (a) visualizes the result using the 2-D slicing technique. The thrust lines from regions A and B reach the buttress at two distinct heights, h_{A} and h_{B} respectively. (b) shows the plan view of the chosen arches. (c) Very flat profile of the most extreme, diagonal section. (d) The thrust line in the main transverse arches with and without fill. It can be seen that the fill is necessary to keep the thrust line within the arch's section.

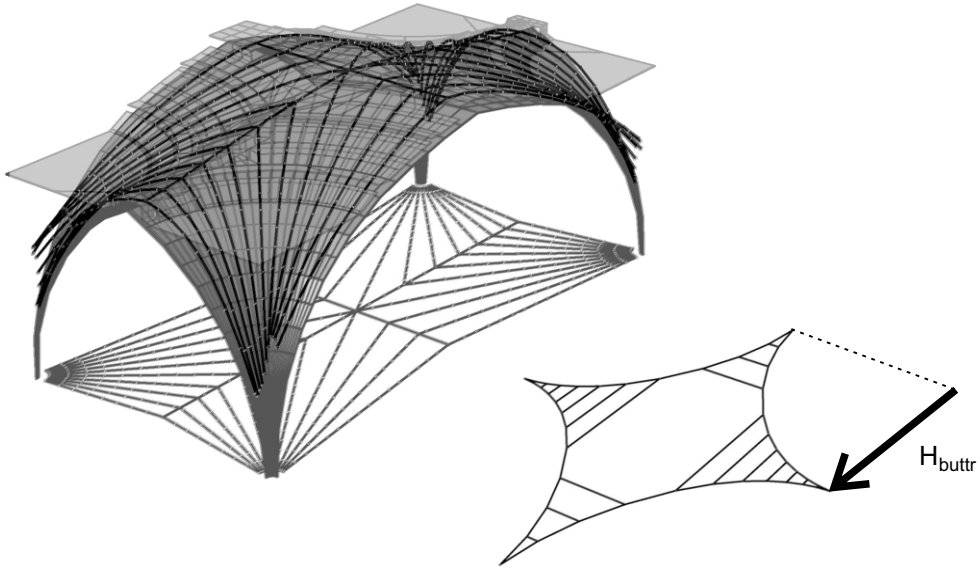

Figure 6.8 – (a) Three-dimensional equilibrium network obtained using TNA for King's fan vaults, with (b) the chosen force pattern and (c) its corresponding thrust diagram from which the thrust onto the buttresses can easily be obtained.

the entire weight of the heavy boss at the center. The problematic effect is similar to what happened with the barrel vault example in §4.1.1. These two punishing effects combine to cause these funicular arches to have very high thrust values while hitting the buttress much higher. Using the unrealistically high thrust values (four times higher than Heyman's results) could lead to erroneous conclusions, such as claiming that the buttresses are barely stable due to those high thrust values. This result shows that the slicing technique can be very unsatisfactory.

When performing a three-dimensional analysis using TNA, the resulting horizontal thrust per buttress is 176kN, or about 18 tons, which is still 1.8 times more than the 10 tons obtained from a membrane solution by Heyman [1995]. Figure 6.8 shows (a) the equilibrium result, for (b) the chosen force pattern and (c) its corresponding thrust diagram. From the thrust diagram, half of the total horizontal thrust on the buttress can be found graphically as well. In the three-dimensional network (Figure 6.8a), the connection between all arches in the center distributes the weight of the boss over all of them, resulting in a solution which follows the intrados of the fan vaults much closer.

This analysis was done iteratively by hand, and like Heyman's analysis the thrust of the transverse arches is not considered. With the non-linear extension of TNA laid out in §5.2, the overall minimum thrust state could be found, though it has not been implemented for this example. If completed, it would result in an even lower thrust value, likely much closer to Heyman's result. Part of the discrepancy between the results could be explained by different assumptions. For example it is not clear what assumptions Heyman made about the level of fill or how he reduces the thrust values from 16 tons to 10 tons because of the in plan interesecting conoids, resulting in rectangular bays. Furthermore, the CAD model could vary from the actual geometry of the fan vaults due to misinterpretations by the author of the historical documents. This would influence both the limits on the nodal heights as well as the computed weights used in the analysis.

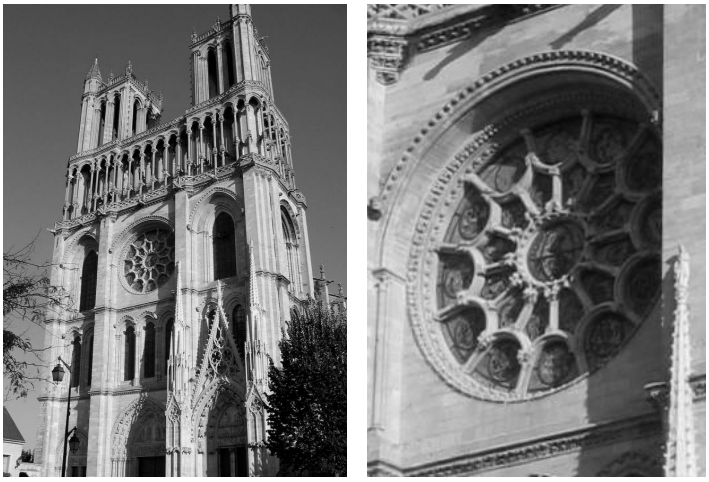

Figure 6.9 – Rose window of the Notre Dame de Mantes, France (c. 1180).

6.4 Rose windows

The delicate stone tracery of large rose windows provide an additional challenge in the three dimensional analysis of masonry structures. The main loading of large windows of Gothic churches and cathedrals is the pressure and suction caused by wind. Assessing their out-of-plane stability is therefore crucial. In order to withstand these lateral loads, these windows have to develop flat arch action in their shallow depth [Heyman, 2002]. The structural action of rose windows is similar to flat circular vaults, but they differ in that the force paths are defined and limited by the layout of the mullions and ribs in the window tracery. The geometry of a rose window can be abstracted by a bar-node system. Most rose windows have a statically determinate force pattern, with a maximum of three bars coming together per node, resulting in only triangles in the force diagrams. This means that all forces in the system are known except for a scale which will be defined by the loading and the depth of the mullions. Neglecting the contribution of the self-weight of the window, this means that the same reaction force is required from all sides.

Thrust Network Analysis can be used to model the flat vault action of the rose window of the Notre Dame de Nantes, or Mantes-la-Jolie Cathedral, France, originally constructed around 1180 (Figure 6.9). Figure 6.10 shows (a) the assumed primal grid, which approximates the structure as a bar-node system; and (b) the unique corresponding dual grid. The grey dotted lines in Figure 6.10a contour the tributary areas of the loaded nodes, found using Voronoi diagrams on the vertical plane of the window. This is a variation of the second approach for computing the nodal loads as discussed in §4.3.1, since here the tributary areas for the wind related to each node needs to be known. The corresponding compressive equilibrium solution in Figure 6.10c visualizes the flat-vault action of the structure. The force network is in equilibrium with the wind loads and stays within the depth of the rib structure.

The solution obtained is compared with Heyman's [2002] results. Using this fully three-dimensional approach, for the same geometry (diameter of the rose window is 8 m and mullions of 25 cm by 25 cm) and wind loading (2 kN/m^2), the minimum thrust of the final spokes is 49.6 kN. Heyman used a simplified two-dimensional approach to determine a value of 67 kN which is 35% higher, and hence more conservative. For this case, Thrust Network Analysis provides a significant improvement over existing hand methods of analysis.

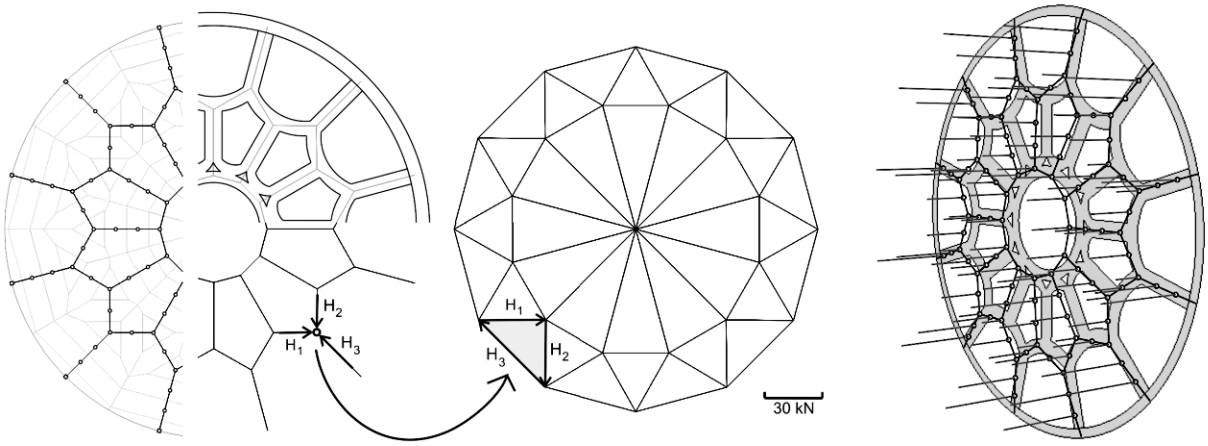

Figure 6.10 – Thrust-network analysis of the rose window of Notre Dame de Mantes, France. (a) The structural action is reduced to a bar-node system (after [Heyman, 2002]). (b) The in-plane forces in the rose window due to the wind loading can be measured from the reciprocal force diagram. (c) The equilibrium network demonstrates flat vault action.

In this analysis, the potential failure due to the shear forces at the perimeter of the window is not checked. Because the joints between the stones making up the mullions are parallel to the dominant wind loading and the proportion of the cross-sectional area of the mullions compared to the loaded area is small, this failure mode can be critical and sliding due to the shear forces needs to be checked at the interfaces of the outer spokes with the outer ring. To prevent this failure, iron connecting dowels were often inserted to transfer the shear forces [Heyman, 2002; Clifton and Willis, 2007].

The obtained flat vault action causes stresses less than 800 kN/m^2 which is more than an order of magnitude below the crushing strength of even the softest lime-stone (12,000 kN/m^2). This result needs to be considered carefully though, since the analysis assumed that the window has a perfect geometry which can generate the suggested minimum thrust flat vault action. For even small out-of-plane deflections of the window, which is not unthinkable for large area windows, the thrust network, constrained by the formation of hinges in the mullions and the decreased height due to the "sagging" of the window, quickly becomes nearly flat, resulting in very high thrust values and hence high stresses on reduced sections. This makes windows one case where not only geometry and stability, but also elasticity matters because of the potential for snap-through failures of the slender ribs.

6.5 Thin-shelled spiral staircases

Thrust Network Analysis can also be used for the structural analysis of thin shell spiral staircases, which have presented a challenge for engineers due to their complex geometry and their extreme thinness. The R. Guastavino Company built thousands of thin-shelled masonry vaults in the late 19th and early 20th century [Collins, 1968; Huerta, 2003; Ochsendorf, 2009]. They were commissioned to construct structural vaults of many important buildings, such as the Boston Public Library and Carnegie Hall in New York. Lesser known are their thin-shell staircases in tile (Figure 6.11a-b). These spectacular thin-shelled vaults work quite differently than the typical cantilevered stone staircases shown in Figure 6.11c [Price, 1996;

(a) (b) (c)

Figure 6.11 – (a) An example of a Guastavino thin-tiled helicoidal stairway at the Union League Club of the City of New York, 1901-1902 (Guastavino/Collins Collection, Avery Library); and (b) stair at Carnegie Mellon University, Pittsburgh, 1914 (Picture by Michael Freeman). (c) shows cantilevering spiral stone stair at the Castle Drogo in England [Maunder, 2005].

Maunder, 2005]). Calladine [2005] suggests that the Guastavino spiral stairs behave as elastic shells and estimates their natural frequencies through finite element modeling (see also [Mandal and Calladine, 2008]). García Ares [2007] proposes a lower-bound solution which demonstrates the static equilibrium of these helical shells.

TNA can demonstrate the stability of these stairs by finding a three-dimensional compression-only equilibrium solution for several loading cases. First of all, it can be noted that there is a topological relationship between (a) a dome spiral, (b) a flat vault, and (c) a helical staircase with an oculus, as illustrated in Figure 6.12. In plan, the assumptions for an appropriate force network for all three structures are identical: a compression central ring and meridian "hoops" and radial arches. For the dome (Figure 6.12a) or flat vault (Figure 6.12b), the compression ring of the oculus (and each meridian hoop) is in the same horizontal plane and is therefore in equilibrium by itself under applied vertical loads. This is clearly different for the helical stair (Figure 6.12c) where the compression ring, also circular in plan, now spirals in the z-direction. Since the compression hoops are not closed, they will require external reactions at the landings to keep them in equilibrium. As discussed in §4.1.3, the circular inner compression ring requires the horizontal thrusts of all radial arches to be equal, since the circle is the funicular shape for uniform loading applied radially. This assumed force pattern for these helicoidal stairs (Figure 6.12d) counts on a continuous wall support and supports at the landings.

The results obtained using TNA for the minimum thrust state under certain loading condition will be compared to the results of García Ares [2007]. Figure 6.13b shows the definition of his parameters: an angle in plan γ_d of 180 degrees, an inner radius r_1 of 1.5 m, an outer radius r_2 of 2.5 m, a height h of 4m, a thickness g of 15 cm and an equivalent density ρ_e of 33.3 kN/m^3, combining the loading of the self-weight, with a density of 20 kN/m^3, and a surcharge of 2 kN/m^3.

A perfect helical spiral has some interesting properties. Because the spiral has a constant slope, or "climb angle", the intersection of the spiral with a cylinder of the same central axis is a straight line if unrolled

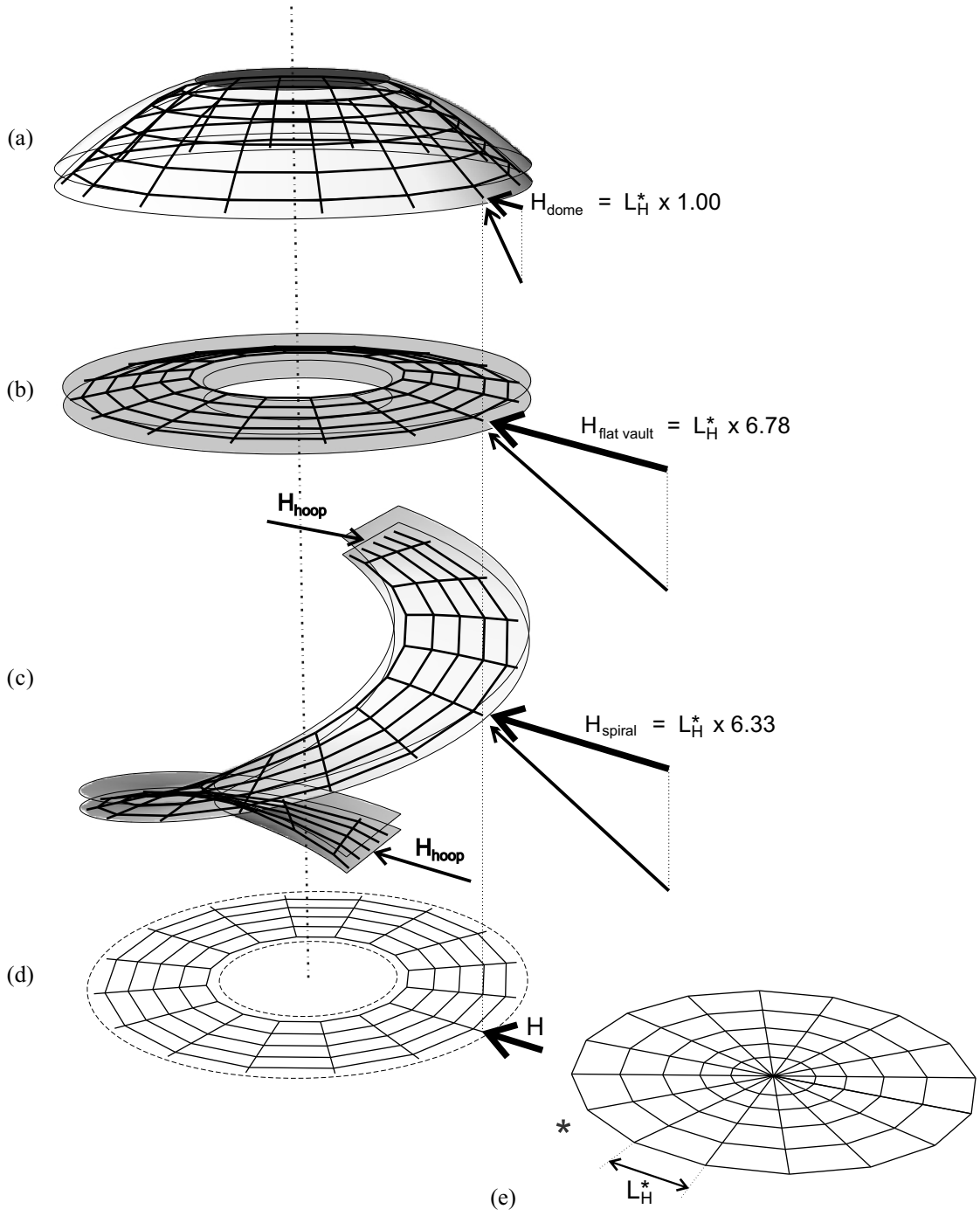

Figure 6.12 – Identical force pattern topologies for (a) a dome with a circular oculus, (b) a circular flat vault with an oculus, and (c) a helical spiraling stair with compression hoops. (d) shows their primal grid and (e) their dual grid. The horizontal thrust of the flat vault or spiral are respectively 6.78 and 6.33 times larger than the dome's horizontal thrust.

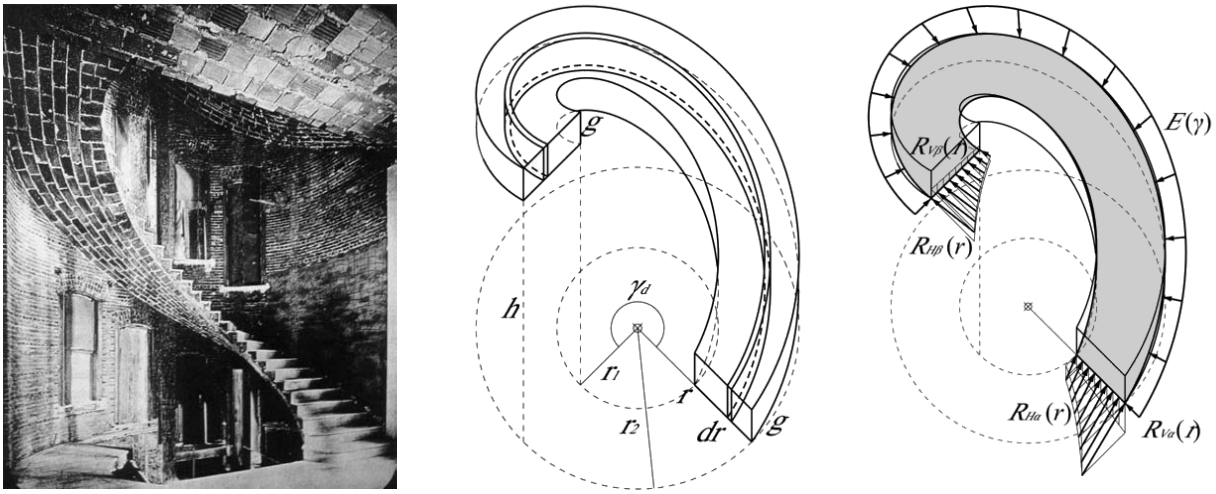

(a) (b) (c)

Figure 6.13 – (a) Elliptical spiral staircase in the first National Bank of Paterson, New Jersey, ca. 1890 (Guastavino/Collins Collection, Avery Library). (b-c) show the parameters used by García Ares [2007].

(Figure 6.14a-b). García Ares [2007] uses this knowledge to find the minimum thrust state of such a strip, which is the deepest parabolic funicular. Figure 6.14c shows the outlines of the funicular polygons of these parabolas. He then finds the minimum horizontal thrust $R_H(r)$ given in kN/m per strip to be:

$$R_H(r) = \frac{wL^2}{8h} = \frac{\rho(g\Delta r)\cdot(\gamma_d r)^2}{8g} = \frac{\rho\Delta\gamma_d^2 r^2}{8} \tag{6.1}$$

where Δr is the tributary width of the strip. The distributed reaction forces E at the wall are equal to

$$E_{r_2-r_1} = \frac{\gamma_d^2\rho(r_2^2 - r_1^2)}{16} \tag{6.2}$$

To allow comparison with García Ares' results, the horizontal thrusts in the spiraling hoops are chosen proportional to (6.1). This is controlled by defining the branch lengths proportional to these values. The horizontal components of the end reactions at the two landings will therefore have the same distribution as García Ares' results.

The resulting horizontal thrust $R_H(r_i)$ using TNA is about 50% higher than García Ares' results. This difference can be explained because a connected network is used in TNA to approximate continuous thrust surfaces, which means that all spiraling funiculars, all connected in the radial direction, cannot be as deep as the deepest parabolas of each strip, as assumed in García Ares' analysis. The horizontal thrust resulting from the spiraling "arches" will therefore have to increase. On the other hand, the wall reactions E are within 5% of his values. As can be seen in equation (6.2), the linear wall reaction forces E are only dependent on the plan geometry of the spiral.

García Ares' approach and the assessment using TNA are very similar. An important difference though is that TNA did not demand the fairly elaborate derivation of equations, obtained after careful inspection of

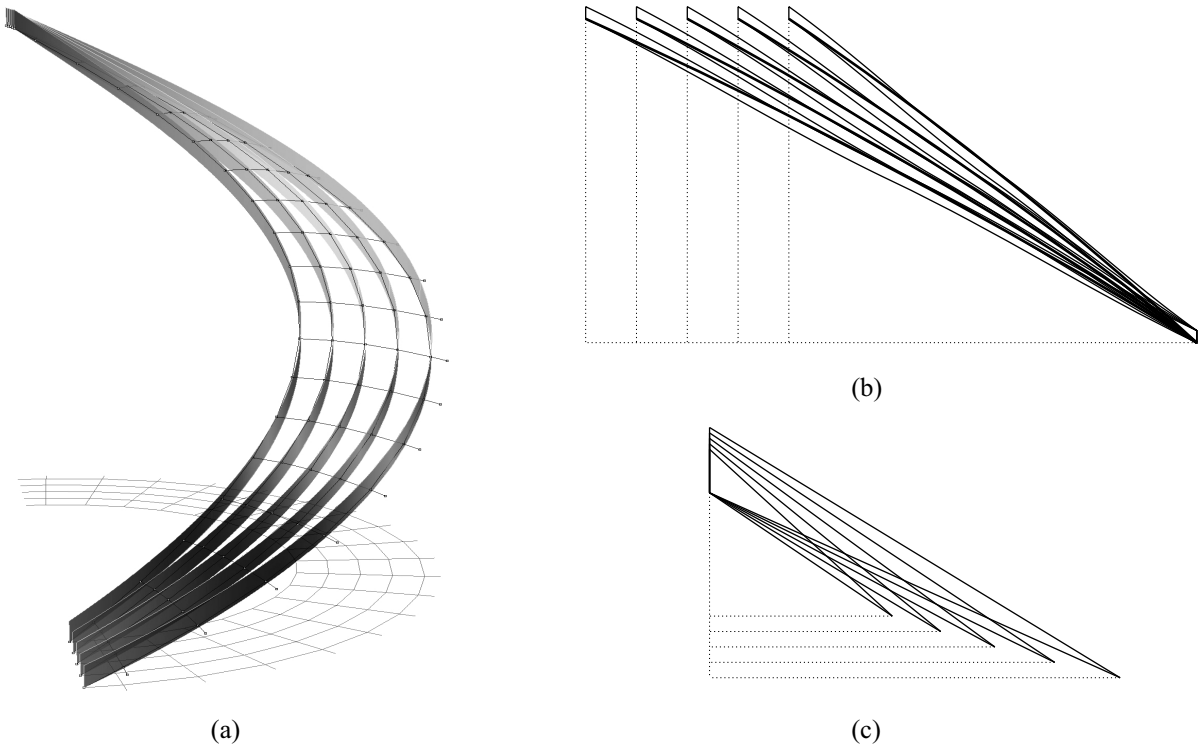

Figure 6.14 – (a) The intersections of the spiraling vault and concentric cylinders form straight strips when unrolled (b). (c) are the outlines of the funicular polygons of the deepest parabolas fitting the straight, unrolled sections in (b).

the specific problem and geometry. Instead, the process was intuitive and the solution was easily checked by the graphical diagrams. More importantly perhaps, TNA can just as easily be applied to winding stairs with inner edges with arbitrary geometries in plan as in the example shown in Figure 6.11b.

The Guastavino Company used load testing to demonstrate the safety of their spiraling stairs (Figure 6.15a). The following upper-bound analysis attempts to define the collapse load factor λ_c of a line load applied at $\gamma_d = 60$ degrees (Figure 6.15b). The objective function introduced in §5.1.2 is used. It is found that the load factor grows virtually to infinity (order of magnitude of seven). This surprising result can be explained by the spiraling "straight" sections (Figure 6.14). Similar to a straight (or barely arched) flying buttress, a direct line can be drawn in the section, so theoretically the horizontal thrust value can grow to infinity. Of course, this state of maximum thrust will be limited by the capacity of the supporting walls or by the material failure. This suggests that spiral stairs in masonry will be limited by their material strength, which is unusual for historical structures.

This upper bound analysis demonstrates that, if the supporting walls are rigid, then the stairs have an extremely effective shape to support both uniform and point loads. Before this theoretical upper-bound would be reached, compressive crushing, sliding at the landings or instabilities, such as buckling would occur. To identify the actual collapse load factor λ_c of these stairs, material properties will need to be taken into consideration. The visual results from this collapse load analysis do start to suggest possible three-dimensional collapse mechanisms. Where the 3-D thrust surface touches the extremities of the stair's geometry, possible hinge lines can be postulated (Figure 6.15c). Notice that only three hinge lines are identified which because of the straight profile of the spiraling strips and thinness of the structure is enough to cause instability (Figure 6.15d).

6.6 Discussion and summary

This chapter demonstrated the ability of Thrust Network Analysis to obtain lower- and upper-bound solutions for masonry vaulted structures with complex geometries, allowing the incorporation of structural discontinuities. It demonstrated the value of TNA as a powerful new tool for understanding, visualizing and exploring the equilibrium of historic vaults in unreinforced masonry. With the same framework, a variety of vaulted masonry structures were explained in an intuitive manner.

When using TNA of masonry vaults, various parameters can be changed: (a) different force patterns can be chosen to compare assumptions on how forces may be traveling through the structure; (b) the force diagrams can be manipulated to redistribute the internal forces; (c) the solution envelopes can be chosen to constrain the solutions, for example to the middle third of the vault thickness or to include the level of fill or the thickness of ribs; (d) different support conditions can be defined; and (e) the level of fill or other imposed loads can be integrated by adding load to the affected nodes. In addition, the spiral stair demonstrates the potential of this approach to suggest possible three-dimensional failure mechanisms. These and other topics deserve to be explored further.

However, there are some shortcomings to the method at present. It is clear that the extension of the basic TNA framework as formulated in §5.2 is crucial to make TNA a viable assessment tool for complex three-dimensional structures in unreinforced masonry. Due to the fairly simple network topologies, the examples shown in this chapter were still possible to carry out iteratively and by hand. However, this process is time consuming and should be automated in the future. In summary, the method shows great potential with significant room for improvement.

In the examples of the rose window and the thin-shelled spiral staircase, it became clear that stability,

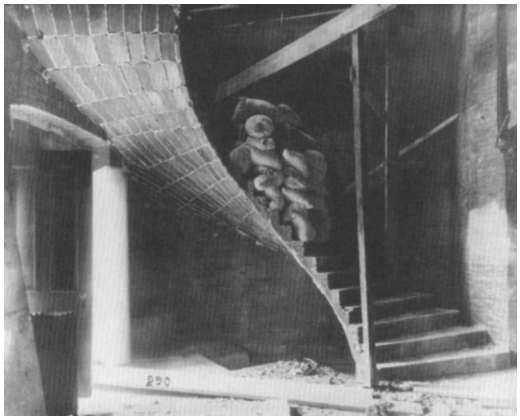

(a)

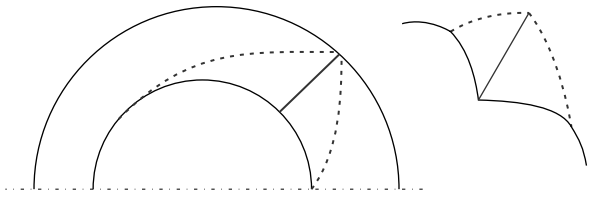

(c)

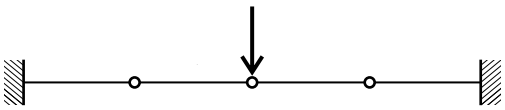

(d)

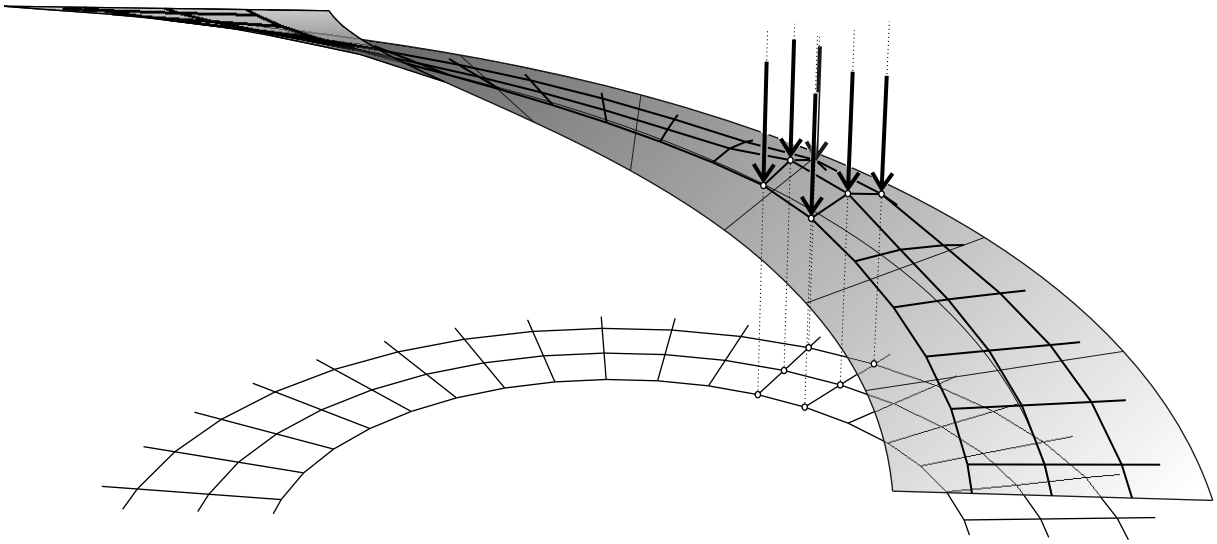

(b)

Figure 6.15 – (a) Sand bag test on a stair under construction in the First Church of Christ Scientist, New York City, 1903 (Guastavino/Collins Collection, Avery Library). (b) shows the result of a collapse load factor analysis. The network shown is the upper-bound, limit state. (c) Diagram of possible hinge lines where the thrust surface touches the extremities of the stair's geometry, whith (d) only needs three hinges to cause instability because of its straight section and thinness.

explained using TNA, only gave a partial answer to their safety. Their limit states, or collapse, were not limited by only stability but also by elasticity issues. This border-line cases need to be considered further. It is important to discuss the limits of limit analysis where elastic phenomena can no longer be neglected since the basic assumptions for limit analysis (§3.2.1) may be violated.

It is also important to point out that for three-dimensional structures Heyman's safe theorem framework (§3.2.1) might not be satisfactory to conclusively assess the stability of rigid block assemblies. The existence of a possible three-dimensional, compression-only solution which stays within the boundaries of the vault, does not necessarily guarantee the stability of the vault. As Parland [1979; 1995] points out, there could exist other equilibrium states which could cause sliding problems. This important issue is equivalent to the typical sliding failure observed at the interface of flying buttresses and the cathedral walls [Nikolinakou et al., 2005]. This problem only occurs when the flyers are in a state of minimum thrust. Many more internal force distribution are imaginable, and hence possible, for complex, three-dimensional vaulted structures. An exhaustive analysis should thus run through all the possible variations in force pattern and internal force distribution to identify the critical equilibrium states for sliding. The nonlinear extension in §5.2 is a first step in that direction, but this issue also asks for an "optimization" procedure varying the used force pattern topologies.

By developing a method for analyzing three-dimensional unreinforced masonry vaulted structures with complex geometries, a powerful tool emerges for exploring sophisticated three-dimensional good structural form, as will be demonstrated in Chapter 7. Many historic masterpieces have quite challenging geometries, and in order to model their structural behavior, Thrust Network Analysis can be used to discover new funicular shapes.

Chapter 7

Design of equilibrium vaults

7.1 Introduction

This chapter demonstrates the use of Thrust Network Analysis (TNA) as a powerful interactive method for designing funicular vaulted structures. The method finds possible equilibrium solutions under gravitational loading within a defined envelope. Using reciprocal diagrams and linear optimization, it provides a graphical and intuitive method, adopting the same advantages of techniques such as graphic statics, but offering a viable extension to fully three-dimensional problems. TNA gives the designer a high level of control of all the degrees of freedom of a three-dimensional funicular system resulting in a flexible and controlled manipulation of the final shape and the discovery of new structural forms.

This chapter will demonstrate that the TNA framework is a powerful method for discovering new funicular systems. It is a form-finding method, but not framed in the typical context of structural optimization: the goal is not to improve a given shape, but instead to combine free-form design, structural optimization and analysis in one integrative and holistic design exploration.

7.1.1 Three-dimensional graphical method

The TNA method can be considered as a three-dimensional equivalent of graphic statics, in that it offers clear graphical feedback and control of the forces in the system, allowing the exploration of the infinite number of equilibrium solutions for three-dimensional systems.

The constraints which can be controlled are

- the choice of network topology, represented by the primal grid Γ, which is the horizontal projection of the final equilibrium solution, the thrust network G;
- the distribution of the (horizontal) forces in the system, visualized and controlled by the dual grid Γ^*, and geometrically related to the network's geometry;
- the solution space, defined by lower and upper bounds on the nodal height and the outline of the supporting edges;

- the overall depth of the solution, controlled by the scale of the forces in the system, represented in the dual grid; and
- the boundary conditions, from fully supported to partially supported boundaries.

7.1.2 Constraint-driven design

There is no design without constraints. Constraints do not have to be considered as limiting factors, but can instead become the drivers of design. By understanding the constraints and their interdependencies, innovative design solutions can emerge [Kilian, 2006a]. Laurent Ney argues that the art of structural design is in the translation of the design problem into the definition of boundary conditions [Ney and Strauven, 2006]. The shape of the structure will follow from these constraints, so the setup is the crucial step. Ney points out that this is the important difference between architectural and structural design, i.e. that "the form of things [. . . is] not a sculptural mass, but a geometry that is in part self-determining once the boundary conditions have been chosen" [Ney and Strauven, 2006]. There is a natural state for a structure, and it could be argued that this natural state has elegance to it since it expresses where the forces want to go. The interesting challenge is how to define the boundary conditions.

The TNA setup allows constraint-driven design explorations and helps to understand the interdependencies of the constraints and their repercussions for the equilibrium solutions.

7.1.3 Bidirectional design explorer

Kilian [2006a] defined a design explorer as a "construct that combines design representations and constraints in order to support design exploration within the defined conditions," and bidirectional as "the relation between two entities in which the role of driver and driven can switch." Gaudí's physical hanging models fit the notion of design explorer since they address both structural and formal considerations and present the designer at all times with a status of the design that reflects the cumulative changes applied to the model. Graphic statics is a classical example of bidirectional exploration of a constraint network. The force polygon and force diagram are linked through geometric constraints and change can occur in both the form polygon or the force polygon. This allows for the exploration of either form or force while each change in one representation affects the results in the other through the graphic statics constraints [Kilian, 2006a].

Kilian [2006a] argues that "replacing commonly used analytical, unidirectional models for linking representations with bidirectional ones further supports design exploration." To be truly supportive of design exploration, constraint solvers need to be bidirectional [Mahdavi et al., 1997]. This means that the constraint network cannot be implemented as a hierarchically structured dependency tree that allows only propagation of effects towards the tree leaves [Kilian, 2006a]. The TNA set-up is a perfect example of a bidirectional design explorer as defined by Kilian [2006a]. It offers a high level of control over the boundary conditions and gives direct, visual feedback of user interaction: structural repercussions are clearly visualized in the reciprocal force diagrams; spatial, or architectural, qualities can be observed and evaluated in the thrust network.

7.2 Interactive design process

The introduction of indeterminate reciprocal force diagrams allows the linearization of the constraint formulations, resulting in very fast solving times for reasonably sized networks. This virtually real-time response, combined with the graphical and planar representation of forces and structure, make TNA very interactive. Section 4.2 demonstrated that the automatic generation of a possible reciprocal diagram is computationally the most demanding, but this step only needs to happen once, for the initial force diagram. For each iteration, the new geometry of the updated reciprocal is used directly. Updating the reciprocal, or redistributing the internal forces in the network, can happen by literally "tweaking" the dual grid. This process was described earlier in §4.6, but several examples in this chapter will show how it is used for exploring new form.

Figure 7.1 shows a series of compression-only solutions for a uniformly applied loading, starting from a regular rectangular grid. This entire exploration was done using TNA in less than an hour. It shows the relationship between the primal and dual grids and the corresponding solution. From the dual grids, the internal distribution of all horizontal forces in the networks can be understood in a glimpse, and since all dual grids are drawn at the same scale (except for (h) which is drawn at 2/3 of the scale), the overall magnitude of horizontal forces in the different solutions can be compared directly.

7.3 Discovering form

The methodology allows the designer freedom to sculpt three-dimensional shapes. Because of the extreme flexibility and freedom given by the multiple layers of constraints, the notion of free-form versus funicular design is blurred. The TNA framework balances control and discovery. The interdependencies caused by the geometrical constraints allow the understanding of the boundary conditions, but when optimized, natural shapes emerge within these definable boundaries. The designer has the impression that he can freely manipulate the form, but the solutions always satisfy equilibrium.

Figure 7.2 shows an example exploring some of the possible equilibrium solutions for the chosen radial primal grid Γ. All iterations have equal loads applied at each node. Since the scale factors of the dual grids vary largely, all dual grids are drawn to the same scale. Their scale factors are given as a function of the scale of the first solution, $\zeta^{(a)}$ (Figure 7.2). The dual grids have been rotated by 90 degrees in this example to more clearly relate the changes in them to their corresponding three-dimensional equilibrium solutions.

The exploration in Figure 7.2 starts from (a) which uses the default, automatically generated dual grid $\Gamma^{*(0)}$ which is symmetrical with approximately equal dual branch lengths. Its principal axes of symmetry are labeled as I and II. The actual scales, $\zeta^{(i)}$, of the dual grids for each iteration are given proportional to the scale factor $\zeta^{(a)}$ of the first solution. Starting from (a), several parameters are changed to demonstrate the elements which can be altered to explore and discover new funicular forms.

The first solution (a) uses the default dual grid $\Gamma^{*(0)}$. Both the inside and outside boundaries are fully supported. The solution space is defined by the horizontal planes $z = z^{LB}$ and $z = z^{UB}$. This results in a symmetrical solution $\Gamma^{(a)}$ and scale $\zeta^{(a)}$ for the dual grid $\Gamma^{*(a)}$.

Iteration (b) varies only one parameter of $\Gamma^{*(0)}$: stretching all dual branches crossing the axis of symmetry II. This means that more force is attracted to the corresponding set of branches along axis I in the primal grid, resulting in a shallower arch in the equilibrium solution $G^{(b)}$. The solution still has two axes of

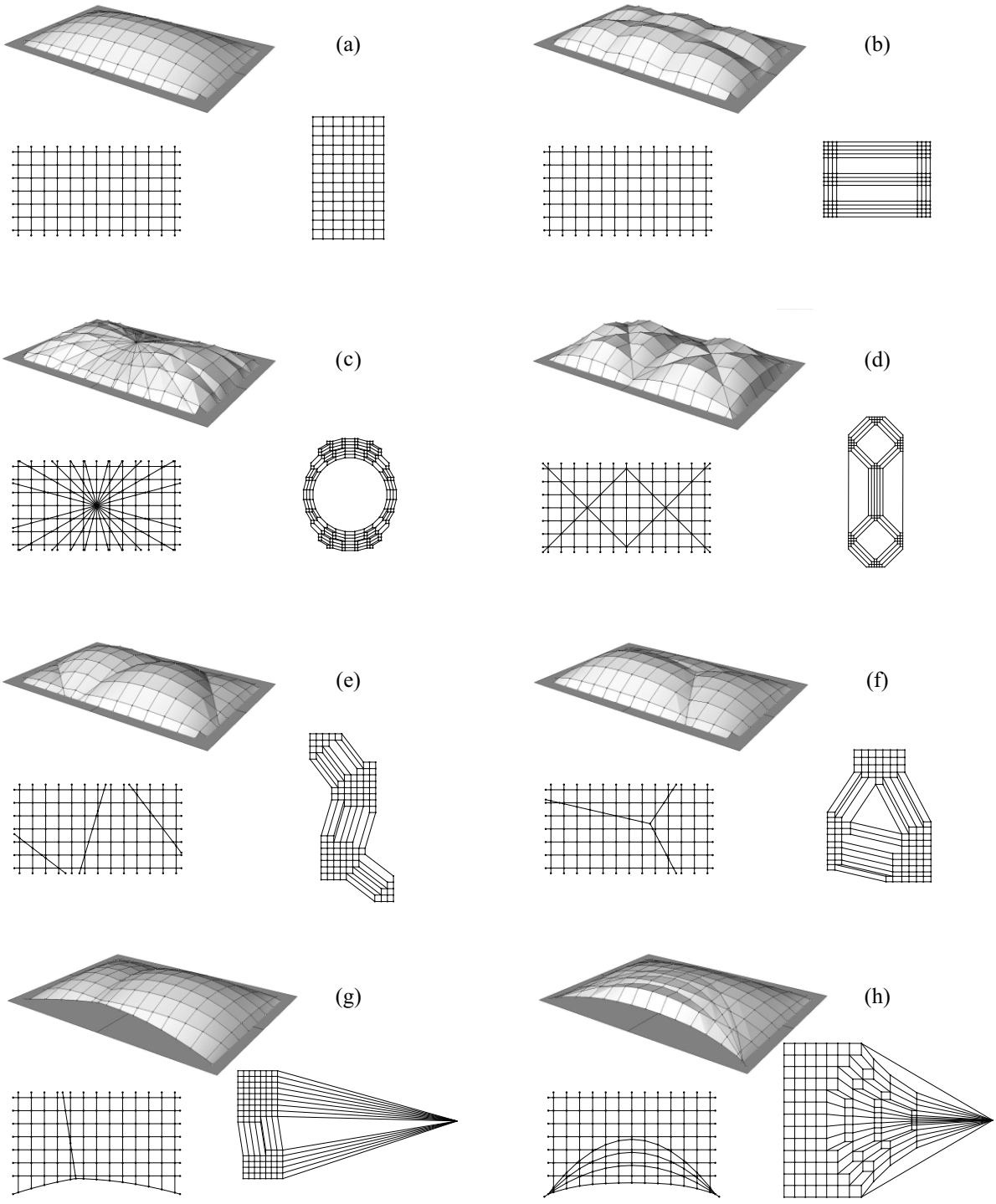

Figure 7.1 – A series of funicular compression forms, starting from a regular rectangular grid, showing the relationship between the geometries of the primal and dual grids and the corresponding equilibrium solution.

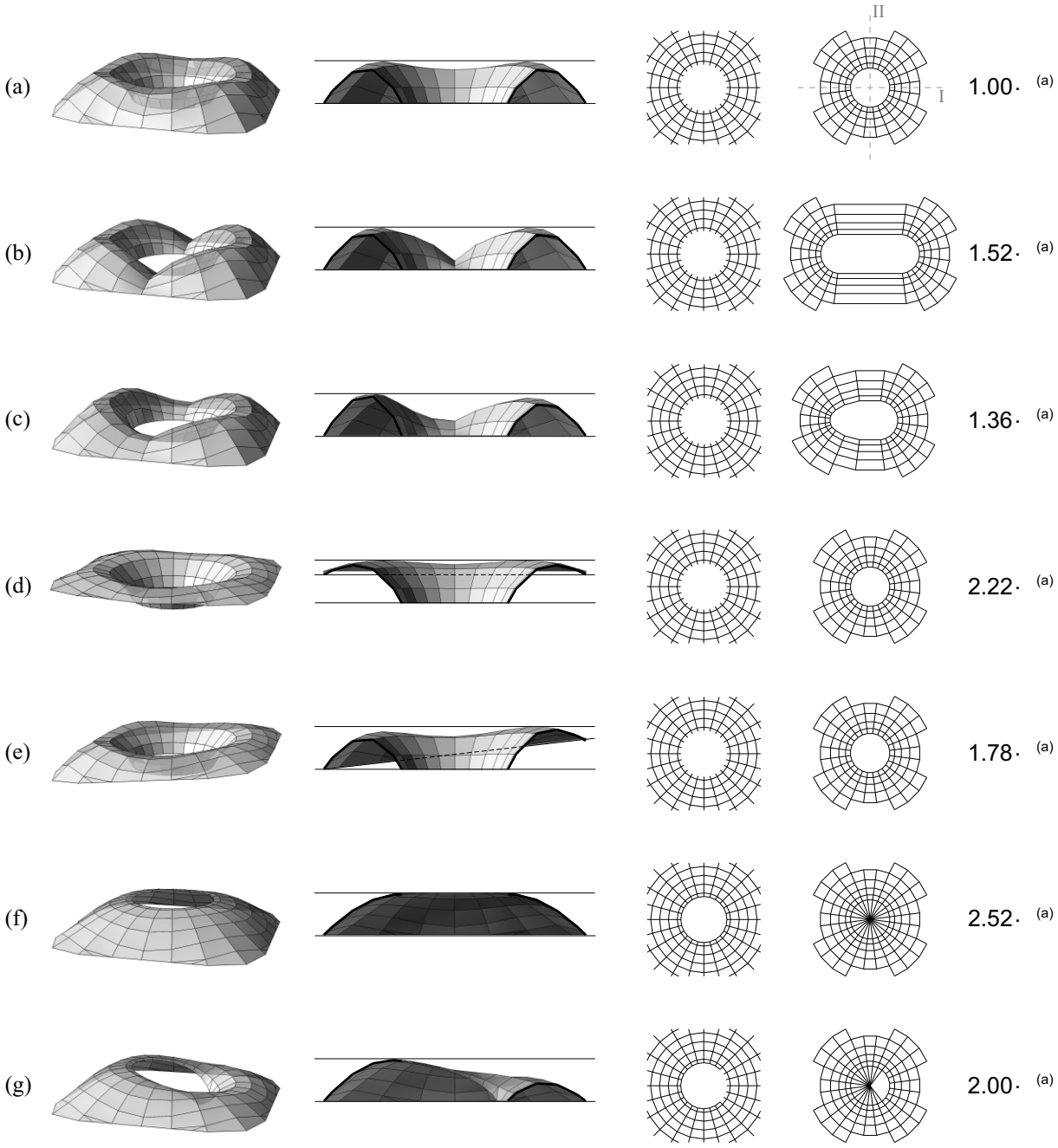

Figure 7.2 – A fast exploration using TNA showing for each iteration (from left to right) the 3-D equilibrium shape $G^{(\mathrm{i})}$, a section through $G^{(\mathrm{i})}$ within the solution space, the primal grid $\Gamma^{(\mathrm{i})}$ and dual grid $\Gamma^{*(\mathrm{i})}$ and its scale factor $\zeta^{(\mathrm{i})}$, defined as a function of the scale $\zeta^{(\mathrm{a})}$ of (a).

symmetry. The scale factor of $\zeta^{*(b)}$ is $1.52 \cdot \zeta^{(a)}$. The increase in scale factor can be understood because part of the structure is shallower, resulting in larger horizontal thrust.

Iteration (c) stretches the dual branches of $\Gamma^{*(0)}$ asymmetrically with respect to the axis I, resulting in the asymmetrical equilibrium solution $\Gamma^{(c)}$. The scale factor of $\zeta^{*(c)}$ is $1.36 \cdot \zeta^{(a)}$. The more gradual tweaks of the dual grid result in a shallower solution than (a), but slightly deeper than (b).

Iteration (d) uses the default dual $\Gamma^{*(0)}$ again, but changes the solution space. The lower bounds on the height of the outside boundary nodes are all increased by 3/4 of the height difference of the initial solution space, resulting in a funnel solution, $\Gamma^{(d)}$. The scale factor of $\zeta^{*(d)}$ is $2.2 \cdot \zeta^{(a)}$.

Iteration (e) heightens the lower bounds on the outside boundary nodes linearly from 0 to 3/4 of the height difference of the initial solution space, resulting in the tilted funnel, $\Gamma^{(e)}$. The scale factor of $\zeta^{*(e)}$ is $1.78 \cdot \zeta^{(a)}$.

Iteration (f) starts again from $\Gamma^{*(0)}$ and the initial solution space. Now, the inner edge support is released and $G^{(f)}$ receives an oculus. The equilibrium of the compression ring of the oculus is represented by the extra radiating branches in the center of $\Gamma^{*(f)}$. Since the compression ring is circular in plan, it forces the horizontal components of the branch forces ending in it to be equal, visualized by the equal lengths of the radiating branches. The scale factor of $\zeta^{*(f)}$ is $2.52 \cdot \zeta^{(a)}$.

In iteration (g), not all of the inner edge is released. The equilibrium of the freed inside boundary edge is again represented by the radiating branches in the center of $\Gamma^{*(g)}$. The scale factor of $\Gamma^{*(g)}$ is $2.0 \cdot \zeta^{(a)}$.

7.4 Exploiting indeterminacy

Perhaps even more so than the distribution of the internal forces, which can be controlled by manipulations of the dual grid, the choice of topology of the force network, represented in the primal grid, has an effect on the 3-D equilibrium solution. In §4.1.1 and §6.3, it was shown that for the assessment of masonry, not all networks are appropriate for certain load cases. In design on the other hand, the choice of primal grid can limit which shapes can be obtained, but it can also begin to suggest form. This will be illustrated with the two examples in Figure 7.3 which carry the same loads.

For both these examples, the front edge is no longer fully supported but instead a three-dimensional edge arch brings down the forces to the corner supports (Fig. 7.3). The edge arches for both cases have the same sag in plan. The primal and dual grids of the example in Figure 7.3a are the same, up to a scale, as for the pillow result in Figure 7.1a. So, the same force pattern, equally thrusting in both directions, is maintained until the forces are brought down to the supports by a single arch at the free edge. This arch is pretty shallow in plan, resulting in the large fan-like "funicular polygon" added to the right edge of the dual grid (see §4.1.3). This funicular polygon represents the equilibrium of the horizontal forces in the edge arch which grew very large in comparison to the forces inside the rest of the structure. This does not seem to be the most efficient way of re-directing the forces to the corner supports.

A more efficient way to bring down the thrusting forces to the supports is by having several three-dimensional arches pick up the forces earlier than in the edge arch, as shown in Figure 7.3b. In the corresponding force diagram the forces are now more equally distributed, i.e. the forces in the edge arch are less extreme compared to the forces inside the vault. In this result, slight "rippling" occurs due to the increased attraction of forces along these 3-D edge arches.

The difference in internal forces in the system can now drive the design of the profile of the actual

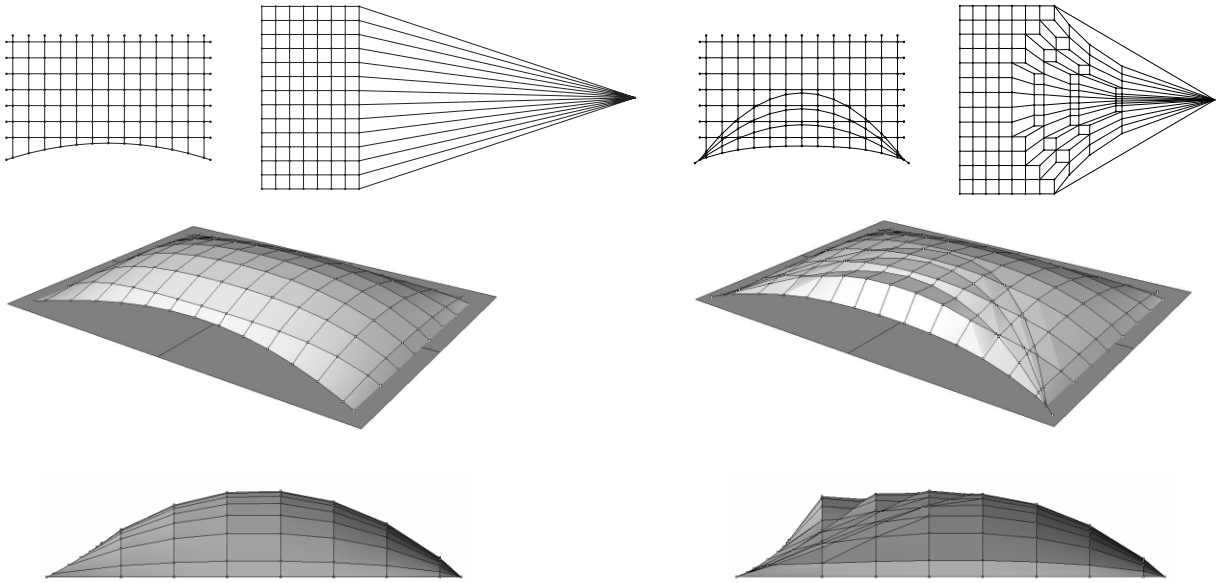

Figure 7.3 – Two grid shells supported on three edges. In (a) a single arch supports the free edge; and in (b) multiple arches support the free edge. [Note: the dual grid of (a) is drawn at 2/3 of the scale of (b).]

vault. When giving thickness to these equilibrium networks, the magnitude of the internal forces can be expressed. The first solution could be translated in a thin vault with a heavy edge arch. When realising the second equilibrium solution, a continuous vault containing the entire network could be chosen or the multiple internal arch action could be accentuated by following the rib pattern representing the designer's force logic and perhaps suggesting the actual flow of forces in this solution. These arches have attractive spatial and lighting qualities, and by actually making these creases in the surface, the structure is being stiffened locally, hence attracting more force. The structure will thus behave more as the designer imagined it.

7.5 Duality

For the spherical dome in Figure 7.4a the sunflower force pattern was inspired by the rib pattern of the Palazetto dello Sport by Pier Luigi Nervi and Annibale Vitellozzi in Rome, Italy, built in 1958 [Huxtable, 1960] .

The dual grid (Fig. 7.4b) for this sunflower pattern was generated automatically. It represents the equilibrium of the forces in the primal grid (Fig. 7.4a). Since the two grids have a reciprocal, or dual, relationship, their role can be reversed: the original primal grid (Fig. 7.4a) then becomes the representation of the forces in the original dual grid (Fig. 7.4b). Note that the force pattern with the oculus in Figure 7.4 is a solution with approximately equal horizontal forces in all elements since all branch lengths in its dual grid (Fig. 7.4a) are approximately the same.

Instead of generating the dual grid, one can also start from the dual force diagram to generate possible primal force patterns. In Figure 7.5a, starting from a piece of the aperiodic Penrose tiling [Penrose,

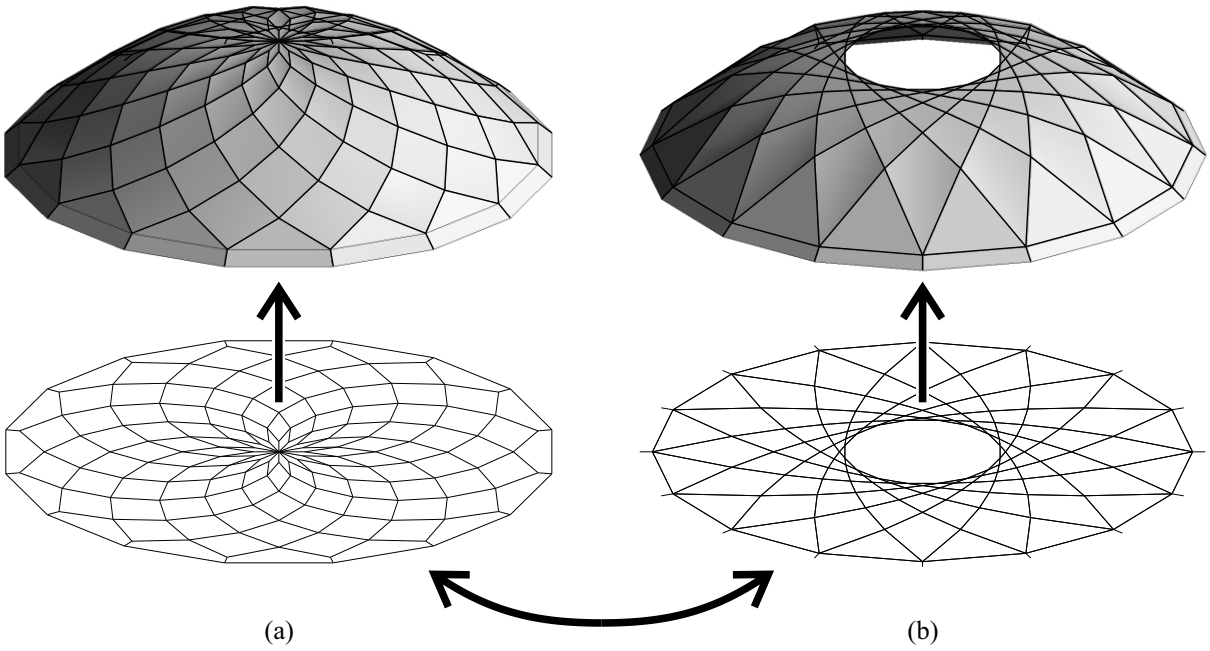

Figure 7.4 – The meaning of primal and dual grid can switch, since their relationship is reciprocal, as shown by these compression dome examples.

1989], which has equal branch lengths, the interesting five-way symmetric pentagrid was generated as a primal pattern. Figure 7.5b shows a small exhibition by the author in collaboration with the late Prof. Ture Wester of the Danish Royal Academy of Arts in Copenhagen, Denmark extending these ideas to the four-valent patterns obtained using a random stack of hairs. These hair patterns have a very similar topology as the pentagrid shown in Figure 7.5a, and their dual therefore looks like a distorted Penrose pattern.

These examples show that the automatic generation of a viable dual grid (see §4.2) not only allows the representation of an initial, possible distribution of the forces in the system in a visual manner, but can also lead to the discovery of new designs. The surprising emergence of a related pattern and the blurring of the boundaries between what drives the form exploration and what is driven, is particularly powerful in the TNA framework.

7.6 Designing the vault's section

The funicular shape is designed for the expected dead loading. This provides the overall geometry of the vault which will bring down the forces due to that specific, dominant loading using axial, compressive forces only. Theoretically, if this funicular loading is applied and the construction of the vault follows precisely the equilibrium solution and neglecting material crushing or elastic instabilities such as buckling, the vault could have a zero thickness. This is of course never the case. For long-span structures, the dead loads can be used to define the overall geometry, but the live loads should inform the shape or profile of the vault's section.

Two main strategies can be utilized to keep a funicular shape stable under live loading. Resistance to live

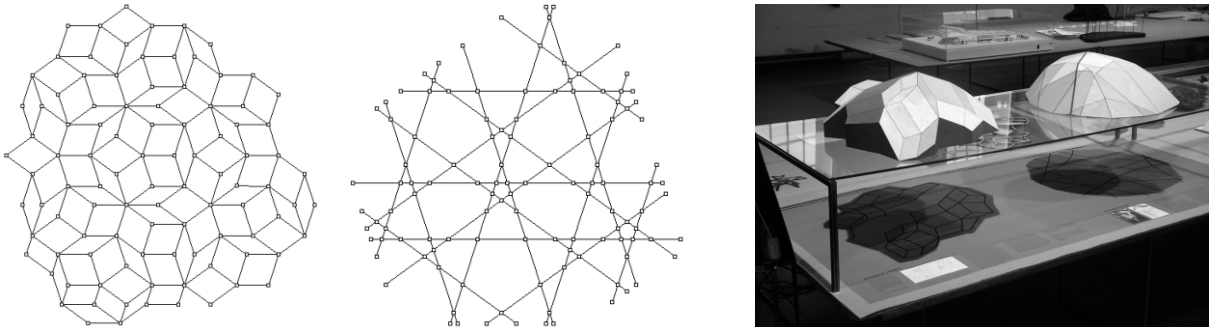

(a) (b)

Figure 7.5 – (a) The aperiodic Penrose tiling and the pentagrid are reciprocal figures. (b) Exhibition Digital Practice, organized by the Centre for Information Technology and Architecture (CITA), School of Architecture, The Royal Danish Academy of Fine Arts, March-April 2008.

loading can be achieved by 1) providing enough depth for all thrust lines or networks under live loading to cross through the vault's (middle third) section, or 2) providing bending stiffness. Providing enough depth (1) can be obtained by e.g. thickening the vault, adding stiffeners or diaphragms, undulating or "folding" in the other direction or by connecting shells. Ochsendorf and Block [2009] present a masonry design example exploring some of these concepts.

Finally, the funicular solutions under live loading can be used to quantify the amount of bending stiffness that needs to be added by relating it to the geometry of the vault. This is explained by Gerhardt [2002a; 2002b], Gerhardt et al. [2003], and Zalewski and Allen [1998] for 2-D examples, but wants to be extended to fully 3-d problems.

7.7 Summary

Like graphic statics for 2-D, Thrust Network Analysis is a holistic, bidirectional design and analysis tool. It is a truly 3-D extension, which allows for structurally informed architectural explorations, but also for sculptural escapades because of the possibility to exploit the structural indeterminacy. Instead of trying to find the "right" answer for the indeterminacy, the variations in equilibrium solutions become an added level of control and flexibility for the designer.

This chapter has illustrated the immense potential of the Thrust Network Analysis setup for the design of novel funicular structures.

Part IV

Conclusions

Chapter 8

Conclusions

8.1 Summary of results

The results of this dissertation are discussed in three parts: 1) the general development of the methodology; 2) its applications and contributions for the safety assessment of historical masonry vaults; and 3) applications for the design exploration of funicular vaulted structures.

8.1.1 Thrust Network Analysis Methodology

This dissertation presented Thrust Network Analysis (TNA), a novel computational methodology for exploring three-dimensional equilibrium. The approach allows the user to interactively find possible funicular solutions under gravitational loading within a defined envelope, and through the use of intuitive graphical methods, to gain control over the exploration of form.

TNA extends O'Dwyer's Force Network Method for funicular analysis of vaulted masonry structures [O'Dwyer, 1999] by introducing reciprocal figures to relate the geometry of the three-dimensional equilibrium networks to their internal forces, inspired by Williams [1986]. By using the duality between the network geometry and its reciprocal force diagram and by constraining the external loads to parallel loading cases, the equilibrium constraints are able to be linearized. To negotiate between the multiple degrees of freedom resulting from the structural indeterminacy of fully three-dimensional funicular networks, the form-finding problem is solved using optimization methods.

The TNA framework can be considered as a viable three-dimensional equivalent of graphic statics in that it offers clear graphical feedback of the forces in the system and a high level of control of the infinite number of equilibrium solutions for three-dimensional systems. The constraints which can be varied are:

- the network topology, represented by the primal grid Γ, which is the horizontal projection of the final equilibrium solution, the thrust network G;
- the distribution of the (horizontal) forces in the system, visualized and controlled by the dual grid Γ^*, which is geometrically constrained by its relation to the network's geometry;

- the solution space, defined by lower and upper bounds on the nodal height and the outline of the supports;
- the overall depth of the solution, controlled by the overall scale of the forces in the system; and
- the boundary conditions, i.e. fully or partially supported boundaries.

8.1.2 Assessment of masonry vaults

This dissertation has shown the ability of Thrust Network Analysis to obtain lower bound solutions for masonry vaulted structures with complex geometries and structural discontinuities. It demonstrated the value of TNA as a powerful new tool for understanding, visualizing and exploring the static stability of historic vaults in masonry. With this framework, a variety of structures have been analyzed in a very intuitive manner.

For the application as an assessment tool for unreinforced masonry structures the following properties are valuable. TNA allows the analyst to:

- find the range of lower-bound solutions bounded by a minimum and maximum thrust state, characterize the load capacity of a vault, and understand the indeterminate character of three-dimensional masonry;
- visualize clearly how forces are balanced in the vaults, using reciprocal force diagrams, or *horizontal thrust diagrams*;
- compare different assumptions on the principal structural action of vaults, and combine different structural actions
- in the chosen network topologies to capture the full indeterminacy of 3-D masonry vaults;
- include different measures of geometric safety, and establish limits or measures of stability for the vaults;
- obtain the vault's geometry and loads directly from detailed CAD models without abstraction or simplification;
- model structural discontinuities, such as cracks, crevices or block misalignments, by altering or constraining the allowable network geometries and topologies;
- examine and compare a wide range of different vault typologies, independent of the complexity of their geometry; and
- deal with non-proper boundary conditions, as for example, a vault supported only at the corners, and complex loading combinations.

8.1.3 Design of funicular vaults

Thrust Network Analysis (TNA) has tremendous potential as an interactive method for designing funicular vaulted structures. The form-finding method allows the designer to find possible equilibrium solutions under gravitational loading within a defined envelope. Using reciprocal diagrams and linear optimization,

it provides a graphical and intuitive method, adopting the same advantages of techniques such as graphic statics, but offering a viable extension to fully three-dimensional problems. TNA gives the designer a high level of control of all the degrees of freedom of a three-dimensional funicular system resulting in a flexible, "free" manipulation of the final shape and the creation of shapes going well beyond what is typically imagined as being funicular. It is a fast and interactive design tool for three-dimensional equilibrium systems, bringing structural intuition into the design process through intuitive, graphical diagrams and constructions and blurring the boundaries between funicular and free-form design.

8.2 Future work

This section identifies possible directions for the TNA framework to be developed further.

8.2.1 Assessment of complex masonry structures

The nonlinear extension of TNA (§5.2) needs to be fully implemented and validated. This would be an important improvement over the existing basic set-up. Within that new framework, if started from an overly redundant mesh containing all imaginable force paths, the optimal principal paths of force for complex structures could be identified. Rather than a brute force approach, a more interesting route would be to incorporate rules to actively suggest topological improvements, e.g. based on simple local mesh operations. The equivalence between reciprocal figures and (discrete) Airy stress functions as in Fraternali and Rochetta [2002] (§5.5) should be explored further. Their implementation of the geometric convex hull method has potential for simultaneously optimizing force pattern and distribution.

As discussed in §6.6, it is important to consider sliding. For three-dimensional structures, this might mean that the analysis runs through all the possible variations in force pattern and internal force distribution to identify the critical equilibrium states for sliding. The nonlinear extension in §5.2 is a first step in that direction, but this issue also asks for an "optimization" procedure varying the force topologies.

There is much research to be done in the area of understanding collapse mechanisms of fully three-dimensional systems. The possibility of using upper-bound analyses generating limit state thrust surfaces (§6.5) should be explored further with this regard. Discrete element modeling (DEM) (e.g. [Bićanić et al., 2003; DeJong et al., 2007; DeJong, 2009]) and experiments with physical models [Danyzy, 1732; Furstenau et al., 2010] could help to find correlations between thrust surfaces and possible collapse mechanisms. Once possible mechanisms have been identified, *combined kinematics and statics* could be added to the models to explore the limits of stability under imposed support displacements [Smars, 2000; Ochsendorf, 2002; Block et al., 2006].

Tilting a model can be used as an initial measure of the stability of vaults under lateral acceleration. The inclination is equivalent to applying an equivalent static horizontal force, for a first-order estimate of the seismic capacity of a vault [Gaß and Otto, 1990; Block et al., 2006; DeJong, 2009]. This may also be the best measure to compare the overall stability of different solutions. Since it is an upper-bound solution this solution is unique and is therefore independent of the choice of internal force distribution. For a given angle of tilt, the vault either stands or collapses.

Several interesting questions emerged when attempting a tilt analysis of three-dimensional structures, and applying TNA is not as simple as tilting the input geometry. First of all, the original force pattern chosen for the pure dead load case is not necessarily an appropriate pattern for the model in a tilted

state. Consider a simple spherical dome. Abraham's [1934] gradient approach to define sensible force trajectories immediately shows that the center of the radial pattern chosen for a dome wants to shift perpendicular to the rotation axis of the tilt. Furthermore, if started from a dome with typical radial cracks up to a certain height, the connectivity of the equilibrium network may need to be updated during the tilt.

Secondly, it exposes the inaccuracy of thrust line analysis (TLA) compared to the computation of the *locus of pressure points* [Moseley, 1833; Ochsendorf, 2002]. For vaulted structures with no tilt, the difference between the results obtained with TLA and LOP are minimal. In fact, TLA will result in a slightly more conservative solution. When centroids start to line up vertically, as for buttresses, or even "go back", as is the case for tilting models, the inaccuracies of TLA begin to appear. The thrust lines no longer make sense, but they can still be used to compute the locus of pressure points. Because TNA is a three-dimensional equivalent of TLA, this problem has an important implication for TNA since the force pattern cannot fold back onto itself which happens due to the non-sequential order of the centroids during a tilt. This issue needs to be addressed.

8.2.2 Revival of vaulted masonry design

From the author's stone pavilion project in Texas, it became very clear that the translation of the force patterns to an actual structure is far from obvious [Block et al., 2009]. During the design process, many interesting computational questions arose, such as how to offset a discretized, non-smooth network with non-planar faces, or how to best cut up a volumetric solution into stone voussoirs. It would be particularly interesting to develop algorithms to inform and automate the generation of cutting patterns for stone, inspired by the vault's typology, its topology, and also by the structural intent, as realized and made possible through the choice of force pattern.

Furthermore, masonry does not need to be limited to the traditional notion of stone or brick. Because funicular shapes tend to have low stresses, *block* structures could be built of different compression materials, such as glass, ice or even cement-stabilized pressed soil or compressed and recycled material.

The Guastavino vaulting technique allows the fast construction of vaulted structures with minimal formwork. One of the challenges to extend the use of this technique to more complex forms is the incorporation even within the initial form-finding method of all constraints related to the sequence of construction and the stability of the partly constructed vaults at any stage during construction. It also becomes significantly more challenging to control the curvature of more sophisticated, complex forms being built without formwork.

8.2.3 Beyond masonry

An interesting challenge is to extend the interpretation of the thrust network beyond being a representation of possible force paths through a vaulted structure. If considered as a possible bar-node system, then questions arise about rigidity, local buckling of elements and global geometric and elastic deformations and instabilities. In the case of such open structural systems, the issue of cladding comes up, which often brings in its own set of fabrication concerns [Schlaich and Schober, 2005; Pottmann et al., 2007]. Additional constraints related to materials, fabrication, erection, construction, cost or aesthetics could optimally all be included into a complex multi-objective optimization problem.

Furthermore, if single surface structures are used, the sensitivity of the structure to asymmetric loads

becomes much higher. Shell solutions are very sensitive to small changes in geometry; which can have an important effect on the performance of the structure [Ramm et al., 1997; Chilton, 2000]. Although the TNA approach is meant to be the initial design explorer, it would benefit from having some checks incorporated to give feedback on the sensitivity of certain solutions over others, as for example the idea that double curvature makes the surface stiffer, or that buckling can be checked using a simple global buckling equation [Chilton, 2000]. Another observation is that two variations in the exploration might not have significant structural differences under the design loads, but might be drastically different concerning their aerodynamic properties, water drainage or lighting qualities. In summary, the literal translation of the thrust networks obtained using TNA to "free-form" bar-node structures is not obvious and much more work can be done in this area.

8.2.4 Development of a design tool

Chapter 7 argued that the TNA framework has the potential to be a powerful *bidirectional design explorer* for discovering novel funicular shapes. The methodology and solving procedure has been developed in this dissertation, but has not been implemented in a fully interactive environment.

One important question is if the tool should be platform dependent or platform independent, i.e. implemented for a specific software platform or usable by itself such as interactive applets made in Java or Processing [Reas and Fry, 2007]. A clear benefit of such an approach is that the tool is independent of commercial licenses, but an important disadvantage is that the entire user interface and 3-D design environment needs to be developed, which is not at all an obvious task, particularly on the solver end. These tools are only considered useful when they have some way to export the geometry which can then be opened and manipulated in a commercial drawing software package.

Developing an independent (and hence very specific) design tool is less valuable than developing a plug-in for an existing, well-developed CAD environment, familiar to the computational and architectural designers. The software Rhinoceros is put forward as the best choice since it is widely used by architects, because of its reasonable license fees, active development team, open-source attitude, flexibility to add extra functionalities through scripting and external plug-ins, and large online user community, actively sharing knowledge and progress.

Several software companies recognize the value of linking or implementing their software to Rhinoceros, as a "companion with Rhino support" or as a "Rhino plug-in." The prototype of TNA, as currently implemented, can be considered as a crude "companion with Rhino support" in that it uses Rhino for both input and output. The current TNA tool could easily be made independent using MATLAB's Compiler [The Mathworks, 2009a], which lets you share a MATLAB application as an executable. Executables and libraries created with the MATLAB Compiler product use a runtime engine called the MATLAB Compiler Runtime (MCR). The MCR is provided with MATLAB Compiler for distribution with the application and can be deployed royalty-free [The Mathworks, 2009a].

A Rhino plug-in on the other hand is a software module that extends the functionality of Rhino by adding commands, features, or capabilities. The Rhino 4.0 Software Development Kit (SDK) provides the tools to develop native C++ or .NET plug-ins for Rhino 4.0 [McNeel, 2007]. This would allow the development of a fully interactive and bidirectional implementation of TNA, due to the fast solving times inherent to the implementation using matrix algebra and occasional (linear) optimization. The flexible Half-Edge data structure (§4.4) furthermore allows the user to interactively update both primal and dual topologies.

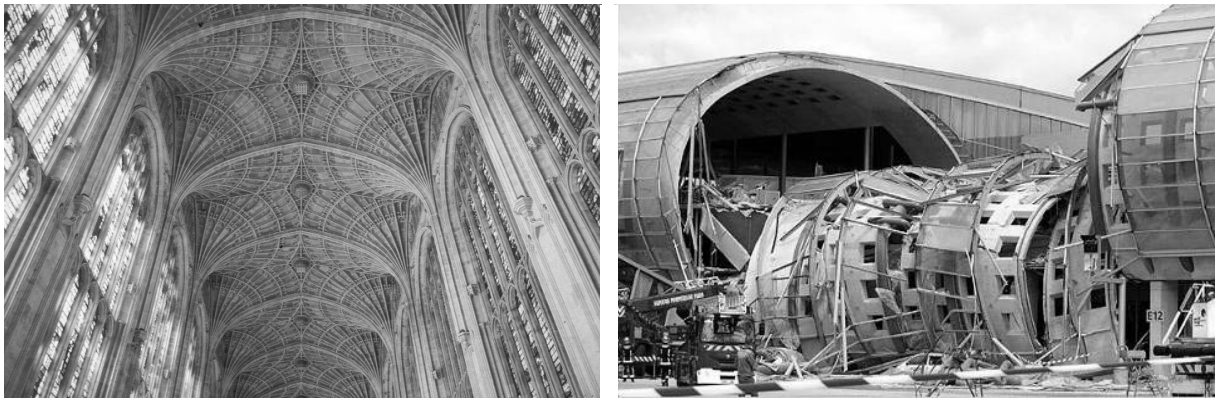

(a) (b)

Figure 8.1 – (a) King's College Chapel in Cambridge, England; (b) partially collapsed Terminal E of the Charles de Gaulle International Airport, France.

8.3 Final reflection

This dissertation is not just about advocating funicular form, but is grounded in the notion that designers have an important responsibility towards preserving architectural and historical heritage, nature's resources, and human life. The last image of this dissertation captures the essence – or at least the motivation – of this work.

Figure 8.1a illustrates the fan vaults of King's College Chapel in Cambridge, England, built by master mason John Wastell (c.1460-c.1515) from 1512 to 1515. These vaults are constructed of unreinforced stone, spanning 12.66 m, 28 m above the ground with a minimum thickness of only 10 cm, and complex anticlastic curvature. Though the stone vaults are filled with cracks, they have stood for 500 years.

Figure 8.1b illustrates the elliptical vaults of Terminal 2E of the Charles de Gaulle International Airport, France, by architect Paul Andreu (1938–), constructed from 1999 to 2004. It is a double shell assembly of 10cm thick reinforced concrete inner shell and glass and aluminum outer shell, spanning 33.5m, single curvature, construction cost of 750 million, which collapsed on 23 May 2004 at 7am, just one year after opening, killing 6 people with a reconstruction cost of 100 million.

This dissertation presented the Thrust Network Analysis method, a novel approach which explains why the fan vaults of King's College Chapel are standing, and allows the discovery of exciting, but structurally informed design alternatives for vaulted buildings.

References

Abraham, P. (1934). *Viollet-le-Duc et le Rationalisme Médiéval*. Paris: Fréal & Cie. 14, 65, 109, 110, 112, 142

Addis, B. (2005). A history of using scale models to inform the design of structures. In S. Huerta (Ed.), *Essays in the history of the theory of structures. In honour of Jacques Heyman*, Madrid, pp. 9–44. Instituto Juan de Herrera. 38

Addis, B. (2007). *Building: 3,000 Years of Design, Engineering and Construction*. London/NYC: Phaidon Press. 37

Airy, G. B. (1863). On the strain in the interior of beams. *Philosophical Transactions 153*, 49–79. 104

Andreu, A., L. Gil, and P. Roca (2007). Computational analysis of masonry structures with a funicular model. *Journal of Engineering Mechanics 133*(4), 473–480. 33, 40

Argyris, J. (1964). *Recent Advances on Matrix Methods in Structural Analysis*. Oxford: Pergamon Press. 56

Ash, P., E. Bolker, H. Crapo, and W. Whiteley (1988). Convex polyhedra, Dirichlet tessellations, and spider webs. In M. Senechal and G. Fleck (Eds.), *Shaping Space: A Polyhedral Approach*, Chapter 17, pp. 231–250. Boston: Birkhuser. 14, 47, 67, 68, 104, 106

Avis, D. and K. Fukuda (1992). A pivoting algorithm for convex hulls and vertex enumeration of arrangements and polyhedra. *Discrete and Computational Geometry 8*, 295–313. 106

Barber, C. B., D. P. Dobkin, and H. T. Huhdanpaa (1996). The Quickhull algorithm for convex hulls. *ACM Transactions on Mathematical Software 22*(4), 469–483. http://www.qhull.org. 83

Barnes, M. R. (1999). Form-finding and analysis of tension structures by dynamic relaxation. *International Journal of Space Structures 14*(2), 89–104. 37, 39

Barthel, R. (1993). *Tragverhalten gemauerter Kreuzgewölbe*. Number 34 in Aus Forschung und Lehre. Karlsruhe: Institut für Tragkonstruktionen, Universität Karlsruhe. 14, 28, 110, 112

Bertsimas, D. and J. N. Tsitsiklis (1997). *Introduction to Linear Optimization*. Belmont: Athena Scientific. 61, 90

Bićanić, N., C. Stirling, and C. J. Pearce (2003). Discontinuous modeling of masonry bridges. *Computational Mechanics 31*, 60–68. 141

Biggs, N. L. (1993). *Algebraic Graph Theory* (2nd ed.). Cambridge: Cambridge University Press. 56

Block, P. (2005, June). Equilibrium Systems: Studies in masonry structure. MS thesis, Massachusetts Institute of Technology, Cambridge, MA. 13, 21, 24, 28, 30, 85

Block, P., T. Ciblac, and J. A. Ochsendorf (2006). Real-time limit analysis of vaulted masonry buildings. *Computers and Structures 84*(29-30), 1841–1852. 20, 24, 28, 85, 141

Block, P., J. Curry, D. Escobedo, and J. Ochsendorf (2008-2009). Equilibrium y'all: Free-form unreinforced stone vault. `http://equilibriumstone.wordpress.com`. (Accessed March 1 2009). 142

Block, P., M. DeJong, and J. Ochsendorf (2006). As hangs the flexible line: Equilibrium of masonry arches. *The Nexus Network Journal 8*(2), 13–24. 141

Block, P. and J. Ochsendorf (2005). Interactive thrust line analysis for masonry structures. In G. Mochi (Ed.), *International Seminar on Theory and Practice of Construction: Knowledge, Means, and Models*, Ravenna, Italy, pp. 473–483. 51

Bondy, J. A. and U. S. R. Murty (1976). *Graph theory with applications*. New York: Elsevier Science Publishing Co. 56

Boothby, T. E. (2001). Analysis of masonry arches and vaults. *Progress in Structural Engineering and Materials 3*, 246–256. 27, 28

Bow, R. H. (1873). *Economics of construction in relation to framed structures*. London: Spon. 46

Calladine, C. R. (1978). Buckminster Fuller's 'tensegrity' structures and Clerk Maxwell's rules for the construction of stiff frames. *International Journal of Solids and Structures 14*(2), 161–172. 73

Calladine, C. R. (1983). *Theory of Shell Structures*. Cambridge: Cambridge University Press. 30

Calladine, C. R. (2005). Preliminary structural analysis of a Guastavino spiral staircase shell. In S. Huerta (Ed.), *Essays in the history of the theory of structures. In honour of Jacques Heyman*, Madrid, pp. 79–102. Instituto Juan de Herrera. 120

Chilton, J. (2000). *Heinz Isler*. The Engineer's Contribution to Contemporary Architecture. London: Thomas Telford Publishing. 37, 38, 143

Clifton, G. and G. Willis (2007). Dean's eye window: The reconstruction of a medieval rose window at Lincoln Cathedral. *The Structural Engineer 85*(3), 40–46. 119

Collins, G. R. (1968). The transfer of thin masonry vaulting from Spain to America. *The Journal of the Society of Architectural Historians 27*(3), 176–201. 119

Cremona, L. (1879). *Le Figure Reciproche nella Statica Grafica*. Milano: Ulrico Hoepli. 35, 46

Cremona, L. (1890). *Graphical Statics: Two Treatises on the Graphical Calculus and Reciprocal Figures in Graphical Statics. Translated by Thomas Hudson Beare*. Oxford: Clarendon Press. 35, 46

Culmann, C. (1864/1866). *Die graphische Statik*. Zürich: Verlag von Meyer & Zeller. 35

Culmann, C. (1875). *Die graphische Statik* (2., neubearbeite Auflage ed.). Zürich: Verlag von Meyer & Zeller. 35

Danyzy, A. A. H. (1732). Méthode générale pour déterminer la résistance qu'il faut opposer à la poussée des voûtes. *Histoire de la Société des Sciences établie à Montpellier 2*, 40–56. 13, 30, 32, 141

DeJong, M., L. De Lorenzis, and J. Ochsendorf (2007). Numerial modeling of masonry arch stability under impulse base motion. In M. Papadrakakis, D. C. Charmpis, N. D. Lagaros, and Y. Tsompanakis (Eds.), *ECCOMAS Conference on Computational Methods in Structural Dynamics and Earthquake Engineering, COMPDYN 2007*, Chania-Crete, Greece. 141

DeJong, M. J. (2009, June). *Seismic Assessment Strategies for Masonry Structures*. PhD dissertation, Massachusetts Institute of Technology, Cambridge, MA. 141

Dritsas, S. (2006). Voronoi diagrams. http://dritsas.net/doku.php?id=articles:voronoi_diagrams. (Accessed March 1, 2009). 14, 83

Eastman, C. M. (1982). Introduction to computer-aided design. unpublished. 84

Fenves, S. J. and F. H. Branin (1963). Network topological formulation of structural analysis. *Journal of the Structural Division, ASCE 89*, 483–514. 56

Föppl, A. (1892). *Das Fachwerk im Raume*. Leipzig: Verlag von B.G. Teubner. 13, 35, 36

Fraternali, F. (2003). Formulazione variazionale del problema di equilibrio di solidi elastici non reagenti a trazione. In *Proceedings of the 32nd Conference of the Italian Society for Stress Analysis, AIAS'03*, Salerno, Italy, pp. 1–10. 34

Fraternali, F., M. Angelillo, and A. Fortunato (2002). A lumped stress method for plane elastic problems and the discrete-continuum approximation. *International Journal of Solids and Structures 39*, 6211–6240. 14, 34, 105

Fraternali, F. and G. Rocchetta (2002). Shape optimization of masonry vaults. In *Proceedings of the Second International Conference on Advances in Structural Engineering and Mechanics, ASEM'02*, Busan, Korea, pp. 1–8. 13, 34, 40, 66, 105, 106, 141

Furstenau, J., W. W. Lau, P. Block, and J. Ochsendorf (2010). Equilibrium analysis of cracked masonry domes. *ICE Engineering and Computational Mechanics*. to be pblished. 141

García Ares, J. A. (2007). Un enfoque para el análisis límite de las escaleras de fábrica helicoidales. In M. Arenillas, C. Segura, F. Bueno, and S. Huerta (Eds.), *Actas del Quinto Congreso Nacional de Historia de la Construcción*, Madrid, pp. 335–343. Instituto Juan de Herrera. 15, 120, 122

Gaß, S. and F. Otto (1990). *Experiments*. Number 25 in Mitteilungen des Instituts fr Leichte Flchentragwerke (IL). Stuttgart: Universität Stuttgart. 141

Gerhardt, R. (2002a). *Anschauliche Tragwerklehre. Experimentele Darstellung von Biegemomenten mit Hilfe der Seillinie*. Aachen: Shaker Verlag. 35, 135

Gerhardt, R. (2002b). Reflections on the application of graphical methods to statical problems. In A. Becchi, M. Corradi, F. Foce, and O. Pedemonte (Eds.), *Towards a History of Construction*, Basel/Boston/Berlin, pp. 377–384. Birkhäuser. 135

Gerhardt, R., K.-E. Kurrer, and G. Pichler (2003). The methods of graphical statics and their relation to the structural form. In S. Huerta (Ed.), *Proceedings of the First International Congress on Construction History*, Madrid, pp. 997–1006. Instituto Juan de Herrera. 135

Gill, P. E. and W. Murray (1978). Algorithms for the solution of the nonlinear least-squares problem. *SIAM Journal on Numerical Analysis 15*(5), 977992. 98, 99

Gill, P. E., W. Murray, and M. H. Wright (1981). *Practical Optimization*. New York: Academic Press. 97

Gore, A. (2008). *Our purpose. The Nobel Peace Prize Lecture 2007*. Rodale Press. 20

Green, A. E. and W. Zerna (1968). *Theoretical elasticity* (2nd ed.). Oxford: Oxford Univeristy Press. 30

Greenwold, S. and E. Allen (2001). Active Statics [Computer software]. http://acg.media.mit.edu/people/simong/statics/data/index.html. (Accessed March 1, 2009). 35

Gründig, L., E. Moncrieff, P. Singer, and D. Ströbel (2000). A history of the principal developments and applications of the force density method in germany 1970-1999. In E. Papadrakakis (Ed.), *Proceedings of the Fourth International Colloquium on Computation of Shell & Spatial Structures, IASS-IACM 2000*, Chania-Crete, Greece. 37

Head, P. (2009). Entering an Ecological age: The engineer's role. *Civil Engineering 162*(2), 70–75. 20

Henrici, O. and G. C. Turner (1903). *Vectors and Rotors*. London: Edward Arnold. 47, 48

Heyman, J. (1966). The stone skeleton. *International Journal of Solids and Structures 2*, 249–279. 30, 44

Heyman, J. (1967). Spires and fan vaults. *International Journal of Solids and Structures 3*, 243–257. 114

Heyman, J. (1968). On the rubble vaults of the middle ages and other matters. *Gazette des Beaux-Arts 71*, 177–188. 109

Heyman, J. (1977). *Equilibrium of Shell Structures*. Oxford Engineering Science Series. Oxford: Clarendon Press. 13, 30, 31, 114

Heyman, J. (1982). *The Masonry Arch*. Chichester: Ellis Horwood. 91

Heyman, J. (1995). *The Stone Skeleton: Structural engineering of masonry architecture*. Cambridge: Cambridge University Press. 24, 27, 110, 114, 117

Heyman, J. (2002). Rose windows. In H. R. Drew and S. Pellegrino (Eds.), *New Approaches to Structural Mechanics, Shells and Biological Structures*, Dordrecht/Boston/London, pp. 115–125. Kluwer Academic Publishers. 118, 119

Hooke, R. (1675). *A description of helioscopes, and some other instruments*. London: John Martyn. 33

Huerta, S. (2001). Mechanics of masonry vaults: The equilibrium approach. In P. B. Lourenço and P. Roca (Eds.), *Proceedings of Historical Constructions*, Guimarães, pp. 47–69. 24, 27

Huerta, S. (2003). Mechanics of timbrel vaults: A historical outline. In A. Becchi, M. Corradi, F. Foce, and O. Pedemonte (Eds.), *Essays on the History of Mechanics: In Memory of Clifford Ambrose Truesdell and Edoardo Benvenuto*, Basel/Boston/Berlin, pp. 89–133. Birkhäuser. 119

Huerta, S. (2004). *Arcos bóvedas y cúpulas. Geometría y equilibrio en el cálculo tradicional de estructuras de fábrica*. Madrid: Instituto Juan de Herrera. 27

Huerta, S. (2008). The analysis of masonry architecture: A historical approach. *Architectural Science Review 51*(4), 297–328. 27, 28

Huerta, S. and K.-E. Kurrer (2008). Zur baustatischen Analyse gewölbter Steinkonstruktionen. In W. Jäger (Ed.), *Mauerwerk-Kalender*, pp. 373–422. Berlin: Ernst & Sohn. 27

Huxtable, A. L. (1960). *Pier Luigi Nervi*. Masters of world architecture series. New York: G. Braziller. 133

Isler, H. (1959). New shapes for shells. In *International Colloquium on construction Processes of Shell Structures, IASS Bulletin*, Volume 8, Madrid. IASS, Alfonso XII. 13, 24, 25

Kilian, A. (2004a). CADenary tool v.1 [Computer software]. http://www.designexplorer.net/projectpages/cadenary.html. (Accessed March 1, 2009). 13, 39, 40

Kilian, A. (2004b). Linking digital hanging chain models to fabrication, fabrication: Examining the digital practice of architecture. In *Proceedings of the 23rd Annual Conference of the Association for Computer Aided Design in Architecture and the 2004 Conference of the AIA Technology in Architectural Practice Knowledge Community*, Cambridge, ON, pp. 110–125. 39, 65

Kilian, A. (2006a, February). *Design Exploration through Bidirectional Modeling of Constraints*. PhD dissertation, Massachusetts Institute of Technology, Cambridge, MA. 35, 37, 65, 128

Kilian, A. (2006b). Hanging modeler: CADenary tool v.2 [Computer software]. http://www.designexplorer.net/newscreens/cadenarytool/cadenarytool.html. (Accessed March 1, 2009). 13, 39, 40

Kilian, A. (2007). Steering of form. *Journal of the International Association for Shell and Spatial Structures 48*(4), 17–21. 33

Kilian, A. and J. Ochsendorf (2005). Particle-spring systems for structural form finding. *Journal of the International Association for Shell and Spatial Structures 46*(2), 77–85. 39, 50

Leedy, W. C. (1980). *Fan vaulting: A study of form, technology, and meaning*. Santa Monica: Arts + Architecture Pres. 114

Legakis, J. (1998). Half-Edge data structures. http://groups.csail.mit.edu/graphics/classes/6.838/S98/meetings/m4/homepage.html. (Accessed March 1 2009). 14, 84, 85

Levenberg, K. (1944). A method for the solution of certain non-linear problems in least squares. *The Quarterly of Applied Mathematics 2*, 164–168. 98

Lin, L. H. and W. Sobek (1998). Structural hierarchy in spider webs and spiderweb-type systems. *The Structural Engineer 76*(4), 59–64. 14, 69

Linkwitz, K. and H.-J. Schek (1971). Einige bemerkung von vorsgepannten seilnetzkonstruktionen. *Ingenieur-Archiv 40*, 145 158. 37, 59

Livesley, R. K. (1978). Limit analysis of structures formed from rigid blocks. *Journal for Numerical Methods in Engineering 12*, 18531871. 31

Livesley, R. K. (1992). A computational model for the limit analysis of three-dimensional masonry structures. *Meccanica 27*(3), 161–172. 31

LoveToKnow (2006). Diagrams in mechanics (based on the 11th edition of the Encyclopedia Britannica, pub. 1911). http://www.1911encyclopedia.org/Diagrams_in_mechanics. (Accessed March 1, 2009). 46

Mackenzie, F. (1840). *Observations on the construction of the roof of King's College Chapel, Cambridge. With illustrative plans, sections, and details, from actual measurement*. London: J. Weale. 14, 114, 115

Mahdavi, A., P. Mathew, S. Kumar, and N.-H. Wong (1997). Bi-directional computational design support in the SEMPER environment. *Automation in Construction 6*, 353–373. 128

Mandal, P. and C. R. Calladine (2008). Vibrational frequencies of a Guastavino spiral staircase shell. In J.-F. Chen, J. Y. Ooi, and J. G. Teng (Eds.), *Structures and granular solids. From Scientific Principles to Engineering Application*, London, pp. 231–244. Taylor & Francis Group. 120

Mark, R. (1982). *Experiments in Gothic structure*. Cambridge: The MIT Press. 14, 109, 110

Marquardt, D. (1963). An algorithm for least-squares estimation of nonlinear parameters. *SIAM Journal on Applied Mathematics 11*, 431441. 98

Maunder, E. A. W. (2005). Staircases as cantilevers or arches? A question for limit analysis. In C. Modena, P. Lourenço, and P. Roca (Eds.), *Structural Analysis of Historical Constructions*, London, pp. 569–576. Taylor & Francis Group. 120

Maxwell, J. C. (1864). On reciprocal figures and diagrams of forces. *Philosophical Magazine and Journal Series 4*(27), 250–261. 46, 50, 72

Maxwell, J. C. (1869). On reciprocal diagrams in space and their relation to Airy's function of stress. *Proceedings of the London Mathematical Society 2*, 58–60. 44, 104, 105

McNeel, R. (2007). RHINOCEROS©: NURBS modeling for Windows [Computer software]. http://www.rhino3d.com/. 64, 87, 143

Mehrotra, S. (1992). On the implementation of a primal-dual interior point method. *SIAM Journal on Optimization 2*, 575–601. 90

Micheletti, A. (2008). On generalized reciprocal diagrams for self-stressed frameworks. *International Journal of Space Structures 23*(3), 153–166. 46

Moseley, H. (1833). On a new principle in statics, called the principle of least pressure. *Philosophical Magazine 3*, 285–288. 31, 142

Ney, L. and I. Strauven (2006). *Ney & Partners: Freedom of Form Finding*. Number 6 in Young Architects in Flanders. Antwerpen: VAi - Vlaams Architectuurinstituut. 128

Nikolinakou, M., A. Tallon, and J. Ochsendorf (2005). Structure and form of early flying buttresses. *Revue Européenne de Génie Civil 9*(9-10), 1191–1217. 28, 126

Ochsendorf, J. (2009). *Guastavino Vaulting: The Art of Structural Tile*. New York: Princeton Architectural Press. 119

Ochsendorf, J. and P. Block (2009). Designing unreinforced masonry. In E. Allen and W. Zalewski (Eds.), *Form and Forces: Designing Efficient, Expressive Structures*, Chapter 8. New York: John Wiley Sons. 135

Ochsendorf, J. A. (2002, June). *Collapse of masonry structures*. PhD dissertation, University of Cambridge, Cambridge, UK. 27, 31, 141, 142

O'Dwyer, D. W. (1991, June). Limit state analysis of masonry vaults. M.Eng.Sc. thesis, University College, Galway, Ireland. 31

O'Dwyer, D. W. (1999). Funicular analysis of masonry vaults. *Computers and Structures 73*(1-5), 187–197. 13, 14, 31, 32, 40, 43, 44, 65, 66, 91, 92, 110, 139

Parland, H. (1979). Basic principles of the structural mechanics of masonry : a historical review. *International Journal of Masonry Construction 2*, 48–58. 126

Parland, H. (1995). Instability of rigid body assemblages with dilatant interfacial contact sliding. *International Journal of Solids and Structures 32*(2), 203–234. 126

Pellegrino, S. and C. R. Calladine (1986). Matrix analysis of statically and kinematically indeterminate frameworks. *International Journal of Solids and Structures 22*(4), 409–428. 74

Penrose, R. (1989). *The Emperor's New Mind: Concerning Computers, Minds and The Laws of Physics*. Oxford: Oxford University Press. 133

Pew Center (2008). Pew Center on Global Climate Change. `http://www.pewclimate.org/`. (Accessed March 1, 2009). 20

Pieper, K. (1983). *Sicherung historischer Bauten*. Berlin: Ernst. 110

Poleni, G. (1748). *Memorie istorische della Gran Cupola del Tempio Vaticano*. Padova: Nella Stamperia del Seminario. 33

Pottmann, H., A. Asperl, M. Hofer, and A. Kilian (2007). *Architectural Geometry*. Bentley Institute Press. 14, 83, 110

Pottmann, H., Y. Liu, J. Wallner, A. Bobenko, and W. Wang (2007). Geometry of multi-layer freeform structures for architecture. In *ACM SIGGRAPH 2007*, New York. ACM. 142

Preparata, F. R. and M. I. Shamos (1985). *Computational Geometry: An Introduction*. New York: Springer-Verlag. 83

Price, S. (1996). Cantilevered staircases. *Architectural Research Quarterly 1*, 76–87. 119

Pugnale, A. and M. Sassone (2007). Morphogenesis and structural optimization of shell structures with the aid of a genetic algorithm. *Journal of the International Association for Shell and Spatial Structures 48*(3), 161–166. 35

Ramage, M., J. Ochsendorf, P. Block, and P. Rich (2008). Advanced geometry, rudimentary construction: Structural formfinding for unreinforced thin-shell masonry vaults. In H. Pottmann, A. Kilian, and M. Hofer (Eds.), *Advances in Architectural Geometry, AAG08*. Poster. 20

Ramm, E., K.-U. Bletzinger, and K. Maute (1997). Structural optimization. In J. Abel, R. Astudillo, and N. Srivastava (Eds.), *Current and Emerging Technologies of Shell and Spatial Structures. Proceedings of the IASS Colloquium*, Madrid, Spain, pp. 201–216. 35, 143

Ramm, E., K.-U. Bletzinger, and R. Reitinger (1993). Shape optimization of shell structures. *Bulletin of the International Association for Shell and Spatial Structures 34*(2), 103–122. 35

Rave, W. (1939). Uber die statik mittelalterlicher gewölbe. *Deutsche Kunst- und Denkmalpflege 1939/1940*, 193–198. 14, 109, 111

Reas, C. and B. Fry (2007). *Processing: A Programming Handbook for Visual Designers and Artists*. Cambridge: The MIT Press. 39, 143

Rutten, D. (2007). *RhinoScript^{TM} 101 for Rhinoceros 4.0*. Robert McNeel Associates. 64, 87

Sabouret, V. (1928). Les voûtes d'arrètes nervures. rôle simplement décoratif des nervures. *Le Génie Civil 92*, 205–209. 109, 110

Schek, H.-J. (1974). The force density method for form finding and computation of general networks. *Computer Methods in Applied Mechanics and Engineering 3*(1), 115–134. 13, 39, 43, 55, 58, 97, 100

Schlaich, J. and K. Schäfer (1991). Design and detailing of structural concrete using strut-and-tie models. *The Structural Engineer 69*(6), 113125. 44

Schlaich, J. and H. Schober (2005). Freeform glass roofs. In *Metropolis & Beyond, Proceedings of the 2005 Structures Congress and the 2005 Forensic Engineering Symposium*, NYC, New York. 142

Serebryakova, Y. (2006). Von der natur gefangen. Frei Otto, Architekt. http://www.uni-stuttgart.de/impulse/imp/alles.php?id=6. (Accessed March 1 2009). 37

Smars, P. (2000, March). *Etudes sur la stabilité des arcs et voûtes. Confrontation des méthodes de l'analyse limite aux voûtes gothiques en Brabant.* PhD dissertation, Katholieke Universiteit Leuven, Leuven, Belgium. 13, 28, 30, 141

Sobek, W. (1987). *Auf pneumatisch gestützten Schalungen hergestellte Betonschalen.* PhD dissertation, Universität Stuttgart, Stuttgart, Germany. 96

Swain, G. F. (1927). *Structural Engineering Stresses, Graphical Statics, and Masonry.* New York: McGraw-Hill Book Company. 28

The Mathworks (1994-2009a). MATLAB® Compiler™. http://www.mathworks.com/products/compiler/. 143

The Mathworks (1994-2009b). MATLAB®: The language of technical computing [Computer software]. http://www.mathworks.com/products/matlab/. 64, 87

The Mathworks (1994-2009c). Optimization Toolbox™ for MATLAB®. http://www.mathworks.com/products/optimization/. 61, 64, 87, 97

Tombesi, P. (2004). Sloppily built or precisely loose? The technology of the curtain and the ideology of Disney Hall. *Architectural Research Quarterly 8*(3-4), 246–259. 22

Tomlow, J., R. Graefe, F. Otto, and H. Szeemann (1989). *Das Modell / The Model / El Modelo.* Number 34 in Mitteilungen des Instituts fr Leichte Flchentragwerke (IL). Stuttgart: Universität Stuttgart. 35, 38

Ungewitter, G. (1890). *Lehrbuch der gotischen Konstruktionen* (III. Auflage neu bearbaitet von K. Mohrmann ed.). Leipzig: T.O. Weigel Nachfolger. 13, 14, 27, 28, 29, 109, 111

Viollet-le Duc, E. E. (1854-1868). *Dictionnaire raisonné de l'architecture franaise du XIe au XVIe siècle*, Volume Vol. 2, 'Construction'. Paris: B. Bance. 14, 86, 109

Voronoi, G. (1907). Nouvelles applications des paramètres continus à la théorie des formes quadratiques. *Journal für die reine und angewandte Mathematik 133*, 97–178. 83

Wester, T. (1997). The structural morphology of basic polyhedra. In J. F. Gabriel (Ed.), *Beyond the Cube: The Architecture of Space Frames and Polyhedra*, Chapter 11, pp. 301–342. New York: John Wiley & Sons. 8

Whiteley, W. (1986). Two algorithms for polyhedral pictures. In *Proceedings of the Second Annual Symposium on Computational Geometry. SCG '86*, New York, NY, pp. 142–149. ACM Press. 14, 105

Whiting, E., F. Durand, and J. Ochsendorf (2009). Procedural modeling of structurally-sound masonry buildings. unpublished. 13, 31, 32, 40

Williams, C. J. K. (1986). Defining and designing curved flexible tensile surface structures. In J. A. Gregory (Ed.), *The mathematics of surfaces*, pp. 143–177. 13, 39, 43, 46, 47, 139

Williams, C. J. K. (1990). The generation of a class of structural forms for vaults and sails. *The Structural Engineer 68*(12), 231–235. 94

Wittmann, W. (1879). Zur Theorie der Gewölbe. *Zeitschrift für Bauwesen 26*, 61–74. 13, 28, 29

Wolfe, W. S. (1921). *Graphical Analysis: A handbook on graphic statics*. New York: McGraw-Hill Book Company. 13, 14, 28, 29, 88

Zalewski, W. and E. Allen (1998). *Shaping Structures*. New York: John Wiley & Sons. 35, 46, 135

Zhang, Y. (1995). Solving large-scale linear programs by interior-point methods under the MATLAB environment. Technical report, Department of Mathematics and Statistics, University of Maryland, Baltimore, MD. 90

Relevant publications by author

Block, P. (2005, June). Equilibrium Systems: Studies in masonry structure. MS thesis, Massachusetts Institute of Technology, Cambridge, MA.

Block, P. and J. Ochsendorf (2005). Interactive thrust line analysis for masonry structures. In G. Mochi (Ed.), *Theory and Practice of Construction: Knowledge, Means, and Models*, Ravenna, Italy, pp. 473–483.

Block, P., M. DeJong, and J. Ochsendorf (2006). As hangs the flexible line: Equilibrium of masonry arches. *The Nexus Network Journal 8*(2), 13–24.

Block, P., T. Ciblac, and J. A. Ochsendorf (2006). Real-time limit analysis of vaulted masonry buildings. *Computers and Structures 84*(29-30), 1841–1852.

Block, P. and J. Ochsendorf (2007). Thrust Network Analysis: A new methodology for three-dimensional equilibrium. *Journal of the International Association for Shell and Spatial Structures 48*(3), 167–173.

Ramage, M., J. Ochsendorf, P. Block, and P. Rich (2008). Advanced geometry, rudimentary construction: Structural formfinding for unreinforced thin-shell masonry vaults. In H. Pottmann, A. Kilian, and M. Hofer (Eds.), *Advances in Architectural Geometry, AAG08*, Vienna, Austria. Poster.

Block, P. and J. Ochsendorf (2008). Lower-bound analysis of masonry vaults. In D. D'Ayala, E. Fodde (Eds.), *Structural Analysis of Historical Constructions: Proceedings of the VI International Conference on Structural Analysis of Historic Construction, SAHC08*, Bath, UK.

Ochsendorf, J. and P. Block (2009). Designing unreinforced masonry. In E. Allen and W. Zalewski (Eds.), *Form and Forces: Designing Ecient, Expressive Structures*, Chapter 8. New York: John Wiley Sons.

Block, P. and J. Ochsendorf (2009). Exploiting structural indeterminacy for shell design. In *Proceedings of the IASS Symposium 2009, Evolution and Trends in Design, Analysis and Construction of Shell and Spatial Structures*, Valencia, Spain. In preparation.

Furstenau, J., W. W. Lau, P. Block, and J. Ochsendorf (2010). Equilibrium analysis of cracked masonry domes. *ICE Engineering and Computational Mechanics*. To be published.

Block, P. and J. Ochsendorf (2010). Thrust network analysis of vaulted masonry structures. *International Journal of Architectural Heritage*. In preparation.